Flow in Porous Media with Special Reference to Breakwater Structures

Andersen, O. Holst

Publication date:
1994

Document Version
Publisher's PDF, also known as Version of record

Hydraulics & Coastal Engineering Laboratory
Department of Civil Engineering
Aalborg University
SERIES PAPER No. 7

ISSN 0909 - 4296

FLOW IN POROUS MEDIA

WITH SPECIAL REFERENCE

TO BREAKWATER STRUCTURES

Ole Holst Andersen

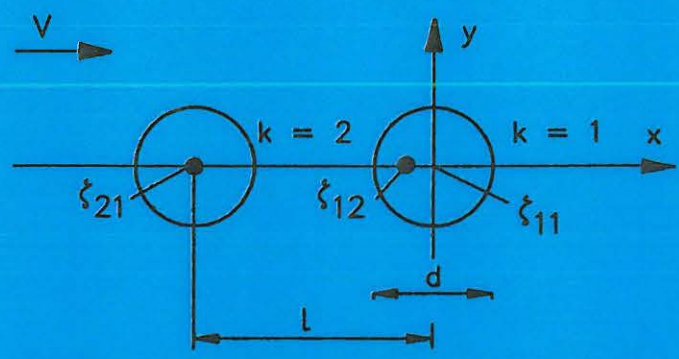

Hydraulics and Coastal Engineering Laboratory
Aalborg University
in collaboration with
Danish Hydraulic Institute
supported by
the Danish Research Academy

April 1994

Hydraulics & Coastal Engineering Laboratory
Department of Civil Engineering
Aalborg University
Sohngaardsholmsvej 57
DK-9000 Aalborg, Denmark

ISSN 0909-4296
SERIES PAPER No. 7

FLOW IN POROUS MEDIA WITH SPECIAL REFERENCE TO BREAKWATER STRUCTURES

by

Ole Holst Andersen

April 1994

FLOW IN POROUS MEDIA

WITH SPECIAL REFERENCE

TO BREAKWATER STRUCTURES

Ole Holst Andersen

Hydraulics and Coastal Engineering Laboratory
Aalborg University
in collaboration with
Danish Hydraulic Institute
supported by
the Danish Research Academy

April 1994

Published 1994 by
Hydraulics and Coastal Engineering Laboratory
Aalborg University
in collaboration with
Danish Hydraulic Institute
supported by
the Danish Research Academy

Printed in Denmark by
Centertrykkeriet, Aalborg University

ISBN 87-90034-06-6
ISSN 0909 - 4296

PREFACE

The present thesis is submitted as a requirement for obtaining the Ph.D. degree at Aalborg University, AU, according to notice No 627 of 17 October 1988 from the Danish Ministry of Education. The study was carried out as a collaboration between the Hydraulics and Coastal Engineering Laboratory at AU and Danish Hydraulic Institute, DHI. The study was financed by DHI together with the Danish Research Academy.

The author is grateful to his principal supervisor Professor H.F. Burcharth, AU, to Ph.D. Per A. Madsen, International Centre for Computational Hydrodynamics, ICCH, who was co-supervisor during the last period of the study concentrating on numerical modelling and to M.Sc. Ole Juul Jensen, DHI, who was initially co-supervisor. Further the author wishes to express his gratitude to M.Sc. Michael Fischer, DHI, who made SYSTEM 3xz forming the hydrodynamic basis for the berm breakwater model, to M.Sc. Jørgen Juhl, DHI, who was involved in the development of SYSTEM 3xz and for interesting discussions on berm breakwaters and to Ph.D. Erik Asp Hansen, DHI, for valuable discussions on virtual mass and the image method. Thanks are also directed to Mrs Yolande Rosenqvist, DHI, for careful typing of the report and to Mrs Grete Jespersen, DHI, for preparing the illustrations.

Hørsholm, April 1994

Ole Holst Andersen

Ole Holst Andersen

CONTENTS

LIST OF SYMBOLS

A	[m^2]	area
C_D		drag coefficient
C_L		lift coefficient
C_M		virtual mass coefficient
C_a		added mass coefficient
C_a^*		added mass coefficient
C_d		drag coefficient
C_d^*		drag coefficient
C_d^W		drag coefficient
C_m		virtual mass coefficient
C_m^*		virtual mass coefficient
C_m^G		virtual mass coefficient
C_m^S		virtual mass coefficient
C_m^W		virtual mass coefficient
D	[m]	characteristic length
D_n	[m]	nominal diameter (equivalent cube length)
D_{n50}	[m]	nominal diameter, 50 percent exceedance
F	[N]	force on area, A
F	[N] or [N/m]	force or force per unit length on single obstacle
F_D	[N]	drag force
F_I	[N]	inertia force
F_L	[N]	lift force
F_N	[N]	normal force
$F(V)$	[s/m]	linearised flow resistance
G		gradation parameter
H	[m]	wave height
H_{ref}	[m]	reference wave height
H_{input}	[m]	input wave height
H_{m0}	[m]	wave height based on 0'th moment of spectral density
H_s	[m]	significant wave height
H^*		dimensionless wave height
I		hydraulic gradient
J	[m/s]	volumetric flux
K	[m/s]	permeability coefficient
K_s	[m^2]	specific permeability (intrinsic permeability)
K_{cyl}		coefficient in virtual mass expression
K_{sph}		coefficient in virtual mass expression
KC		Keulegan-Carpenter number
L_o	[m]	deep water wave length
M	[m^2] or [m^3]	strength of doublet
M_{50}	[kg]	mass of armour stone, 50 percent exceedance
N		total number of surface particles within reference area, A
N_{disp}		number of displaced particles within reference area, A
N_w		number of waves
P		permeability coefficient
Q	[m^3/s]	volumetric flow
R	[m]	hydraulic radius
R_χ	[m]	modified hydraulic radius
Re		Reynolds number
Re^*		grain Reynolds number

R_U	[m]	run-up level
R_D	[m]	run-down level
S	[m^{-1}]	grain surface area per unit volume
S		flow direction parameter
S		cumulated damage
T		turtuosity
T	[s]	wave period
T_{ref}	[s]	reference wave period
T_{02}	[s]	wave period based on 0'th and 2nd moments of spectral density
T_m	[s]	average wave period
T^*		dimensionless wave period
T'	[s]	characteristic period
U	[m/s]	characteristic velocity
U_f	[m/s]	friction velocity
Ur		Ursell parameter
V	[m/s]	velocity
		far field velocity
		discharge velocity (filter velocity, macroscopic velocity, bulk velocity)
V/n	[m/s]	pore velocity (seepage velocity)
$V_{1,max}$	[m/s]	maximum uprush velocity
$\tilde{V}_{1,max}$	[m/s]	maximum uprush velocity
$V_{2,max}$	[m/s]	maximum downrush velocity
$\tilde{V}_{2,max}$	[m/s]	maximum downrush velocity
V_{G1}	[m/s]	mean upwards particle transport velocity
V_{G2}	[m/s]	mean downwards particle transport velocity
W	[N]	weight of armour stone
W_s	[N]	submerged weight of armour stone
a	[m]	near bed wave amplitude
a^*	[m]	total water particle migration
a	[s/m]	linear flow resistance coefficient, Forchheimer flow regime
a'	[s/m]	linear flow resistance coefficient, fully turbulent flow regime
b	[s^2/m^2]	quadratic flow resistance coefficient, Forchheimer flow regime
b'	[s^2/m^2]	quadratic flow resistance coefficient, fully turbulent flow regime
b_h	[m]	initial berm width
b_v	[m]	initial berm height above SWL
c	[s^2/m]	extended Forchheimer inertia coefficient
	[m/s]	phase velocity
c_s	[m/s]	speed of sound associated with artificial compressibility
d	[m]	diameter
		equivalent spherical diameter
d_s	[m]	characteristic dimension of surface undulations
f		friction factor
f_v		viscous friction factor
f_K		friction factor
f_{Kv}		viscous friction factor
f_r		friction factor
f_w		wave friction factor
f_0		friction factor
g	[m/s^2]	acceleration of gravity
h_o	[m]	height above datum
h	[m]	local water depth
h_s	[m]	water depth in front of structure

h_{01}	[m]	depth of maximum uprush velocity
h_{02}	[m]	depth of maximum downrush velocity
h'	[m]	depth below free surface
k		cylinder/sphere number
k	[m]	surface roughness
l	[m]	distance between adjacent cylinders
ℓ	[m]	maximum length of stone
m		air fraction
n		porosity
n_a		relative area of the pores in a cross-section
p	[N/m²]	pressure
p_0	[N/m²]	pressure including gravity term
p^+	[N/m²]	excess pressure relative to hydrostatic pressure counted from SWL
p'	[N/m²]	excess pressure relative to local hydrostatic pressure
p_1		fraction of displaced particles, uprush
p_2		fraction of displaced particles, downrush
q_1	[m²/s]	upwards stone transport
q_2	[m²/s]	downwards stone transport
r	[m]	spherical polar coordinate
r	[m]	berm recession
s_o		fictitious wave steepness
t	[s]	time
t	[m]	perpendicular minimum length of stone
u	[m/s]	horizontal particle velocity
v	[m/s]	velocity
w	[m/s]	vertical particle velocity
x	[m]	coordinate
y	[m]	coordinate
z	[m]	coordinate
α	[rad]	slope angle
α		linear flow resistance coefficient, Forchheimer flow regime
α'		linear flow resistance coefficient, fully turbulent flow regime
α_E		Engelund's linear flow resistance coefficient
α_i	[rad]	initial slope angle
α_d	[rad]	dynamic equilibrium slope angle
α_s	[rad]	static equilibrium slope angle
β		quadratic flow resistance coefficient, Forchheimer flow regime
β'		quadratic flow resistance coefficient, fully turbulent flow regime
γ_1	[rad]	angle between flow and horizontal
$\tilde{\gamma}_1$	[rad]	angle between flow and horizontal
γ_2	[rad]	angle between flow and horizontal
$\tilde{\gamma}_2$	[rad]	angle between flow and horizontal
δ_1	[s]	duration of transport associated with uprush
δ_2	[s]	duration of transport associated with downrush
Δ		relative density of armour stone
ϵ		error on continuity equation due to artificial compressibility
ζ	[m]	location of doublet
η	[m]	free surface elevation
η_o	[m]	local wave amplitude
Θ	[rad]	spherical polar coordinate
Θ		Shields parameter
Θ_c		critical Shields parameter

Θ_1		Shields parameter related to $V_{1,max}$
Θ_2		Shields parameter related to $V_{2,max}$
κ		Kozeny-Carman constant ($\simeq 5$)
λ		distance factor
μ_s		static friction coefficient
μ_d		dynamic friction coefficient
ν	[m²/s]	kinematic viscosity
ξ_o		surf similarity parameter (Iribarren number)
π		3.14159...
ρ	[kg/m³]	density of water
ρ_a	[kg/m³]	density of armour stone
σ		coefficient
σ_x		courant number
τ		coefficient
τ_b	[N/m²]	bed shear stress
ϕ	[m²/s]	velocity potential
ϕ_K	[m²/s]	velocity potential
ϕ_b		non-dimensional bed load transport
χ		grain shape factor
ψ	[m²/s]	stream function
ω	[s⁻¹]	cyclic frequency
		vorticity

Overbar denotes complex conjugate or time average.

ABSTRACT

A literature study concerning porous flow is carried out. For the stationary case, the hydraulic radius theory, for which some justification can be given based on Navier-Stokes equations, appears to be adequate. Three different porous flow regimes are identified and the associated flow resistance coefficients are found from the literature. For the non-stationary flow case, existing expressions are discussed, and with the aim of decribing the inertia term a new analogy based on cylinders/spheres is presented. The predicted variation of the virtual mass coefficient with the porosity compares to a series of large scale physical experiments carried out in collaboration with other researchers.

Existing literature on breakwater stability is studied including numerical models. With the objective of describing the physics of reshaping of berm breakwaters, a new model is established. DHI's computer model, SYSTEM 3xz, is applied as the hydrodynamic basis for the reshaping model. The porous flow resistance parameters derived previously are used in the hydrodynamic model, and a sensitivity analysis is carried out. The reshaping model is based on a static force balance associated with the downrush for relatively low values of the wave height and period. For intensified wave climate, there is clearly a shift in the type of solution implying that the lower slope of the equilibrium profile is described by the theory for bed shear stresses partly transferred by occasional encounters of moving and fixed stones. The model leads to an S-shaped profile with a steep lower slope (assumed equal to the angle of repose), a middle slope and an upper slope. The model has been calibrated on a series of tests with physical scale models.

1 INTRODUCTION

1.1 Unidirectional Oscillatory Porous Flow Model

Porous flow in coarse granular materials plays an important role in evaluation of scale effects in scale models and in formulation of numerical models for wave-rubble mound structure interactions comprising reflection/transmission problems as well as structural stability.

As a basis for further deduction, some of the fundamental governing equations from the hydrodynamic theory are presented in Chapter 2.

Dealing with porous media, highly irregular at a microscopic level, it is obvious that an exact solution of the flow equations in a microscopic domain defined by the voids between the solid particles would be very comprehensive. Traditionally parametric descriptions based on various analogies have been applied for the variation of the flow resistance with the porosity. Often, alternative analogies exist based on different assumptions, and to some extent the most appropriate models must be found through comparison to measurements, if available. A literature study gives an overview of the most commonly used analogies, cf Chapter 3.

With the objective of giving some theoretical justification for the hydraulic radius theory, Navier-Stokes equations are considered in Chapter 4. The different flow regimes and the transition between them are discussed. For sake of practical applications, the variation of the flow resistance coefficients with the porosity, the gross shape and orientation of the grains, the surface roughness and the gradation is emphasised. A dimensional analysis leads to the influence of the gross shape and the surface roughness. Flow resistance coefficients for the Darcy and Forchheimer flow regimes are given in Section 4.4 and for the fully turbulent flow regime in Section 4.5.

For unidirectional oscillatory flow, a new cylinder/sphere analogy based on potential theory and derived by the image method is presented in Chapter 5. The analogy describes the variation of the virtual mass with the porosity. Comparison is made to large scale physical model tests carried out as a part of the present study in collaboration with other researchers under the MAST programme.

1.2 Breakwater Response Model

The overall purpose of the present part of the work is to get better insight into the physics of berm breakwater stability, rather than obtaining design methods. It is noticeable that reasonably good design values can be obtained from empirical methods alone. Nevertheless, it is commonly agreed that numerical modelling will contribute to our knowledge about berm breakwaters and may likely be developed to a level of design method.

A literature study including numerical models available gives the state-of-the-art of modelling breakwater stability, cf Chapter 6.

For the two-dimensional case, Navier-Stokes equations are solved by DHI's numerical model, SYSTEM 3xz, with the objective of describing the macroscopic flow on and in straight porous slopes exposed to wave attack, cf Chapter 7. In the porous flow domain is applied the vector form of the porous flow model derived in Chapters 4 and 5 together with an

additional term for macroscopic convective accelerations. As a part of the present study further calibration and verification is carried out in Chapter 7. Various aspects concerning the application of SYSTEM 3xz including the friction factor describing the bed shear stress acting on the slope are discussed.

With the objective of describing a berm breakwater equilibrium profile, a theory is developed in Chapter 8 based on an existing theory for bed load transport of sand and coarse granular particles by introducing additional gravity terms. The theory is formulated in terms of the Shields parameter in order to utilise the results obtained within the description of bed load transport of sand and coarse granular materials. Two different types of solutions are sought, both formulated in terms of the equilibrium slope: A static solution based on a Shields' approach and dynamic solutions based on the theory for the bed shear stress associated with occasional encounters of stones.

In Chapter 9, the new theory for the equilibrium profile is coupled to the model simulations with SYSTEM 3xz, thus utilising the simulations of the macroscopic flow field. The coupled models lead to an equilibrium profile developing with intensified wave climate. The sensitivity of the berm breakwater model to the flow resistance parameters is examined.

2 GENERAL FLOW EQUATIONS

In the present chapter, some of the fundamental governing equations from the hydrodynamic theory for newtonian fluids are presented. These equations are applied as basis for further deduction in all of the proceeding chapters.

2.1 Navier-Stokes and Reynolds Equations

The continuity equation

$$\frac{\partial \upsilon_i}{\partial x_i} = 0 \tag{2.1}$$

Navier-Stokes equations

$$\frac{d\upsilon_i}{dt} = \frac{\partial \upsilon_i}{\partial t} + \frac{\partial \upsilon_i}{\partial x_j}\,\upsilon_j = -\frac{1}{\rho}\frac{\partial p}{\partial x_i} + g_i + \nu\,\frac{\partial^2 \upsilon_i}{\partial x_j \partial x_j} \tag{2.2}$$

$d\upsilon_i/dt$ is the Eulerian derivative of velocity
$\partial\upsilon_i/\partial t$ is the local acceleration due to the change of velocity at a given point with time
$\partial\upsilon_i/\partial x_j\,\upsilon_j$ is the convective acceleration due to translation

The pressure and gravity terms can be merged together into p_o, defined by

$$p_o = p + \rho g h_o \tag{2.3}$$

where h_o is the height over an arbitrarily chosen datum, and such that

$$g_i = \frac{\partial}{\partial x_i}(-gh_o) \tag{2.4}$$

Now, eq (2.2) can be written as

$$\frac{d\upsilon_i}{dt} = \frac{\partial \upsilon_i}{\partial t} + \frac{\partial \upsilon_i}{\partial x_j}\,\upsilon_j = -\frac{1}{\rho}\frac{\partial p_o}{\partial x_i} + \nu\,\frac{\partial^2 \upsilon_i}{\partial x_j \partial x_j} \tag{2.5}$$

Navier-Stokes equations are never used for solving turbulent flow problems because the complexity of the flow makes it impossible. Instead, eq (2.5) is reformulated by introducing velocity mean values and velocity fluctuations. The influence of the latter is the so-called Reynolds stresses signified by an extra term in eq (2.5), arising from the convective acceleration term

$$\frac{d\upsilon_i}{dt} = \frac{\partial \upsilon_i}{\partial t} + \frac{\partial \upsilon_i}{\partial x_j}\,\upsilon_j = -\frac{1}{\rho}\frac{\partial p_o}{\partial x_i} + \nu\,\frac{\partial^2 \upsilon_i}{\partial x_j \partial x_j} + \frac{\partial}{\partial x_j}\left(-\overline{u_i u_j}\right) \tag{2.6}$$

where p_o and v_i now represent time averages, and u_i and u_j are the velocity fluctuations.

In case of no shear forces, we get the Euler equations

$$\frac{dv_i}{dt} = \frac{\partial v_i}{\partial t} + \frac{\partial v_i}{\partial x_j} v_j = - \frac{1}{\rho} \frac{\partial p_o}{\partial x_i} \tag{2.7}$$

An important parameter in characterising the flow is Reynolds number, Re, defined as the ratio between the convective inertia forces and the viscous forces leading to

$$Re = \frac{UD}{\nu} \tag{2.8}$$

where U is a characteristic velocity, and D is a characteristic length.

2.2 Potential Flow

Irrotational motion is equivalent to zero vorticity

$$\omega_{ij} = \frac{\partial v_j}{\partial x_i} - \frac{\partial v_i}{\partial x_j} = 0 \tag{2.9}$$

The left-hand side of eq (2.7) can be written as

$$\frac{dv_i}{dt} = \frac{\partial v_i}{\partial t} + \frac{\partial v_i}{\partial x_j} v_j = \frac{\partial v_i}{\partial t} + \frac{\partial}{\partial x_i} \left(\frac{1}{2} v^2 \right) \tag{2.10}$$

where, in this context, v^2 equals $v_j v_j$.

A velocity potential, ϕ, can be defined

$$v_i = - \frac{\partial \phi}{\partial x_i} \tag{2.11}$$

leading to

$$\frac{\partial v_i}{\partial t} = - \frac{\partial}{\partial x_i} \left(\frac{\partial \phi}{\partial t} \right) \tag{2.12}$$

and hence

$$- \frac{\partial}{\partial x_i} \left(\frac{\partial \phi}{\partial t} \right) + \frac{\partial}{\partial x_i} \left(\frac{1}{2} v^2 \right) = - \frac{1}{\rho} \frac{\partial p_o}{\partial x_i} \tag{2.13}$$

or

$$\frac{\partial}{\partial x_i} \left(- \frac{1}{g} \frac{\partial \phi}{\partial t} + \frac{p_o}{\rho g} + \frac{v^2}{2g} \right) = 0 \tag{2.14}$$

or

$$- \frac{1}{g} \frac{\partial \phi}{\partial t} + \frac{p_o}{\rho g} + \frac{v^2}{2g} = C(t) \tag{2.15}$$

which is known as the Bernoulli equation. It can be shown that C(t) can be included in $\partial\phi/\partial t$ and hence the right-hand side of eq (2.15) can be substituted by 0.

Alternatively, the square of the speed can be expressed as

$$v^2 = v_1^2 + v_2^2 + v_3^2 = \left(\frac{\partial \phi}{\partial x_1}\right)^2 + \left(\frac{\partial \phi}{\partial x_2}\right)^2 + \left(\frac{\partial \phi}{\partial x_3}\right)^2 \tag{2.16}$$

leading to

$$- \frac{1}{g} \frac{\partial \phi}{\partial t} + \frac{p_o}{\rho g} + \frac{1}{2g} \left[\left(\frac{\partial \phi}{\partial x_1}\right)^2 + \left(\frac{\partial \phi}{\partial x_2}\right)^2 + \left(\frac{\partial \phi}{\partial x_3}\right)^2 \right] = 0 \tag{2.17}$$

The continuity equation reads

$$\frac{\partial v_i}{\partial x_i} = 0 \tag{2.18}$$

By use of the velocity potential, we get

$$\frac{\partial^2 \phi}{\partial x_i \partial x_i} = 0 \quad \text{or} \quad \Delta\phi = 0 \tag{2.19}$$

which is known as Laplaces' equation.

In case of two-dimensional flow, a stream function, ψ, can be defined

$$v_1 = - \frac{\partial \psi}{\partial x_2} \tag{2.20}$$

$$v_2 = + \frac{\partial \psi}{\partial x_1} \tag{2.21}$$

thus fulfilling the continuity equation

$$\frac{\partial}{\partial x_1} \left(- \frac{\partial \psi}{\partial x_2} \right) + \frac{\partial}{\partial x_2} \left(\frac{\partial \psi}{\partial x_1} \right) = 0 \tag{2.22}$$

The streamlines of the flow are characterised by

$$\frac{dx_1}{v_1} = \frac{dx_2}{v_2} \tag{2.23}$$

or

$$v_2 dx_1 - v_1 dx_2 = 0 \tag{2.24}$$

Inserting eqs (2.20) and (2.21), we get

$$\frac{\partial \psi}{\partial x_1} dx_1 + \frac{\partial \psi}{\partial x_2} dx_2 = 0 \tag{2.25}$$

or

$$d\psi = 0 \tag{2.26}$$

or

$$\psi = \text{constant} \tag{2.27}$$

ie ψ is constant along the streamlines.

The stream function can be defined also in case of rotational flow. For irrotational flow, ie

$$\omega_{12} = \frac{\partial v_2}{\partial x_1} - \frac{\partial v_1}{\partial x_2} = 0 \tag{2.28}$$

where ω is the vorticity, we get by application of eqs (2.20) and (2.21)

$$\frac{\partial^2 \psi}{\partial x_1 \partial x_1} + \frac{\partial^2 \psi}{\partial x_2 \partial x_2} = 0 \quad \text{or} \quad \Delta \psi = 0 \tag{2.29}$$

ie also ψ satisfies Laplaces' equation.

If ϕ and ψ are equated to constant values, eg $\phi = C_1$ and $\psi = C_2$, we get two sets of curves. These curves are orthogonal, ie in the points of intersection their tangents are at right angles, see eg Milne-Thomson (1968), Section 5.31.

The complex potential is defined as

$$w(z) = w(x+iy) = \phi(z) + i\psi(z) \tag{2.30}$$

and ϕ and ψ are called conjugate functions.

2.3 Linear Porous Flow

Another type of irrotational flow is the linear porous flow. Defining a velocity potential by

$$\phi_K = K \frac{p_o}{\rho g} \tag{2.31}$$

and

$$V_i = - \frac{\partial \phi_K}{\partial x_i} \tag{2.32}$$

we get

$$V_i = K\, I_i \tag{2.33}$$

with

$$I_i = - \frac{1}{\rho g} \frac{\partial p_o}{\partial x_i} \tag{2.34}$$

ie Darcys' law, cf Chapter 3. By introducing the continuity equation (2.1), we find

$$\frac{\partial^2 \phi_K}{\partial x_i \partial x_i} = 0 \quad \text{or} \quad \Delta \phi_K = 0 \tag{2.35}$$

ie Laplaces' equation. Physically this type of flow differs from that of Section 2.2 as viscous forces are now included in K. For convenience, also in some numerical formulations, the expression for unlinear porous flow resistance, cf Chapter 4, is linearised, and the equivalent of eq (2.35) is solved. The linearisation reads

$$I_i = a' V_i + b' V_j V_j e_i \tag{2.36a}$$

$$I_i = (a' + b' V)\, V_i , \quad V^2 = V_j V_j \tag{2.36b}$$

$$I_i = F(V) V_i \tag{2.36c}$$

$$\frac{\partial}{\partial x_i} \left[F^{-1}(V) \frac{\partial}{\partial x_i} \left(\frac{p_o}{\rho g} \right) \right] = 0 \tag{2.36d}$$

where $p_o/\rho g$ is the piezometric head.

2.4 Forces on a Single Obstacle in Accelerating Flow

For the case of a single cylinder exposed to an ambient fluid moving with the complex velocity, V, and assuming potential flow, the complex potential field is described by

$$w = - \overline{V} z + \frac{MV}{z} \tag{2.37}$$

where $\overline{V}$ is the complex conjugate of V, see eg Milne-Thomson (1968), Section 6.22. The first term arises from the uniform flow and the second term represents a doublet with strenght, M, located in the centre of the cylinder

$$M = - \frac{1}{4} d^2 e_1 \tag{2.38}$$

where e_1 is defined by

$$V = |V| e_1 \tag{2.39}$$

It should be noted that in the present text, V follows the positive direction of the x-axis.

Together, the two terms of eq (2.37) produce a stream line at the cylinder contour.

The force per unit length acting on a single cylinder can be found by integration of the excess pressure over the contour of the cylinder. In complex notation the integration reads

$$F = F_x + iF_y = i \oint p_o \, dz \tag{2.40}$$

It should be noted that the complex quantity idz is a normal vector pointing into the contour of the cylinder.

By use of the Bernoulli equation (2.15), the excess pressure can be found as

$$p_o = \rho \frac{\partial \phi}{\partial t} - \frac{1}{2} \rho v^2 \tag{2.41}$$

and hence the force per unit length equals

$$F = i\rho \oint \frac{\partial \phi}{\partial t} dz - i \frac{1}{2} \rho \oint v^2 dz \tag{2.42}$$

For unseparated flow, the second term vanishes due to symmetry in the velocity distribution. As z and t are independent, the temporal inertia force can be written as

$$F = i\rho \frac{\partial}{\partial t} \oint \phi dz \tag{2.43}$$

The first term in eq (2.37) leads to the Froude-Krylov force. By choosing the coordinate axes with x in the direction of V, ie $e_1=(1,0)$, the first term of the complex potential can be written as

$$w = - V_x z \tag{2.44}$$

and the potential, ϕ, becomes

$$\phi = - V_x x \tag{2.45}$$

ie the force per unit length equals

$$F = - i \rho \frac{\partial V_x}{\partial t} \oint x dz \tag{2.46}$$

which by integration equals

$$F = \rho \frac{\pi}{4} d^2 \frac{\partial V_x}{\partial t} \tag{2.47}$$

ie the force per unit length of the cylinder equals the product of the density of water, the cross-sectional area and the local acceleration. As no imaginary part appears in eq (2.47),the force acts in the direction of the flow.

The potential, ϕ, associated with the doublet equals

$$\phi = - \frac{1}{4} d^2 V_x \, Re \frac{1}{z} \tag{2.48}$$

where Re denotes the real part. The force per unit length equals

$$F = - i \rho \frac{1}{4} d^2 \frac{\partial V_x}{\partial t} \oint Re \frac{1}{z} dz \tag{2.49}$$

which is integrated to

$$F = \rho \frac{\pi}{4} d^2 \frac{\partial V_x}{\partial t} \tag{2.50}$$

ie a force of same magnitude and direction as the Froude-Krylov force.

For the case of axisymmetrical flow, ϕ and ψ can be defined as in the two-dimensional case, but the concept of complex potential is not applicable. For the flow around a single sphere, the potential reads in spherical polar coordinates, cf Milne-Thomson (1968), Section 16.30.

$$\phi = - Vr\cos\theta + \frac{MV\cos\theta}{r^2} \tag{2.51}$$

with the strength of the sphere centrered doublet given as

$$M = - \frac{1}{16} d^3 \tag{2.52}$$

It should be noted that in the present text, V follows the positive direction of the r-axis.

Similar calculations as in the case of two-dimensional flow yield a Froude-Krylov force of

$$F = \rho \frac{\pi}{6} d^3 \frac{\partial V_x}{\partial t} \tag{2.53}$$

and a force from the doublet of

$$F = \frac{1}{2} \rho \frac{\pi}{6} d^3 \frac{\partial V_x}{\partial t} \tag{2.54}$$

In general, the force from the doublet also appears in case of an obstacle accelerating in a fluid at rest, and hence the term

$$C_a \rho \, Vol = \frac{1}{2} \rho \frac{\pi}{6} d^3 \tag{2.55}$$

is denoted the added mass, as it must be added to the mass of the obstacle when solving the equations of motion for the obstacle. The sum of the Froude-Krylov force and the added mass force is called the virtual mass force. A set of coefficients can be defined accordingly

$$F_{added} = C_a \rho \, Vol \frac{\partial V_x}{\partial t} \tag{2.56}$$

$$F_{virtual} = C_m \rho \, Vol \frac{\partial V_x}{\partial t} \tag{2.57}$$

$$C_m = 1 + C_a \tag{2.58}$$

where C_a is the added mass coefficient and C_m is the virtual mass coefficient. For two-dimensional flow, F is the force per unit length of the cylinder, and Vol represents the cross-sectional area.

For a single cylinder, eqs (2.47) and (2.50) together with eqs (2.56) and (2.57) lead to $C_a=1$ and $C_m=2$. For a single sphere, we find from eqs (2.53) and (2.54) that $C_a=0.5$ and $C_m=1.5$.

The definitions of C_a and C_m are also applied to non-cylindrical and non-spherical shapes, to rough obstacles and to separated flow, ie to real flow conditions. For these cases, the coefficients C_a and C_m depend on the gross shape, the surface roughness and on Reynolds' number, Re, and the Keulegan-Carpenter number, KC, defined as

$$Re = \frac{V_{max} \, d}{\nu} \tag{2.59}$$

and

$$KC = \frac{V_{max} \, T}{d} \tag{2.60}$$

The coefficients have been subject to comprehensive parametric studies, see eg Sarpkaya and Isaacson (1981).

For separated flow, the Bernoulli equation (2.15) cannot be applied at the entire contour of the obstacle. Application of eq (2.15) to the unseparated part of the flow leads to a drag term proportional to the square of the velocity. The velocity at the stagnation point is denoted v^+ and the velocity at the separation point is denoted v^-, cf Fig 2.1. As $v^+=0$ and defining a coefficient, C_d, from

$$v^- = \sqrt{C_d}\, V \tag{2.61}$$

we get

$$0 + \frac{|V|V}{2g} = \frac{p^-}{\rho g} + C_d \frac{|V|V}{2g} \tag{2.62}$$

leading to

$$\frac{p^-}{\rho g} = \frac{|V|V}{2g}(1-C_d) \tag{2.63}$$

and

$$0 + \frac{|V|V}{2g} = \frac{p^+}{\rho g} + 0 \tag{2.64}$$

leading to

$$\frac{p^+}{\rho g} = \frac{|V|V}{2g} \tag{2.65}$$

Neglecting the difference in the projected area of the zones exposed to positive and negative pressures respectively, and neglecting the variation in the positive pressures, the total drag force on the obstacle can be written as

$$F \sim d\,(p^+-p^-) = C_d\, d\, \rho \frac{|V|V}{2} \tag{2.66}$$

in case of a cylinder (force per unit length) and

$$F \sim \frac{\pi}{4} d^2\,(p^+-p^-) = C_d \frac{\pi}{4} d^2\, \rho \frac{|V|V}{2} \tag{2.67}$$

in case of a sphere, where C_d is a drag coefficient.

Also the drag coefficient is generalised

$$F = C_d\, A\, \rho \frac{|V|V}{2} \tag{2.68}$$

where A is the projected area. C_d depends on the gross shape, the surface roughness, Reynolds' number and for oscillatory motion also on the Keulegan-Carpenter number.

The above derivation, eqs (2.61) to (2.68), is applicable to both the smooth and rough turbulent cases, as in both cases the flow separation is governing for the pressure distribution.

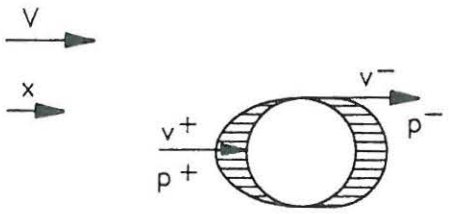

Fig 2.1 Separated flow around single obstacle.

3 LITERATURE STUDY OF POROUS FLOW

3.1 Stationary Flow

In 1856 D'Arcy described empirically the relation between the hydraulic gradient, I, and the discharge velocity, V, through porous sands and sandstones as

$$V = KI \tag{3.1}$$

which may also be written as

$$I = K^{-1}V \tag{3.2}$$

where K is the permeability coefficient (m/s).

These expressions, which have later been referred to as the Darcy law, apply to the laminar flow case without convective inertia forces, ie creeping flow. As a heuristic correlation, Forchheimer in 1901 extended this expression with a quadratic term where a and b are coefficients

$$I = aV + b|V|V \tag{3.3}$$

The Forchheimer expression applies to porous flow regimes dominated by convective inertia forces.

In order to describe the coefficients a and b, various analogies have been applied. Darcy's law compares to the Hagen-Poiseuille equation, see eg Scheidegger (1974), which is an exact solution to Navier-Stokes' equation for laminar flow in a number of parallel circular capillaries with diameter, d_c, ie without convective accelerations. This yields a parabolic velocity distribution and the relation between the hydraulic gradient and the average velocity reads

$$I = 32 \frac{\nu}{g d_c^2} V \tag{3.4}$$

where ν is the kinematic viscosity.

Often Darcy's law is written in the form

$$I = \frac{\nu}{g K_s} V \tag{3.5}$$

where K_s is the specific or intrinsic permeability (m^2).

In order to include the variation with the porosity, n, defined as the pore volume relative to the total volume of the sample, Dupuit in 1863 extended Darcy's law by applying as characteristic velocity the pore velocity, V/n. This assumption has later been denoted the Dupuit-Forchheimer assumption, leading to

$$I = K_1^{-1} \frac{V}{n} \tag{3.6}$$

Slichter in 1897 assumed the channels between the grains to be triangular and deduced expressions for the flow resistance dependent on the grain diameter and the porosity, by correcting the Hagen-Poiseuille equation. This was the first attempt to establish a model taking the pore geometry into account. The model by Slichter was later modified by Terzaghi in 1925 who introduced a further empirical constant.

Kozeny in 1927 applied a pipe analogy with a parabolic distribution of the pore velocity, V/n, but now a hydraulic radius, R, was defined as the ratio between the pore volume and the wet surface area, ie the surface area of the grains

$$R = \frac{n}{S} \tag{3.7}$$

where S is the surface area of the grains per unit volume of the sample, leading to

$$I = \kappa_1 \frac{\nu S^2}{g n^3} V \tag{3.8}$$

Assuming the porous sample equivalent to a group of channels, a tortuosity, T, was defined as the ratio of the length of the equivalent channels to the length of the sample thus increasing the flow resistance

$$I = \kappa_1 \frac{\nu T S^2}{g n^3} V \tag{3.9}$$

Carman (1937) expressed S as a function of the pore geometry assuming spherical obstacles with diameter d

$$S = \frac{6\,(1-n)}{d} \tag{3.10}$$

This together with eq (3.8) lead to

$$I = 36\,\kappa_1 \frac{(1-n)^2}{n^3} \frac{\nu}{g d^2} V \tag{3.11}$$

Further Carman argued that due to the curvatures of the flow channels the gradient must be increased by T squared

$$I = 36\,\kappa \frac{(1-n)^2}{n^3} \frac{\nu}{g d^2} V \tag{3.12}$$

where $\kappa = \kappa_1 T^2$.

Comparing to experiments Carman found $\kappa=5$. Eq (3.12) has later been referred to as the Kozeny-Carman expression.

Also in the Forchheimer flow regime both terms in eq (3.3) can be expressed as function of

the pore geometry. Carman (1937) established an expression for the non-linear term from dimensional analysis and fitting to experimental data, leading to a variation with the discharge velocity raised to a power of 1.9. This expression, however, has only little theoretical interest. Ergun (1952) kept the Kozeny-Carman expression for the linear flow resistance, although with a new constant applicable in the Forchheimer regime. For the quadratic term, he applied a pipe analogy with hydraulic radius, R, valid for high Reynolds numbers.

$$I = 150 \frac{(1-n)^2}{n^3} \frac{\nu}{gd^2} V + 1.75 \frac{1-n}{n^3} \frac{1}{gd} |V|V \tag{3.13}$$

Ergun verified the expressions involving n by experiments, cf Section 4.3.

For the purpose of graphical presentation, the two terms in the Forchheimer equation can be merged into one term in two different ways, which are both treated in the paper by Ergun (1952). A traditional friction factor, f, can be defined from

$$I = f \frac{1-n}{n^3} \frac{1}{gd} |V|V \quad \text{or} \quad f = \frac{Igd}{|V|V} \frac{n^3}{1-n} \tag{3.14}$$

which together with eq (3.13) gives

$$f = 150 \frac{1-n}{Re} + 1.75, \quad Re = \frac{|V|d}{\nu} \tag{3.15}$$

Alternatively, a viscous friction factor, f_v, can be defined from

$$I = f_v \frac{(1-n)^2}{n^3} \frac{\nu}{gd^2} V \quad \text{or} \quad f_v = \frac{Igd^2}{V\nu} \frac{n^3}{(1-n)^2} \tag{3.16}$$

which together with eq (3.13) gives

$$f_v = 150 + 1.75 \frac{Re}{1-n}, \quad Re = \frac{|V|d}{\nu} \tag{3.17}$$

f and f_v are plotted against Re/(1-n) in Figs 3.1 and 3.2 respectively. It should be noted, however, that none of these plots are complete with respect to the variation with Re, as also the constants depend on Re, cf Chapter 4.

Engelund (1953) did like Ergun for the quadratic term, but for the linear term he assumed an expression of the type

$$I = \alpha_E \frac{(1-n)^\sigma}{n^\tau} \frac{\nu}{gd^2} V \tag{3.18}$$

which was then fitted to experiments with porous flow in sand

$$I = \alpha_E \frac{(1-n)^3}{n^2} \frac{\nu}{gd^2} V \tag{3.19}$$

Eq (3.18) was preferred rather than an expression of the type $I \sim n^{-p}$, as Rose in 1945 had shown that such an expression implies a variation of p with n, ie $p=p(n)$.

Dybbs and Edwards (1984) presented the results of physical model tests with flow in porous structures. The porous structures consisted of plexiglass spheres in hexagonal packing and glass and plexiglas rods arranged in a complex, fixed three-dimensional geometry. Both water and oil was used for testing. Laser anemometry and flow visualisation was carried out.

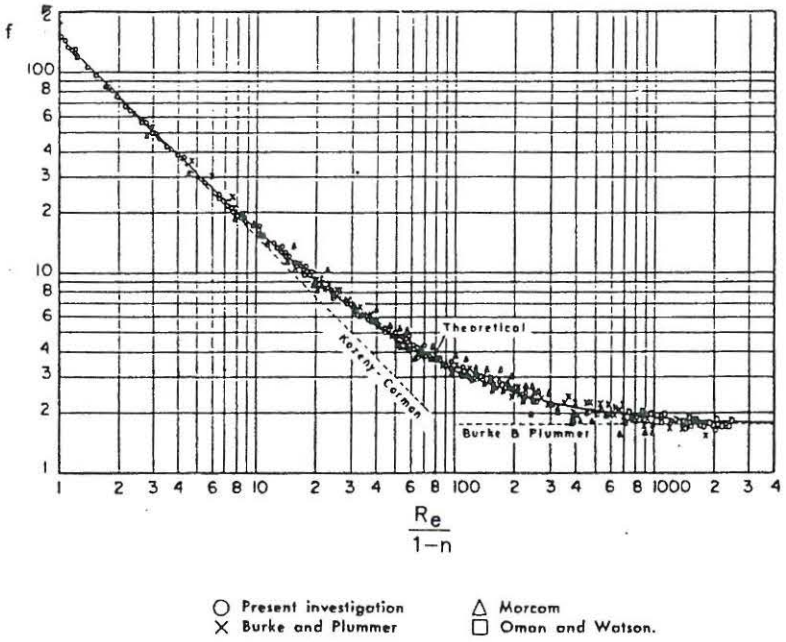

Fig 3.1 Plot of traditional friction factor vs Re/(1-n). From Ergun (1952).

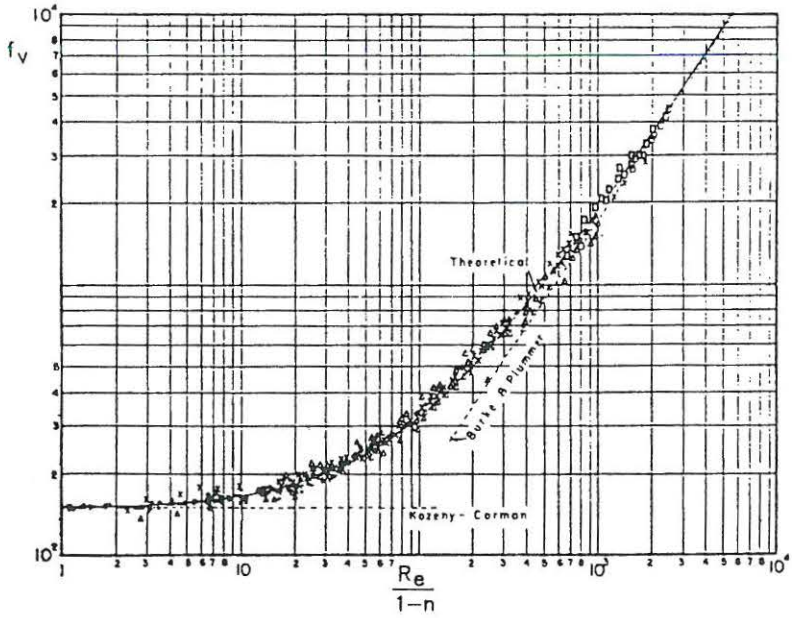

Fig 3.2 Plot of viscous friction factor vs Re/(1-n). From Ergun (1952).

Four flow regimes were identified in this manner, the description is quoted directly from the above reference:

1) *The Darcy or creeping flow regime where the flow is dominated by viscous forces and the exact nature of the velocity distribution is determined by local geometry. This type of flow occurs at $Re < 1$. At $Re \simeq 1$, boundary layers begin to develop near the solid boundaries of the pores.*

2) *The inertial flow regime. This initiates at Re between 1 and 10 where the boundary layers become more pronounced and an 'inertial core' appears. The developing of these 'core' flows outside the boundary layers is the reason for the non-linear relationship between pressure drop and flow rate. As the Re increases, the 'core' flows enlarge in size and their influence becomes more and more significant on the overall flow picture. This steady non-linear laminar flow regime persists to a Re ~ 150.*

3) *An unsteady laminar flow regime in the Reynolds number range of 150 to 300. At a Re ~ 150, the first evidence of unsteady flow is observed in the form of laminar wake oscillations in the pores. These oscillations take the form of travelling waves characterised by distinct periods, amplitudes and growth rates. In this flow regime, these oscillations exhibit preferred frequencies that seem to correspond to specific growth rates. Vortices form at Re ~ 250 and persist to Re ~ 300.*

4) *A highly unsteady and chaotic flow regime for Re > 300, qualitatively resembling turbulent flow.*

Dybbs and Edwards presented the pressure drop vs discharge velocity relationship as a friction factor diagram of the type given by eq (3.14).

In the following, the flow regimes will be denoted as follows:

1) the Darcy flow regime
2) the Forchheimer flow regime
4) the fully turbulent (rough turbulent) flow regime

Flow regime 3) is a transitional flow regime between the Forchheimer and the fully turbulent flow regimes.

Fand et al (1987) examined experimentally the variation of the a and b coefficients with the Reynolds number for smooth spheres. Eq (3.3) was changed into

$$\frac{Igd}{V\nu} = a\,\frac{gd}{\nu} + bgRe, \quad Re = \frac{|V|d}{\nu} \tag{3.20}$$

resembling eq (3.17), whereafter a plot similar to Fig 3.2 was made. It appeared that three different flow regimes can be identified in this way: the Darcy, the Forchheimer and the fully turbulent flow regimes. The Reynolds number separating the Forchheimer flow regime and the fully turbulent flow regime was found to be in the order of 100, ie lower than found by Dybbs and Edwards. For the variation of the a and b terms with the pore geometry Fand et al applied the expressions given by Ergun (1952) with new individual constants for each flow regime.

Some authors, eg Ward (1964), have established expressions for both terms in the Forchheimer flow regime with no direct dependency on neither porosity nor grain diameter. From dimensional analysis and fitting to experiments he found

$$I = \frac{\nu}{gK_s}\,V + \frac{c}{g\sqrt{K_s}}\,|V|V \tag{3.21}$$

where K_s is the specific permeability (m^2) and c is a dimensionless constant which has the same value 0.550 for all porous media. The first term compares to Darcy's law, eq (3.5). Some authors apply eq (3.21) also in the turbulent flow regime with a lower value of c than given by Ward. Sollitt and Cross (1972) found values of c ranging from 0.28 to 0.41 for the

transition region between the Forchheimer and the turbulent flow regimes. As also the linear term is different from the Forchheimer to the turbulent flow regime, the constant '1' should be changed as well.

Also in case of a description based on specific permeability, two different friction factors can be defined. Ward (1964) defined a friction factor, f_K

$$I = \frac{f_K}{g\sqrt{K_s}} |V|V \quad \text{or} \quad f_K = \frac{Ig\sqrt{K_s}}{|V|V} \tag{3.22}$$

which together with eq (3.21) gives

$$f_K = \frac{1}{Re_K} + c \,, \quad Re_K = \frac{|V|\sqrt{K_s}}{\nu} \tag{3.23}$$

McCorquodale et al (1978) defined a viscous friction factor, f_{Kv}

$$I = f_{Kv} \frac{\nu}{gK_s} V \quad \text{or} \quad f_{Kv} = \frac{IgK_s}{V\nu} \tag{3.24}$$

which together with eq (3.21) gives

$$f_{Kv} = 1 + cRe_K \,, \quad Re_K = \frac{|V|\sqrt{K_s}}{\nu} \tag{3.25}$$

Several authors have proposed expressions for the variation of a and b with the porosity. Some of these are shown in Table 3.1, in which the two first expressions refer to the Darcy flow regime and for the other expressions the constants refer to the Forchheimer flow regime.

3.2 Non-Stationary Flow

For the case of non-stationary flow in coarse granular media, the Forchheimer expression can be extended with an inertia term

$$I = aV + b|V|V + c \frac{\partial V}{\partial t} \tag{3.26}$$

This was originally suggested by Polubarinova-Kochina in 1952. Like the stationary terms the inertia term varies with the porosity. In case of non-uniform flow, macroscopic convective accelerations are present in addition to the local acceleration, $\partial V/\partial t$. For a breakwater, the boundary conditions for the porous medium are the finite extension of the waves, the free surface and the impervious bottom. Due to the non-linear interaction between the grains in the porous medium in combination with the boundary conditions, the inertia coefficient, c, defined from eq (3.26) cannot in general be applied to the convective accelerations, ie the local derivative, $\partial V/\partial t$, in eq (3.26) cannot in general be substituted by the total derivative, dV/dt. This is in contradiction to single obstacles exposed to a non-steady and non-uniform flow, where it is sometimes possible to merge the local and convective accelerations into one inertia term, ie the coefficients are identical, see Sarpkaya and Isaacson (1981). Considering porous flow, it is thus necessary to treat the local and the

macroscopic convective accelerations separately. As the local accelerations are usually dominating over the convective accelerations and as the local accelerations are much easier to deal with than the total accelerations in theory, $\partial V/\partial t$ is applied in the definition of c, cf eq (3.26). Hence, in case of non-uniform flow, the macroscopic convective accelerations must be added as a separate term in supplement to the inertia term in eq (3.26). Usually, a quadratic term of the type 1/g V/n $\partial/\partial x$ (V/n) is applied. The procedure described above is applied in most literature. It should be noticed that for a typical breakwater, the quadratic term in eq (3.26) is dominating over the inertia term in eq (3.26), which is dominating over the gradient associated with the macroscopic convective accelerations.

Table 3.1 Expressions for the a and b terms

Authors	a	b
Kozeny (1927)	$\kappa_1 \frac{\nu TS^2}{gn^3}$	
Carman (1937)	$36\ \kappa \frac{(1-n)^2}{n^3} \frac{\nu}{gd^2},\ \kappa = 5$	
Ergun (1952)	$150 \frac{(1-n)^2}{n^3} \frac{\nu}{gd^2}$	$1.75 \frac{1-n}{n^3} \frac{1}{gd}$
Engelund (1953)	$\alpha_E \frac{(1-n)^3}{n^2} \frac{\nu}{gd^2}$	$\beta \frac{1-n}{n^3} \frac{1}{gd}$
Ward (1964)	$\frac{\nu}{gK_s}$	$\frac{c}{g\sqrt{K_s}},\ c = 0.550$

Sollitt and Cross (1972) considered a condition for a fluid element together with the pore velocity as characteristic velocity. In addition to the acceleration of the fluid element, they added a virtual mass related to the volume of solids

$$C_m^s (1-n) \frac{\partial}{\partial t}\left(\frac{V}{n}\right) \tag{3.27}$$

which was then, according to the authors, distributed over the volume of water and considered as an extra force acting on the fluid element. Quoting: *The resistance force due to the*

virtual mass is equal to the product of the displaced fluid mass, the virtual mass coefficient, and the acceleration in the approach velocity. The resulting force is distributed over the fluid mass within the pore so that the force per unit mass of fluid is simply

$$C_m^s \frac{1-n}{n} \frac{\partial}{\partial t}\left(\frac{V}{n}\right) \tag{3.28}$$

The entire force balance for the fluid element reads

$$-\frac{1}{\rho}\frac{\partial p_o}{\partial x} = \frac{\partial}{\partial t}\left(\frac{V}{n}\right) + C_m^s \frac{1-n}{n} \frac{\partial}{\partial t}\left(\frac{V}{n}\right) \tag{3.29}$$

where the term on the left-hand side denotes the part of the hydraulic gradient associated with the inertia term. This can also be written as

$$-\frac{1}{\rho g}\frac{\partial p_o}{\partial x} = \frac{1 + C_m^s \frac{1-n}{n}}{ng} \frac{\partial V}{\partial t} \tag{3.30}$$

The applied procedure seems unclear and the result not applicable as the pressure gradient does not only act on the fluid element but on the entire sample of water and solids as shown below.

Madsen (1974) and Hannoura and McCorquodale (1978) considered a unit volume of the sample and related the inertia term to the volume of water and the volume of solids. As characteristic velocity they applied the pore velocity

$$-\frac{\partial p_o}{\partial x} = \rho n \frac{\partial}{\partial t}\left(\frac{V}{n}\right) + \rho C_m^* (1-n) \frac{\partial}{\partial t}\left(\frac{V}{n}\right) \tag{3.31}$$

leading to

$$-\frac{1}{\rho g}\frac{\partial p_o}{\partial x} = \frac{1 + C_m^* \frac{1-n}{n}}{g} \frac{\partial V}{\partial t} \tag{3.32}$$

C_m^* is the virtual mass coefficient. Eq (3.32) is general as no assumptions are made about the geometry of the porous medium, cf the cylinder/sphere analogy based on the pore velocity presented in Section 5.2, which leads to the same inertia term as in eq (3.32).

Madsen (1974) did not give an expression equal to eq (3.32) but merged the Froude-Krylov force in eq (3.31) with the first term on the right-hand side leading to

$$-\frac{\partial p_o}{\partial x} = \rho \frac{\partial}{\partial t}\left(\frac{V}{n}\right) + \rho C_a^* (1-n) \frac{\partial}{\partial t}\left(\frac{V}{n}\right) \tag{3.33}$$

where C_a^* is the added mass coefficient

$$C_m^* = 1 + C_a^* \tag{3.34}$$

Eq (3.31) can be written as

$$-\frac{1}{\rho g}\frac{\partial p_o}{\partial x} = \frac{1 + C_a^* (1-n)}{ng}\frac{\partial V}{\partial t} \tag{3.35}$$

In most analytical solutions for reflection and transmission from rectangular porous cross-sections, cf Section 6.1, the inertia term is described as

$$-\frac{1}{\rho g}\frac{\partial p_o}{\partial x} = \frac{1}{ng}\frac{\partial V}{\partial t} \tag{3.36}$$

According to eqs (3.32) and (3.35), which are considered to be correct, this corresponds to $C_a^*=0$, ie only the acceleration of the pore water and the Froude-Krylov force, but not the added mass force, are included. According to eq (3.30) this corresponds to $C_m^s=0$.

Wang and Gu (1988) related the inertia term to the volume of water and the volume of solids together with the pore velocity. For the pressure, however, they applied only the part acting on the water, ie

$$n_a\left(-\frac{\partial p_o}{\partial x}\right) = \rho n \frac{\partial}{\partial t}\left(\frac{V}{n}\right) + \rho C_m^w (1-n)\frac{\partial}{\partial t}\left(\frac{V}{n}\right) \tag{3.37}$$

where n_a is the relative area of the pores in a cross-section. As for an irregular porous medium, n_a is constant from one cross-section cut to another, we have from a simple integration over a unit volume that $n=n_a$, see eg Underwood (1970). Hence, eq (3.37) leads to an expression equal to the expression of Sollitt and Cross (1972), cf eq (3.30).

$$-\frac{1}{\rho g}\frac{\partial p_o}{\partial x} = \frac{1 + C_m^w \frac{1-n}{n}}{ng}\frac{\partial V}{\partial t} \tag{3.38}$$

Van Gent (1992) derived an expression for the inertia term from a condition for a fluid element. In this derivation, as done by Sollit and Cross (1972), the same transformation of the pressure forces related to the volume of solids to the volume of water is carried out. This leads to

$$-\frac{1}{\rho g}\frac{\partial p_o}{\partial x} = \frac{1 + C_m^G \frac{1-n}{n}}{ng}\frac{\partial V}{\partial t} \tag{3.39}$$

Further, an unconventional virtual mass coefficient is defined, as it is related to the volume of water and not the displaced volume

$$C_M^G = C_m^G \frac{1-n}{n} \tag{3.40}$$

In the description of the inertia term, it is necessary to consider the force balance for the entire sample, ie taking the volume of water as well as the volume of solid into account. As discussed in Section 5.2, the pressure is acting over the entire sample, implying that the entire pressure must be applied in the force balance. From this reason, among the above formulations of the variation of the inertia term with the porosity, only the formulation by Madsen (1974) and Hannoura and McCorquodale (1978) is considered to be correct.

3.3 Air-Water Flow

A parametric expression for the hydraulic conductivity under two phase flow conditions is given by Hannoura and McCorquodale (1978b) and (1985a). Three different conceptual models are considered. In all the models, the basic derivation is made for either a turbulent co-current of air in the same direction as the flow of water or a turbulent countercurrent of air opposing the flow of water.

1) In the homogeneous model, the air is dispersed in the water, ie the mixed fluid is described by average properties of density and viscosity. The hydraulic gradient is given by

$$I = (a+b|V|)V(1-m) \pm m \tag{3.41}$$

where m is the fraction of air and the sign on the right-hand side is negative for co-current flow and positive for countercurrent flow.

2) In the separated model, the equations of state, continuity and momentum are treated separately for the two fluids. As this model is a complex model, it is usually applied to flow problems with much simpler kinematics than in porous flow problems.

3) The drift-flux model relates the motion of one fluid, the air fraction, to the average motion of the mixed fluid. This model forms a special case of the separated model. Observations with crushed rock wave absorbers indicate that the flow through the pores is either bubble flow or slug flow. For bubble flow, the dimensions of the discrete bubbles are small compared to the pores of the rock sample, whereas in case of slug flow, the discrete slugs almost fill the pores. Like in the homogeneous model, the hydraulic gradient is given by eq (3.41).

For bubble flow, the fraction of air is given by

$$m = \frac{Q_a}{Q_m}\left(1 - \frac{J_{aw}}{J_m}\right) \tag{3.42}$$

$$J_{aw} = m\,v_\infty\,(1-m)^\sigma \tag{3.43}$$

where (originally the length unit applied was (cm))
Q_a is the volumetric flow of air (m^3/s)
Q_m is the total volumetric flow (m^3/s)
J_{aw} is the volumetric drift flux (m/s)
J_m is the total volumetric flux (m/s)
v_∞ is the terminal velocity of the bubbles (m/s)
σ varies between 0 and 2

In case of slug flow, the air fraction is given by

$$m = \frac{Q_a}{C_1(Q_a+Q_w) + C_2 A_f v_\infty} \tag{3.44}$$

$$C_1 = 1.0$$

$$C_2 = \exp\left[29 \left(\frac{d\upsilon_\infty}{\upsilon_w} \right)^{-0.43} \left(\frac{Q_a}{Q_a + |Q_w|} \right) \right]$$

where

A_f is the flow area (m^2)

υ_w is the velocity of water (m/s)

d is the stone diameter (cm)

Figs 3.3 to 3.5 show the comparisons between the different models and the observations. The best agreement is obtained with the slug drift-flux model for both crushed rock and river gravel.

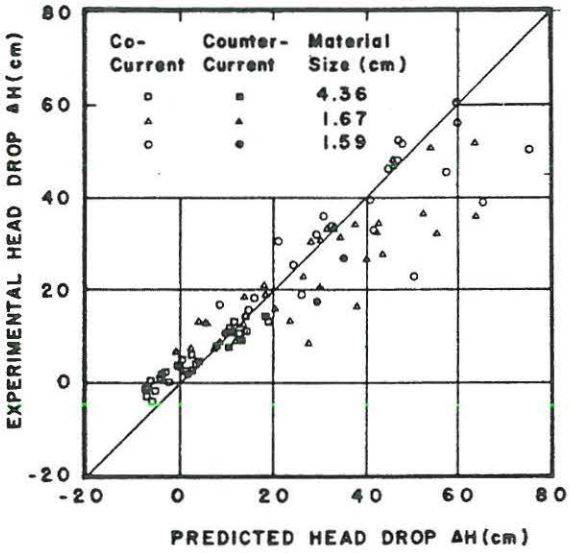

Fig 3.3 Homogeneous model. From Hannoura et al (1978b)

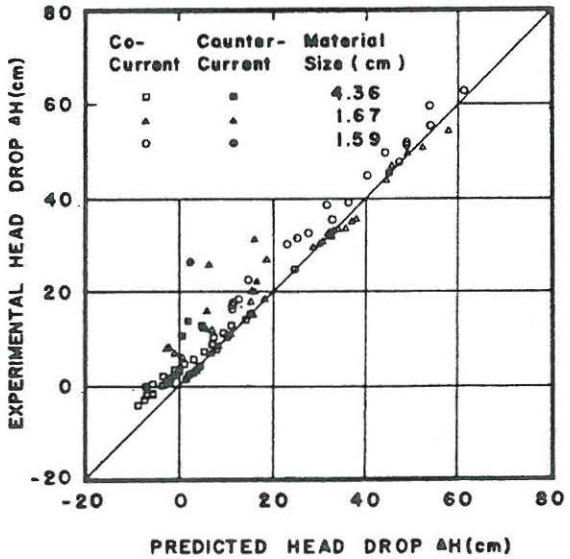

Fig 3.4 Bubble drift-flux model. From Hannoura et al (1978b)

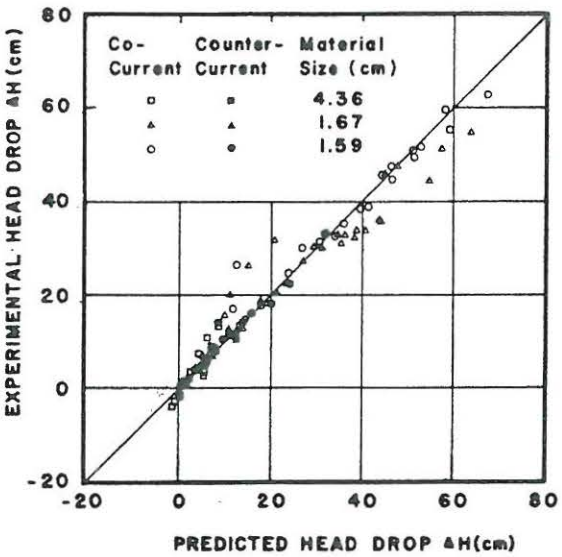

Fig 3.5 Slug drift-flux model. From Hannoura et al (1978b)

With the purpose of demonstrating the influence of entrained air on the hydraulic conductivity, the relative conductivity defined in eq (3.45) is plotted against the air fraction, cf the data points in Fig 3.6.

$$\frac{I_{aw}}{I_w} = \frac{(a_{2p} + b_{2p}|V|)V}{I_w} \tag{3.45}$$

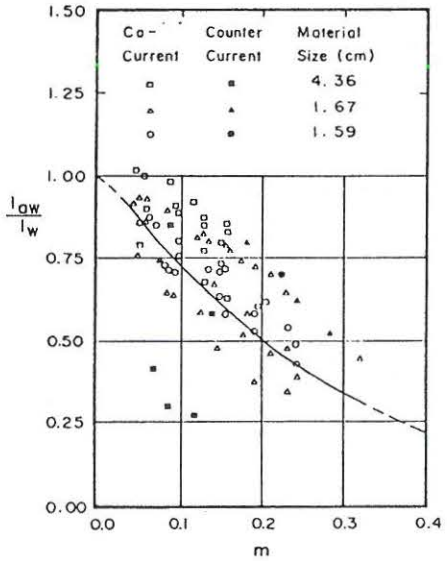

Fig 3.6 Relative conductivity vs air fraction. From Hannoura et al (1985a)

In 1985, the authors presented a simple expression, eq (3.46) for the dependency of the relative conductivity on the air fraction based on Fig 3.6.

$$\frac{I_{aw}}{I_w} = (1-m)^3 \tag{3.46}$$

In eq (3.46) the direction of the flow of air is not included.

4 STATIONARY POROUS FLOW MODEL

In the present chapter, the Forchheimer equation for stationary flow is derived from the the Navier-Stokes equations with the emphasis put on the variation of the Forchheimer coefficients with the porosity, the gross shape and orientation of the grains, the surface roughness and the gradation. By applying the hydraulic radius as a characteristic length scale together with the pore velocity as a refence velocity, the Navier-Stokes equations valid in a microscopic domain formed by the voids between the solid particles are transformed into the Forchheimer equation valid on a pore and solid averaged level. In this way, the same coefficients as described in Section 3.1 are derived. The influence of the gross shape and the surface roughness respectively are derived from a dimensional analysis.

Before discussing any coefficients for the flow resistance, it is important to notice the various characters of the flow, ie creeping flow, laminar flow with non-linear convective inertia forces due to flow separation and fully turbulent flow. These flow regimes are referred to as the Darcy, the Forchheimer and the fully turbulent flow regimes, respectively. Darcy flow is not relevant for the case of coarser rubble mounds. Because no sharp limits exist, the separations between the flow regimes are quantified by Reynolds number ranges.

Finally, characteristic values of the flow resistance coefficients for the Darcy and Forchheimer flow regimes are given in Section 4.4 and for the fully turbulent flow regime characteristic values of the quadratic flow resistance coefficient are given in Section 4.5.

4.1 Considerations Based on Navier-Stokes Equations

Chapter 4 is mainly based on Burcharth and Andersen (1993) considering one-dimensional porous flow. In the present Section 4.1, however, the deduction is extended to the three-dimensional case, leading to the vector form of the Forchheimer equation.

The kinematic and dynamic conditions for a fluid element in laminar porous flow can in principle be described by Navier-Stokes equations

$$\frac{dv_i}{dt} = \frac{\partial v_i}{\partial t} + \frac{\partial v_i}{\partial x_j} v_j = - \frac{1}{\rho} \frac{\partial p}{\partial x_i} + g_i + \nu \frac{\partial^2 v_i}{\partial x_j \partial x_j} \tag{4.1}$$

with the appropriate boundary conditions along the grain surfaces and the boundary of the space in question. t and x are the independent time and space variables, respectively. v is the velocity, p is the pressure, ρ is the density, ν is the viscosity and g is the acceleration of gravity.

Due to flow separation behind the single obstacles, the flow is rotational on a microscopic level. The convective acceleration term is re-written from

$$\frac{\partial}{\partial x_j} (v_i v_j) = \frac{\partial v_i}{\partial x_j} v_j + \frac{\partial v_j}{\partial x_j} v_i \tag{4.2}$$

On a microscopic level the continuity equation reads, cf eq (2.1)

$$\frac{\partial v_j}{\partial x_j} = 0 \tag{4.3}$$

and hence the last term on the right-hand side of eq (4.2) vanishes. Inserting eq (4.2) into eq (4.1) leads to

$$\frac{\partial v_i}{\partial t} + \frac{\partial}{\partial x_j}(v_i v_j) = -\frac{1}{\rho}\frac{\partial p}{\partial x_i} + g_i + \nu \frac{\partial^2 v_i}{\partial x_j \partial x_j} \tag{4.4}$$

The pressure and gravity terms can be merged together into p_o, defined by

$$p_o = p + \rho g h_o \tag{4.5}$$

where h_o is the height over an arbitrarily chosen horizontal datum, and such that

$$g_i = \frac{\partial}{\partial x_i}(-gh_o) \tag{4.6}$$

Now, eq (4.4) can be written as

$$\frac{\partial v_i}{\partial t} + \frac{\partial}{\partial x_j}(v_i v_j) = -\frac{1}{\rho}\frac{\partial p_o}{\partial x_i} + \nu \frac{\partial^2 v_i}{\partial x_j \partial x_j} \tag{4.7}$$

Introducing the hydraulic pressure gradient as an average over the sample of water and solid

$$I_i = -\frac{1}{\rho g}\frac{\partial p_o}{\partial x_i} \tag{4.8}$$

we obtain

$$I_i = -\frac{\nu}{g}\frac{\partial^2 v_i}{\partial x_j \partial x_j} + \frac{1}{g}\frac{\partial}{\partial x_j}(v_i v_j) + \frac{1}{g}\frac{\partial v_i}{\partial t} \tag{4.9}$$

which, for the stationary case reduces to

$$I_i = -\frac{\nu}{g}\frac{\partial^2 v_i}{\partial x_j \partial x_j} + \frac{1}{g}\frac{\partial}{\partial x_j}(v_i v_j) \tag{4.10}$$

Introducing U and D as any characteristic velocity and length, respectively, and averaging over a samlple of water and solid, eq (4.10) can be written in the dimensionally correct form

$$I_i = \alpha \frac{\nu}{g} \frac{U_i}{D^2} + \beta \frac{1}{g} \frac{U\, U_i}{D} \qquad (4.11)$$

or

$$I_i = AU_i + BU\, U_i \qquad (4.12)$$

where, in this context, U^2 equals U_jU_j.

Eq (4.12) is known as the Forchheimer equation (Forchheimer 1901), and the coefficients A and B (or α and β) are often taken as constants for a given fluid viscosity and a given geometry of the porous structure. This, however, is not a correct assumption because the coefficients depend on the kinematics of the flow including curvature of the flow paths. The various flow domains are usually characterised by a Reynolds number, Re.

In case of 'creeping flow', in which the velocities are very small, the convective inertia term can be neglected and we obtain the solution

$$I_i = \alpha'' \frac{\nu}{gD^2} U_i = A''U_i \qquad (4.13)$$

which is well-known as the 'Darcy' equation, cf eq (3.2). Creeping flow is as mentioned earlier not relevant for the case of coarser rubble mounds.

If the velocities are larger, but the flow still stationary and laminar, then curvatures (perturbations) of the flow paths introduce additional pressure drop which is described by the non-linear convective inertia term. For such conditions, the flow can be described by eqs (4.11) and (4.12).

For large velocities, turbulence will occur. Also turbulent porous flow can in principle be described by eq (4.1) with appropriate boundary conditions. The inertia terms will for fully turbulent (rough turbulent) flow completely dominate over the viscous term, and we obtain an equation of the form

$$I_i = \beta' \frac{1}{g} \frac{U\, U_i}{D} = B'U\, U_i \qquad (4.14)$$

If for fully turbulent flow an equation of the form (4.11) or (4.12) is used, it is important to notice that the linear term is to some extent a fitting term which has no physical meaning if we assume viscous forces to be negligible.

The Navier-Stokes equation (4.1) is never used for solving turbulent flow problems because the complexity of the flow makes it impossible. Instead, eq (4.1) is reformulated by introducing velocity mean values and velocity fluctuations. The influence of the latter is the so-called Reynolds stresses signified by an extra term in eq (4.1), arising from the convective acceleration term

$$\frac{dv_i}{dt} = \frac{\partial v_i}{\partial t} + \frac{\partial v_i}{\partial x_j} v_j = - \frac{1}{\rho} \frac{\partial p_o}{\partial x_i} + \nu \frac{\partial^2 v_i}{\partial x_j \partial x_j} + \frac{\partial}{\partial x_j} \left(- \overline{u_i u_j} \right) \qquad (4.15)$$

where p_o and v_i now represent time averages, and u_i and u_j are the velocity fluctuations.

This re-formulated equation is known as the Reynolds equation. Written in the form of eq (4.10) for the stationary case, eq (4.15) yields:

$$I_i = - \frac{\nu}{g} \frac{\partial^2 v_i}{\partial x_j \partial x_j} + \frac{1}{g} \frac{\partial}{\partial x_j} (v_i v_j) + \frac{1}{g} \frac{\partial}{\partial x_j} \left(\overline{u_i u_j} \right) \qquad (4.16)$$

Assuming the velocity fluctuations to vary proportionally to the velocity time average, represented by the characteristic value U, and taking D as a characteristic length scale, very naturally the Reynolds stress term takes the same form as the convective term, and hence they can be merged together into one term, cf eq (4.14). It should be noticed that it is not necessary to apply the Reynolds equation, as the Navier-Stokes equation leads to (4.11) and (4.12) and by neglecting the viscous term, also to (4.14). The above considerations on the Reynolds equation are included in order to demonstrate the relation to turbulent flow problems which are solved from the Reynolds equation.

The coefficients α, β and β' (and A, B and B') depend on the flow regime. In principle, eqs (4.13) and (4.14) represent two asympthotic expansions for very small and very large Re, respectively. Note that the coefficients β and β' are generally not equal.

It follows that the two coefficients in eqs (4.11) and (4.12) cannot be regarded as constants over the whole range, $0 < Re < \infty$, but must be related to certain intervals of Re. For smooth spheres with uniform diameter, the transition zones between the different flow regimes are expected to be narrow and easy to identify. For irregular and graded materials, the transition zones are likely to be blurred and difficult to identify. Burcharth and Christensen (1991) use as a practical engineering approach a separation into a Forchheimer flow regime, given by eq (4.11) and a turbulent flow regime, given by eq (4.14), within each of which the coefficients can be taken as constants with good accuracy, cf Fig 4.1 and the following considerations.

If in eq (4.11) U is substituted by V/n, where V is the discharge velocity, n is the porosity, and D is substituted by a hydraulic radius, R, defined as the ratio of pore volume over pore surface area for spheres with diameter, d

$$R = \frac{n}{1-n} \frac{d}{6} \qquad (4.17)$$

we obtain

$$I_i = \alpha \left(\frac{1-n}{n} \right)^2 \frac{\nu}{gd^2} \frac{V_i}{n} + \beta \frac{1-n}{n} \frac{1}{gd} \left(\frac{V}{n} \right) \left(\frac{V_i}{n} \right) \qquad (4.18)$$

or

$$I_i = aV_i + bVV_i \tag{4.19}$$

with

$$a = \alpha \frac{(1-n)^2}{n^3} \frac{\nu}{gd^2} \quad \text{and} \quad b = \beta \frac{1-n}{n^3} \frac{1}{gd} \tag{4.20}$$

where α depends on the gradation and grain shape, and β depends on the same parameters plus the relative surface roughness of the grains.

Similarly, if U is substituted by V/n and D is substituted by R, the Darcy equation (4.13) will vary with the porosity like the linear term in eq (4.18), and the turbulent flow equation (4.14) will vary with the porosity like the quadratic term in eq (4.18).

Irmay (1958) considered the derivation of the Darcy and Forchheimer equations from Navier-Stokes' equations. The detailed microscopic flow pattern including separation was discussed. After averaging over the sample, this lead to the same a and b coefficients as in eq (4.20). In Irmay's derivation, however, the expression for p_o, cf eq (4.5), was extended with the term $\rho V^2/2$.

The Forchheimer equation (4.12) provides no information on the dependency of the coefficients on the Reynolds number. In order to distinguish between various flow regimes, it is, however, necessary to introduce the ratio between the convective inertia forces and the viscous forces

$$\frac{\text{inertia forces}}{\text{viscous forces}} = \frac{B}{A} U \tag{4.21}$$

This way of defining a Reynolds number was first done by Engelund (1953).

With U=V/n and D=R as above, we get

$$\frac{\text{inertia forces}}{\text{viscous forces}} = \frac{\beta}{\alpha} \frac{Vd}{\nu(1-n)} \sim \frac{Vd}{\nu(1-n)} \tag{4.22}$$

where, in this context, V^2 equals V_jV_j.

Only in the Darcy and Forchheimer flow regimes, α is well-determined, and hence β/α has been removed. For convenience, it is chosen to apply the following definition of the Reynolds number

$$Re = \frac{Vd}{\nu} \tag{4.23}$$

Moreover, this definition is identical to the definition usually applied considering a single obstacle exposed to an ambient fluid. For practical purposes with respect to scale models, eq (4.22) shows that scale effects may appear when applying usual Froude scaling, see also Jensen and Klinting (1983). Besides the flow regimes may differ, resulting in different flow resistance coefficients, cf Sections 4.4 and 4.5.

Defining a viscous friction factor, cf eq (3.16)

$$I_i = f_v \frac{(1-n)^2}{n^3} \frac{\nu}{gd^2} V_i \qquad (4.24)$$

eq (4.18) can be written in the form

$$f_v = \alpha + \beta \frac{Re}{1-n} \qquad (4.25)$$

where α and β depend on the porous material and on Re. The principal variation of f_v is shown in Fig 4.1, see Fand et al (1987).

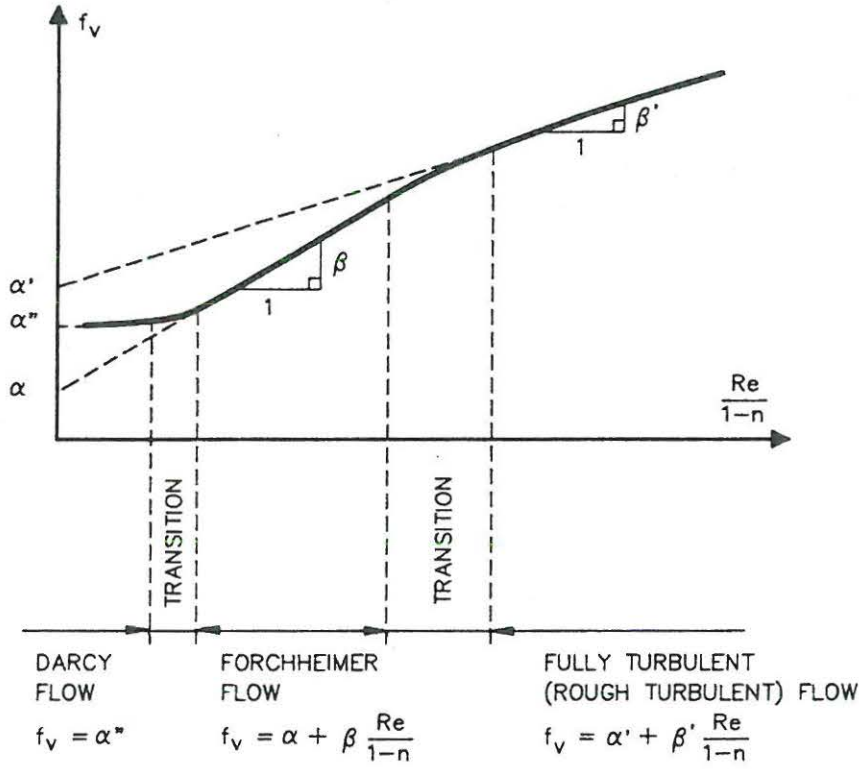

Fig 4.1 Representation of flow regimes for porous flow based on a Forchheimer equation analysis. The coefficients in the figure are related to eq (4.25).

4.2 Gross Shape and Surface Roughness

Hydraulic radius theory may be critisised for not taking the gross shape of the grains and the surface roughness into account. Also the grading of the material may affect the flow resistance. The gross shape of the stones can be resolved into two contributions:

- the aspect ratio, ℓ/t, where ℓ is the maximum length of the grain and t is the perpendicular minimum length
- the ratio, d_s/d, where d_s is a characteristic dimension of the surface undulations as compared to a sphere, and d is the equivalent spherical diameter

From a tortuosity point of view, the flow resistance must depend on the direction of the flow

relative to the orientation of the stones, with a minimum of flow resistance for flow parallel to the length axes of the stones and a maximum of flow resistance with perpendicular flow. As shown in Section 4.5, only little information exists on stones exposed to parallel flow. It seems, however, as if the flow resistance is lower for parallel flow than for perpendicular flow, cf Table 4.5.

The influence of the surface undulations is a lowered hydraulic radius and generation of extra separation zones as compared to a material consisting of spheres. For a typical irregular stone, it is reasonable to set

$$\frac{d_s}{d} \sim 0.1 \tag{4.26}$$

Instead of d_s/d the surface undulations are more conveniently expressed through a grain shape factor. For non-spherical particles, Carman (1937) suggested a modified hydraulic radius, cf eqs (3.7) and (3.10). The grain surface area per unit volume equals

$$S = \chi \frac{6(1-n)}{d} \tag{4.27}$$

where χ is a grain shape factor defined from the surface properties of the particles, which is unity for a sphere, and since a sphere has minimum specific surface, is larger than unity for all non-spherical shapes. Carman denoted $1/\chi$, a surface factor. For the modified hydraulic radius, R_χ, we get

$$R_\chi = \frac{n}{S} = \frac{1}{\chi} \frac{n}{1-n} \frac{d}{6} \tag{4.28}$$

Also the surface roughness, k, may contribute to the flow resistance in the upper Forchheimer flow regime for irregular rock and in the fully turbulent (rough turbulent) flow regime for all materials. By applying a dimensional analysis, it is easily shown that a variety of expressions for the linear and quadratic terms can be established. Burcharth and Christensen (1991) applied a dimensional analysis in order to obtain expressions for A and B in eq (4.12). A very similar derivation is given here:

$$I = I\left(\frac{V}{n},\ \nu,\ g,\ R,\ \text{geometry}\right) \tag{4.29}$$

where the hydraulic radius R is defined by eq (4.17) and the geometry is characterised partly by the surface undulations expressed through χ, and the surface roughness, k, of the grains and partly by a parameter, S, taking the flow direction and the aspect ratio, ℓ/t, into account and by a gradation parameter, G.

Dimensional analysis yields the gradient to be a function of a linear term dependent on the viscosity and a quadratic term, $I = I(I_1, I_2)$ where:

$$I_1 = I_1\left[\left(\frac{1-n}{n}\right)^2 \frac{\nu}{gd^2} \frac{V}{n} \chi^{N_1},\ S,\ G\right] \quad \text{for all } N_1 \tag{4.30}$$

$$I_2 = I_2 \left[\frac{1-n}{n} \frac{1}{gd} \left|\frac{V}{n}\right| \left(\frac{V}{n}\right) \chi^{N_2} \left(\frac{k}{R}\right)^{N_3}, S, G \right] \quad \text{for all } N_2 \text{ and } N_3 \tag{4.31}$$

If the assumption is made that I equals the sum of I_1 and I_2, we obtain

$$\begin{aligned} I = I_1 + I_2 = I_1 & \left[\left(\frac{1-n}{n}\right)^2 \frac{\nu}{gd^2} \frac{V}{n} \chi^{N_1}, S, G \right] \\ + I_2 & \left[\frac{1-n}{n} \frac{1}{gd} \left|\frac{V}{n}\right| \left(\frac{V}{n}\right) \chi^{N_2} \left(\frac{k}{R}\right)^{N_3}, S, G \right] \text{ for all } N_1, N_2 \text{ and } N_3 \end{aligned} \tag{4.32}$$

The factor χ is introduced in order to modifiy R, cf eq (4.28). If, in the dimensional analysis, R is subsituted by R_χ, we should have $N_1=2$ and $N_2=1$. As the impact of the surface undulations is not only related to the increased surface area, but is also related to extra flow separation, it is to be expected that N_1 and N_2 can deviate from the above values.

McCorquodale et al (1978) examined experimentally the grain shape factor, χ, for different types of material from 100 particle random samples. The results are summarised in Table 4.1.

Table 4.1 Typical grain shape factors

Material	χ
River gravel	1.31
Rounded quartz	1.52
Crushed rock	1.56-2.27

Carman (1937) refers to microscopic measurements of $1/\chi$ carried out by Heywood. With relevance to this study, the value for sand (rounded grains) is given as $1/\chi=0.81$ or $\chi=1.23$.

In the case of a smooth sphere, we have $\chi=1$ and $k=0$, and hence we get the same expression as eq (4.18)

$$I = I_1 + I_2 = \alpha \left(\frac{1-n}{n}\right)^2 \frac{\nu}{gd^2} \frac{V}{n} + \beta \frac{1-n}{n} \frac{1}{gd} \left|\frac{V}{n}\right| \left(\frac{V}{n}\right) \tag{4.33}$$

where α and β both depend on G.

For the case of non-linear laminar flow, as it is found in the lower end of the Forchheimer regime, the gradient is not dependent on k, and hence, $N_3=0$.

For irregular material, we have $\chi>1$, and further in the upper end of the Forchheimer flow regime and in the fully turbulent flow regime, there are three contributions to the flow resistance: viscous, inertia and turbulent forces, and hence we also have $N_3 \neq 0$. In these cases, the extra factor associated with k implies an altered dependency of I on n as compared to eq (4.33), as R depends on n.

It is difficult to verify which is the best formulation of the factors A and B with respect to the dependency on the porosity. Further, from permeameter tests, it is not possible to

distinguish between the influence of the surface undulations and the influence of the surface roughness. As the hydraulic radius theory is correct in the reference case of spheres, and as it gives good results in case of irregular materials, cf Section 4.3, eqs (4.18) and (4.33) are preferred for all types of material.

As shown in Sections 4.4 and 4.5, the variation in β/β_{sphere} for the Forchheimer flow regime, within the accuracy of the measurements, equals the variation in β'/β'_{sphere} for the turbulent flow regime. As the surface roughness has no influence on the lower Forchheimer flow regime, this indicates that the surface undulations are the most governing parameter.

One effect which is not implemented in any of the above equations is a possible change of the coefficients α, β and β' with n. When n is increased without changing the shape of the grains, the pores become less tortuous leading to a relative reduction in the flow resistance. However, this effect is probably insignificant within the practical range of n.

4.3 Dependence of the Forchheimer Coefficients on the Porosity

Ergun's equation (3.13) follows the general Forchheimer equation form, eq (3.3), in which the coefficients are denoted a and b and also eq (4.18). In order to verify the variation of a and b with the porosity, Ergun performed experiments with porous gas flow in the Forchheimer regime. Crushed porous material was packed with different porosities, ranging between 0.44 and 0.53. It appeared that the variation with the porosity conforms to eq (4.18), cf Fig 4.2.

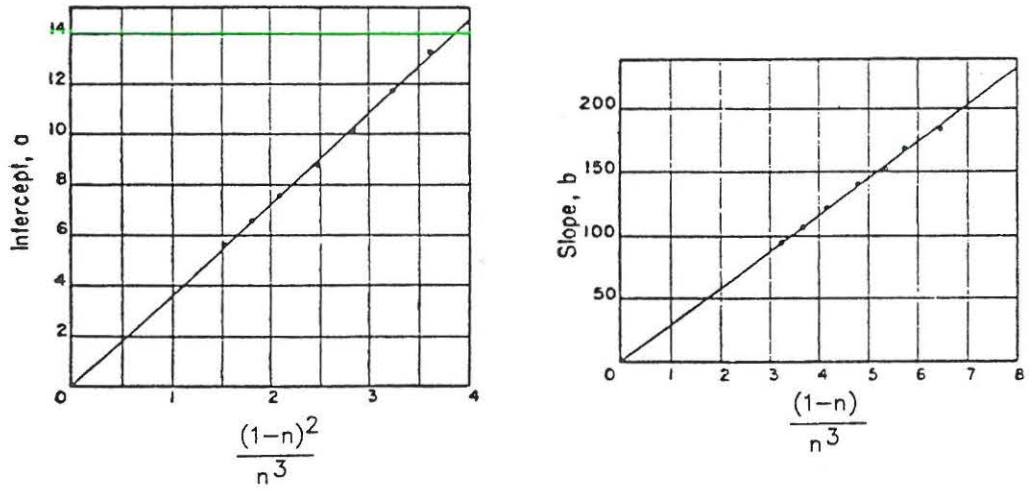

Fig 4.2 Dependence of a and b on porosity (n). From Ergun (1952).

4.4 Coefficients for the Darcy and Forchheimer Flow Regimes

Rewriting the Forchheimer expression, eq (3.3) in the following manner

$$\frac{Igd}{V\nu} = a\,\frac{gd}{\nu} + bgRe \qquad (4.34)$$

we get a way of plotting the gradient vs Re, which is familiar to the expression given by eq (4.25). The type of plot governed by eq (4.34) was chosen by Fand et al (1987), cf Figs 4.3 and 4.4. It should be noticed that the quantities agd/ν and bg depend on the porous material and Re and also on the porosity and the grain diameter, cf eq (4.20).

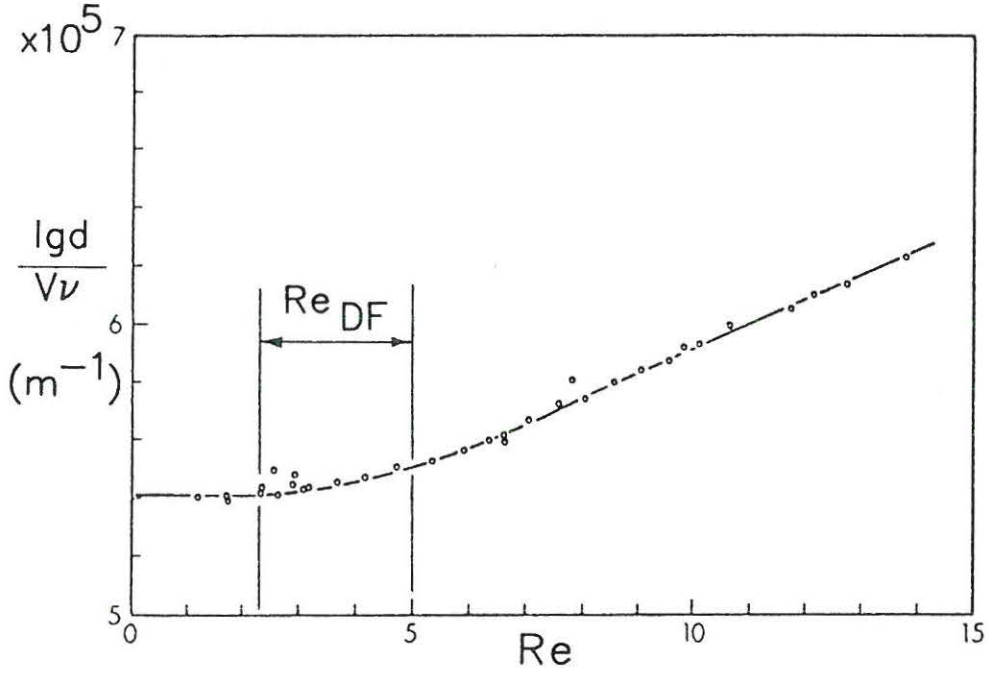

Fig 4.3 Example of data for Darcy flow through spheres. From Fand et al (1987)

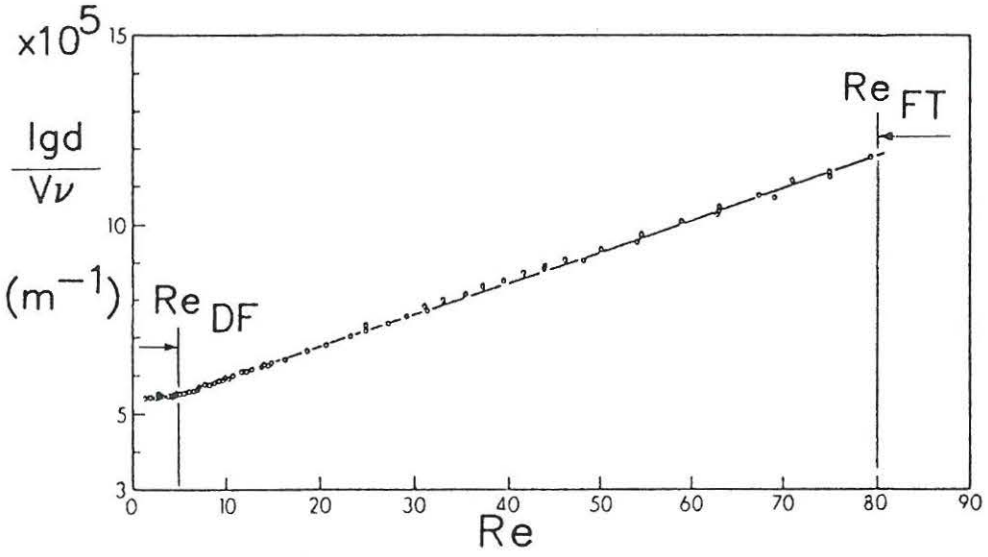

Fig 4.4 Example of data for Forchheimer flow through spheres. From Fand et al (1987)

According to Fand et al (1987), the Reynolds number range, Re_{DF}, for the transition from

Darcy flow to Forchheimer flow varies from 2 to 5, cf Fig 4.3. This corresponds well to the value of 4 given by Engelund (1953). The upper limit for the Forchheimer flow regime is found at a Reynolds number of 80, cf Fig 4.4.

Table 4.2 α and β values for the Forchheimer flow regime. From Fand et al (1987).

	d, d_h (mm)	n	κ	α	β
Simple media	2.098	0.357	5.33	184.2	1.925
	3.072	0.360	5.28	177.8	1.902
	4.029	0.359	5.12	174.0	1.811
Complex media	3.690	0.348	5.33	180.6	1.920
	3.276	0.344	5.38	183.5	1.935
	2.759	0.342	5.28	179.5	1.882

Table 4.3 Engelund coefficients transformed to fit eq (4.18). α and β coefficients from Burcharth and Christensen (1991).

	α	β	β/β_{sphere}
Uniform, spherical particles	~190	~1.8	1.0
Uniform, rounded sand grains	~240	~2.8	~1.6
Irregular, angular grains	up to 360 or larger	up to 3.6 or larger	up to 2.0 or larger

As to the α-value of 190 for uniform spherical particles reported by Engelund, cf Table 4.3, it represents truly the lower asymptotic value for the Forchheimer flow regime because it is quantitatively identical to the uniform diameter sphere coefficient, $36\ \kappa = 36 \cdot 5.34 = 192$, given in the Darcy flow equation

$$I = 36\ \kappa\ \frac{(1-n)^2}{n^3}\ \frac{\nu}{gd^2}\ V \qquad (4.35)$$

where κ is the Kozeny-Carman constant, cf Fand et al (1987).

The variation of the α and β-values with the grain shape can be seen in Table 4.3. For the Darcy and the lower end of the Forchheimer flow regimes in consideration, the variation in β can only be caused by the gross shape of the grains and not the roughness of the surface. McCorquodale et al (1978) fitted an expression of the Forchheimer type to experiments. Comparing to eq (4.32), N_1 was assumed equal to 0 and the best value of N_2 was found to be 1. Hence, the variation of β with the material must compare to the variation in χ, cf Table 4.1. As seen from Table 4.3, this is actually the case within the accuracy of the measurements. From Table 4.3, it appears that in the Forchheimer flow regime, also the value of N_1 must be close to 1, ie β/α is independent of the grain size with $\beta/\alpha \sim 0.01$.

As pointed out in Burcharth and Andersen (1993), it is plausible that Re_{FT} is higher than 300. From eq (4.22), the ratio between the convective inertia forces and the viscous forces can be expressed by the Reynolds number, cf eq (4.23)

$$\frac{\text{inertia forces}}{\text{viscous forces}} = \frac{\beta\ Re}{\alpha(1-n)} \tag{4.36}$$

If we insert a value of $Re_{FT}=300$ corresponding to transition to the fully turbulent flow regime, we find

$$\frac{\text{inertia forces}}{\text{viscous forces}} \simeq 5 \tag{4.37}$$

which is a surprisingly low value. This indicates that the Reynolds number, Re_{FT}, corresponding to the lower value of the fully turbulent flow regime should be somewhat larger, ie $Re_{FT}=600\text{-}1000$. Further, eq (4.37) shows that the data validated by Engelund (1953) must correspond to the Darcy flow regime and the lower end of the Forchheimer flow regime.

By use of eq (4.23), the Forchheimer expression given by eq (4.18) can be written in the following form, with the critical values I_{FT} and Re_{FT} corresponding to transition to fully turbulent flow inserted

$$I_{FT} = \frac{\nu^2}{gd^3}\left(\frac{1-n}{n}\right)^3\left[\alpha\ \frac{Re_{FT}}{1-n} + \beta\left(\frac{Re_{FT}}{1-n}\right)^2\right] \tag{4.38}$$

The critical velocity equals

$$V_{FT} = \frac{Re_{FT}\nu}{d} \tag{4.39}$$

If we, for practical purposes, insert the following values, as done by Burcharth and Christensen (1991)

$n = 0.45$
$\alpha = 500$
$\beta = 5$
$\nu = 1.14 \cdot 10^{-6}\ s^2/m$
$Re_{FT} = 300$

we find the values shown in Table 4.4.

Table 4.4 Typical values of I_{FT} and V_{FT}. From Burcharth and Christensen (1991).

Characteristic diameter, d (m)	I_{FT}	V_{FT} (m/s)
0.001	430	0.34
0.01	$4.3 \cdot 10^{-1}$	0.034
0.03	$1.6 \cdot 10^{-2}$	0.011
0.06	$2.0 \cdot 10^{-3}$	0.006
0.20	$5.3 \cdot 10^{-5}$	0.002

For sand with diameter 0.001 m, it is evident from Table 4.4 that fully turbulent flow never occurs in sand due to the very large critical gradient.

For practical purposes, Table 4.4 shows that the Forchheimer flow regime is relevant to breakwater sand cores. Dealing with rock material, the Forchheimer flow regime is only relevant to the inner parts of physical scale models and never to prototype breakwaters.

4.5 Coefficient for the Fully Turbulent Flow Regime

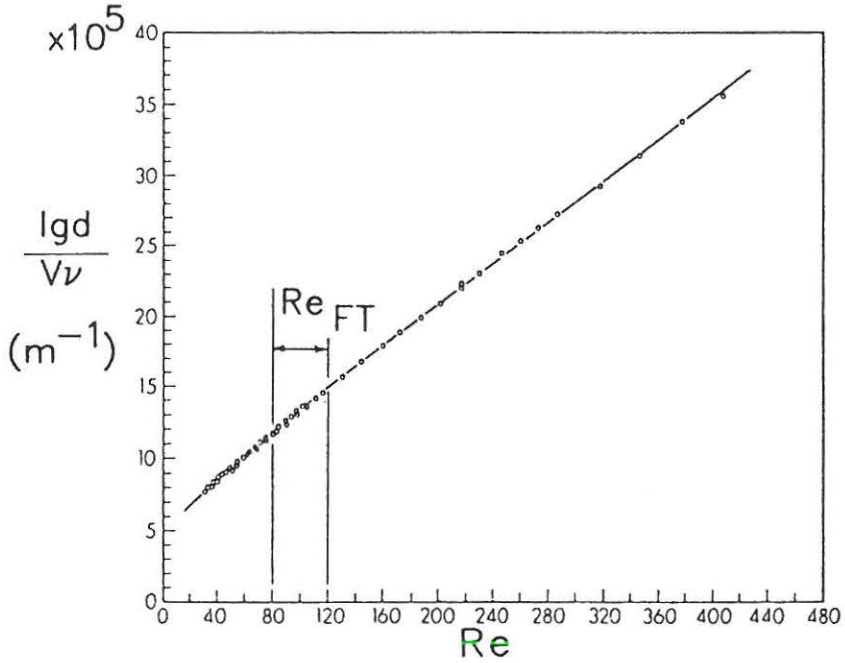

Fig 4.5 Example of data for fully turbulent flow through spheres. From Fand et al (1987)

According to Fand et al (1987), the Reynolds number range for the transition between the Forchheimer flow and the turbulent flow is rather narrow, $80 \leq Re_{FT} \leq 120$, for randomly packed spherical particles, cf Fig 4.5. For this case, it can be assumed as an approximation that $Re_{FT}=100$ separates the Forchheimer flow range and the fully turbulent range. For stone samples, the corresponding Reynolds number ranges are wider and a larger value of Re_{FT} must be chosen. A re-analysis of available data on porous flow in coarse granular media has shown that $Re_{FT}=300$ is a characteristic value, see Burcharth and Christensen (1991).

For the complex media examined by Fand et al (1987), values of β' are around 1.6 and for the simple medium with the largest diameter, β' is approximately 1.5, ie lower than the corresponding β-values for the Forchheimer flow regime.

All data in Table 4.5, showing characteristic values of β' related to d_{50} have been corrected for wall effects where it was necessary, cf Burcharth and Christensen (1991). The data for rock from Williams (1992) are related to the equivalent spherical diameter. The original data from Williams were related to the nominal diameter (equivalent cube length). It is uncertain which reference diameter has been applied for the data from Hannoura et al (1978). The other data for rock are related to either the equivalent spherical diameter or the sieve diameter, which based on experience, are approximately identical. For the tests of Hannoura

and McCorquodale, the direction between the flow and the underlayer during construction of the sample is not known. In the tests of Smith, the flow was parallel to the underlayer during construction of the sample, and in all other tests the flow was perpendicular to the underlayer during construction.

Table 4.5 Listing of β' coefficients for fully turbulent flow. The values are related to d_{50}. From Burcharth and Christensen (1991) and Burcharth and Andersen (1993).

Material	Packing	d_{85}/d_{15}	β'	Data source
Spheres	Cubic	1.0	1.0-1.3	Sm
	Rhomb	1.0	0.47-1.1	Sm
	Random	1.0	1.1-1.5	D
	Random	1.8	1.6	D
	Random	1.0	1.5	F
	Random	2.0	1.6	F
Round rock	Random	1.4	2.2	B
		1.7	2.2-2.9	D
		?	1.7-2.2	H
		1.3	1.9	W
Semi-round rock	Random	1.9	2.7	B
		1.3	2.4	W
Irregular rock	Random	1.4-1.8	2.4-3.0	B
		1.6	4.1-11	D
		?	3.0-3.7	H
		1.3-1.4	2.5-2.9	Sh
		1.3	3.7	W
Equant rock	Random	1.2	3.6	W
Tabular rock	Random	1.4	1.5	Sm
		1.2	3.7	W

Legend: B: Burcharth et al (1991), D: Dudgeon (1966), F: Fand et al (1987), H: Hannoura et al (1978), Sh: Shih (1990), Sm: Smith (1991), W: Williams (1992)

Solvik and Svee (1976) found the following values of β' related to a reference diameter equal to 1.7 d_{10}:

- crushed stones, a little rounded: $\beta' = 3.1$
- crushed stones, sharp edged: $\beta' = 3.6$

The direction between the flow and the underlayer during construction is not known.

The β' values shown in Table 4.5 correspond to Reynolds numbers up to 10,000, which are smaller than those of a prototype breakwater reaching 10^6 in the surface layers. It has still not been proved that β' is constant over this large range of Reynolds numbers, although it is most likely from a theoretical point of view: once the flow has become fully turbulent or rough turbulent, the character of the flow does not change further. This phenomenon is known from eg rough turbulent pipe flow, where the pipe friction factor becomes constant when a certain value of Re is exceeded, and from eg rough turbulent flow around cylinders, where the drag coefficient becomes constant when a certain value of Re is exceeded.

Table 4.5 shows that the tests of Smith (1991), carried out with flow parallel to the length axes of the stones, result in lower β' values than with perpendicular flow, ie for the same flow conditions and with approximately identical surface undulations and surface roughness, the flow direction in combination with the aspect ratio has significant influence. The measurements indicate that the β' value for parallel flow is in the order of half the value of β' for perpendicular flow.

Like with the Darcy and Forchheimer flow regimes, the ratio between the β' values and the β' value for uniform spheres can be calculated. Table 4.6 shows some characteristic values, based on Table 4.5.

Table 4.6 Characteristic values of β' and β'/β'_{sphere}

	β'	$\beta'/\beta'_{spheres}$
Spheres	~1.4	1.0
Round rock	~2.2	~1.6
Irregular rock	2.4-4.0	1.7-2.9

It is noticeable that, within the accuracy of the measurements, the same ratios are found as in the case of Darcy and Forchheimer flow, cf Table 4.3. This indicates that for fixed flow direction, the variation in β and β' is mainly governed by the surface undulations of the grains, also for fully turbulent flow, and not by the surface roughness, ie $N_3 \ll 1$, cf eqs (4.26) to (4.28) and (4.32).

Due to the changed velocity distribution when entering the fully turbulent flow regime, there is an apparent increase in the linear flow resistance coefficient, α', as compared to α. For rock, it appears that α' is in the order of 1000 with a large scatter from one test to another. As mentioned previously, α' is to some extent a fitting coefficient which may explain the large scatter. Anyway, for the fully turbulent flow regime, the linear term is much smaller than the quadratic term, and hence it can be omitted. Like in the preceeding section, the ratio between the convective inertia forces and the viscous forces can be calculated as

$$\frac{\text{inertia forces}}{\text{viscous forces}} = \frac{\beta' Re}{\alpha'(1-n)} \tag{4.40}$$

For a prototype breakwater in the surface layers, Re is in the order of 10^6 yielding as a high bound for practical applications

$$\frac{\text{inertia forces}}{\text{viscous forces}} \simeq 5{,}000 \tag{4.41}$$

cf eq (4.14).

5 NON-STATIONARY POROUS FLOW MODEL

This chapter extents the stationary porous flow model, described in Chapter 4, with an inertia term. The inertia term and the variation with the porosity is found by applying a cylinder/sphere analogy, which basically originates from Navier-Stokes equations. By neglecting the viscous flow resistance terms, Navier-Stokes equations turn into the Euler equations, which for this purpose are transformed into the Bernoulli equation under the assumption of irrotational flow, ie potential flow. In case of a single obstacle, the Bernoulli equation leads to the inertia term of the well known Morison equation.

Two different models are derived. In one model, cf Section 5.2, the variation with the porosity is included by applying the pore velocity as a reference velocity. The model is purely empirical, as the virtual mass coefficient, which appears to be constant, is derived from the measurements described in Section 5.5. This model, derived from a cylinder/sphere analogy, results in the same equation and virtual mass coefficient as the more general definition given by Madsen (1974) and Hannoura and McCorquodale (1978), cf Section 3.2.

Another model, cf Sections 5.2 and 5.3, is based on potential theory as applied in the description of groups of cylinders exposed to accelerating flow. The discharge velocity is used as reference velocity. The potential theory results in a model equation, which qualitatively predicts the variation of the virtual mass coefficient with the porosity for cylinders as well as spheres. The model shows good agreement with the measurements described in Section 5.5.

The drag term of the cylinder/sphere analogies is discussed as well. As mentioned in Section 2.4, the drag term of the Morison equation cannot be derived directly from the Bernoulli equation based on the assumption of irrotational flow, but is usually derived through a stepwise semi-theoretical application of the Bernoulli equation, taking the flow separation into account. In principle, the quadratic flow resistance term of the Forchheimer equation can be described by the drag term. As compared to the hydraulic radius theory, the drag models give a more detailed flow description including flow separation. This leads to a better understanding of the phenomenon, but for practical purposes, the dependence of the drag coefficient on the porosity is unknown. Concordingly, the a' and b' coefficients found from the measurements are decomposed after the expression by Ergun leading to α' and β' coefficients.

The dependency of β' on the Keulegan-Carpenter number is discussed theoretically and compared to the measurements.

5.1 One-Dimensional Unsteady Flow Equations

The one-dimensional unsteady porous flow equation is often taken as

$$I = a'V + b'|V|V + c\,\frac{\partial V}{\partial t} \tag{5.1}$$

where I is the hydraulic gradient and V is a characteristic velocity. Eq (5.1) can in principle be derived from the Navier-Stokes equation, eq (4.1). The two first terms compare to the steady flow Forchheimer equation. Moreover, eq (5.1) compares to the Morison equation if the linear viscous term is either neglected or included in the quadratic term through the

variation of the coefficient, b'. The coefficients b' and c depend on the geometry (inclusive surface texture) of the stones, on Re, on $\partial V/\partial t$ and the flow history. Thus, the coefficients are not constants and should in principle be treated as instantaneous values, even for oscillatory flow conditions. However, in engineering practice, for the sake of simplicity or inattention, the coefficients are taken as constants. For oscillatory flow, a much more correct method would be to take b' and c as constants within a cycle defined by characteristic Reynolds' and Keulegan-Carptenter numbers signifying the oscillatory flow. This is still a simplification because b' and c actually vary within the cycle. Instantaneous values are too complicated to deal with in practice, for which reason the following discussion is based on time invariant coefficients within a cycle. This on the other hand involves fitting of the coefficients over a complete cycle and the values of the coefficients will then specifically relate to cyclic flow. The question still remains to which extent such values can be used for non-cyclic flow for which a Keulegan-Carpenter number cannot be defined.

5.2 Cylinder/Sphere Analogy

In order to describe the local acceleration and the associated virtual mass for the case of non-steady porous flow, it is necessary to distinguish between the volume of water in the porous matrix and the displaced volume of water, ie the volume of solids. In the present Section 5.2, which is based on Burcharth and Andersen (1993), the virtual mass coefficient is related to the volume of the solids corresponding to the usual approach for calculation of flow forces on single bodies.

Initially, the flow through an array of fixed pipes with 'large porosity' is considered, Fig 5.1.

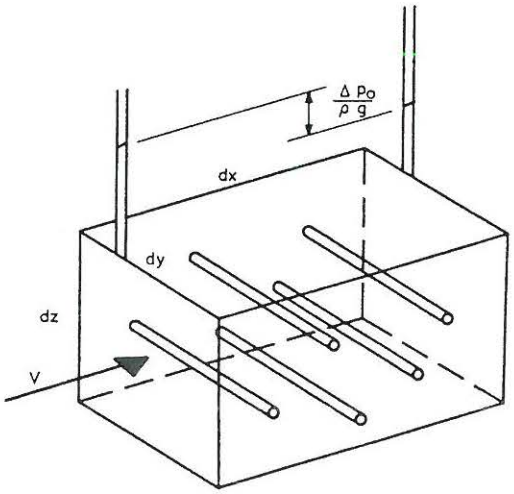

Fig 5.1 Large porosity cylinder analogy.
d = pipe diameter, n = porosity = fluid vol./total vol.
volume of pipes = (1-n)dxdydz, no of pipes = $4/\pi d^2$ (1-n)dxdz

In this case, it is obvious to use the far field velocity, V, as the characteristic velocity. The pressure acting on the entire sample of grains and water is considered, and the reactive force from the porous sample comprises forces associated with the water as well as the solid. The force balance in the direction of the flow considered as an average over the sample of water and solid reads, cf Section 2.4 ($\partial p_o/\partial x$ is negative in the direction of the flow)

$$- \frac{\partial p_o}{\partial x} \, dxdydz - F_{drag}^{pipes} - F_{iner}^{pipes} - F_{iner}^{fluid} = 0 \tag{5.2}$$

where

$$F_{drag}^{pipes} = C_d(n) \; ½\rho \, |V| V \; d \; dy \; \frac{4}{\pi d^2} \; (1-n)dxdz \tag{5.3}$$

$$F_{iner}^{pipes} = C_m(n)\rho \; \frac{\pi d^2}{4} \; dy \; \frac{\partial V}{\partial t} \; \frac{4}{\pi d^2} \; (1-n)dxdz \tag{5.4}$$

$$F_{iner}^{fluid} = \rho \; ndxdydz \; \frac{\partial V}{\partial t} \tag{5.5}$$

The above equations yield

$$I = - \frac{\partial\left(\frac{p_o}{\rho g}\right)}{\partial x} = C_d(n) \; \frac{2}{\pi} \; \frac{1-n}{gd} \; |V|V + \frac{n+C_m(n) \; (1-n)}{g} \; \frac{\partial V}{\partial t} \tag{5.6}$$

In general for a fixed body exposed to an ambient flow, $C_m = 1 + C_a$, where C_m is the virtual mass coefficient, 1 relates to the Froude-Krylov force and C_a is the added mass coefficient. For a single smooth cylinder assuming potential flow $C_a = 1$ and $C_m = 2$. C_d and C_m correspond to the conventional definition of the Morison Equation and depend on the Reynolds number, Re, the Keulegan-Carpenter number, KC, and the relative surface roughness, k/d.

Alternatively, the gradient associated with the local acceleration may be written as, cf eq (5.6)

$$- \frac{\partial\left(\frac{p_o}{\rho g}\right)}{\partial x} = \frac{1 + C_a(n) \; (1-n)}{g} \; \frac{\partial V}{\partial t} \tag{5.7}$$

The drag coefficient, C_d, depends on n, as for separated flow the pressure distribution around the cylinder depends on the velocity distribution which depends on n. In fact, the flow pattern associated with the drag model is much more complicated than the hydraulic radius theory, cf Chapter 4, which is merely averaged over the sample of water and solid when defining the hydraulic radius. The details of the drag term are further discussed at the end of this section.

The virtual mass phenomenon is associated with the generation of the potential field around the obstacles, ie an irrotational flow problem. As the potential and streamlines depend on n, also C_m must depend on n.

The Keulegan-Carpenter number is defined as

$$KC = \frac{V_{max} T}{d} \tag{5.8}$$

In case of a sphere analogy, the same structure of the formula appears

$$I = -\frac{\partial\left(\frac{p_o}{\rho g}\right)}{\partial x} = C_d(n)\ \frac{3}{4}\ \frac{1-n}{gd}\ |V|V + \frac{n+C_m(n)\ (1-n)}{g}\ \frac{\partial V}{\partial t} \tag{5.9}$$

For a single smooth sphere assuming potential flow $C_a=0.5$ and $C_m=1.5$.

In case of a dense sample of cylinders, the ambient flow is now taken as the pore velocity, V/n. The force balance (5.1) is still valid, but now

$$F_{drag}^{pipes} = C_d(n)\ \frac{1}{2}\rho\left|\frac{V}{n}\right|\frac{V}{n}\ d\ dy\ \frac{4}{\pi d^2}\ (1-n)dxdz \tag{5.10}$$

$$F_{iner}^{pipes} = C_m(n)\ \rho\ \frac{\pi d^2}{4}\ dy\ \frac{\partial}{\partial t}\left(\frac{V}{n}\right)\ \frac{4}{\pi d^2}\ (1-n)dxdz \tag{5.11}$$

$$F_{iner}^{fluid} = \rho\ n dxdydz\ \frac{\partial}{\partial t}\left(\frac{V}{n}\right) \tag{5.12}$$

This yields

$$I = -\frac{\partial\left(\frac{p_o}{\rho g}\right)}{\partial x} = C_d^*(n)\ \frac{2}{\pi}\ \frac{1-n}{n^2}\ \frac{1}{gd}\ |V|V + \frac{1+C_m^*(n)\ \frac{1-n}{n}}{g}\ \frac{\partial V}{\partial t} \tag{5.13}$$

and with spheres, the constant '$2/\pi$' must be replaced by '3/4'.

By definition, the virtual mass coefficient can be separated into the Froude-Krylov coefficient and the added mass coefficient, $C_m^*=1+C_a^*$, both related to V/n as characteristic velocity.

Like with a single cylinder exposed to an ambient flow, it is expected that for a porous medium, a similar dependency of the quadratic flow resistance coefficient as well as the inertia coefficient, cf eqs (5.6) and (5.13), on Re, KC and k/d exists.

It is apparent from eqs (5.6) and (5.13) that not both C_m and C_m^* can be constant with regard to n.

The present approach is different from that of Chapter 4 only dealing with a condition for a fluid element. If in eq (4.1) the pressure term is multiplied by n_a, where n_a is the relative area of the pores in a cross-section, and all other terms are multiplied by n, and as $n_a=n$ as discussed in Section 3.2, we see that the condition equation (4.1) for a fluid element is equivalent to the force balance for the wet volume alone, ie eq (4.1) integrated over the wet volume.

Some authors, eg Wang and Gu (1988), use for the driving force

$$\frac{\partial p_o}{\partial x} dx n_a dy dz \tag{5.14}$$

where n_a is the relative area of the pores in a cross-section (as an approximation, Wang and Gu assume n_a equal to n).

This yields (still using V/n as characteristic velocity)

$$I = -\frac{\partial\left(\frac{p_o}{\rho g}\right)}{\partial x} = C_d^w(n)\,\frac{3}{4}\,\frac{1-n}{n^3}\,\frac{1}{gd}\,|V|V + \frac{1+C_m^w(n)\,\frac{1-n}{n}}{ng}\,\frac{\partial V}{\partial t} \tag{5.15}$$

However, this equation involving the area factor, $n_a=n$, should not be applied because integration of the x-axis component of the pressure forces acting on a cross-section, cutting through pores and grain contact points only, yields pdydz, where p is taken as the average pressure along the cut section, cf Fig 5.2. This reasoning has for many years been applied within highdam engineering related to calculation of cross-section stresses in concrete exposed to large pore pressures. Another way of arriving at the same conclusion is to consider the pressure drop over the sample length recorded by transducers placed just outside each end of the sample (boundary effects can be disregarded for long sample lengths), in which case it is clear that the driving force is Δpdydz, cf Fig 5.2.

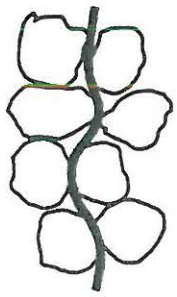

Fig 5.2 Cross-section cut through pores and grain contact points

For sake of completeness, the details of the drag term of the Morison equation applied to porous media is discussed. The derivation is applicable to both the smooth and rough turbulent cases, ie to both the Forchheimer and the fully turbulent flow regimes. The following kinematic definitions are introduced, cf Fig 5.3.

$$v^- = \frac{V}{f(n)} \tag{5.16}$$

V is the far field velocity
v^+ is the velocity at the stagnation point, $v^+=0$
v^- is the velocity at the separation point
f is a function increasing with n and dependent on Re and KC

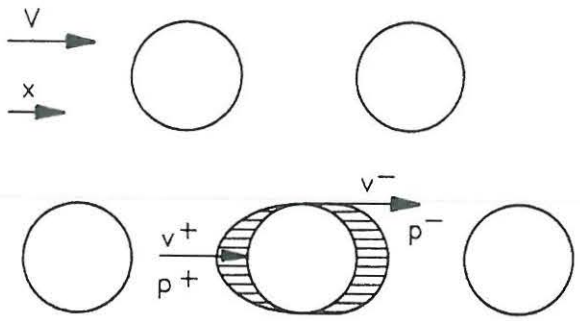

Fig 5.3 Kinematic and dynamic properties

A stepwise application of the Bernouilli equation, as usually done in the case of one obstacle, cf Section 2.4, gives

$$\frac{p^-}{\rho g} = \frac{|V|V}{2g}\left(1 - f^{-2}(n)\right) \tag{5.17}$$

and

$$\frac{p^+}{\rho g} = \frac{|V|V}{2g} \tag{5.18}$$

Within the sample, the total number of cylinders and the total projected area are found as above. Hence, the total drag force integrated over the sample can be written as, assuming the areas related to p^- and p^+ identical for simplicity

$$-\frac{\partial p_o}{\partial x}\,dxdydz \sim \frac{4}{\pi}\,\frac{1-n}{d}\,(p^+ - p^-)\,dxdydz = \frac{2}{\pi}\,\frac{1-n}{f^2(n)}\,\frac{1}{d}\,\rho\,|V|V\,dxdydz \tag{5.19}$$

and the gradient related to the drag term becomes

$$-\frac{1}{\rho g}\,\frac{\partial p_o}{\partial x} \sim \frac{2}{\pi}\,\frac{1-n}{f^2(n)}\,\frac{1}{gd}\,|V|V = C_d(n)\,\frac{2}{\pi}\,\frac{1-n}{gd}\,|V|V \tag{5.20}$$

where C_d is a drag coefficient dependent on the porosity, the Reynolds number, Re, the Keulegan-Carpenter number, KC, and the relative surface roughness, k/d.

In case of a sphere analogy, we get in the same manner

$$-\frac{1}{\rho g}\,\frac{\partial p_o}{\partial x} \sim \frac{3}{4}\,\frac{1-n}{f^2(n)}\,\frac{1}{gd}\,|V|V = C_d(n)\,\frac{3}{4}\,\frac{1-n}{gd}\,|V|V \tag{5.21}$$

Comparing to the quadratic term of the hydraulic radius theory

$$-\frac{1}{\rho g}\,\frac{\partial p_o}{\partial x} = \beta'\,\frac{1-n}{n^3}\,\frac{1}{gd}\,|V|V \tag{5.22}$$

cf Section 4.1, we obtain the same variation of the flow resistance with the porosity by setting

$$f(n) \sim n^{3/2} \tag{5.23}$$

ie there is no contradiction between the two different derivations.

In case the reference velocity is chosen as V/n, we have

$$v^- = \frac{V/n}{f^*(n)} \tag{5.24}$$

For the cylinder case, we find as above

$$-\frac{1}{\rho g}\frac{\partial p_o}{\partial x} \sim \frac{2}{\pi}\frac{1-n}{n^2 f^{*2}(n)}\frac{1}{gd}|V|V = C_d^*(n)\frac{2}{\pi}\frac{1-n}{n^2}\frac{1}{gd}|V|V \tag{5.25}$$

and similarly for the case of spheres, the constant '$2/\pi$' must be replaced by '3/4'.

If we set

$$f^*(n) \sim n^{1/2} \tag{5.26}$$

we get the same dependency on n as with the hydraulic radius theory.

Hence, it can be concluded that in principle, the quadratic flow resistance term of the Forchheimer equation can be described by the drag term, but as the detailed velocity distribution as function of the porosity is unknown, it has no practical importance. For practical purposes, the best description is obtained by the hydraulic radius theory presented in Chapters 3 and 4.

As discussed in Section 4.5, measurements indicate that for flow parallel to the length axes of the stones, the flow resistance is approximately half of the flow resistance for flow perpendicular to the stones. This conforms to eq (5.3) if for the projected area, d dy is substituted by t dy and ℓ dy respectively, where ℓ is the maximum length of the stone and t is the perpendicular minimum length of the stone, where for most rock $\ell/t \sim 2$.

5.3 Potential Model Based on Discharge Velocity

From the previous section, we have the following definition of C_m based on the discharge velocity, cf eq (5.9), ie related to cylinders in arrays with large porosity

$$c = \frac{n + (1-n)\,C_m}{g} \tag{5.27}$$

With the purpose of estimating C_m, cylinders are now added until a dense sample is reached, and a summation of the interaction forces is carried out with the discharge velocity as reference velocity, ie C_m is defined from eq (5.9)/(5.27). It is assumed that the flow locally around the single obstacles is irrotational. For high Reynolds numbers, flow separation occurs and the potential description is no longer valid. Nevertheless, this procedure is usually applied in the basic derivation of virtual mass for cylinders.

Any potential flow can be described by the complex potential field, cf Section 2.2

$$w(z) = w(x+iy) = \phi(z) + i\psi(z) \tag{5.28}$$

where

w	is the complex potential
ϕ	is the potential
ψ	is the stream function

The velocity components are found as

$$V_x = - \frac{\partial \phi}{\partial x} \tag{5.29}$$

$$V_y = - \frac{\partial \phi}{\partial y} \tag{5.30}$$

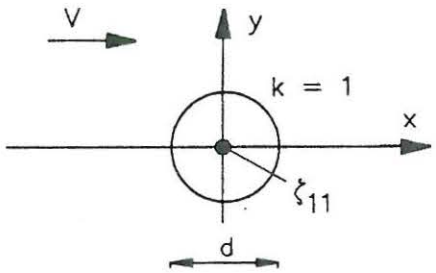

Fig 5.4 One cylinder

For the case of a single cylinder with the number, k=1, exposed to an ambient fluid moving with the velocity, V, cf Fig 5.4, the complex potential field is described by

$$w = - \overline{V} z + \frac{M_1 V}{z - \zeta_{11}} \tag{5.31}$$

where $\overline{V}$ is the complex conjugate of V. The first term arises from the uniform flow and the second term represents a doublet with strength M_1 located in the centre of the cylinder, k=1

$$M_1 = - \frac{1}{4} d^2 e_1 \tag{5.32}$$

where e_1 is defined by

$$V = |V| e_1 \tag{5.33}$$

The temporal inertia force acting on the cylinder is found from integration of the excess pressure over the surface, which is found by the Bernouilli equation, cf Chapter 2

$$p_o = \rho \frac{\partial \phi}{\partial t} \tag{5.34}$$

$$F = i\rho \oint \frac{\partial \phi}{\partial t} \, dz \tag{5.35}$$

This integration results in a force per unit length of the cylinder, F, proportional to the local acceleration, $a_x = \frac{\partial V_x}{\partial t}$

$$F = \rho(1+C_{a1})Aa_x, \quad 1+C_{a1} = C_{m1}, \quad A = \frac{\pi}{4} d^2 \tag{5.36}$$

where the first part, the Froude-Krylov force, arises from the uniform flow contribution to the potential field, and the second is caused by the doublet.

For a system of multiple cylinders, as a first approximation, neglecting the interaction between the cylinders, the complex potential can be written as

$$w = -\overline{V}z + \sum_{k=1}^{N} \frac{M_k V}{z-\zeta_{k1}} \tag{5.37}$$

where N is the number of cylinders in consideration. For a porous medium, N is large. These doublets are referred to as the first order doublets.

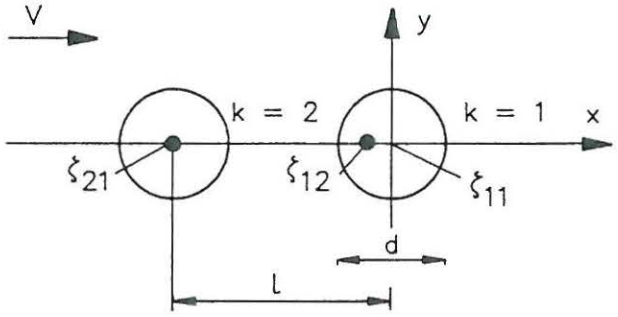

Fig 5.5 Interaction of two cylinders

According to Milne-Thomson (1968), Section 8.81, the interaction of two cylinders can be described mathematically by adding extra doublets inside each of the cylinders in order to produce streamlines at the cylinder contours, ie ψ = constant at the cylinder contours. This method, also called the method of images, is used by Yamamoto (1976) in order to calculate inertia forces on groups of cylinders. A cylinder, denoted k=2, with strength M_1 is placed near the cylinder k=1, cf Fig 5.5. The image doublet of M_1 in cylinder k=1 is denoted M_2

$$M_2 = - \overline{M_1} \frac{d^2}{4} \frac{1}{(\overline{\zeta}_{21} - \overline{\zeta}_{11})^2} \tag{5.38}$$

The centre of the image doublet is given by

$$\zeta_{12} = \zeta_{11} + \frac{d^2}{4} \frac{1}{\overline{\zeta}_{21} - \overline{\zeta}_{11}} \tag{5.39}$$

ζ_{12} is denoted the inverse point of ζ_{21} as for $\zeta_{11}=(0,0)$ we have

$$\zeta_{12} \, \overline{\zeta}_{21} = \left(\frac{d}{2}\right)^2 \tag{5.40}$$

This leads to an iterative procedure in which the complex potential can be described as

$$w = - \overline{V} z + \sum_{k=1}^{N} \sum_{j=1}^{\infty} \frac{M_{kj} V}{z - \zeta_{kj}} \tag{5.41}$$

M_{kj} is the strength of the doublets
ζ_{kj} is the location of the doublets

Eq (5.38) shows that for $\zeta_{11}=(0,0)$ and for ζ_{21} located on the x-axis, ie in the direction of the flow, M_2 becomes oppositely directed to M_1, which means that obstacles lined in the direction of flow tend to lower the added mass as compared to a single obstable. If instead ζ_{21} is located along the y-axis, ie the imaginery axis, we get from eq (5.38) that M_2 has the same direction as M_1 which means that a line of cylinders traversing the flow direction tend to increase the added mass. In general, if x_c and y_c denote the centre of an arbitrary cylinder different from $k=1$, the interaction between the cylinder and $k=1$ will imply alternating signs concerning the series of image doublets when $x_c^2 - y_c^2 > 0$. For $x_c^2 - y_c^2 < 0$, we have that all image doublets will have the same direction as the original doublets. Hence, in total, for one cylinder as well as all cylinders together, there will be a dominance of doublets with the same direction as the original doublets implying a positive force on the cylinders larger than in case of just a single cylinder.

For cylinders arranged in a quadratic pattern, the porosity, n, of the two-dimensional porous medium can be expressed by the distance between adjacent cylinders, l

$$1 - n = \frac{\pi}{4} \left(\frac{d}{l}\right)^2 \tag{5.42}$$

and hence

$$\frac{1}{4} \left(\frac{d}{l}\right)^2 = \frac{1}{\pi} (1 - n) \tag{5.43}$$

n for the two-dimensional porous medium should not be confused with n_a, which is the relative area of the pores in a cross-section of a three-dimensional medium. A simple integration over a unit volume for any three-dimensional medium yields that on average in

the direction orthogonal to the cross-section cuts, $\overline{n}_a=n$, which for the case of spheres in cubic packing yields $\overline{n}_a=n=1-\pi/6(d/l)^3$, cf eq (5.63).

The strength of the second order doublets can be written as, cf eqs (5.38) and (5.43)

$$|M_2| = |M_1|\frac{1}{\pi}(1-n) \tag{5.44}$$

where $|M|$ is the modulus of M.

Similarly, the strength of the j order doublets can be written as

$$|M_j| = |M_1|\frac{1}{\pi^{j-1}}(1-n)^{j-1} \tag{5.45}$$

For cylinders in the distance λl from the cylinder k=1, where λ is a distance factor larger than unity, the strength of the image doublets inside k=1 will vary like

- second order:

$$|M_2| = |M_1|\frac{1}{4}\left(\frac{d}{\lambda l}\right)^2 = |M_1|\frac{1}{\pi\lambda^2}(1-n) \tag{5.46}$$

- order j:

$$|M_j| = |M_1|\frac{1}{\pi^{j-1}\lambda^{2(j-1)}}(1-n)^{j-1} \tag{5.47}$$

For other cylinder arrangements than the quadratic, we have in general

$$1-n \sim \left(\frac{d}{l}\right)^2 \tag{5.48}$$

eg for rhombohedral packing, we have

$$1-n = \frac{\pi}{2\sqrt{3}}\left(\frac{d}{l}\right)^2 \tag{5.49}$$

and hence

$$\frac{1}{4}\left(\frac{d}{l}\right)^2 = \frac{\sqrt{3}}{2}\frac{1}{\pi}(1-n) \simeq 0.87\,\frac{1}{\pi}(1-n) \tag{5.50}$$

ie in eqs (5.44) to (5.47), an additional constant of 0.87 must be introduced in case of rhombohedral packing. As the cubic and rhombohedral packings represent the maximum and minimum porosities respectively for regular samples for a given value of d/l, we have that in general a coefficient ranging between 0.87 and 1 must be applied to the above equations.

Now the force on the cylinder, k=1, can be found from integration of p_o over the surface, cf eqs (5.34) to (5.36). The complex potential field is given as the sum of the potential fields

associated with the uniform flow field, the original doublets and the imaginery image doublets in all cylinders

$$w = -\overline{V}z + \sum_{k=1}^{N} \sum_{j=1}^{\infty} \frac{M_{kj} V}{z - \zeta_{kj}} \tag{5.51}$$

As the purpose of these considerations is to establish a simple model equation valid for highly irregular media, an exact integration is not carried out. All doublets inside the cylinder k=1, when integrated over the contour of k=1, contribute to the force per unit length, F, on k=1 dependent on the strength of the doublet. Hence, the extra doublets can be considered as an increase of the strength of the original doublet with strength, M_1. At the contour of cylinder k=1, the original doublets and the image doublets located inside cylinders k>1 contribute to the potential and hence also the force on k=1 in the same order of magnitude as the associated image doublets inside k=1 with respect to the dependency on n. The integration leads to

$$F = C_m \rho \frac{\pi}{4} d^2 \frac{\partial V_x}{\partial t} \tag{5.52}$$

with

$$\begin{aligned} C_m &= 1 + C_{a1} \left(1 + \frac{\sigma_1}{\pi} (1-n) + \frac{\sigma_2}{\pi^2} (1-n)^2 + ... \right) \\ &= C_{m1} + C_{a1} \left(\frac{\sigma_1}{\pi} (1-n) + \frac{\sigma_2}{\pi^2} (1-n)^2 + ... \right) \end{aligned} \tag{5.53}$$

where σ_1 and σ_2 are constants dependent on the packing of the cylinders. As the summation over k in eq (5.51) is infinite, all water expressed by the far field velocity, V, is forced through the porous matrix yielding equal flow conditions around all cylinders, ie no water escapes past the group of cylinders, as in the case of a finite number of cylinders, which obviously approaches the behaviour of one large cylinder.

If the higher order terms are neglected, eq (5.53) can also be written as

$$C_m = C_{m1} + K_{cyl} (1-n) \tag{5.54}$$

where K_{cyl} is a constant dependent on the packing of the cylinders.

For n=1, the virtual mass coefficient equals the coefficient for a single cylinder, ie $C_m = C_{m1} = 2$. In Section 5.6, K_{cyl} is calibrated against large scale physical model tests.

A physically more abstract but mathematically more clear summation can be carried out if we apply the following method, as done by Yamamoto (1976) for a group of cylinders. By means of eqs (5.28) and (5.35), the force per unit length, F, acting on one cylinder can be expressed as

$$F = i\rho \oint \frac{\partial \phi}{\partial t} dz = i\rho \oint \frac{\partial w}{\partial t} dz + \rho \oint \frac{\partial \psi}{\partial t} dz \tag{5.55}$$

As the cylinders do not move, we have that ψ = constant at the contour, where ψ relates to the total flow field, and hence the last integral vanishes.

Considering w, the uniform flow field implies

$$\oint w dz = 0 \tag{5.56}$$

as w is constant. It should be noticed that the Froude-Krylov force is still included in eq (5.55). The contributions to eq (5.55) left arise from the original doublets and the image doublets. Cauchy's formula reads, see eg Milne-Thomson (1968), Section 5.59:

M is a function of the complex variable z, and C is a closed contour

$$\oint_{(c)} \frac{M(z)}{z-\zeta} dz = 2\pi i M(\zeta) \quad \text{or} \quad 0 \tag{5.57}$$

according as ζ is inside or outside C.

Hence, only doublets located inside the cylinder in consideration contribute to the integral of $\partial w/\partial t$. The contributions are proportional to the doublet strengths irrespective of their locations. From eqs (5.51), (5.55) and (5.57), we get

$$F = i\rho \oint \frac{\partial w}{\partial t} dz = i\rho \frac{\partial V_x}{\partial t} \sum_{j=1}^{\infty} \oint \frac{M_{kj}}{z-\zeta_{kj}} dz = -2\pi\rho \frac{\partial V_x}{\partial t} \sum_{j=1}^{\infty} M_{kj} \tag{5.58}$$

The original doublet inside the cylinder has a strength given by eq (5.32). As previously the second and j order image doublets inside the cylinder can be expressed by eqs (5.44) to (5.47). Hence, we have

$$\begin{aligned} F &= -2\pi\rho \left(-\frac{1}{4}d^2\right)\left(1 + \frac{\sigma_1'}{\pi}(1-n) + \frac{\sigma_2'}{\pi^2}(1-n)^2 + \ldots.\right)\frac{\partial V_x}{\partial t} \\ &= \left(2 + 2\frac{\sigma_1'}{\pi}(1-n) + 2\frac{\sigma_2'}{\pi^2}(1-n)^2 + \ldots.\right)\rho\frac{\pi}{4}d^2\frac{\partial V_x}{\partial t} \end{aligned} \tag{5.59}$$

By neglecting the higher order terms in (1-n), we get

$$F = C_m \rho \frac{\pi}{4} d^2 \frac{\partial V_x}{\partial t} \tag{5.60}$$

with

$$C_m = 2 + K_{cyl}(1-n) \tag{5.61}$$

cf eq (5.54).

Also in case of spheres, the image method can be applied. Considering the axisymmetrical flow around a single sphere, we have a Froude-Krylov force and an added mass force as described in Section 2.4. In Milne-Thomson (1968), Section 16.41 is given an example of such an application. If a sphere of equal size is placed in a distance, *l*, from the first sphere

in the direction of the flow, an image doublet appears inside sphere number one at the inverse point with a strength equal to

$$|M_2| = |M_1| \frac{1}{8} \left(\frac{d}{l}\right)^3 \tag{5.62}$$

if we require ψ = constant at the surface of sphere number one, ie the streamlines follow the surface of the sphere. In the present example, limited to the case of a second sphere placed in the direction of the flow, the image doublet becomes oppositely directed like in the two-dimensional case of interaction between two cylinders placed along the flow direction.

Assuming the same dimensional relation for the ratio between $|M_2|$ and $|M_1|$ to be valid for the ratio between all other second order image doublets and $|M_1|$ and similarly for the j order doublets, the porosity can be introduced in the same manner as in the two-dimensional case. For spheres in cubic packing yielding maximum porosity for a given value of d/l, we have for the porosity, n, of the three-dimensional porous medium

$$1-n = \frac{\pi}{6} \left(\frac{d}{l}\right)^3 \tag{5.63}$$

leading to

$$\frac{1}{8} \left(\frac{d}{l}\right)^3 = \frac{3}{4\pi} (1-n) \tag{5.64}$$

and for rhombohedral packing yielding minimum porosity

$$1-n = \sqrt{2}\, \frac{\pi}{6} \left(\frac{d}{l}\right)^3 \tag{5.65}$$

yielding

$$\frac{1}{8} \left(\frac{d}{l}\right)^3 = \frac{1}{\sqrt{2}}\, \frac{3}{4\pi} (1-n) \approx 0.71\, \frac{3}{4\pi} (1-n) \tag{5.66}$$

Thus, the relation between the strenth of the doublet sphere number one and the additional doublets can be expressed as in eqs (5.44) to (5.47) with the constant '$1/\pi$' substituted by '$3/(4\pi)$'. The variation with the packing is obtained by applying a factor ranging between 0.71 and 1.

As mentioned previously, n for the three-dimensional medium equals $\overline{n}_a$, where n_a is the relative area of the pores in a cross-section, and $\overline{n}_a$ denotes the average in the direction orthogonal to the cross-section cuts, eg $\overline{n}_a = n = 1-\pi/6(d/l)^3$, for the case of cubic packing of spheres.

The integration of the force on one sphere yields

$$F = C_m \rho \frac{\pi}{6} d^3 \frac{\partial V_x}{\partial t} \tag{5.67}$$

with

$$C_m = 1 + C_{a1}\left(1 + \sigma_3 \frac{3}{4\pi}(1-n) + \sigma_4\left(\frac{3}{4\pi}\right)^2 (1-n)^2 + \ldots.\right)$$
$$= C_{m1} + C_{a1}\left(\sigma_3 \frac{3}{4\pi}(1-n) + \sigma_4\left(\frac{3}{4\pi}\right)^2 (1-n)^2 + \ldots.\right) \quad (5.68)$$

where σ_3 and σ_4 are coefficients dependent on the packing of the spheres. Like with the cylinders, the higher order terms are neglected and we have

$$C_m = C_{m1} + K_{sph}(1-n) \quad (5.69)$$

where K_{sph} is a constant dependent on the packing of the spheres. In this case, $n=1$ yields $C_m=C_{m1}=1.5$, which is the virtual mass coefficient for a single sphere. In Section 5.6, K_{sph} is calibrated against large scale physical model tests.

Hence, the virtual mass coefficient for a porus medium is deduced from a summation in force. The detailed velocity distribution for the porous matrix arises from the uniform velocity field and the velocity fields associated with the single doublets included in the force summation. Hence, no further assumptions concerning the detailed velocity distribution are made.

5.4 Existing Data on Virtual Mass

Hannoura and McCorquodale (1978) carried out experiments with non-stationary flow through coarse granular media, applying a free fall U-tube technique. Large accelerations only appeared in time intervals of 0.15 to 0.25 s. Four types of material were tested. Only one of the test series showed some consistency, resulting in an average value of C_m^* equal to 2.41 and with a standard deviation of 2.48, cf Table 5.1. Values of $C_m^*<1$ were found in a number of tests. This, however, implies negative added mass coefficients which from a physical point of view makes no sense. The occurrence of the negative C_a^* values is most likely due to either experimental uncertainties and/or the averaging method related to the determination of the per definition time invariant coefficients C_d^* (or a' and b') and C_m^*. The latter probem is well-known from fitting of the Morison equation with time invariant coefficients to flow forces in oscillatory flow. The values of c and C_m in Table 5.1 have been calculated for the present purpose. C_m is based on the discharge velocity, cf eq (5.9).

Table 5.1 Experiments of Hannoura and McCorquodale. Average values.

Material	d (m)	n	c (s^2/m)	C_m	C_m^*
Crushed rock	0.044	0.441	0.413	6.47	2.41

Burcharth and Christensen (1991) also applied a free fall u-tube technique. Eight rock samples with different grading and shape class were tested. Like with the tests of Hannoura and McCorquodale, large accelerations only appeared in short-time intervals, typically in the order of 0.3 s. From the proceeding deceleration phase, values of C_m^* between 12 and 35 were found. However, the authors do not regard these results as reliable due to the limitations of the experimental method.

Smith (1991) carried out experiments in oscillatory flow, but with relatively small accelerations. The results are shown in Table 5.2. The values of c are average values based on eight tests. The porosities are the values given by Smith.

Table 5.2 Experiments of Smith. Average values.

Matr. No	n	c (s^2/m)	C_m	C_m^*
R75	0.26	0.37	4.55	0.92
C75	0.51	0.23	3.56	1.31
R42	0.33	0.65	9.02	2.65
C42	0.52	0.24	3.82	1.47
S	0.47	0.32	5.04	1.90

Legend: C: spheres, cubic packing, R: spheres, rhombohedral packing
S: tabular rock

5.5 Oscillatory Water Tunnel Tests

With the aim of providing experimental justification of the above non-stationary porous flow model, a series of physical large scale model tests with cylinders, spheres and rock were planned and carried out for high Reynolds numbers. At the same time, it was attempted to examine the possible dependency of the flow resistance coefficients on the Keulegan-Carpenter number. The purpose of the cylinder samples was to establish a large variation in the porosity in order to examine the potential phenomenon of virtual mass. The sphere and rock samples aimed at providing data for a parametric study of the variation of all flow resistance coefficients with Re and KC. The tests were carried out at Delft Hydraulics, The Netherlands, in their large oscillating water tunnel as a part of the MAST programme, cf Andersen et al (1993). In subsections 5.5.1 to 5.5.3, a description of the model set-up and the basic data analysis is given to a large extent taken from the above reference. In subsection 5.5.4, the dependency of β' on KC is discussed. An alternative analysis by Van Gent (1993) is presented in subsection 5.5.5. The experiments and analyses are validated in subsection 5.5.6.

5.5.1 Experimental set-up and procedure

The oscillating water tunnel at Delft Hydraulics was used for the tests. The length of the bottom section equals 15 m. A hydraulic system was applied to force the water through the stone samples at various amplitudes and periods.

A reduced cross-section of the flume equal to approximately 0.3x0.5 m^2 was used. This was obtained by inserting an additional bottom in the flume. The stone samples were mounted in the middle of the flume. All sample lengths equalled approximately 0.8 m. The flow was parallel to the underlayer during construction of the sample.

During the stationary tests, the water velocity outside the sample was recorded by a flowmeter and checked with laser doppler anemometer measurements. Under oscillatory flow, the water velocity was recorded by recording of the piston movement and checked by laser doppler.

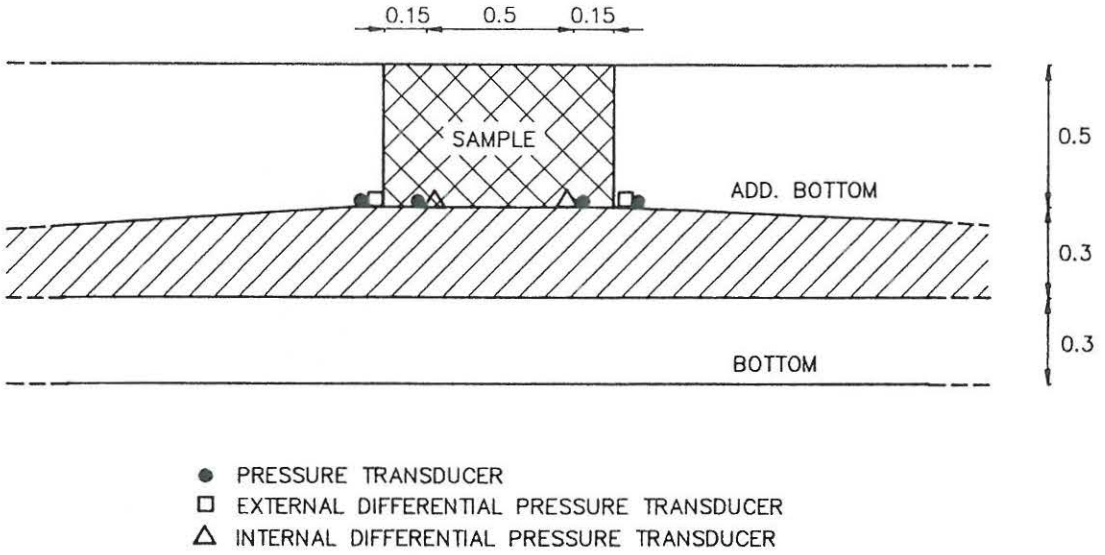

Fig 5.6 Test section with instrumentation.

Inside the sample 0.15 m from each end, a pressure transducer and a pressure difference transducer were mounted. Just outside the sample, a pressure transducer and a pressure difference transducer were mounted.

The continuous transducer signals were recorded with a sampling frequency of 100 Hz and stored.

5.5.2 Test materials

Below is given a summary of the materials tested in the new oscillating water tunnel.

Table 5.3 Test materials. d is the diameter.
For the rock material, d is the equivalent spherical diameter.
ℓ/t is the aspect ratio and n is the porosity.

Matr. No	Matr. Desc.	d	d85/d15	ℓ/t	n
C1	Cyl. in quadratic packing	0.0515	1.00	1.0	0.792
C2	Cyl. in quadratic packing	0.0515	1.00	1.0	0.587
C3	Cyl. in quadratic packing	0.0515	1.00	1.0	0.324
S1	Spheres in cubic packing	0.046	1.00	1.0	0.476
R1	Irregular rock	0.076	1.27	1.9	0.442
R3	Semi round rock	0.0607	1.27	2.0	0.454
R4	Round rock	0.0606	1.26	2.2	0.393
R5	Irregular rock	0.0251	1.30	2.3	0.449
R8	Irregular rock	0.0385	1.74	2.0	0.388

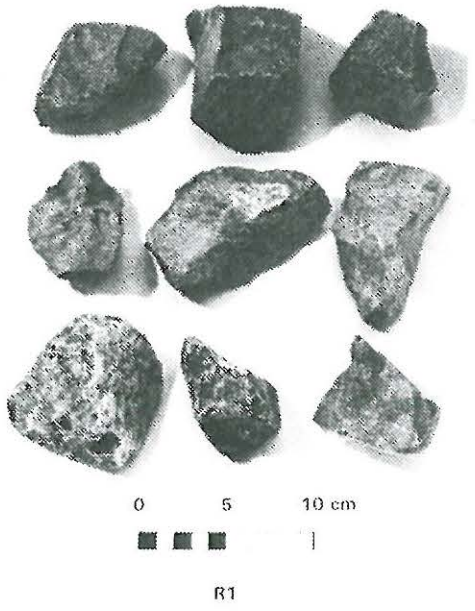

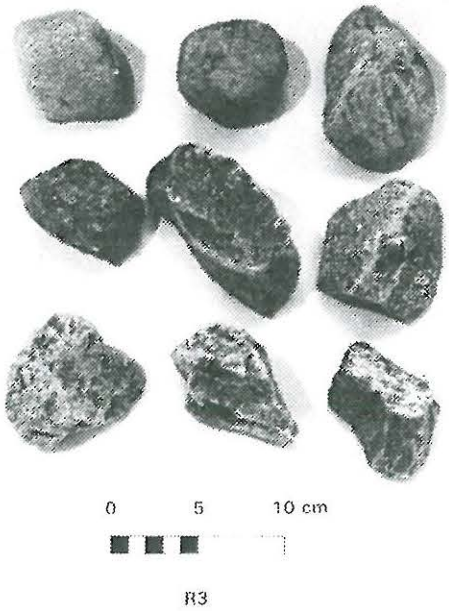

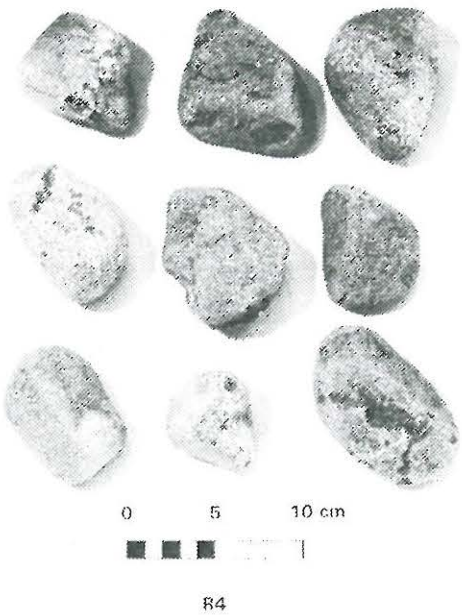

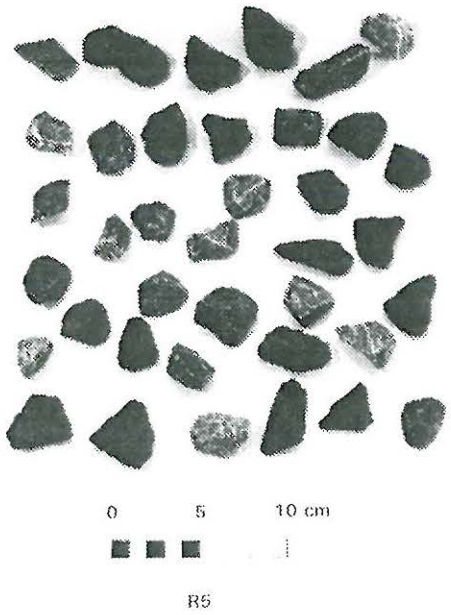

Fig 5.7a Rock R1 to R5

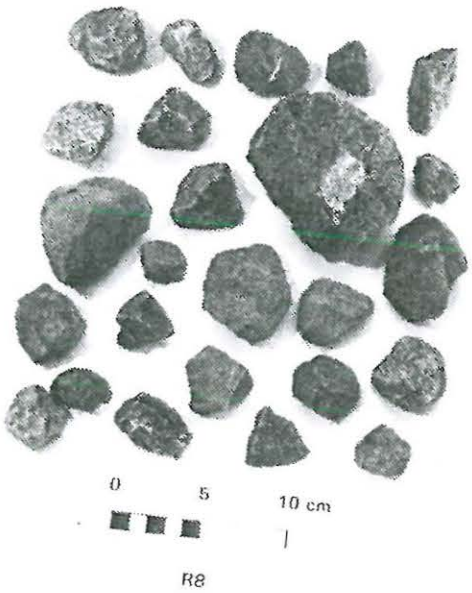

Fig 5.7b Rock R8

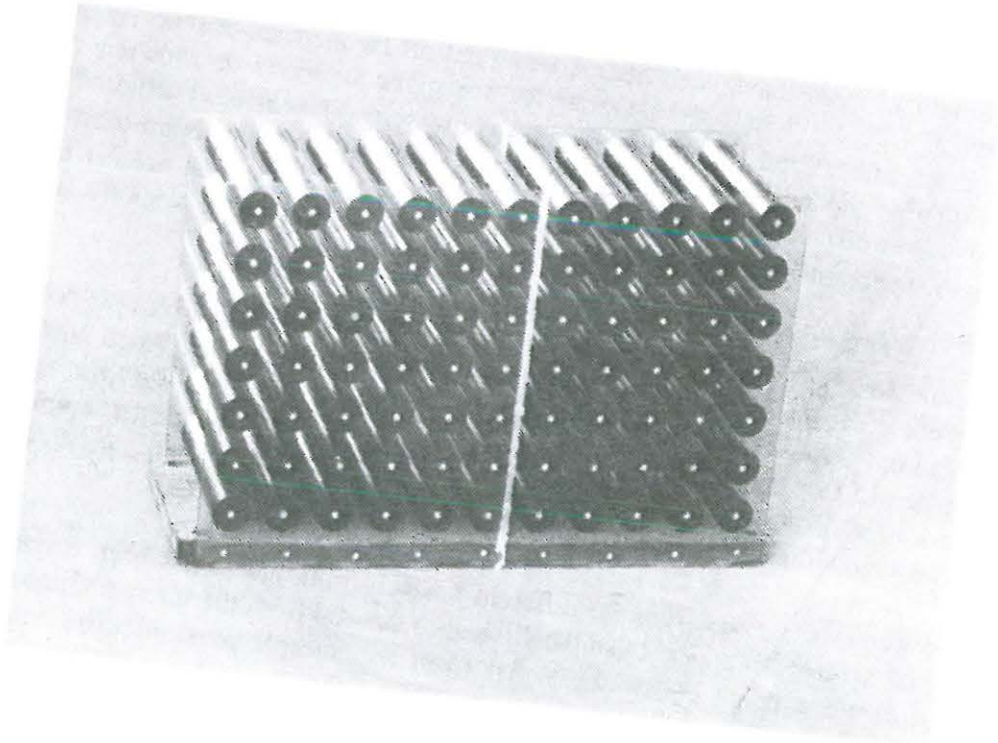

Fig 5.8 Cylinder sample, n=0.587

For the rock material, d is the equivalent spherical diameter defined as:

$$d = \left(\frac{6}{\pi} \frac{M_{50}}{\rho_a} \right)^{1/3} \tag{5.70}$$

where M_{50} is the mass exceeded by 50% of the stones and ρ_a is the density of the stones. The aspect ratio was assessed by measuring the maximum and perpendicular minimum lengths, ℓ and t of a sample of ten stones. The porosity, n, was estimated by weighing the stone sample contained in a box with a volume equal to the volume of the stone sample in the oscillatory water tunnel. The stone volume was found by division by the stone density.

Rock samples R1, R3 and R4 are identical to those applied in the stationary permeameter tests at Hydraulics Research, cf Williams (1992). Rock sample R8 is identical to the core material used in the breakwater tests at Franzius Institute, cf Oumeraci (1991).

For the cylinder samples, no wall effects were present as the gap between the uppermost cylinders and the top of the box equalled half the gap between adjacent cylinders and likewise at the bottom of the box. For the sphere and rock samples, half spheres were glued to the two vertical sides of the box containing the sample in order to reduce wall effects. The top and bottom of the box were smooth.

5.5.3 Basic analysis of results

During testing, it appeared that the piston displacement signals were not sinusoidal as intended causing some problems in the proceeding data analysis. This is probably due to the construction of the oscillating water tunnel originally aiming at much larger amplitudes of motion than used during these tests.

All measured oscillatory signals have been filtered using cut-off frequencies of 0.05 Hz and 4 Hz. Examples of filtered signals for material R1 are given in Fig 5.9, showing the measured piston displacement and the measured internal pressure difference. Further, Fig 5.9 shows the discharge velocity and the discharge acceleration in the test section derived from the filtered piston displacement signal. The difference in cross-sectional area at the piston and in the test section has been accounted for in the calculation of the velocity and acceleration.

For the spheres and for the rock samples, a certain flow of water under the sample took place. The magnitude of this underflow was measured with the laser doppler anemometer for a single rock sample, R1. The underflow velocity is about 10% of the velocity through the sample resulting in a flux beneath the sample of about 6% of the flux through the sample. By assuming the square of the underflow velocity to vary proportionally with the gradient, all velocities and accelerations are corrected for the underflow.

A comparison between the signals from the different pressure transducers has been carried out for a single rock sample. It appears that the difference derived from the internal absolute pressure transducers on average equals the signal from the internal pressure differential transducer and similarly for the external transducers. Comparing the internal and external pressure differential transducers it appears that the external signal is slightly higher than the internal signal, which is probably due to hydraulic losses at the boundaries of the sample. In the following, all analyses are based on the internal differential pressure transducer.

It was attempted to carry out a least-squares-fit in time-domain. However, this method failed due to the fluctuating character of the signals. Instead the following procedure for the analyses has been established:

- the stationary a' and b' coefficients are found
- the oscillatory b' coefficients are found at the points of time with maximum velocity and applying the stationary a' coefficients
- the inertia coefficients, c, are found at the points of time where the velocity is almost zero and applying the stationary a' coefficients

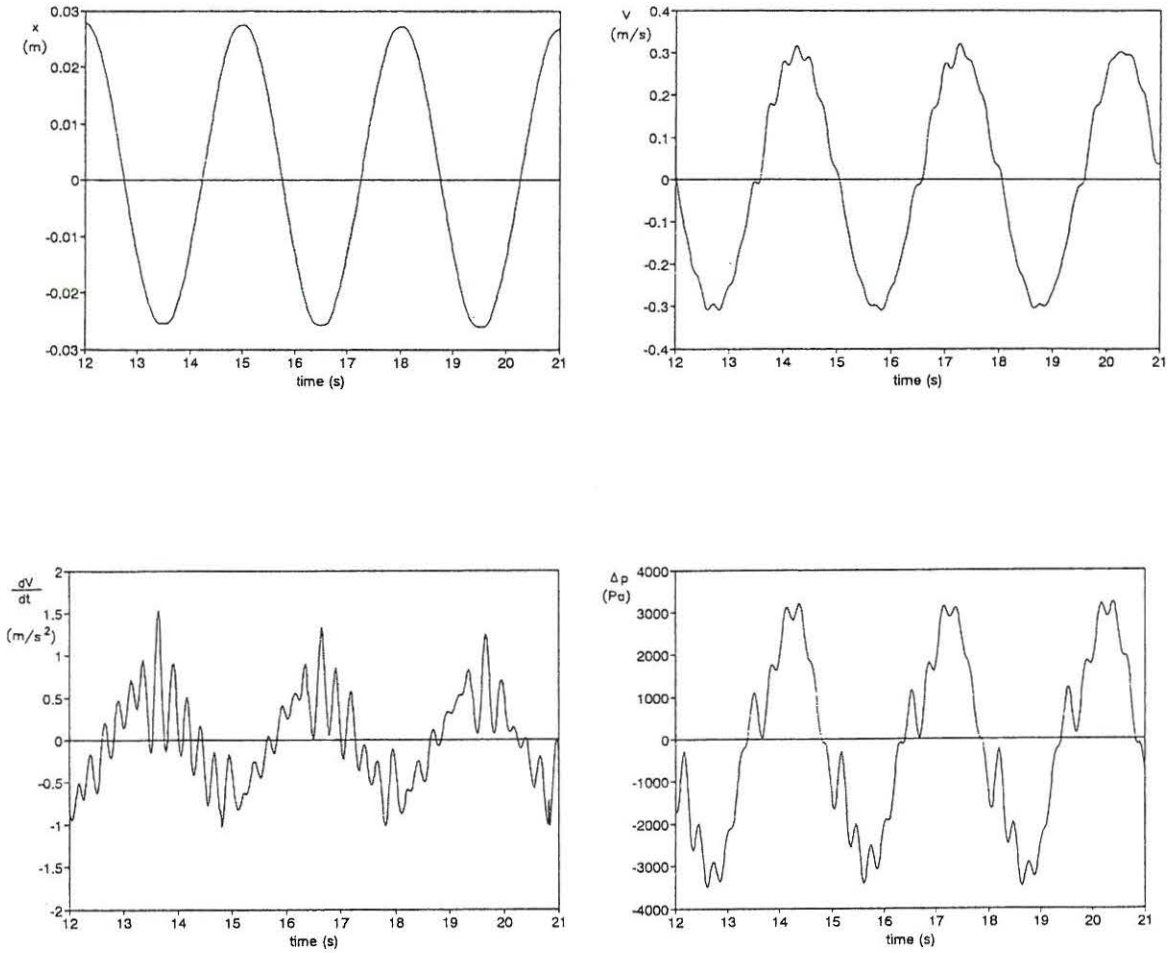

Fig 5.9 Filtered signals for material R1. Piston displacement, discharge velocity, discharge acceleration and internal pressure difference.

Results from constant flow tests in U-tube

Fig 5.10 shows an example of the estimation of a' and b' from the stationary flow tests. The α' and β' values are calculated according to eq (4.20) with α and β substituted by α' and β' respectively. For the rock samples, the α' and β' values are corrected for wall effects according to Burcharth et al (1991). As the vertical sides were covered with half spheres, the wall effects are associated with the smooth top and bottom of the box, and hence the internal height of the box has been used together with the stone diameters in order to find the correction coefficients. For all materials, the α' values must be regarded as uncertain, as the linear flow resistance term is insignificant as compared to the quadratic flow resistance term.

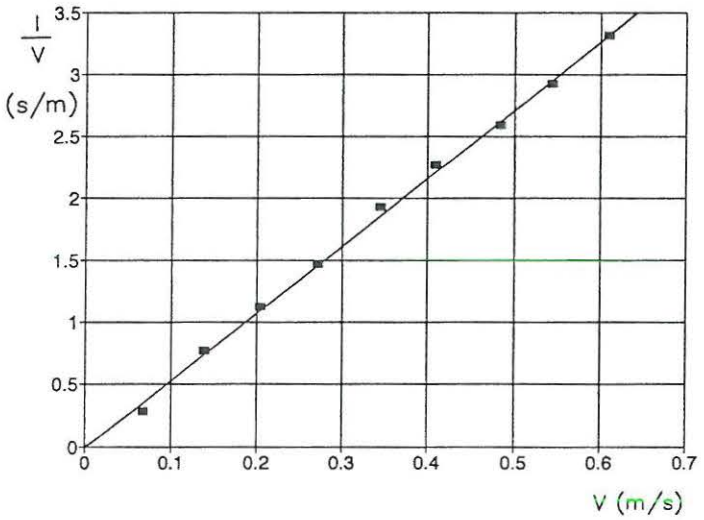

Fig 5.10 I/V vs V for material R1 for all stationary tests

Table 5.4 Results from constant flow tests

Matr. No	a' (s/m)	α' without correction	b' (s^2/m^2)	β' without correction	V_m(m/s)	Re
C1	0.0680	17800	0.277	0.334	0.070-0.49	3200-22000
C2	0.0833	2250	2.52	0.624	0.069-0.49	3100-22000
C3	1.74	2960	26.7	0.679	0.068-0.48	3100-22000
S1	0.259	1850	6.83	0.634	0.067-0.64	2700-26000
R1	0	0	5.46	0.630	0.067-0.61	4500-41000
R3	0	0	8.87	0.905	0.067-0.61	3600-32000
R4	0	0	5.71	0.340	0.065-0.62	3500-33000
R5	1.31	2120	26.03	1.05	0.060-0.44	1300-9700
R8	0.933	1860	17.0	0.613	0.059-0.45	2000-15000

As mentioned previously, the purpose of the cylinder tests is to provide a large variation in the porosity in order to examine the potential phenomenon of virtual mass. It is likely that the separated flow pattern in the regular, and in two cases highly porous, cylinder samples differs from that of porous flow in real stone samples, and hence the α' and β' coefficients for the cylinders may not be representative for porous flow.

Table 5.5 α' and β' from constant flow tests. Rock samples are corrected for wall effects

Matr. No	α'	β'	Correction factor
C1	17800	0.334	1
C2	2250	0.624	1
C3	2960	0.679	1
S1	1850	0.634	1
R1	0	0.875	1/0.72
R3	0	1.16	1/0.78
R4	0	0.435	1/0.78
R5	2440	1.21	1/0.87
R8	2210	0.729	1/0.84

Results from oscillatory flow tests in U-tube

Fig 5.11 shows the β' coefficients as found from the oscillatory tests plotted vs the Keulegan-Carpenter number, KC. As reference also the stationary values of β' are shown as horizontal lines. For high values of KC, the oscillatory β' values must approach the stationary β' values. The variation of β' with KC for the sphere and rock samples is further discussed in Subsection 5.5.4. As with the constant flow tests, the α' and β' values associated with the cylinder samples may not be representative for porous flow.

The c coefficients have been found from a single re-arrangement of the extended Forchheimer eq (5.1) where $\partial V/\partial t$ is substituted by dV/dt as the flow is uniform

$$\frac{I - a'V}{|V|V} = b' + c\,\frac{\frac{dV}{dt}}{|V|V} \tag{5.71}$$

By plotting I-a'V/|V|V vs dV/dt/|V|V, the coefficient c can be found as the slope, independent of b', cf Fig 5.12. The stationary value of a' is applied. This kind of plot emphazises the points of time where the velocity is almost zero. The plot covers a time series of duration 41 s, ie 4100 points, most of them located close to the origin on this type of plot. Finally, the c coefficients for all oscillatory tests have been plotted against KC, cf Fig 5.13. It is seen that there is no relation between KC and the derived values.

Table 5.6 shows ranges of c values as well as characteristic values as obtained from the graphs of c vs KC, with the purpose of comparing the different ways of decomposing the c term. It should be noticed that the values from material R5 are very uncertain. From Table 5.7, it appears that C_m^* can be regarded as a constant for varying porosity. For cylinders the average value of C_m^* equals 3.9, and for spheres and rock C_m^* equals 3.1 on average. It can be argued that for the rock samples, other parameters than the porosity, ie diameter, gradation and stone shape, have been varied, and hence there may be an influence from these parameters on the virtual mass coefficients. The maximum acceleration is given as:

$$a_{max} = \frac{2\pi V_{max}}{T} \tag{5.72}$$

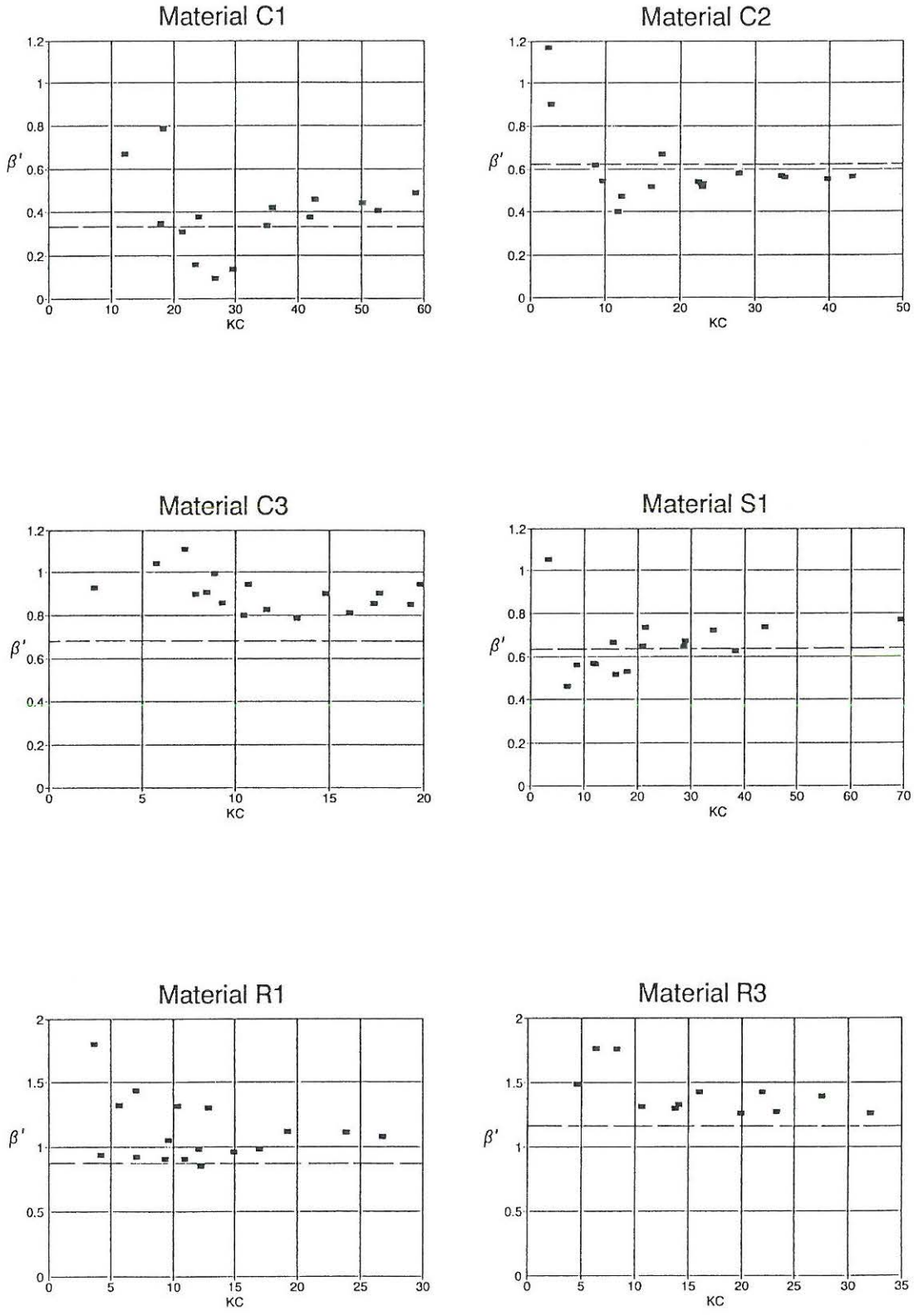

Fig 5.11a β' (with wall effect correction) vs KC from oscillatory tests. Horizontal lines indicate stationary values.

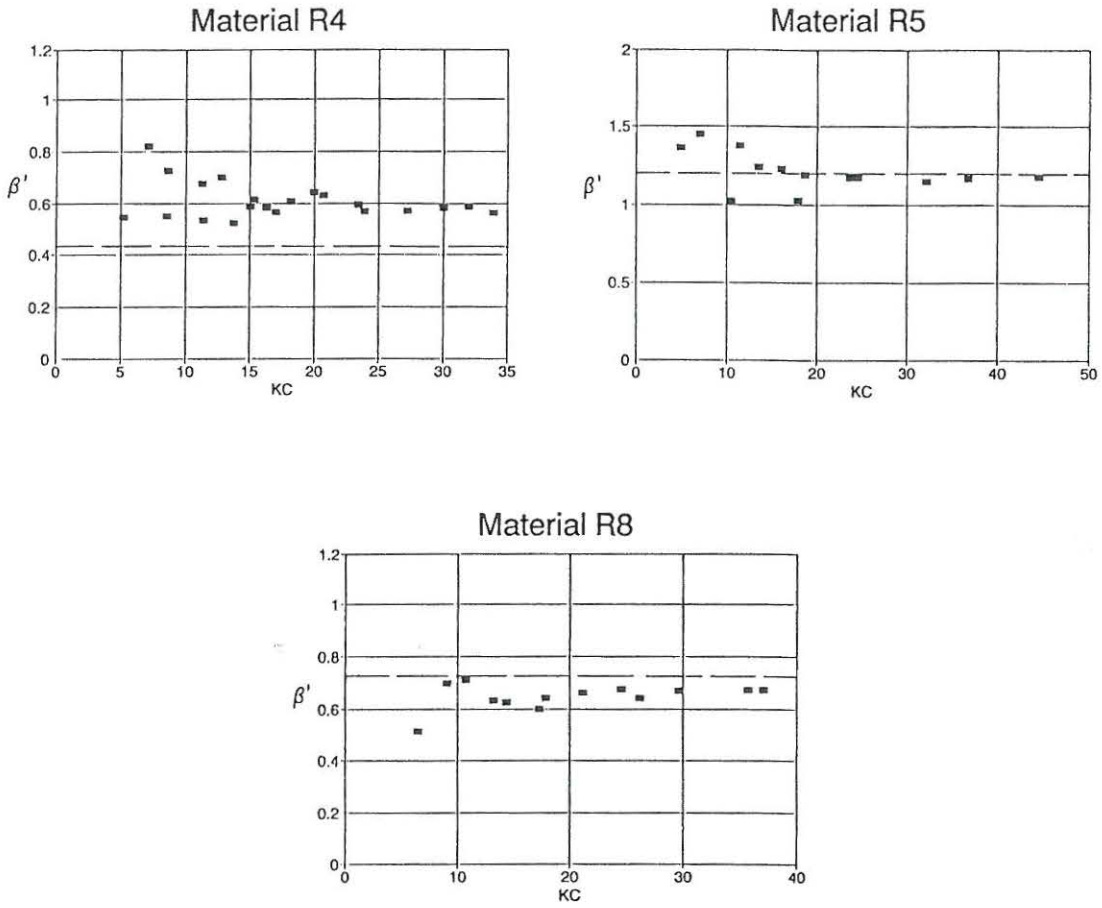

Fig 5.11b β' (with wall effect correction) vs KC from oscillatory tests. Horizontal lines indicate stationary values.

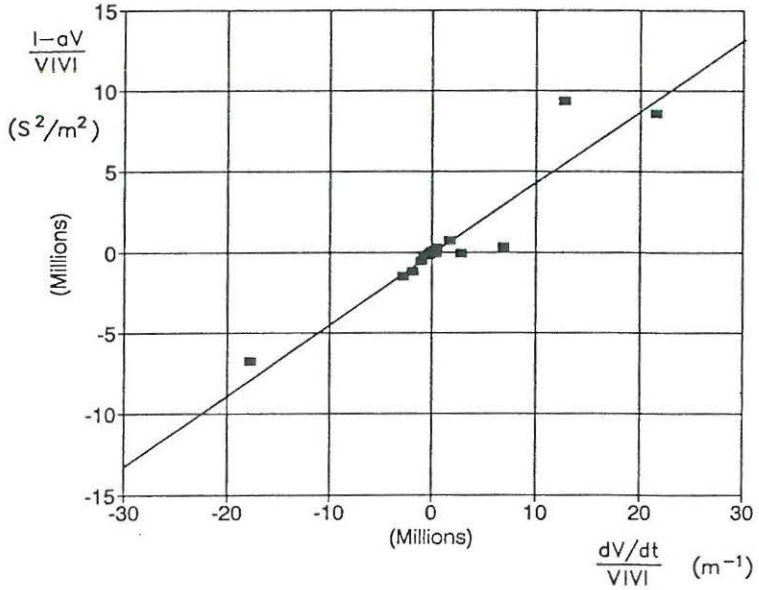

Fig 5.12 I-a'V/|V|V vs dV/dt/|V|V for material R1 for a single oscillatory test

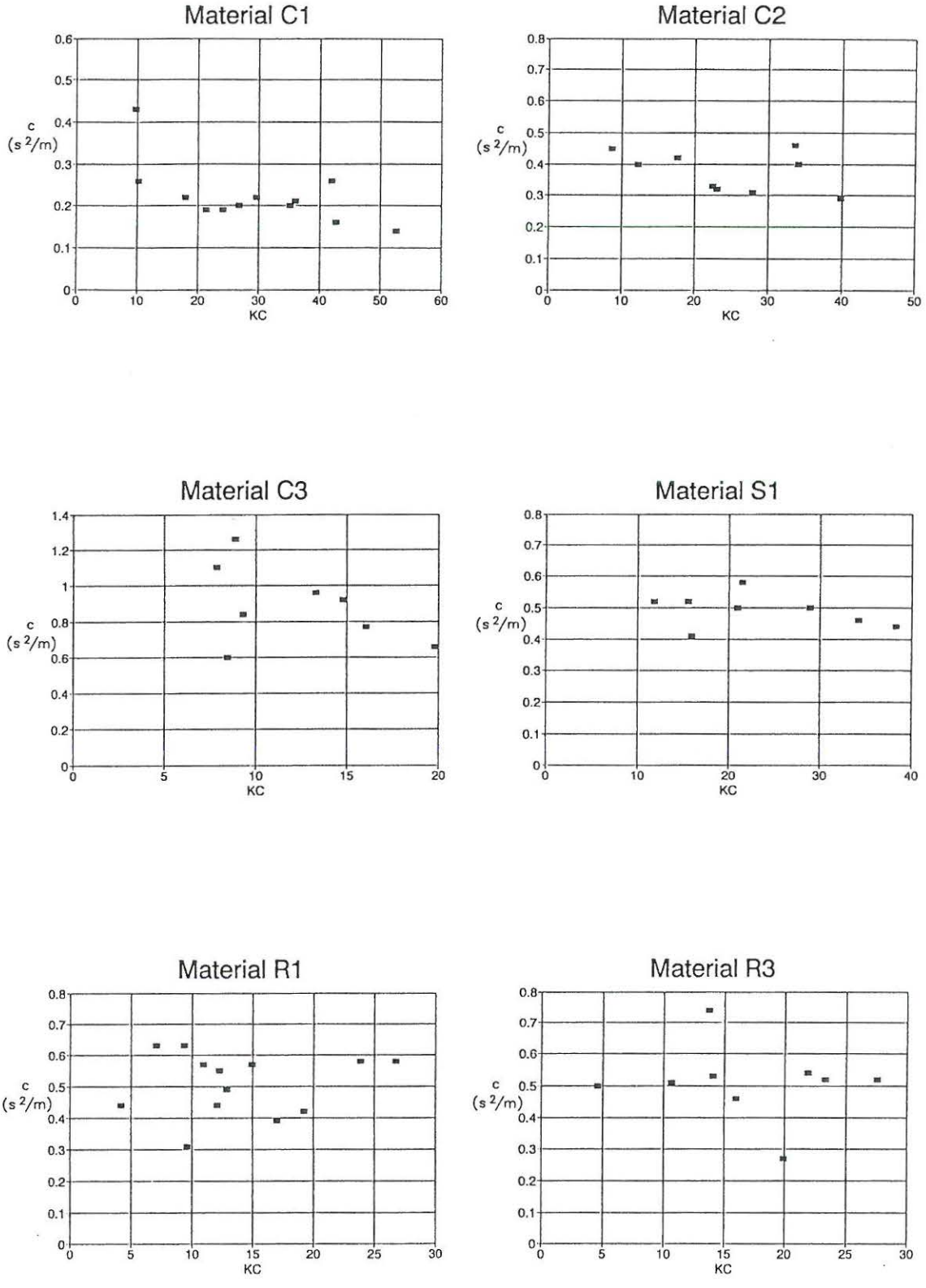

Fig 5.13a c vs KC from oscillatory tests

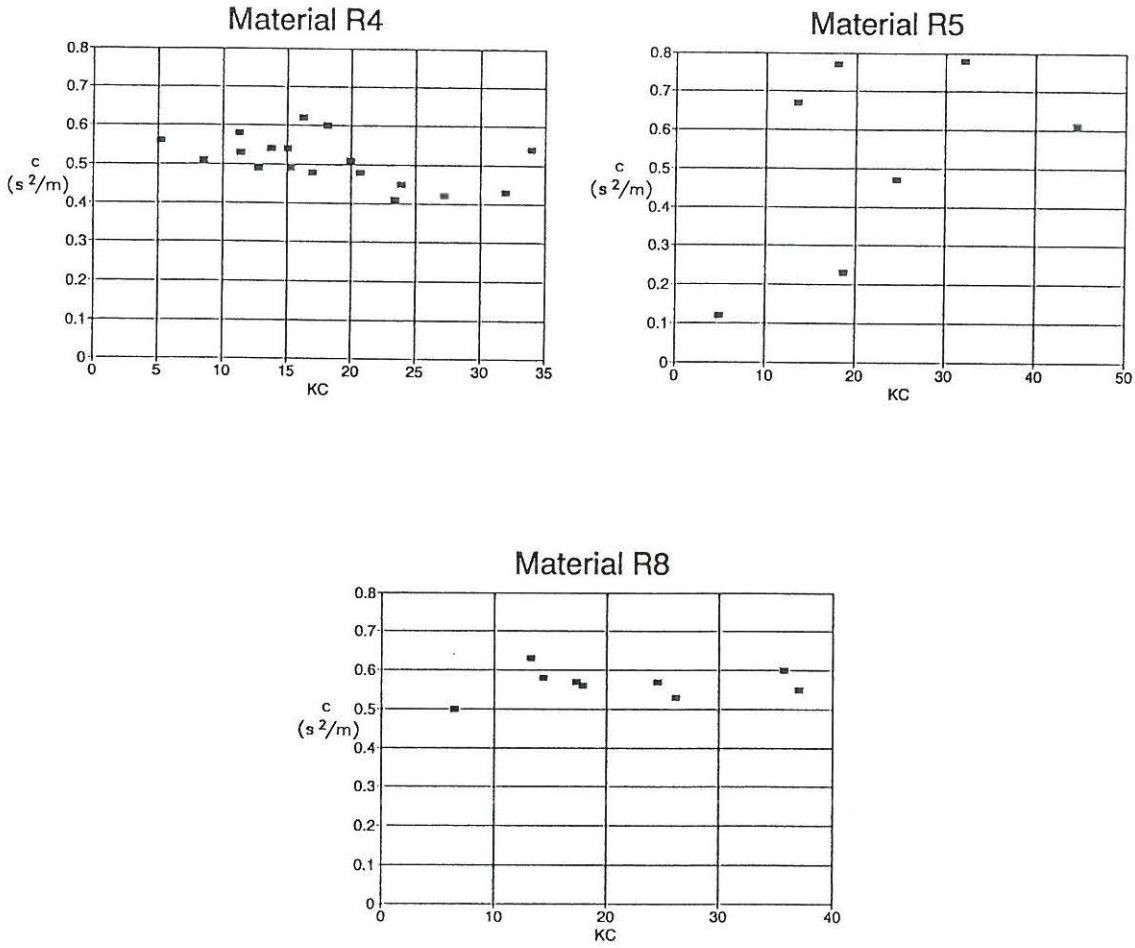

Fig 5.13b c vs KC from oscillatory tests

Table 5.6 Results from oscillatory tests

Matr. No	c (s^2/m) (range)	c (s^2/m) (char.)	V_m (m/s)	Re	T (s)	KC	a_m (m/s^2)
C1	0.14-0.26	0.2	0.17-0.73	7700-33000	2-4	10-53	0.35-1.9
C2	0.29-0.46	0.4	0.22-0.68	9900-31000	2-4	8.7-40	0.36-1.9
C3	0.60-1.26	0.9	0.15-0.28	6800-13000	2-4	7.9-20	0.32-0.75
S1	0.41-0.58	0.5	0.24-0.52	9700-21000	2-4	12-38	0.51-1.6
R1	0.31-0.63	0.5	0.16-0.51	11000-34000	2-4	4.2-27	0.39-1.5
R3	0.27-0.74	0.5	0.14-0.47	7500-25000	2-4	4.6-28	0.38-1.3
R4	0.41-0.62	0.5	0.16-0.51	8500-27000	2-4	5.2-34	0.30-1.5
R5	0.23-0.78	0.5	0.062-0.28	1400-6100	2-4	4.9-45	0.20-0.71
R8	0.50-0.63	0.55	0.13-0.36	4400-12000	2-4	6.5-37	0.39-1.0

Table 5.7 Virtual mass coefficients

Matr. No	C_m (range)	C_m (char.)	C_m^* (range)	C_m^* (char.)
C1	2.8-8.5	5.6	1.4-5.9	3.7
C2	5.5-9.5	8.1	2.6-5.0	4.2
C3	8.2-17.8	12.6	2.3-5.4	3.8
S1	6.8-10.0	8.5	2.7-4.3	3.5
R1	4.7-10.3	8.0	1.6-4.1	3.1
R3	4.0-12.5	8.2	1.4-5.2	3.2
R4	6.0-9.4	7.4	2.0-3.3	2.5
R5	3.3-13.1	8.1	1.0-5.4	3.2
R8	7.4-9.5	8.2	2.5-3.3	2.8

In order to examine whether the extended Forchheimer expression applies to the entire time series, the measured internal pressure difference signal, for a single test case for material R1, is compared to a signal generated from the velocity time series together with the estimated coefficients, cf Fig 5.14. On the upper plot only the a' and b' coefficients have been included in the generated time series, ie $a'=0$, as found from the stationary tests and $b'=6.13$ valid for this specific oscillatory test. It is seen that the generated time signal appears to be too smooth as compared to the measurements. On the lower plot, the generated time series has been extended to include the inertia term with $c=0.44$, which applies to this specific test. The two curves on the lower plot do not fit exactly, possibly partly caused by small phase differences between the instruments. Considering the lower part of the curve, ie with negative gradients, the generated time signal better resembles the character of the measured signal when the inertia term is included. For the upper part of the curve, it may seem as if the c value is too large. This tendency has been experienced from a few other control plots, and hence the method described previously may perhaps over-estimate the c values.

Concerning the coefficients, it appears that the β' coefficients are too low as compared to previous experiments, cf Tables 4.5 and 5.5. This discrepancy may possibly be caused by the difference in stone orientation, in most previous tests the flow was perpendicular to the direction of the underlayer during construction, whereas in the present tests, it was parallel to the underlayer. If it is assumed that a randomly placed stone will have its length axis parallel to the underlayer due to gravity, as shown in Section 4.5, this phenomenon may be responsible for a factor in the order of two between the stationary flow resistance coefficients for the two directions, ie $\beta'_{parr} \simeq \beta'_{perp}/2$, which explains some of the difference between the measurements. The inertia coefficients are higher than the coefficients found by Hannoura and McCorquodale (1978), and Smith (1991), cf Tables 5.1, 5.2 and 5.7.

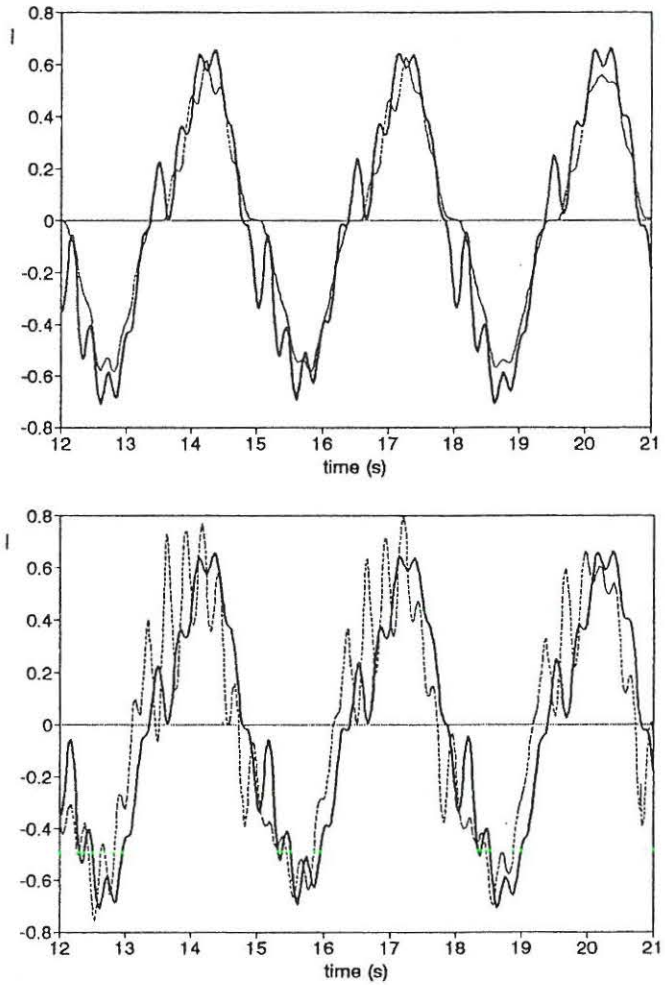

Fig 5.14 Comparison of Measured Signal and Generated Signal for Material R1
Legend: ——: measured gradient; - - - -: generated gradient
Upper plot: generated gradient without inertia term
Lower plot: generated gradient with inertia term

5.5.4 Dependency of β' on the Keulegan-Carpenter number

As discussed in Section 5.2, for practical purposes, the quadratic term of the Forchheimer equation is best described by the hydraulic radius theory, cf Chapters 3 and 4. In order to derive the proper ratio between the convective and local accelerations for the present purpose, now only a fluid element is considered in concordance with the derivations in Chapter 4.

$$\frac{\text{conv. acc. forces}}{\text{local acc. forces}} = \frac{U\,\dfrac{\partial U}{\partial x}}{\dfrac{\partial U}{\partial t}} \sim \frac{UT}{D}\,\frac{1}{2\pi} \tag{5.73}$$

where U and D are a characteristic velocity and length respectively and T is the period of the forced motion. With U=V/n and D=R as in Chapter 4, we get

$$\frac{\text{conv. acc. forces}}{\text{local acc. forces}} \sim \frac{1-n}{n^2}\,\frac{VT}{d}\,\frac{1}{2\pi} = \frac{1-n}{n^2}\,\frac{KC}{2\pi} \qquad (5.74)$$

cf eq (5.8).

Alternatively, the above ratio can be interpreted as the ratio between the period, T, of the forced motion and a characteristic period, T', of the porous flow

$$\frac{T}{T'} = \frac{UT}{D} \qquad (5.75)$$

With U=V/n and D=R like before, we find

$$\frac{T}{T'} \sim \frac{1-n}{n^2}\,\frac{VT}{d} = \frac{1-n}{n^2}\,KC \qquad (5.76)$$

ie as in eq (5.74) apart from the factor of 2π. For convenience, β'/β'_{stat} is plotted against KC, cf Fig 5.15, showing the values for spheres and rock. There appears to be an increase in β' for low values of KC. Some of the variations relative to β'_{stat}, however, may be caused by the experimental procedure.

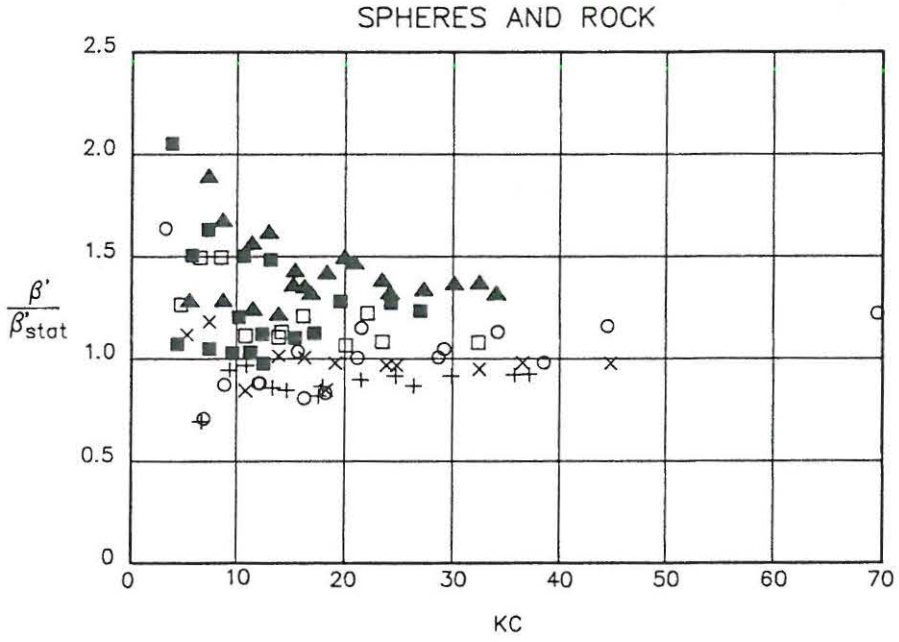

Fig 5.15 β'/β'_{stat} vs KC
Legend: 0: Spheres, ■: R1, □: R3, ▲: R4, x: R5, +: R8

5.5.5 Alternative analysis for the sphere and rock samples

An alternative analysis by Van Gent (1993) was presented shortly after the submission of the paper by Andersen et al (1993). The sphere and rock samples were considered. The filtered signals were applied, adjusted for underflow which appeared during testing with these samples. A slighty higher coefficient for underflow correction than previously was applied. For the rock samples, wall effects were taken into account by a correction factor of 1/0.88 on the β' values. For the stationary tests comparing to the β' values found previously, the

largest deviation equals 21 percent. On average, for the six samples in consideration, β' found by the alternative analysis equals 97 percent of the previous value.

For the non-stationary case, the stationary a' value is applied and b' is found from the point of maximum velocity like in the preceeding analysis. The inertia coefficient, c, is found by fitting as the gradient generated from the extended Forchheimer expression, eq (5.1) is compared to the measured gradient and the c value giving best agreement over the entire wave cycle is chosen.

The difference between the oscillatory and stationary value is plotted against KC/n in Fig 5.16. There appears to be an increase in the flow resistance for low values of KC/n, which resambles that of Fig 5.15.

For the inertia coefficient, it was found that for acceleration numbers, defined as $V_{max}/(nTg)$ lower than approximately 0.01, the inertia coefficient becomes zero. The apparently vanishing inertia term for small acceleration numbers may perhaps be due to the insignificance of the inertia term as compared to the quadratic term, as the inertia coefficient is now fitted to the entire wave cycle and not to the points of time with minimum velocity as in the preceeding analysis. From a theoretical point of view, there will always be an inertia term even for small acceleration numbers, cf the preceeding sections. For the rock samples, an asymptotic value in the order of 0.45 was found for values of the acceleration number above 0.05, which is in the order of 10 percent lower than in the preceeding analysis.

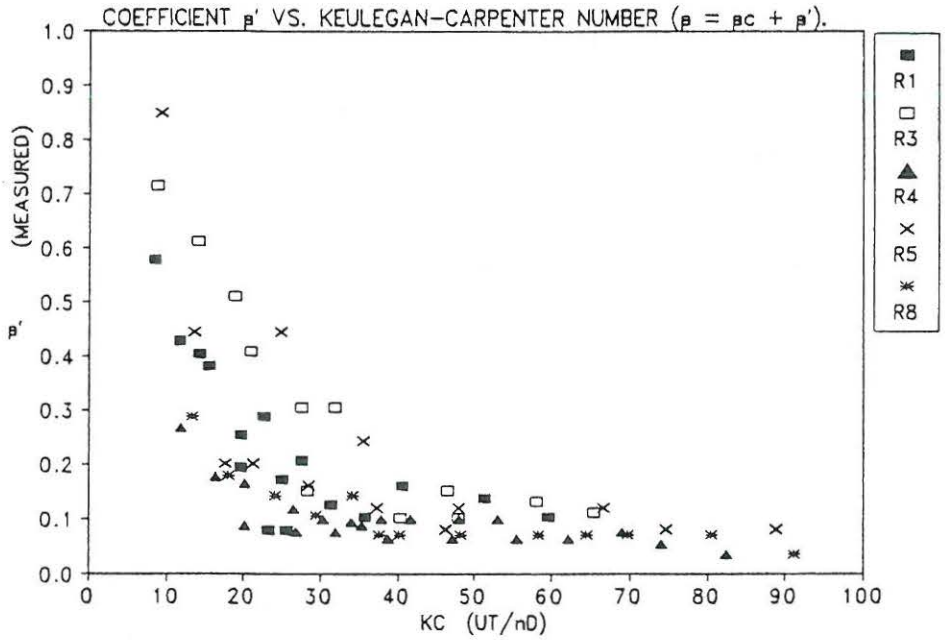

Fig 5.16 β'-β'_{stat} vs KC/n. From Van Gent (1993)

5.5.6 Validation of experiments and analyses

For the stationary and the non-stationary tests, the flow resistance coefficient β' following the definition given in eq (4.20) shows some consistency. The discrepancies appearing may be caused by the experimental procedure, for the rock samples other parameters than the porosity, ie gradation, stone shape and roughness have been varied simultaneously. For the oscillatory tests with the sphere and rock samples, a plot of β'/β'_{stat} vs the Keulegan-Carpenter number, KC, shows some consistency with a slight increase in β'/β'_{stat} for low values of KC. The

cylinder tests aim at providing a large variation in the porosity in order to study the potential phenomenon of virtual mass. It is likely that the separated flow pattern in this case differs from that of porous flow in real stone samples, and hence the α' and β' coefficients for the cylinders may not be representative for porous flow.

From the oscillatory tests, it appears that the virtual mass coefficient, C_m^*, based on the pore velocity, cf eq (5.13), can be regarded as constant with n. The virtual mass coefficient, C_m, based on the discharge velocity, cf eq (5.6), is decreasing with n.

Comparing the coefficients found in the present study to the results of previous measurements it is found that the β' values seem to be too low, whereas the virtual mass coefficients are higher than previously found.

Concerning the alternative analysis for spheres and rock made by Van Gent (1993), the stationary and oscillatory β' values compare to those found by Andersen et al (1993). For the inertia coefficient, the asymptotic value for high acceleration numbers is about ten percent lower than found by Andersen et al (1993). The vanishing inertia term for low acceleration numbers is assumed to be caused by the insignificance of the inertia term as it is fitted to the entire wave cycle.

In the tests with the sphere and rock samples, a certain flow of water took place underneath the samples, and hence in the preceeding data analysis corrections were introduced. Another problem which arose was the non-sinusoidal displacement signals causing some problems in the data analysis. It is suggested that in the future the problems with the underflow should be solved and new experiments with a larger variation in the test material properties carried out in order to further examine the variation of the flow resistance with the Keulegan-Carpenter number, the porosity, gradation, stone shape and surface roughness.

5.6 Comparison of Potential Model and Measurements

In the present section, the potential model based on the discharge velocity, as described in Section 5.3, is compared to the measurements made in the oscillating water tunnel.

From the measurements, the characteristic values of C_m repeated in Table 5.8 have previously been found, cf Table 5.7.

Table 5.8 Measured values of C_m

Matr. No	Matr. Description	n	C_m-meas (char.)
C1	Cylinders	0.792	5.6
C2	Cylinders	0.587	8.1
C3	Cylinders	0.324	12.6
S1	Spheres	0.476	8.5
R1	Irregular rock	0.442	8.0
R3	Semiround rock	0.454	8.2
R4	Round rock	0.393	7.4
R5	Irregular rock	0.449	8.1
R8	Irregular rock	0.388	8.2

For the cylinders, a value of $K_{cyl}=16$ has been fitted to the measurements, cf eq (5.54) and Fig 5.17:

Table 5.9 Measured and fitted values of C_m for cylinders

Matr. No	C_m-meas (char.)	$C_m=2+16(1-n)$
C1	5.6	5.3
C2	8.1	8.6
C3	12.6	12.8

For the spheres and the rock, a value of $K_{cyl}=12$ has been found, cf eq (5.69):

Table 5.10 Measured and fitted values of C_m for spheres and rock

Matr. No	C_m-meas (char.)	$C_m=1.5+12(1-n)$
S1	8.5	7.8
R1	8.0	8.2
R3	8.2	8.1
R4	7.4	8.8
R5	8.1	8.1
R8	8.2	8.8

As shown in Section 5.3, the potential model based on the discharge velocity predicts the same variation of C_m with n for cylinders as well as spheres. As it is difficult to obtain large variations in n with spheres and rock, the comparison made with cylinders becomes an important evidence that the general structures of the expressions for C_m is correct, including the expression for C_m for spheres and rock, which is fitted to measurements with only weak variations in n. As mentioned previously, the cylinder tests are free of wall effects and no underflow appeared during testing.

Summarising the following expressions for the virtual mass coefficient, C_m, are found:

Cylinders: $C_m = 2+16(1-n)$ (5.77)

Spheres and rock: $C_m = 1.5+12(1-n)$ (5.78)

As the idealised potential flow condition is not fulfilled in the measurements, it is likely that the fitted values of the K coefficients to some extent counteract this discrepancy.

The potential model relating the virtual mass coefficient to the discharge velocity has the advantage of being able to predict the qualitative variation of the virtual mass coefficient with the porosity. Only a constant, K, must be found through calibration.

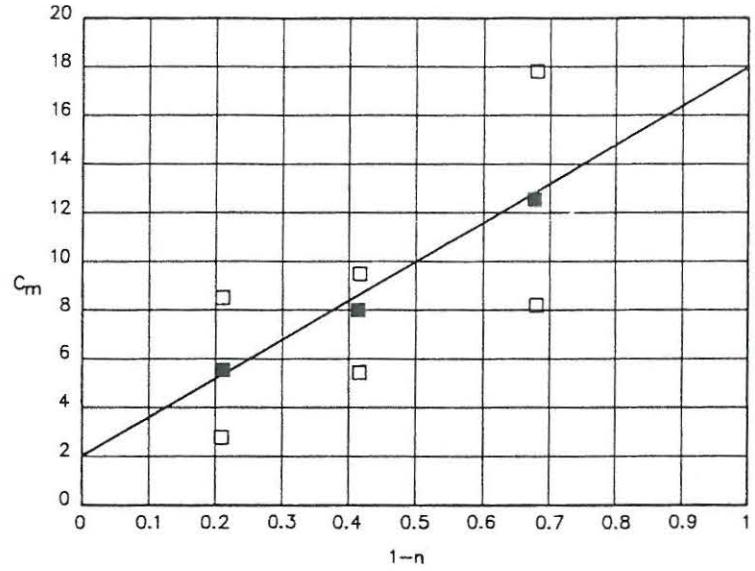

Fig 5.17 C_m vs 1-n for cylinders

Legend: ■: Characteristic values of C_m, □: Ranges for C_m, ——: $C_m = 2+16(1-n)$

It is incidential that the potential model relating the virtual mass coefficient to the pore velocity, cf Section 5.2, results in a constant value of C_m^* as shown in Section 5.5, this constant behaviour has not been predicted. Fig 5.18 compares the virtual mass coefficients of the two alternative descriptions of the inertia term given by eqs (5.6) and (5.13). For C_m in eq (5.6), the expression given by eq (5.77) is plotted. For the latter expression, eqs (5.6) and (5.13) yield:

$$C_m = 1 + \frac{C_m^*}{n} \tag{5.79}$$

which is plotted for a value of $C_m^*=3.9$. It is seen that within the tested range, the two expressions yield approximately the same values of C_m with a constant value of C_m^*.

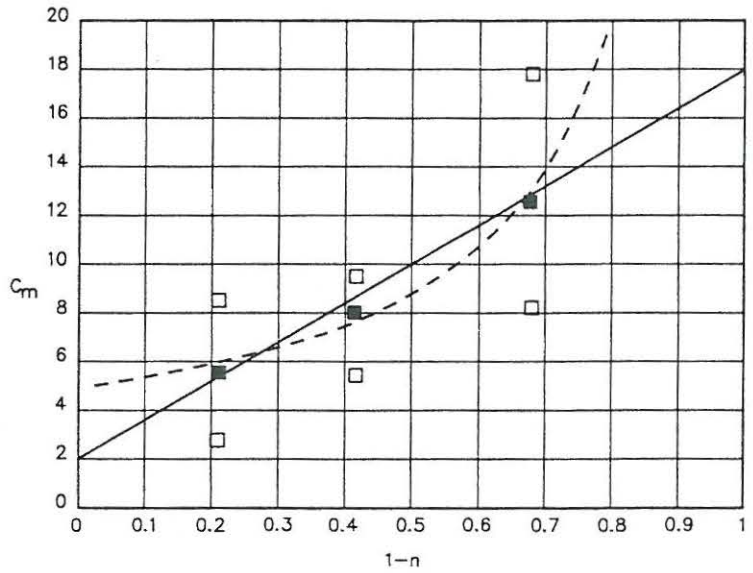

Fig 5.18 Comparison of virtual mass coefficients for cylinders

Legend: ■: Characteristic values of C_m, □: Ranges for C_m, ——: $C_m = 2+16(1-n)$, ---: $C_m = 1 + C_m^*/n$, $C_m^* = 3.9$

5.7 Significance of the Inertia Term

In order to compare the relative importance of the quadratic flow resistance term and the inertia term for sinusoidal motion, the ratio between the maximum values of these has been derived from eqs (4.20) and (5.9) showing the significance of the Keulegan-Carpenter number, KC.

$$\frac{I_{qua}}{I_{iner}} = \frac{\beta' \frac{1-n}{n^3} \frac{V_{max}^2}{gd}}{\frac{n + C_m (1-n)}{g} \left(\frac{\partial V}{\partial t}\right)_{max}} = \frac{\beta' \frac{1-n}{n^3}}{n + C_m (1-n)} \frac{KC}{2\pi} \qquad (5.80)$$

It should be noticed that for sinusoidal flow the two components appear with a phase shift of 90°. For a typical conventional breakwater, KC is in the order of 10 in the surface layers. With n=0.41, β'=3.0 and C_m=8, the above ratio equals 8. For a berm breakwater, KC is larger and hence also I_{qua}/I_{iner}.

With respect to the performance of large scale physical model tests, the above ratio indicates that it is difficult to accurately extract the inertia term from the entire signal in order to determine the virtual mass coefficient. For the oscillatory tests of Smith (1991), the above ratio varied between 1.6 and 20, considering due to measurement errors only the tests where the maximum velocity exceeded 0.1 m/s and the maximum acceleration exceeded 0.1 m/s^2. For the rock material, the tests with velocity above 0.1 m/s, acceleration above 0.1 m/s^2 and $I_{qua}/I_{iner} < 5$, C_m^* ranged between 1.38 and 1.81. These values of C_m^* are considered to be determined with the largest accuracy. The available experimental results are too scattered to support definitive conclusions about the values of C_m^*.

For practical purposes, with respect to scale models, KC is invariant to Froude scaling, and hence no scale effects appear, considering the quadratic term vs the inertia term.

6 APPLICATION TO BREAKWATERS - LITERATURE STUDY

6.1 Analytical Approaches

Analytical solutions are limited to the case of rectangular porous structures assuming linear wave theory with the purpose of estimating the reflection and transmission. Moreover, most solutions are restricted to the shallow water case.

Outside the structure the non-linear shallow water wave equations, NSE are often valid, see eg Svendsen and Jonsson (1980)

$$\frac{\partial \eta}{\partial t} + \frac{\partial}{\partial x}((h+\eta)u) = 0 \qquad (6.1)$$

$$\frac{\partial u}{\partial t} + \frac{\partial u}{\partial x} u + g \frac{\partial \eta}{\partial x} = 0 \qquad (6.2)$$

h is the local water depth
η is the surface elevation
u is the depth averaged horizontal velocity
x is a horizontal coordinate
t is time

Eqs (6.1) and (6.2) can be derived from the Euler equations and the continuity equation, cf Section 2.1, together with proper boundary conditions. Analytical solutions can be obtained if in eqs (6.1) and (6.2) the non-linear terms are neglected, ie

$$\frac{\partial \eta}{\partial t} + h \frac{\partial u}{\partial x} = 0 \qquad (6.3)$$

$$\frac{\partial u}{\partial t} + g \frac{\partial \eta}{\partial x} = 0 \qquad (6.4)$$

which are the governing equations for linear shallow water waves.

Inside the structure, additional flow resistance terms are included according to the Forchheimer formulation. In order to make analytical solutions possible, the quadratic term is linearised.

Solving eqs (6.3) and (6.4) leads to a standing wave in front of the structure due to partial reflection. When applied to a rectangular rubble mound structure, good results are obtained.

Several solutions of this type exist, some of them are given by Le Méhauté (1957), Sollitt and Cross (1972), Madsen (1974), Madsen and White (1975), Massel and Mei (1977), Madsen (1983), and Dalrymple et al (1991).

6.2 Breaking of Standing Waves on a Slope

At present, no theory exists describing the complex flow pattern associated with breaking of standing waves on a slope, and hence empirical knowledge must be introduced. It is, however, possible to give some theoretical justification for the parameters applied. The present section is mainly based on the work of Battjes (1974) and on a review given by Mei (1983).

Iribarren and Nogales in 1949 found empirically that the criterion for breaking of waves encountering a slope can be expressed by the parameter, defined as

$$\xi_o = \frac{\tan \alpha}{\sqrt{s_o}} \tag{6.5}$$

where $\tan\alpha$ is the slope and s_o is the fictitious wave steepness defined as

$$s_o = \frac{H}{L_o} \tag{6.6}$$

The critical value of ξ_o was estimated as

$$\xi_o \simeq 2.3 \tag{6.7}$$

ie, for $\xi_o > 2.3$, no breaking occurs and the reflection is large and for $\xi_o < 2.3$, breaking occurs and the reflection is low.

Munk and Wimbush (1969) introduced a criterion for breaking of standing waves on a slope: the downward fluid acceleration along the slope, governed by the standing waves, cannot exceed the acceleration of a free-falling particle, governed by gravity, without causing separation, which is interpreted as breaking. It is unclear to which extent this criterion describes the onset of breaking, at least it is assumed to give some justification for ξ_o as the governing parameter, cf the deduction below.

The free-fall acceleration downward along the slope is governed by gravity, ie $g\sin\alpha$. The maximum vertical acceleration of the wave equals $\omega^2\eta_0$, where η_0 is the local amplitude, and hence the maximum downward acceleration along the slope equals $\omega^2\eta_0/\sin\alpha$. The breaking criterion reads:

$$\frac{\omega^2\eta_0}{\sin\alpha} \geq g\sin\alpha \tag{6.8}$$

or

$$\frac{\omega^2\eta_0}{g} \geq \sin^2\alpha \simeq \tan^2\alpha \tag{6.9}$$

As

$$\frac{\omega^2\eta_0}{g} = \pi \frac{H}{L_o} \tag{6.10}$$

we get

$$\xi_o = \frac{\tan\alpha}{\sqrt{\frac{H}{L_o}}} \leq \sqrt{\pi} = 1.8 \qquad (6.11)$$

In this way, the same parameter ξ_o as found by Iribarren and Nogales is constituted, only the constants differ slightly.

Also the type of breaking depends on ξ_o, as shown in Fig 6.1. Battjes (1974) introduced the name 'surf parameter' or 'surf similarity parameter'. Sometimes, this parameter is referred to as the Iribarren number.

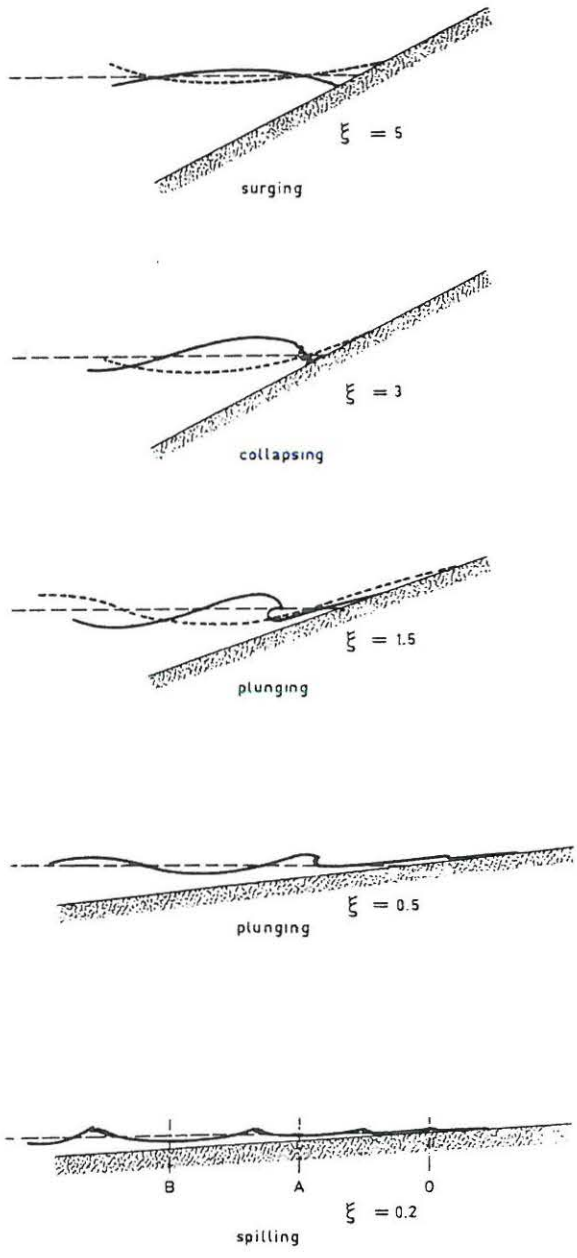

Fig 6.1 Breaker types. From Battjes (1974)

The part of the slope or structure which is periodically covered with water is denoted the swash zone.

Usually, the flow properties on a breakwater, ie velocities run-up and run-down levels are related to $\sqrt{gH}$ and the wave period, T. This can be justified in the following manner. For shallow water waves, linear as well as non-linear, the maximum uprush and downrush velocities can be expressed as

$$V_{1,max} \simeq \sqrt{gh}\,\frac{\eta_{max}}{h} \sim \sqrt{gh}\,\frac{H}{h} \tag{6.12}$$

$$V_{2,max} \simeq \sqrt{gh}\,\frac{|\eta_{min}|}{h} \sim \sqrt{gh}\,\frac{H}{h} \tag{6.13}$$

In the surf zone, ie on the breakwater, the wave heigth, H, and the water depth, h, have the same order of magnitude, see eg Battjes (1974)

$$V_{1,max} \sim \sqrt{gH} \tag{6.14}$$

$$V_{2,max} \sim \sqrt{gH} \tag{6.15}$$

The total water particle migration, a^*, from run-down level to run-up level can be expressed as

$$a^* \sim T_1 \sqrt{gH} \sim T\sqrt{gH} \tag{6.16}$$

$$a^* \sim T_2 \sqrt{gH} \sim T\sqrt{gH} \tag{6.17}$$

The run-up level equals

$$R_u \sim \frac{1}{2}\, a^* \tan\alpha \sim T\sqrt{gH}\,\tan\alpha \sim \sqrt{HL_o}\,\tan\alpha = \xi_o H \tag{6.18}$$

And similarly, the run-down level equals

$$R_D \sim \xi_o H \tag{6.19}$$

According to CIRIA/CUR (1991) for irregular waves, eq (6.18) is applicable to relatively flat rubble slopes, ie for $\xi_o < 1.5$, with H equal to the significant wave height, H_s or H_{m0} and ξ_o based on the mean period, T_m or T_{02}. For $\xi_o > 1.5$, experiments show that ξ_o in eq (6.18) must be raised to a power less than unity.

From measurements, it is known that the maximum run-up level depends on the surf similarity parameter, cf Fig 6.2. It appears that for smooth slopes the run-up level has a maximum for ξ_o around 3 based on the peak period and hence around 2, based on the mean period, T_m or T_{02}. This phenomenon has been called resonance. It is seen that the value of ξ_o for resonance approximately coincides with the critical value for breaking. It should be noted that these are purely deterministic considerations, for a real wave train, which is a stochastic

process, the maximum run-up level on the slope is very much dependent on the interaction between consecutive individual waves. It is, however, possible to detect the dependence on ξ_o also for irregular waves, cf Fig 6.2.

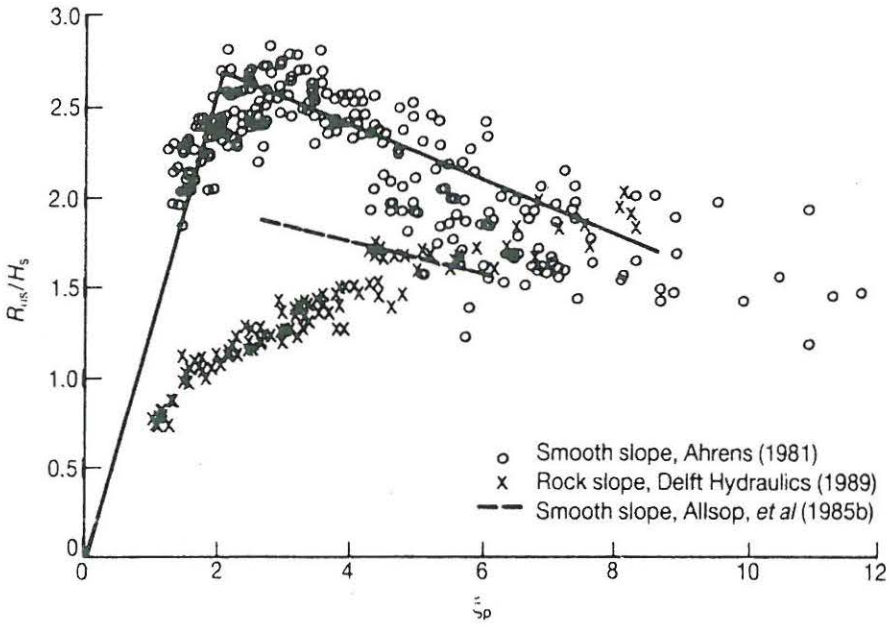

Fig 6.2 Significant run-up level vs ξ_o for irregular waves. From CIRIA/CUR (1991)

Considering the run-up level, R_u, as a potential for a smooth and impermeable slope the velocity squared, uprush as well as downrush, can be expressed as

$$V^2 = 2g\left(R_u - (z+H^+)\right) \tag{6.20}$$

where

z is the surface level of the breakwater
H^+ is the height of the water coloumn above z
$z+H^+$ is the water level relative to SWL

ie the lateral variation in the velocity depends on z and hence also on the local water depth.

Sawaragi et al (1983) found from high speed camera recordings that the maximum slope parallel velocities and accelerations with irregular waves occur for ξ_o between 2 and 3, most pronounced for smooth slopes, but also visible for rubble slopes, cf Fig 6.3. By use of eq (6.20), this observation conforms to the maximum uprush appearing for ξ_o around 2 to 3. Further, they found as a condition for resonance that the wave height to water depth ratio must be larger than 0.45.

In case of resonant conditions, which is denoted by '+' in Fig 6.4, the location of the maximum uprush velocity as well as the maximum downrush velocity is found at $h/h_s \sim 0.25$, where h is the local water depth and h_s is the water depth in front of the structure. For non-resonant conditions and for $\xi_o < 2$, which is relevant for berm breakwaters, shown by filled squares in Fig 6.4, the uprush maximum is located around SWL and the downrush maximum is located around $h/h_s \sim 0.20$.

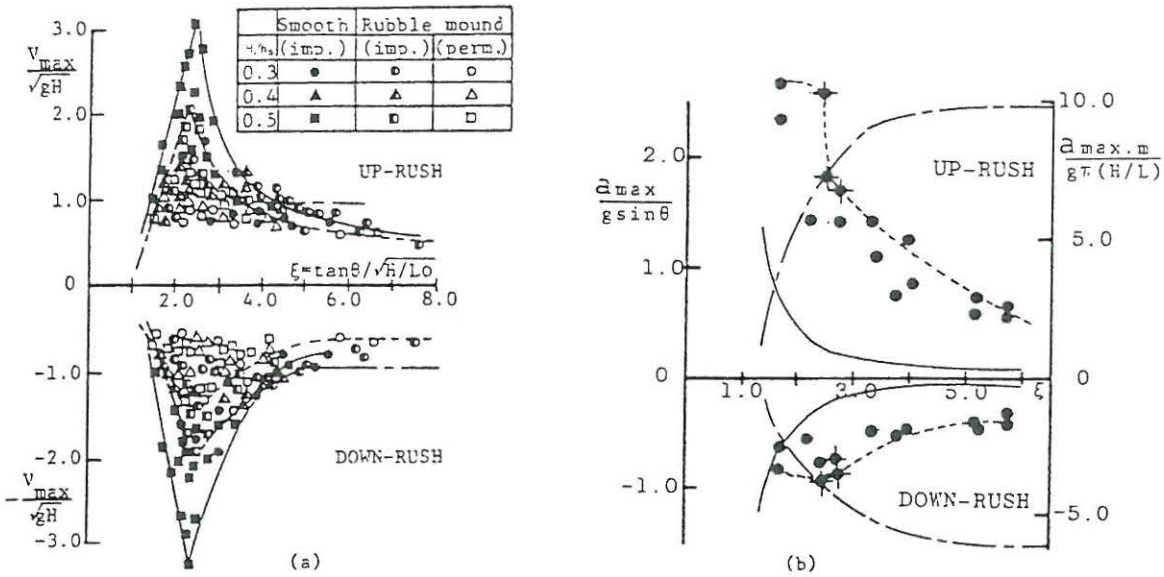

Fig 6.3 Maximum velocity and maximum acceleration vs ξ_o. From Sawaragi et al (1983).

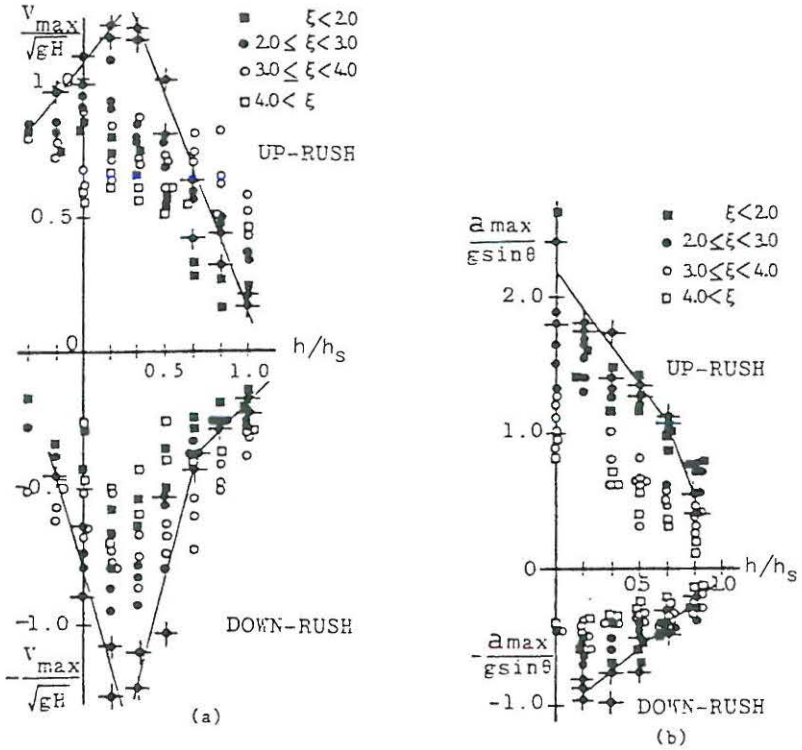

Fig 6.4 Distribution of maximum velocity and maximum acceleration. From Sawaragi et al (1983).

6.3 Structural Stability

Considering a single block on a slope exposed to wave attack, the stability criterion can be expressed by the slope parallel force balance, which for the uprush case reads

$$F_D - W_s\sin\alpha - \mu_s\left(W_s\cos\alpha - F_N\right) + F_I = 0 \qquad (6.21)$$

and for downrush

$$-F_D - W_s\sin\alpha + \mu_s\left(W_s\cos\alpha - F_N\right) - F_I = 0 \qquad (6.22)$$

F_D is the slope parallel drag force
F_N is the slope normal force
F_I is the slope parallel inertia force

Neglecting F_I, we get

$$F_D + \mu_s F_N = W_s\left(\mu_s\cos\alpha + \sin\alpha\right) \qquad (6.23)$$

and

$$F_D + \mu_s F_N = W_s\left(\mu_s\cos\alpha - \sin\alpha\right) \qquad (6.24)$$

Assuming F_D and F_N to vary proportionally to $\rho D_n^2 V^2$, where V is a characteristic velocity, we get

$$\frac{1}{2}C\rho D_n^2 V^2 = W_s\left(\mu_s\cos\alpha + \sin\alpha\right) \qquad (6.25)$$

and

$$\frac{1}{2}C\rho D_n^2 V^2 = W_s\left(\mu_s\cos\alpha - \sin\alpha\right) \qquad (6.26)$$

Usually, the downrush case is the most critical for a conventional breakwater. Taking the downrush velocity as characteristic velocity, we get from eqs (6.18) and (6.20)

$$\xi_o\frac{H}{\Delta D_n} = \frac{1}{C}\left(\mu_s\cos\alpha - \sin\alpha\right) \qquad (6.27)$$

The slope normal force, F_N, can be considered as a combination of a lift force and a slope normal drag force. This is discussed in further detail in Section 8.2.

Summarising the stability of a conventional breakwater depends on

- the shape including slope(s)
- the stability number, $H/\Delta D_n$
- the surf similarity parameter (Iribarren number), ξ_o

Iribarren in 1938 neglected ξ_o, but kept the theoretically correct expression for α

$$\frac{H}{\Delta D_n} = \frac{1}{C}\left(\mu_s\cos\alpha - \sin\alpha\right) \qquad (6.28)$$

which is very often written as

$$W = \frac{K}{(\mu_s \cos\alpha - \sin\alpha)^3} \frac{\rho_a g H^3}{\Delta^3} \quad , \quad K = C^3 \tag{6.29}$$

Also Hudson neglected ξ_0 and further he replaced $(\mu_s \cos\alpha - \sin\alpha)$ by $(\cot\alpha)^{1/3}$ leading to

$$\frac{H}{\Delta D_n} = \frac{1}{C} (\cot\alpha)^{1/3} \tag{6.30}$$

or

$$W = \frac{1}{K_D \cot\alpha} \frac{\rho_a g H^3}{\Delta^3} \quad , \quad K_D = C^{-3} \tag{6.31}$$

In Shore Protection Manual (1984), the K_D values are related to H_{10}, ie the highest 10 percent of the individual waves. In many practical applications, however, the K_D values are related to H_s. The values of K_D correspond to a certain cumulated damage, typically 0 to 5 percent of the stones in the armour layer located within $\pm H$ counted from SWL. Damage is defined as displacent of a stone more than one stone diameter.

For both the above formulae, values of the coefficients can be found in eg Bruun (1985), who also mentions several other similar formulae.

In a series of papers from 1974 to 1983, Günbak, Johannesson and Bruun pointed out the importance of ξ_0 to the stability, see eg Bruun (1985). Ahrens and McCartney (1976) showed that for regular waves the stability depends on ξ_0 with a minimum for ξ_0 between 2 and 4 and also dependent on the slope of the structure, cf Fig 6.5. This is in close agreement with the maximum uprush as discussed in Section 6.2.

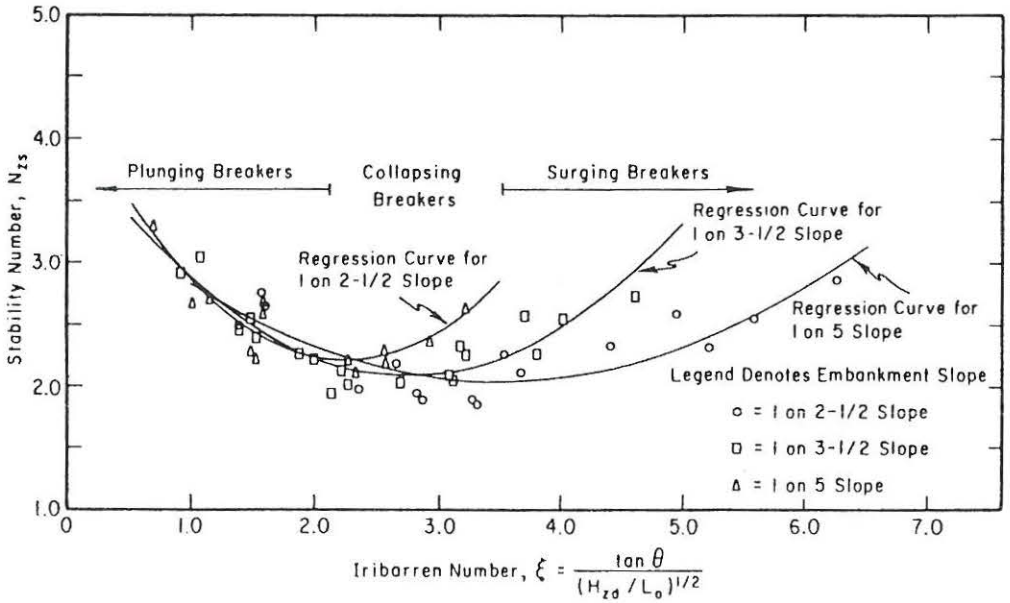

Fig 6.5 Stability of riprap for regular waves. From Ahrens and McCartney (1976)

For a breakwater exposed to irregular waves, the above stability minimum as function of ξ_o is also present.

Van der Meer (1988) proposed formulae for static stability of conventional breakwaters based on extensive physical model tests. One formula is applicable for plunging waves and another for surging waves:

- plunging waves:

$$\frac{H_s}{\Delta D_{n50}} \sqrt{\xi_m} = 6.2\ P^{0.18} \left(\frac{S}{\sqrt{N_w}} \right)^{0.2} \tag{6.32}$$

- surging waves:

$$\frac{H_s}{\Delta D_{n50}} = 1.0\ P^{-0.13} \left(\frac{S}{\sqrt{N_w}} \right)^{0.2} \sqrt{\cot\alpha}\ \xi_m^P \tag{6.33}$$

P is a permeability coefficient
S is the cumulated damage defined as eroded area/D^2_{n50}
N_w is the number of waves

Van der Meer (1988) carried out extensive physical model tests with berm breakwaters and straight porous slopes, 1:3, 1:5, and 1:10. The geometry of the equilibrium profiles was presented as a number of parametric expressions related to the number of waves, N_w, and to either H_s and s_m or H^* and T^* defined as

$$H^* = \frac{H_s}{\Delta D_{n50}} \tag{6.34}$$

$$T^* = \sqrt{\frac{g}{D_{n50}}}\ T_m \tag{6.35}$$

The dimensionless wave period was introduced in order to facilitate comparison between gravel beaches exposed to low values of wave height and wave period and berm breakwaters exposed to high values of wave height and wave period. It was found that the wave height and wave period have the same order of influence on the profile.

Within the tested range, the variation in the profile with N_w is fitted with power functions in N_w, typically in the order of $N_w^{0.05}$. This relatively weak variation indicates that for an increasing number of waves, the profile is approaching an equilibrium profile. Only the crest dimensions show a stronger variation with N_w than the other profile parameters, up to $N_w^{0.15}$.

6.4 Numerical Models

6.4.1 Depth averaged and hybrid models

Nasser and McCorquodale (1975) presented a one-dimensional model for the propagation of long shallow water waves through a porous medium, with the main purpose of predicting the internal motion including transmission and water level fluctuations at the impervious core. The model is based on the non-linear shallow water wave equations, NSE, cf eqs (6.1) and (6.2), which are solved by the method of characteristics. The breakwater is schematised by a homogeneous and rectangular section in front of an impervious core. The dissipation is described by the Forchheimer expression. The model covers phenomena such as reflection, transmission, dissipation, run-up and rush-down. The numerical model has been compared to wave flume tests showing in general good agreement.

Hibberd and Peregrine (1979) solved the depth integrated continuity and momentum equations for a smooth and impermeable slope (a sand beach) exposed to wave attack, ie the non-linear shallow water wave equations, NSE, by means of the method of characteristics. NSE are applicable to impermeable slopes, however, the depth integrated approch has been followed by several authors later on extending the models to cover rough and porous slopes as well by introducing some modifications. In general, the depth integrated approch has the advantage of including broken waves, however, only described as bores. The major disadvantage, which is espescially apparent in the breakwater case, is that the complex two-dimensional flow pattern on and in the structure is not described by this type of model.

The non-linear shallow water equations, NSE, were formulated with the reference coordinate and velocity parallel to the sloping bottom

$$\frac{\partial h^*}{\partial t} + \frac{\partial}{\partial x^*}(h^* u^*) = 0 \qquad (6.36)$$

$$\frac{\partial u^*}{\partial t} + \frac{\partial u^*}{\partial x^*} u^* + g\cos\alpha \frac{\partial h^*}{\partial x^*} + g\sin\alpha = 0 \qquad (6.37)$$

h^* is the total depth of water
u^* is the depth averaged water velocity
x^* is a coordinate parallel to the bottom
t is time

The governing equations were then made dimensionless and a coordinate transformation was introduced yielding a horizontal x-axis, but still formulated in the slope parallel velocity.

Kobayashi et al (1986) presented a one-dimensional hydrodynamic model for determination of armour stability on rough impermeable slopes exposed to monochromatic waves. The model solves the equations of continuity and momentum by a finite difference method, in principle eqs (6.1) and (6.2) with an additional term for bed shear stress resulting in the horizontal velocity. Free surface flow is included. The model covers the flow outside the structure, including reflection, run-up and down-rush. The subsequent evaluation of the armour stability includes drag, lift, inertia and gravity forces, which for the uprush case reads

$$F_D - W_s \sin\alpha - \mu_s (W_s \cos\alpha - F_L) + F_I = 0 \qquad (6.38)$$

and for downrush

$$- F_D - W_s \sin\alpha + \mu_s (W_s \cos\alpha - F_L) - F_I = 0 \qquad (6.39)$$

The model has been and is subject to major developments. A version capable of predicting the flow on smooth and rough impermeable slopes, IBREAK, was presented by Kobayashi and Wurjanto in 1989. Van der Meer and Breteler (1990) compared this model to measurements on a smooth slope. According to the authors, the results for run-down velocities and run-up levels were acceptable, the results for run-up velocities were a little worse and the results for pressures and run-down levels were bad.

Later on, the model has been extended to cover the case of rough slopes with a permeable underlayer, see Kobayashi and Wurjanto (1990a) and (1990b). A coupling algorithm between the exterior and interior flow including mass and momentum flux is applied. The model is capable of simulating flow on and in structures exposed to irregular waves.

Norton and Holmes (1992) followed the line of Kobayashi and Wurjanto applying a one-dimensional model for flow on and in a rough porous slope. A berm breakwater model was made. The berm and armour layer is modelled by spheres of different size with frictional properties as for irregular rock. The initial profile is established by means of a random placement algorithm. The reshaped profiled is modelled by displacement of single spheres once the total destabilising force, based on the hydrodynamic simulation, exceeds a certain threshold value.

Van Gent (1992b) presents a one-dimensional model, ODIFLOCS, which resambles the model by Kobayashi. Also in this model, mass and momentum flux are included in the coupling between the exterior and interior domains. Further, this model includes the discontinuity in the water table at the surface of the structure. ODIFLOCS is stable at low values of the friction factor. Tørum and Van Gent (1992) have compared the model to velocity measurements on a berm breakwater showing in general a fair agreement between the calculated and measured velocities. The points of maximum uprush and maximum downrush velocity respectively are simulated for wave heights ranging between approximately 0.10 m and 0.20 m and wave periods ranging between 1.5 s and 2.1 s. It appears that the maximum uprush velocities are found just below SWL, which conforms to the measurements by Sawaragi et al, cf Fig 6.4, as with a rough slope there is no resonance. For the point of maximum downrush velocity, the simulations show an abrupt change from a location just below SWL for $H \simeq 0.15$ m to a location further down the slope for $H \simeq 0.20$ m. This abrupt change is in disagreement with the measurements, cf Fig 6.4.

Delft Geotechnics (1993) describe a model, MBREAK, consisting of a depth integrated model for the outer flow, LWOS, and a model for the flow in the porous structure, HADEER. A coupling algorithm implying mass and momentum influx is applied. The HADEER code was originally developed as a two-dimensional model. At present, only the one-dimensional version is applicable together with the one-dimensional LWOS model.

The HADEER model has been developed at Delft Geotechnics (DG) (formerly Delft Soil Mechanics Laboratory) through a cooperation between Barends, DG and Hannoura and McCorquodale, University of Windsor, Canada. HADEER is based on the work done by

Hannoura and McCorquodale during the 1970-ties, see below. A summary is given by Hölscher, de Groot and van der Meer (1988). HADEER can be applied for the interior of breakwaters with sloping seaward face and with layers of varying porosity. The model describes linear and quadratic flow resistance, and inertia of the water is included. The wave run-up and the pressure distribution on the exterior slope are used as boundary conditions. The numerical model has been compared to flume tests.

The model presented by Hannoura and McCorquodale (1985b) is a mixed numerical model for the interior flow domain. A one-dimensional finite difference method of characteristics model solves the continuity and momentum equations to obtain the internal water levels. The porous flow description is based on the Forchheimer expression together with an expression for the added mass. Air entrainment due to internal wave breaking is included. An expression for the hydraulic conductivity under two phase flow conditions has been given by Hannoura and McCorquodale (1985a). A two-dimensional finite element model is applied in order to predict the flow properties below the water level. The two-dimensional model is a potential model, which is obtained by linearising the Forchheimer expression, cf Section 2.3. Emphasis is put on the description of the discontinuities appearing at the internal boundaries of multi-layered structures. As a critisism, it can be argued that only the discontinuity at the surface of the structure is significant, as the water motion is rapidly dampened once the first porous layer is entered.

Thompson (1988) presented a hybrid numerical model for flow on and in breakwaters. Outside the structure, the vertically integrated equations of continuity and momentum are solved by a finite difference technique. Phenomena such as reflection, run-up and down-rush are included. Inside the structure, the flow field can be determined by either a two-dimensional finite difference model, solving the linearised flow resistance equations, cf Section 2.3, or from a simplified model, assuming that the flow takes place only in a thin layer just below the surface of the slope. The model has been compared to experimental results.

6.4.2 Vertically two-dimensional models

As the flow field on and in porous structures is strongly two-dimensional, a number of two-dimensional models are at present under development. Further, this is anticipated as a prerequisite for the modelling of plunging breakers, internal breaking and overtopping, processes which are relevant for flow on and in breakwaters and important to eg air entrainment. In contradiction to the depth averaged models and the hybrid models, the theory for the external flow can in the two-dimensional case be deduced without the limiting assumption of an impervious structure.

McCorquodale (1970) presented a two-dimensional model for unsteady non-darcy flow inside porous media. The model is based on the continuity equation and Navier-Stokes equations, which are solved by a finite element technique. Free surface flows can be modelled. The effect of a weak inertial term is included. The model has been compared to experimental results showing in general good agreement.

The model by Austin and Schlueter (1982) solves the continuity equation and Navier-Stokes equations in two dimensions by a volume of fluid (VOF) method capable of modelling free surface flow. The model predicts the flow field in a porous armour layer schematized as a rectangular block system or alternatively as a system of discs, cf Fig 6.6. The drag and inertial forces acting on the individual blocks are derived subsequently by integration of the pressures acting on the surface of the blocks. Finally, the response of the blocks is

determined by a discrete element code solving the equations of motion. Presumably the weak point of such a model is the detailed flow description around the single blocks. At the surface of real structures flow separation occurs at the single blocks strongly affecting the pressure distribution and hence the drag and lift forces. A traditional estimation of the drag and lift forces based on the surface velocity squared in combination with empirical coefficients does not require a description of the local flow around the single blocks.

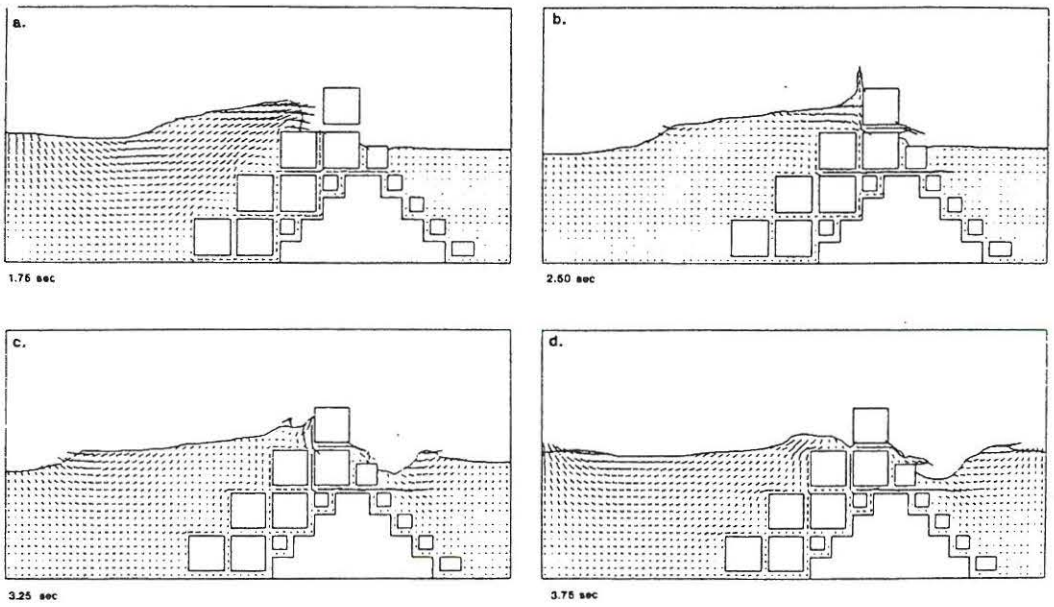

Fig 6.6 From Austin and Schlueter (1982)

The model by Wibbeler and Oumeraci (1992) is applicable to the interior of a breakwater. The model is a finite element potential model which includes a linearised porous flow resistance term. As boundary condition the pressures acting on the surface of the structure are applied. The model has been compared results showing some discrepancies.

Hydraulics Research have developed a model solving the exterior domain by a boundary element model and the interior domain by a finite element model, see Sun et al (1992). The boundary element model is based on the theory of complex potential, cf Section 2.2. The solution to Laplaces' equation everywhere in the computational domain can be described through the value at the boundaries of either the potential or the stream function. The potential is applied at the free surface and for the other boundaries the stream function is applied. The finite element model applied to the interior of the structure is a potential model, which includes a linearisation of the extended Forchheimer equation, cf Section 2.3. The two models are coupled by demanding continuity of flow and pressures at the surface of the structure. No friction at the structure surface is included. Comparison has been made to physical model tests showing good agreement between predicted and observed pressures near the front face of the breakwater mound for waves of moderate height.

Danish Hydraulic Institute has over the last years developed a general three-dimensional hydrodynamic model, SYSTEM 3xz, see Fischer et al (1992) and DHI (1992). The model solves the continuity equation and Navier-Stokes equations by a finite difference method.

Free surface flow can be modelled outside as well as inside a porous structure. A friction factor can be applied to the surface of the structure. The porous flow resistance is modelled by the extended Forchheimer expression. At present, a vertically two-dimensional example with a sloping, multilayered structure can be modelled. Non-stationary simulations have been compared to experimental results. SYSTEM 3xz has the advantage of not including any coupling algorithms between the exterior and interior flow domains. The model is described in more details in Chapter 7.

The SKYLLA model (formerly SAVOF) presently being developed at Delft Hydraulics, see Van der Meer et al (1992), is based on the SOLA-VOF model by Hirt and Nichols (1981). The model, which solves the continuity equation and Navier-Stokes equations in two dimensions, is based on the volume of fluid method. This model is able to compute free surface flow when the fluid domain becomes multiply-connected, and hence plunging waves can be modelled. Air entrainment is not included, the model simulates either fluid or vacuum. At present the model is applicable to smooth impermeable structures, but is not able to simulate flow inside a porous structure.

7 TWO-DIMENSIONAL OSCILLATORY FLOW INCLUDING SURFACE PHENOMENA

The overall objective of Chapters 7, 8 and 9 is to establish a hydrodynamically based description of a berm breakwater equilibrium profile. From Chapters 3 to 5, the pore and solid averaged porous flow description is known. In the present chapter, DHI's numerical model, SYSTEM 3xz, is applied in the description of the water motion on and in a straight porous slope exposed to wave attack. An armour averaged friction factor describing the bed shear stress acting on the slope is applied. The model simulations are compared to the velocity measurements by Tørum (1992b). Various aspects concerning the application of SYSTEM 3xz including the friction factor are discussed and proper modifications are introduced, yielding a correct bed shear stress.

7.1 Porous Flow Equations

Inside the porous medium, the flow is described by the continuity equation

$$\frac{1}{n}\frac{\partial V_i}{\partial x_i} = 0 \tag{7.1}$$

and Navier-Stokes equations extended with the porous flow resistance terms, cf eqs (4.19) and (5.1) written in vector form

$$gc\frac{\partial V_i}{\partial t} + \frac{1}{n^2}\frac{\partial V_i}{\partial x_j}V_j = -\frac{1}{\rho}\frac{\partial p}{\partial x_i} + g_i - ga'V_i - gb'VV_i \tag{7.2}$$

In addition, also convective accelerations on a macroscopic level are included. Considering a condition for a fluid element with the reference velocity V/n, we get the second term listed in eq (7.2).

p	is the pressure
V	is the discharge velocity
n	is the porosity
g	is the acceleration of gravity
a'	is the linear flow resistance coefficient
b'	is the quadratic flow resistance coefficient
c	is the inertia coefficient
x_i	is a cartesian coordinate
t	is time

As the flow resistance coefficients, a', b' and c, are originally defined from the hydraulic gradient together with the discharge velocity, they are multiplied by the acceleration of gravity, g, in eq (7.2).

7.2 Equations for External Flow

Propagating waves at any water depth are described in time domain by Reynolds equations, cf Section 2.1.

The continuity equation reads

$$\frac{\partial V_i}{\partial x_i} = 0 \tag{7.3}$$

and the momentum equation reads

$$\frac{\partial V_i}{\partial t} + \frac{\partial V_i}{\partial x_j} V_j = - \frac{1}{\rho} \frac{\partial p}{\partial x_i} + g_i + \nu \frac{\partial^2 V_i}{\partial x_j \partial x_j} + \frac{\partial}{\partial x_j} \left(-\overline{u_i u_j} \right) \tag{7.4}$$

7.3 Flow on Structure Surface

Due to the strongly turbulent flow above the structure surface, a bed shear stress must be introduced. Madsen and White (1975) presented a friction factor, f_r, for breakwaters, which was found in the following manner. An analytical reflection model was made for a rectangular cross-section including energy dissipation on the surface. In the model, f_r is introduced as a bottom friction coefficient, but it covers all forces associated with energy dissipation on the rough impermeable slope, ie bottom friction and wave breaking. Physical model tests were carried out with rough impermeable slopes 1:2 and 1:3, the reflection coefficient was determined from wave height measurements, and finally f_r was estimated. An empirical expression was fitted to the results of various tests

$$f_r = 0.29 \left(\frac{D}{h_s} \right)^{-0.5} \left(\frac{D}{R_u \cot\alpha} \right)^{0.7} \tag{7.5}$$

where

D	is the characteristic lenght of the armour unit
h_s	is the water depth in front of the breakwater
R_u	is the run up height on the breakwater

The bed shear stress equals

$$\tau_b = f_r \frac{1}{2} \rho V^2 \tag{7.6}$$

By means of eq (6.18) valid for $\xi_o < 1.5$ as deduced in Section 6.2, the dependence on the breakwater slope can be approximately eliminated.

$$R_u = \xi_o H = \frac{\tan\alpha}{\sqrt{\frac{H}{L_o}}} H \tag{7.7}$$

yields

$$R_u \cot\alpha = \sqrt{H L_0} \tag{7.8}$$

For the present application, the following values have been inserted into eqs (7.5) and (7.8)

- $D = 0.034$ m
- $h_s = 0.8$ m
- $H = 0.2$ m
- $T = 2.0$ s

leading to $f_r = 0.12$.

Jonsson and Carlsen (1976) carried out physical model tests in an oscillating water tunnel and found values of a wave friction factor, f_w, varying as a function of the ratio a/k, where a is the near bed wave amplitude and k is the roughness. The wave friction factor, f_w, is defined from

$$\tau_{b,max} = f_w \frac{1}{2} \rho V_{b,max}^2 \tag{7.9}$$

In this way, f_w empirically includes all contributions to the maximum bed shear stress, ie drag, lift and inertia forces.

From measurements of the velocity profile over the bed, the friction factor was found as

$$f_w = 0.30 \text{ for } \frac{a}{k} < 1.57 \tag{7.10}$$

$$\frac{1}{4\sqrt{f_w}} + \log \frac{1}{4\sqrt{f_w}} = -0.08 + \log \frac{a}{k} \quad \text{for } \frac{a}{k} > 1.57 \tag{7.11}$$

Equation (7.10) was suggested by Jonsson (1976).

Applied to the present example, cf Section 7.6, we find from Section 6.2

$$a \sim \frac{V_{1,max} \cdot T}{2\pi} \sim \frac{1 \text{ m/s} \cdot 2\text{s}}{2\pi} = 0.32 \text{ m} \tag{7.12}$$

$$\frac{a}{k} = \frac{0.32}{2.5 \cdot 0.042} \sim 3 \tag{7.13}$$

$$f_w = 0.17 \tag{7.14}$$

For the roughness, a value of 2.5 times the equivalent spherical diameter is applied.

The friction factor actually applied in the model computations equals $f_o=0.9$. The selection is described in Sections 7.6 and 9.3.

Jonsson and Carlsen (1976) also derived the turbulent eddy viscosity, ν_T, from their measurements. From tests with a/k varying between 28.4 and 124, and maximum velocities varying between 1.53 m/s and 2.11 m/s, it appeared that the maximum values of ν_T are in the order of 0.01 m^2/s.

7.4 Computer Model SYSTEM 3xz

Inside the porous medium, the continuity and momentum equations are solved

$$\frac{1}{n}\frac{\partial V_i}{\partial x_i} + \frac{1}{\rho c_s^2}\frac{\partial p}{\partial t} = 0 \tag{7.15}$$

$$gc\,\frac{\partial V_i}{\partial t} + \frac{1}{n^2}\frac{\partial V_i}{\partial x_j}V_j = -\frac{1}{\rho}\frac{\partial p}{\partial x_i} + g_i - ga'V_i - gb'VV_i + \frac{1}{n}\frac{\partial}{\partial x_j}\left(E\frac{\partial V_i}{\partial x_j}\right) \tag{7.16}$$

E is a constant eddy viscosity, which for the present case equals zero, as all viscous forces are included in the linear Forchheimer term, and all convective inertia forces are included in the quadratic Forchheimer term and the macroscopic convective acceleration term. c_s is the speed of sound associated with the artificial compressibility, which is introduced from numerical reasons, to have an extra coupling between the continuity and momentum equations.

Outside the structure, we have

$$\frac{\partial V_i}{\partial x_i} + \frac{1}{\rho c_s^2}\frac{\partial p}{\partial t} = 0 \tag{7.17}$$

$$\frac{\partial V_i}{\partial t} + \frac{\partial V_i}{\partial x_j}V_j = -\frac{1}{\rho}\frac{\partial p}{\partial x_i} + g_i + \frac{\partial}{\partial x_j}\left(E\,\frac{\partial V_i}{\partial x_j}\right) \tag{7.18}$$

E is a constant eddy viscosity, the actual choise of E is further described in Section 7.6.

For eqs (7.17) and (7.18), the pressure and gravity terms are transformed as described below.

The free surface is described by the continuity equation and the momentum equation. Both equations are described by means of the excess pressure, p', relative to the local hydrostatic pressure.

$$p' = p - \rho g h' \tag{7.19}$$

h' is the depth below the free surface. It should be noted that h' is not related to any datum. p' is related to the usual excess pressure relative to hydrostatic pressure counted from SWL, p^+ applied within wave theory by

$$p' = p^+ - \rho g \eta \tag{7.20}$$

cf also Fig 7.1.

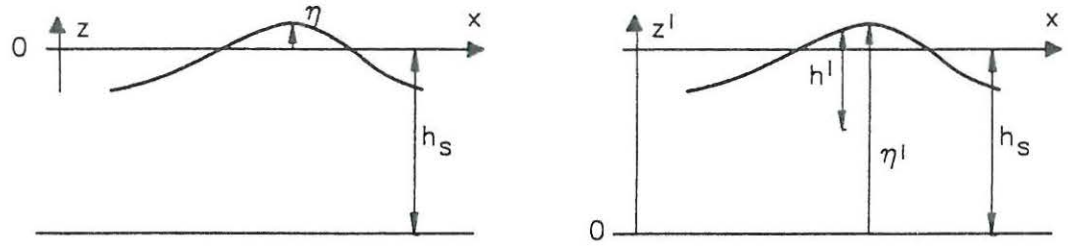

Fig 7.1 Definitions according to wave theory and SYSTEM 3xz respectively

The continuity equation reads

$$\frac{\partial u}{\partial \alpha} + \frac{\partial v}{\partial \beta} + \frac{\partial w}{\partial \gamma} + \frac{1}{\rho c_s^2}\frac{\partial p'}{\partial t} = 0 \qquad (7.21)$$

where α, β and γ are the fractions of volume in the three directions respectively, see the report by Danish Hydraulic Institute (1992) for further details.

For the momentum equation, the x and z-directions are considered in two steps. Eq (7.18) leads to:

$$\frac{\partial u}{\partial t} = -\frac{1}{\rho}\frac{\partial}{\partial x}(p' + \rho g h') = -\frac{1}{\rho}\frac{\partial p'}{\partial x} - g\frac{\partial h'}{\partial x} \qquad (7.22)$$

$$\frac{\partial w}{\partial t} = -\frac{1}{\rho}\frac{\partial}{\partial z'}(p' + \rho g h') - g = -\frac{1}{\rho}\frac{\partial p'}{\partial z'} \qquad (7.23)$$

as h' decreases with z'.

At the surface of the structure, the gradient in the velocity above the slope is governed by f_0, u_b and E, where u_b is the velocity in the distance $\Delta z/2$ above the structure

$$\tau_b = f_0 \frac{1}{2}\rho u_b^2 = \rho E \left(\frac{\partial u}{\partial z}\right)_b \qquad (7.24)$$

leading to

$$E\left(\frac{\partial u}{\partial z}\right)_b = f_o \frac{1}{2} u_b^2 \qquad (7.25)$$

In eq (7.18), at the surface level of the structure, in the last term on the right-hand side, the quantity $E\,\partial V_1/\partial x_3$ is calculated according to eq (7.25).

As boundary condition on the right-hand side of the model area, first order waves are applied, ie $H/L \ll 1$. The boundary condition is a combined velocity and level boundary with the pressure as a free variable

$$\eta(t) = \frac{H}{2} \sin(\omega t) \tag{7.26}$$

$$u(z,t) = -\frac{H}{2}\omega \frac{\cosh kz'}{\sinh kh} \sin(\omega t) \tag{7.27}$$

$$w(z,t) = \frac{H}{2}\omega \frac{\sinh kz'}{\sinh kh} \cos(\omega t) \tag{7.28}$$

The dispersion relation reads:

$$\frac{\omega}{k} = c = \frac{g}{\omega} \tanh kh \tag{7.29}$$

As the model is formulated in time domain, it can in principle cope with a time series of irregular waves imposed as boundary condition. Throughout this thesis, however, H_{m0} and T_{02} are applied as the governing wave parameters together with a regular first order wave.

Wave breaking is not included in the model, which may cause some discrepancies in the simulated velocities and pressures. As described in Section 6.2, the impact of the wave breaking increases with decreasing values of the surf similarity parameter, ie with decreasing slope, and hence the problems associated with the lack of breaking in the computer model are likely to increase with decreasing slope.

SYSTEM 3xz has been verified for the case of a progressive wave. Also the run-up height on a smooth slope has been simulated and compared to the expression by Hunt which is based on experiments, cf Fig 7.2.

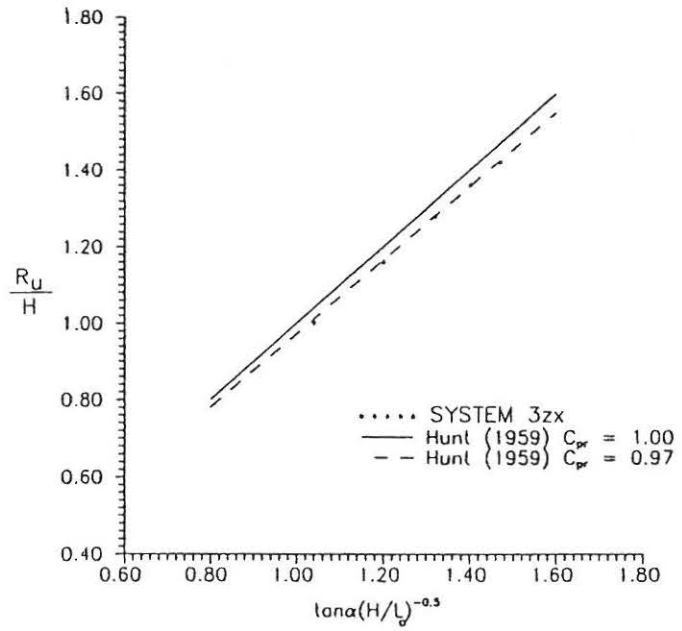

Fig 7.2 Comparison of predicted and measured run-up height. From DHI (1992).

7.5 The Artificial Compressibility

As a part of the present work the influence of the extra term in the continuity equation due to artificial compressibility has been examined. The wave equations below can be found in eg Svendsen and Jonsson (1980).

According to eq (7.17), the error on the continuity equation equals

$$\varepsilon = \left| \frac{\frac{1}{\rho c_s^2} \frac{\partial p'}{\partial t}}{\frac{\partial u}{\partial x}} \right| \tag{7.30}$$

The horizontal particle velocity and its derivative with x equals

$$u = \frac{\pi H}{T} \frac{\cosh k\,(z+h)}{\sinh kh} \cos(\omega t - kx) \tag{7.31}$$

$$\frac{\partial u}{\partial x} = k \frac{\pi H}{T} \frac{\cosh k\,(z+h)}{\sinh kh} \sin(\omega t - kx) \tag{7.32}$$

As the surface elevation is given by

$$\eta = \frac{H}{2} \cos(\omega t - kx) \tag{7.33}$$

and the excess pressure relative to hydrostatic pressure counted from SWL, p^+, by

$$p^+ = \rho g \frac{H}{2} \frac{\cosh k(z+h)}{\cosh kh} \cos(\omega t - kx) \tag{7.34}$$

we get for p' and its derivative with t

$$p' = p^+ - \rho g \eta = \rho g \frac{H}{2} \frac{\cosh k(z+h) - \cosh kh}{\cosh kh} \cos(\omega t - kx) \tag{7.35}$$

$$\frac{\partial p'}{\partial t} = -\omega \rho g \frac{H}{2} \frac{\cosh k(z+h) - \cosh kh}{\cosh kh} \sin(\omega t - kx) \tag{7.36}$$

and hence the error, ϵ, can be found as

$$\epsilon = \frac{g}{c_s^2 k} \tanh kh \left(\frac{\cosh kh}{\cosh k(z+h)} - 1 \right) \tag{7.37}$$

From the dispersion relation, cf eq (7.29), we have

$$\frac{g}{k} \tanh kh = c^2 \tag{7.38}$$

leading to

$$\epsilon = \left(\frac{c}{c_s}\right)^2 \left(\frac{\cosh kh}{\cosh k(z+h)} - 1\right) \tag{7.39}$$

At SWL, ie z=0, we get ϵ=0. At the bottom, ie z=-h, we find

$$\epsilon = \left(\frac{c}{c_s}\right)^2 (\cosh kh - 1) \tag{7.40}$$

In the shallow water limit, we have cosh kh=1 and hence ϵ=0 everywhere in the computational domain.

If the simulations were carried out in p^+ instead of p', the error would be

$$\epsilon^+ = \left(\frac{c}{c_s}\right)^2 \tag{7.41}$$

ie larger than ϵ.

7.6 Calibration and Verification

As a part of the present work, the computer model SYSTEM 3xz has been further calibrated and verified in different manners. Initially, the propagation of a wave over a smooth and impervious horizontal bottom has been modelled and compared to linear wave theory. Secondly, the flow on and in a straight porous slope has been modelled and compared to measurements carried out by Tørum (1992).

7.6.1 Horizontal bottom

In order to validate the propagation of a linear wave over a smooth and impervious horizontal bottom, a model with the following parameters is set up:

h_s = 0.8 m
H = 0.20 m
T = 2.00 s
Δx = 0.08 m
Δz = 0.02 m

Δz is chosen as one tenth of H, and Δx is chosen as four times Δz, cf the proceeding subsection concerning a straight porous slope.

From linear wave theory we get, see eg Svendsen and Jonsson (1980)

$$h_s/L = 0.164$$

where L is the wave length, and for the phase velocity, c, we find

$$c = 2.43 \text{ m/s}$$

The Ursell parameter is defined as

$$Ur = \frac{HL^2}{h_s^3} \tag{7.42}$$

which for the present example equals

$$Ur = 9.26$$

As Ur is less than 15, the sinusoidal wave theory can be applied according to Svendsen and Jonsson (1980).

In order to find an adequate value of c_s, eq (7.40) is applied with the requirement that ϵ must be small. In the present example, we have $\cosh kh_s = 1.589$ and $c = 2.43$ m/s, and hence by choosing $c_s = 20$ m/s, we obtain $\epsilon = 0.0087$, which is considered to be a sufficiently low value.

The courant number is defined as

$$\sigma_x = c_s \frac{\Delta t}{\Delta x} \tag{7.43}$$

The value of σ_x has been chosen at the theoretically correct value of $\sigma_x = 1$ implying $\Delta t = 0.004$ s. The choices of c_s and σ_x result in a phase velocity of the propagating wave of 99 percent of the theoretical value.

7.6.2 Straight porous slope

As a prerequisite for the berm breakwater model developed in the two preceeding chapters, the water motion on and in a straight porous slope, 1:4, is modelled. The uprush and downrush velocities and the ratio between these depend on the permeability of the slope. For a non-porous slope, it is well known that there is an asymmetry in the velocities, the uprush velocity exceeds the downrush velocity. On a porous slope, this asymmetry will be enhanced, espescially in the parts of the profile above SWL.

The model topography is shown in Fig 7.3. The wave boundary condition is imposed on the right-hand side of the model area. In the following, for convenience, all model results from SYSTEM 3xz are related to the i-axis, cf Fig 7.3. For simplicity, the porous slope is homogeneous, ie there is no core, as it is believed that most of the porous wave damping takes place in the berm and armour layer. A vertical increment of $\Delta z = 0.02$ m is applied. For the horizontal increment, Δx is used

$$\Delta x = \Delta z \cdot \cot\alpha \tag{7.44}$$

where α is the slope angle, yielding $\Delta x=0.08$ m. For c_s, the same value as with the horizontal bottom is used, ie $c_s=20$ m/s. Δt is calculated according to eq (7.43) also in this case yielding $\Delta t=0.004$ s. For runs cot4xf, cot4xh and cot4xl, hoewever, Δt was lowered by one percent due to stability problems with the computer model. Comparing the successful part of the simulation with the full value of Δt to the simulations with the lowered Δt, no significant differences in the velocities appear.

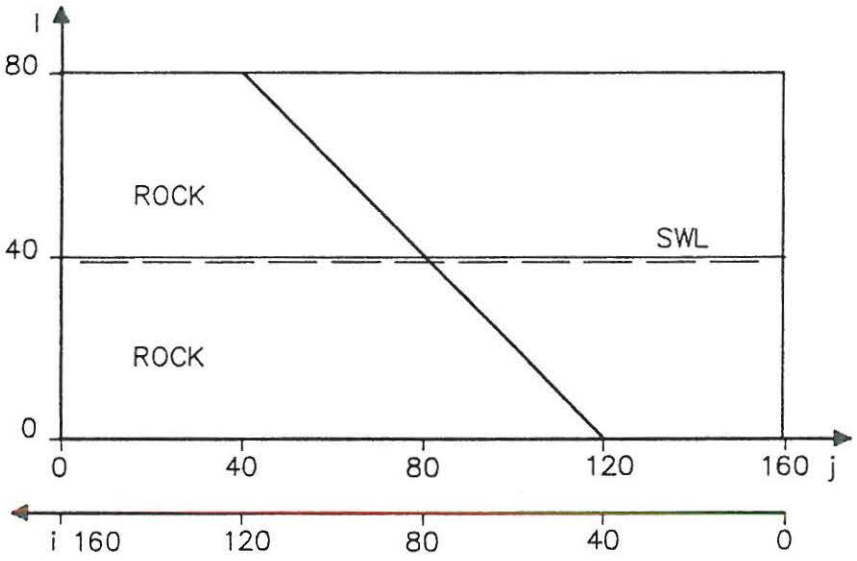

Fig 7.3 Model topography

Inside the structure, the porosity equals 0.41 in the reference case. A few simulations with other values are carried out. Above the structure the porosity equals 1.

Inside the structure, the a', b' and c-coefficients of the extended Forchheimer expression have been set according to eq (4.20), and eq (5.9) together with eq (5.78) dependent on the actual value of the porosity. For the a-coefficient, a value of $\alpha'=1000$ has been chosen for all simulations, cf Section 4.5. The values of β' and C_m are varied as shown in Table 7.1. The choices of β' are made as follows. For flow perpendicular to the stones, we have evidence that $\beta'=3$ is a characteristic value for irregular rock, cf Table 4.5. As mentioned in Section 4.5 for flow parallel to the stones, β' is likely to equal approximately half the value related to perpendicular flow, ie $\beta' \simeq 1.5$. Hence, for the combined two-dimensional flow case, a value of $\beta'=2$ may be representative. For the virtual mass coefficient, eq (5.78) with $n=0.41$ leads to $C_m=8.58$. In addition, the fitted constant of 12 in eq (5.78) is varied in order to examine the influence of possible uncertainties. A value of 10 leads to $C_m=7.40$ and a value of 14 leads to $C_m=9.76$. In all cases, the associated value of C_m^*, related to the pore velocity, is given as well by $C_m^*=n(C_m-1)$, cf eq (5.79).

Inside the structure, the E-coefficient equals 0 according to the discussion in the previous section. Outside the structure in the first 12 points, a turbulent eddy viscosity is applied and concordingly a value of 0.01 m^2/s is applied for the E-coefficient. Above these points, the viscosity of water is applied, ie E is set to $1.14 \cdot 10^{-6}$ m^2/s.

Table 7.1 Computations made with an initial slope of 1:4

Run No	Slope	n	β'	C_m	C_m^*	f_0	H_{input}	H_{ref}	T_{ref}
cot4xj	1:4	0.41	3.0	8.58	3.1	0.6	0.160	0.149	2.00
cot4xc	1:4	0.41	2.0	8.58	3.1	0.9	0.160	0.149	2.00
cot4xa	1:4	0.41	3.0	8.58	3.1	0.9	0.160	0.149	2.00
cot4xh	1:4	0.41	2.0	8.58	3.1	0.9	0.200	0.186	2.00
cot4xd	1:4	0.41	3.0	8.58	3.1	0.9	0.200	0.186	2.00
cot4xi	1:4	0.41	2.0	8.58	3.1	0.9	0.256	0.238	2.21
cot4xf	1:4	0.41	3.0	8.58	3.1	0.9	0.256	0.238	2.21
cot4xg	1:4	0.41	2.0	8.58	3.1	0.9	0.280	0.260	2.21
cot4xe	1:4	0.41	3.0	8.58	3.1	0.9	0.280	0.260	2.21
cot4xk	1:4	0.41	3.0	8.58	3.1	1.2	0.160	0.149	2.00
cot4xl	1:4	0.39	3.0	8.82	$\simeq$3.1	0.9	0.200	0.186	2.00
cot4xm	1:4	0.43	3.0	8.34	$\simeq$3.1	0.9	0.200	0.186	2.00
cot4xn	1:4	0.41	3.0	7.40	2.6	0.9	0.200	0.186	2.00
cot4xo	1:4	0.41	3.0	9.76	3.6	0.9	0.200	0.186	2.00

For all tests, the following parameters have been kept constant:

h_s = 0.80 m
D_n = 0.034 m $\Rightarrow$ d = $(6/\pi)^{1/3}$ D_n = 0.042 m
Δ = 1.68
α' = 1000
ν = $1.14 \cdot 10^{-6}$ m^2/s

The equivalent spherical diameter, d, has been applied for calculation of the porous flow resistance as well as the Shields parameter. In the computer model, the wave height at the toe of the straight slope equals approximately 93 percent of the value at the model boundary, and hence for all runs the reference wave height is chosen as 93 percent of the input wave height at the boundary.

From Table 7.1 is seen that the maximum value of the Ursell parameter, Ur, appears for runs cot4xg and cot4xe with Ur=15.4 based on H_{ref} thus slightly exceeding the limit of 15 indicating the validity of sinusoidal wave theory.

The reference wave cycle has to fulfil two requirements:

- the flow must be stationary, ie two consecutive periods must be identical
- the re-reflected wave from the model boundary must appear later than the reference wave cycle

With a travel length of 3 times 80 grid points times Δx=0.08 m and with a phase velocity of 2.43 m/s, we get for the period free of re-reflections a value of approximately 8 seconds after start of the simulations. From the velocity plot, cf Fig 7.4, it appears that wave cycle No 3 defined from the zero-crossings of the horizontal velocity composant in the section, i=74, is a suitable choice, as both the above requirements are fulfilled.

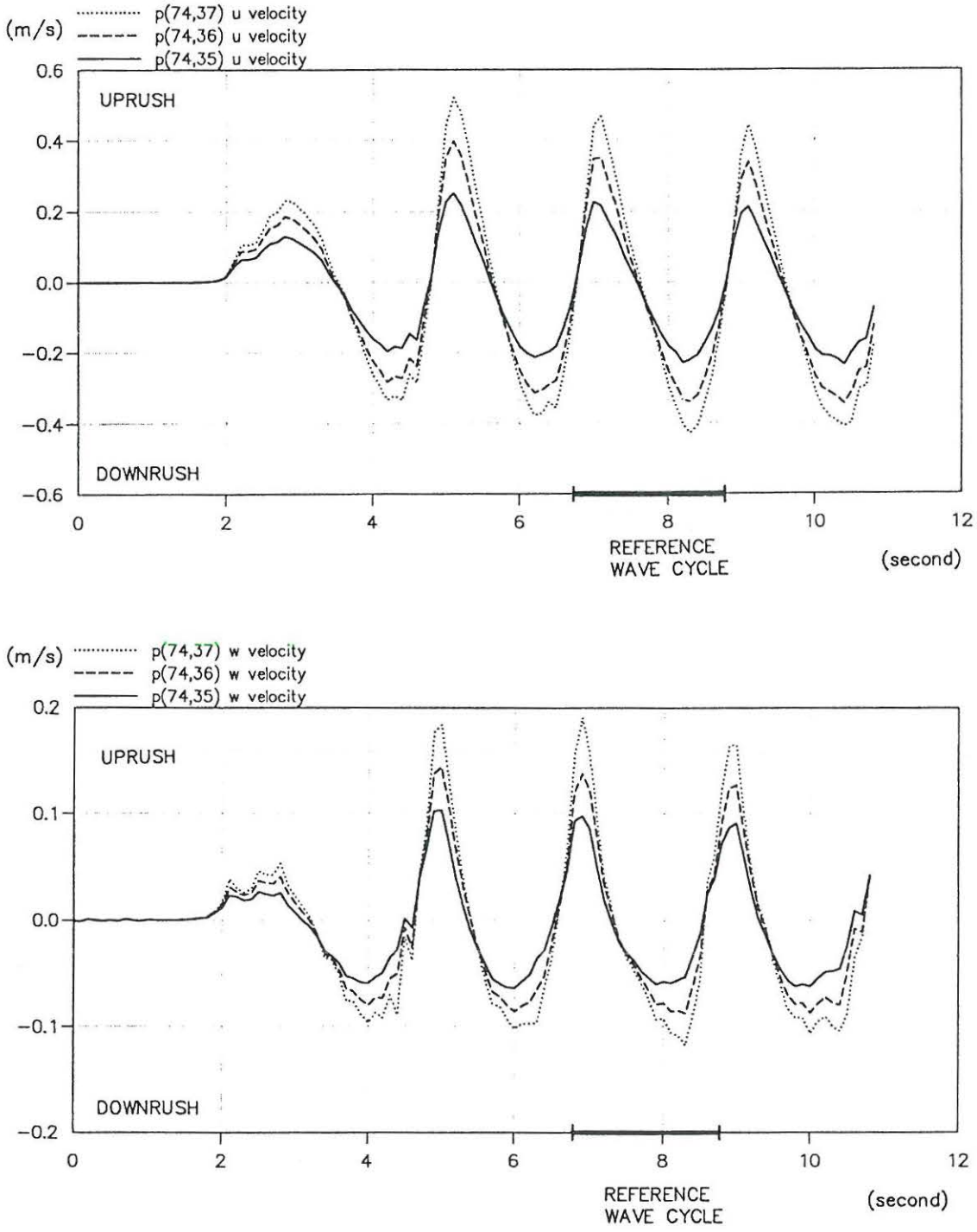

Fig 7.4 Horizontal and vertical velocity time series in Point (74,35) for run no cot4xd

In the present chapter, the maximum uprush and downrush velocities are defined as, cf Fig 7.5, see also Section 8.2.

$$\tilde{V}_{1,max} = \left(V_1 \cos(\tilde{\gamma}_1 - \alpha)\right)_{max} \quad , \quad V_1 = \sqrt{u^2 + w^2} \tag{7.45}$$

$$\tilde{V}_{2,max} = \left(V_2 \left|\cos(\tilde{\gamma}_2 - \alpha)\right|\right)_{max} \quad , \quad V_2 = \sqrt{u^2 + w^2} \tag{7.46}$$

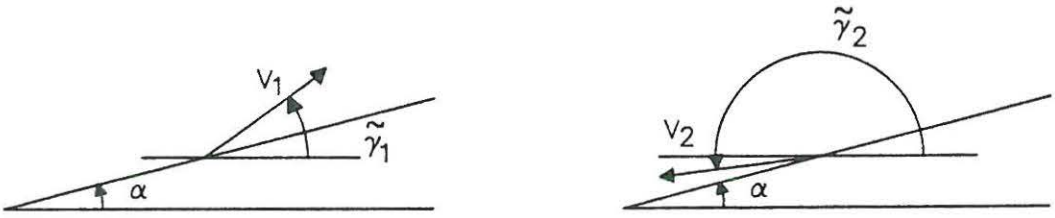

Fig 7.5 Definitions of α and $\tilde{\gamma}$ for uprush and downrush respectively

For a given location, a smoothing of the u and w composants is carried out over five points all located on an inclined line with the same height above the slope. The central point is weighted with a coefficient of 3/9, each of the two neighbouring points with 2/9, and finally 1/9 is applied to the two outermost points.

Table 7.2 shows the simulated maximum parallel velocities and the ratio between these for the first six points above the slope in the section corresponding to the velocity measurements by Tørum (1992b), cf below. Point (74,36) in the numerical model corresponds to Point 22 concerning the measurements. Point (74,35) is located immediately above the slope and Point (74,40) is located at SWL. Fig 7.6 shows the simulated profiles of $\tilde{V}_{1,max}$ and $\tilde{V}_{2,max}$ located two points above the slope. In Fig 7.7 are shown the profiles of the associated $\tilde{\gamma}_1$ and $\tilde{\gamma}_2$ which, for the present purpose only, are smoothed over five points.

Tørum (1992b) has measured the maximum uprush and downrush velocities on a reshaped berm breakwater profile with the following data: $D_{n50}=0.034$ m and $h_s=0.79$ m. The measuring section chosen corresponds to a local water depth of approximately 0.12 m, cf Fig 7.8. According to Tørum (1992b), Point 22 located 0.08 m below SWL, is believed to be outside the boundary layer, and hence it is chosen as a reference point. In the measuring section, the slope equals approximately 1:4. The results are shown in Fig 7.9 and Table 7.3.

From Table 7.2 concerning Point (74,36) and Table 7.3 is seen that the simulated values of $\tilde{V}_{1,max}$ and $\tilde{V}_{2,max}$ are too small as compared to the measurements in the order of three times lower due to the discretisation. It is likely that this discrepancy is due to the stepped surface of the slope in the model due to the discretisation, which makes it difficult to simulate the velocities correctly in this area. This is also indicated by the increasing velocities further away from the surface of the slope. Concerning the ratio between the maximum velocities, it is seen that $\tilde{V}_{1,max}/\tilde{V}_{2,max}$ does not depend significantly on H and T neither in model nor measurements. On average, the simulated values of $\tilde{V}_{1,max}/\tilde{V}_{2,max}$ are eleven percent lower than the measured values, considering the measuring point.

Table 7.2 Simulated maximum parallel velocities

Run No	Point (74,35)			Point (74,36)			Point (74,37)		
	$\tilde{V}_{1,max}$	$\tilde{V}_{2,max}$	$\tilde{V}_{1,max}/\tilde{V}_{2,max}$	$\tilde{V}_{1,max}$	$\tilde{V}_{2,max}$	$\tilde{V}_{1,max}/\tilde{V}_{2,max}$	$\tilde{V}_{1,max}$	$\tilde{V}_{2,max}$	$\tilde{V}_{1,max}/\tilde{V}_{2,max}$
cot4xj	0.22	0.20	1.09	0.34	0.29	1.18	0.44	0.35	1.26
cot4xc	0.22	0.19	1.13	0.33	0.27	1.23	0.43	0.32	1.35
cot4xa	0.22	0.19	1.13	0.33	0.28	1.21	0.43	0.33	1.30
cot4xh	0.26	0.21	1.20	0.40	0.31	1.28	0.56	0.38	1.36
cot4xd	0.23	0.22	1.05	0.37	0.33	1.11	0.48	0.41	1.17
cot4xi	0.29	0.27	1.08	0.46	0.41	1.12	0.59	0.51	1.18
cot4xf	0.29	0.27	1.10	0.46	0.39	1.18	0.60	0.47	1.28
cot4xg	0.31	0.27	1.12	0.49	0.41	1.18	0.63	0.51	1.24
cot4xe	0.30	0.28	1.08	0.49	0.44	1.14	0.65	0.55	1.18
cot4xk	0.20	0.18	1.09	0.31	0.27	1.15	0.40	0.33	1.20
cot4xl	0.25	0.22	1.18	0.40	0.33	1.22	0.52	0.42	1.25
cot4xm	0.25	0.21	1.14	0.38	0.31	1.21	0.50	0.38	1.31
cot4xn	0.25	0.21	1.18	0.39	0.31	1.28	0.52	0.38	1.38
cot4xo	0.24	0.22	1.11	0.38	0.32	1.20	0.50	0.39	1.30

Run No	Point (74,38)			Point (74,39)			Point (74,40)		
	$\tilde{V}_{1,max}$	$\tilde{V}_{2,max}$	$\tilde{V}_{1,max}/\tilde{V}_{2,max}$	$\tilde{V}_{1,max}$	$\tilde{V}_{2,max}$	$\tilde{V}_{1,max}/\tilde{V}_{2,max}$	$\tilde{V}_{1,max}$	$\tilde{V}_{2,max}$	$\tilde{V}_{1,max}/\tilde{V}_{2,max}$
cot4xj	0.52	0.38	1.37	0.59	0.33	1.77	0.66	0.28	2.39
cot4xc	0.51	0.37	1.39	0.58	0.33	1.77	0.63	0.23	2.76
cot4xa	0.52	0.37	1.39	0.61	0.33	1.86	0.66	0.22	2.98
cot4xh	0.62	0.43	1.45	0.72	0.38	1.91	0.80	0.27	3.00
cot4xd	0.58	0.44	1.31	0.68	0.45	1.49	0.76	0.26	2.94
cot4xi	0.71	0.60	1.19	0.85	0.53	1.61	0.94	0.40	2.37
cot4xf	0.72	0.52	1.39	0.83	0.49	1.71	0.95	0.39	2.40
cot4xg	0.76	0.59	1.27	0.87	0.52	1.69	0.98	0.45	2.19
cot4xe	0.79	0.63	1.25	0.93	0.66	1.41	1.06	0.66	1.61
cot4xk	0.47	0.37	1.29	0.55	0.35	1.58	0.60	0.21	2.83
cot4xl	0.62	0.48	1.31	0.74	0.50	1.48	0.84	0.34	2.50
cot4xm	0.60	0.49	1.24	0.69	0.37	1.88	0.77	0.25	3.10
cot4xn	0.62	0.46	1.35	0.74	0.37	1.99	0.82	0.24	3.35
cot4xo	0.61	0.47	1.29	0.72	0.43	1.70	0.80	0.32	2.54

In order to counteract the too low velocities, uprush as well as downrush, an artificially high value of the friction factor, f_o, is applied, cf eq (7.24). In Section 9.3 is found that $f_o=0.9$ together with a realistic value of the critical Shields parameter, Θ_c, conform to observed initiation of armour stone movements applying a static stability criterion. According to Section 7.3, it is to be expected that the physically correct friction factor is in the order of 0.1 to 0.2. Hence, the value of $f_o=0.9$ is equivalent to an increase in the velocities with a factor of 2 to 3, cf eq (7.9) which approximately corresponds to the discrepancy between the simulated and measured velocities. It should be noticed that $f_o=0.9$ is applied in SYSTEM 3xz as well as the preceeding model describing the reshaping of berm breakwaters.

It is possible that the lack of wave breaking in the numerical model may affect the ratio between the uprush and downruch velocities. This may possibly hinder a correct description of the variation of the ratio between the velocities with the water depth, as the impact of lowering the water depth, which is equivalent to increasing the Ursell parameter, is an increase in the ratio between the uprush and downrush velocities, in the case of a plane and impervious bottom. When waves are breaking on a slope, this ratio is likely to be altered by the wave breaking.

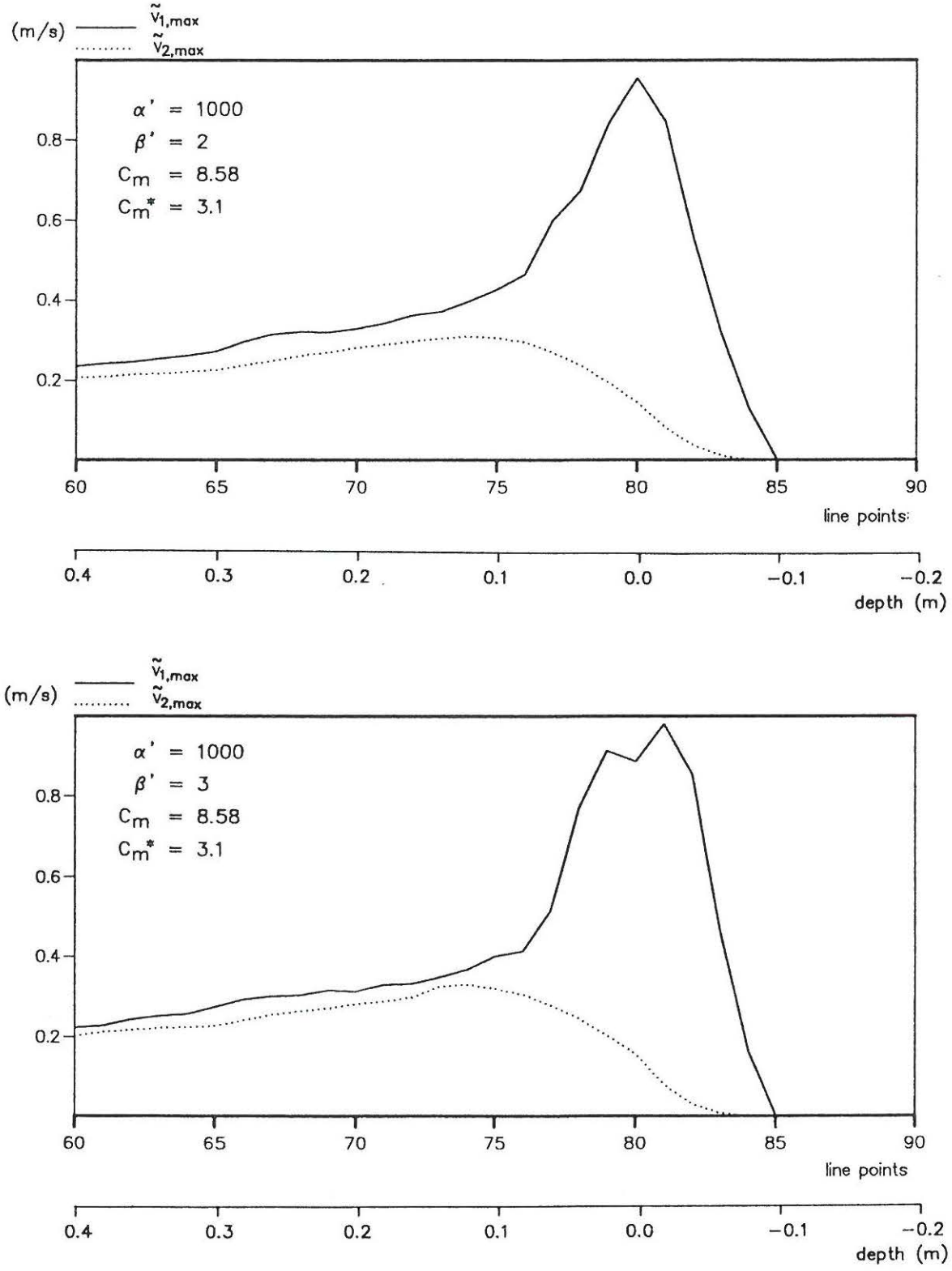

Fig 7.6 Simulated $\tilde{V}_{1,max}$ and $\tilde{V}_{2,max}$ two points above the slope for runs nos cot4xh and cot4xd

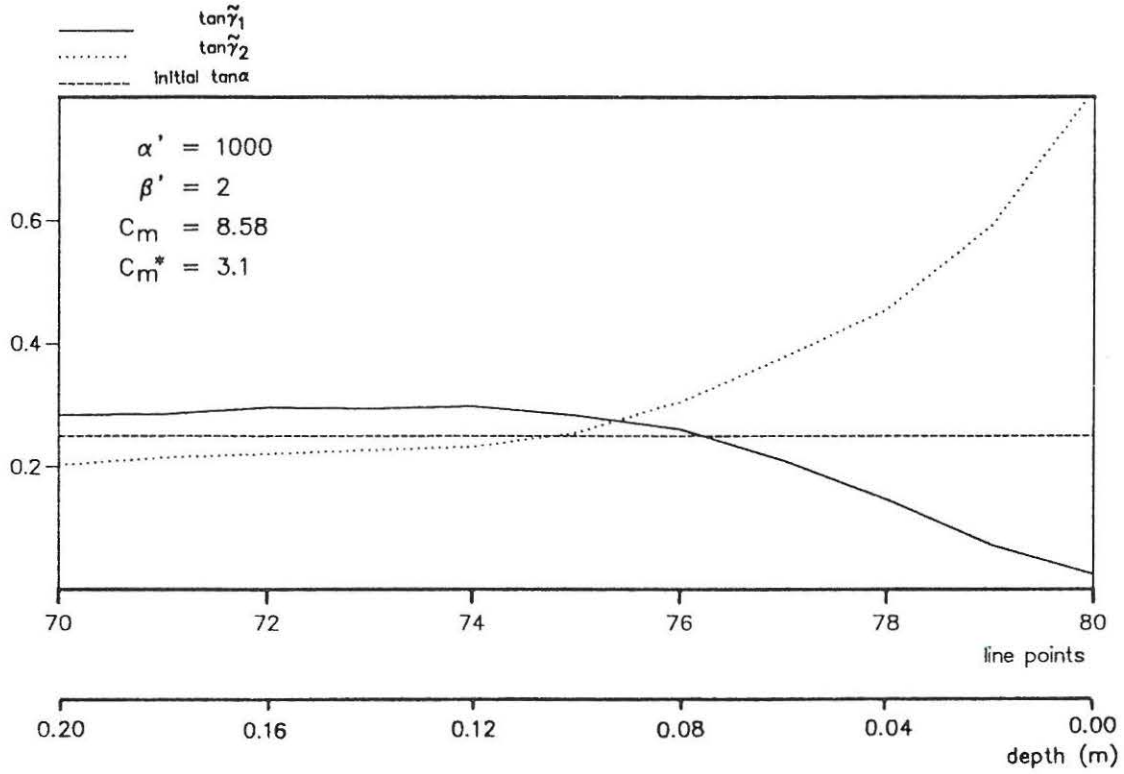

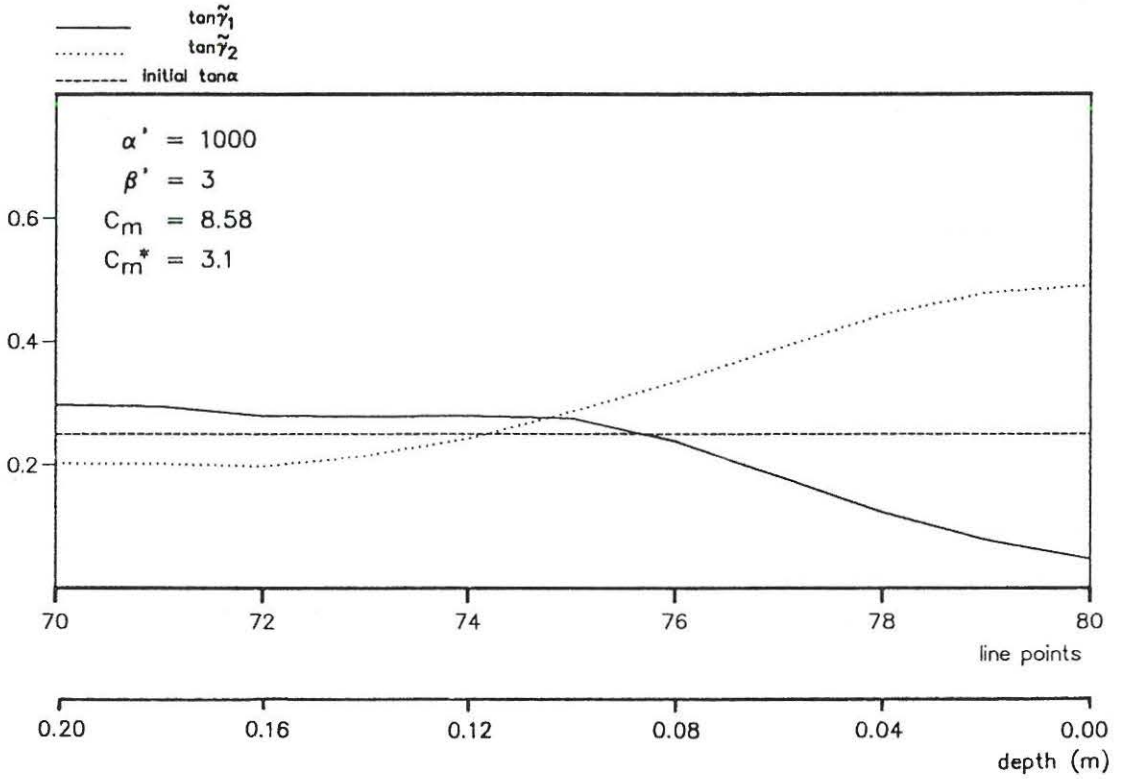

Fig 7.7 Simulated $tan\tilde{\gamma}_1$ and $tan\tilde{\gamma}_2$ two points above the slope for runs nos cot4xh and cot4xd

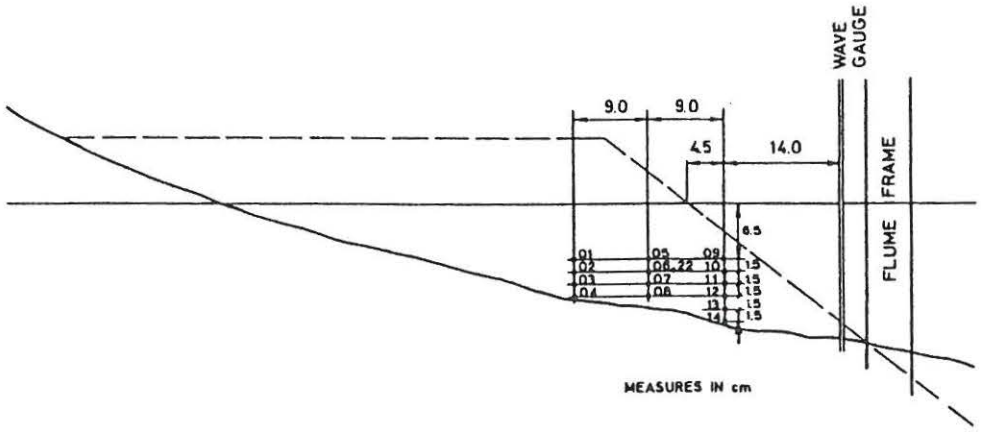

Fig 7.8 Berm breakwater profile and measuring section. From Tørum (1992b).

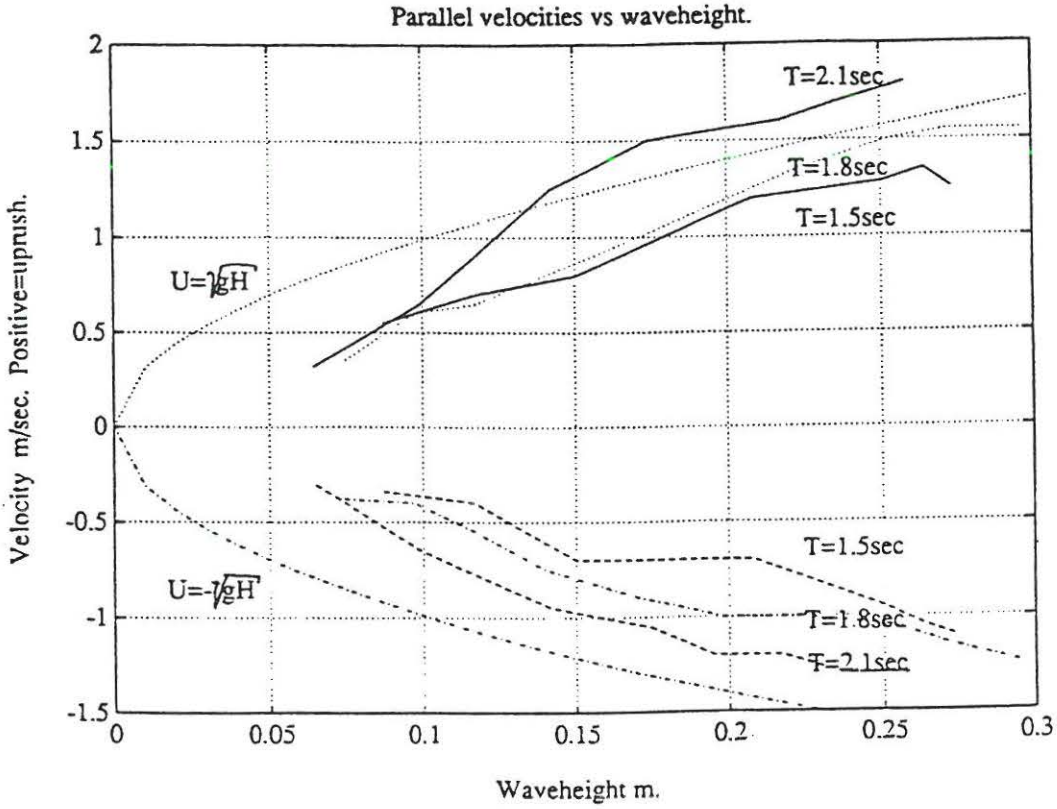

Fig 7.9 Mean maximum parallel velocities in measurement Point 22 for different wave periods and wave heights. From Tørum (1992b).

Table 7.3 Mean maximum parallel velocities in measurement Point 22 for different wave periods and wave heights. Obtained from Fig 7.7.

T	H	$\tilde{V}_{1,max}$	$\tilde{V}_{2,max}$	$\tilde{V}_{1,max}/\tilde{V}_{2,max}$
1.5	0.10	0.61	0.36	1.69
	0.15	0.79	0.69	1.14
	0.20	1.14	0.69	1.65
	0.25	1.27	0.95	1.34
1.8	0.10	0.61	0.42	1.45
	0.15	0.86	0.80	1.08
	0.20	1.19	0.99	1.20
	0.25	1.50	1.05	1.43
2.1	0.10	0.67	0.67	1.00
	0.15	1.31	0.97	1.35
	0.20	1.56	1.20	1.30
	0.25	1.77	1.29	1.37

On average, $\tilde{V}_{1,max}/\tilde{V}_{2,max}$ equals 1.33.

8 ARMOUR DYNAMICS

In this chapter, the microscopic description of the forces acting on a single stone is transformed into armour averaged expressions. The influence of gravity, as it appears on a breakwater slope, is deduced. The theory is formulated in terms of the Shields parameter in order to utilise the results obtained within the description of bed load transport of sand and coarse granular materials. As the Shields parameter is defined from a drag/lift model, this parameter is applicable to berm breakwaters, but not to conventional breakwaters, where inertia forces on the armour stones become important, due to the larger stone size, in which case a description based on the Morison equation is more relevant. A static solution to the equilibrium slope and two slightly different dynamic solutions are established. The dynamic solutions are based on a force balance taking the moving stones into account, appearing beyond the statically stable conditions. The transition between the static and dynamic solutions is discussed. Finally, the matching of the equilibrium profile to the initial profile is deduced.

8.1 Phenomenology

One of the special features concerning berm breakwaters is that a certain movement of the armour stones is allowed in the design condition. An S-shaped profile develops with a steep lower slope approaching the angle of repose, a middle slope with armour stones moving forth and back for sufficiently intense wave attack and an upper slope, cf Fig 8.1. When stones are moving on the middle slope of a berm breakwater, the type of motion can be characterised as rolling-sliding, the stones dominantly being in contact with the surface of the breakwater or the bed, but also jumping appears.

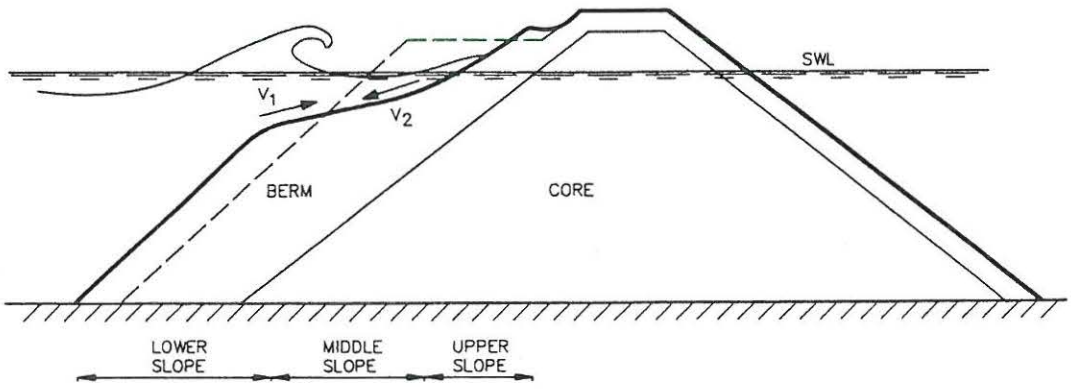

Fig 8.1 Typical developed berm breakwater profile

8.2 Static Solution

For a single stone placed on a horizontal bed exposed to a horizontally oscillating velocity in the critical condition just before rolling-sliding, the static force balance, written as a Morison type of equation, reads

$$F_{DC} - \mu_s (W_s - F_{LC}) + F_{IC} = 0 \qquad (8.1)$$

where

F_{DC} is the drag force
F_{LC} is the lift force
F_{IC} is the inertia force
W_s is the submerged weight
μ_s is the static friction coefficient

Tørum (1992b) measured the forces acting on a single stone on a berm breakwater. One of the conclusions was that the inertia term is small compared to the drag term, and hence the inertia term is neglected as an approximation. The ratio between the drag and inertia forces can be calculated as

$$\frac{F_{DC}}{F_{IC}} = \frac{C_D \frac{1}{2} \rho \frac{\pi}{4} d^2}{C_M \rho \frac{\pi}{6} d^3} \frac{V_c^2}{\frac{\partial V_c}{\partial t}} = \frac{3}{4} \frac{C_D}{C_M} \frac{KC}{2\pi} \tag{8.2}$$

where the Keulegan-Carpenter number, KC, is defined as

$$KC = \frac{V_c T}{d} \tag{8.3}$$

where d is the equivalent spherical diameter.

In the measurements and analyses of Tørum, however, the nominal diameter equal to 0.034 m was used as reference. With $V_c \sim 1$ m/s and $T \sim 2$ s, we get $KC \sim 60$ for the surface flow. For the slope parallel forces, Tørum found as characteristic values $C_D = 0.35$ and $C_M = 0.2$ leading to $F_{DC}/F_{IC} \sim 12$.

The remaining terms are rearranged, the coefficients C_D and C_L are the drag and lift coefficients respectively, μ_s is the static friction coefficient, and V_c is the critical velocity parallel to the bed:

$$F_{DC} - \mu_s (W_s - F_{LC}) = 0 \tag{8.4a}$$

$$F_{DC} + \mu_s F_{LC} = \mu_s W_s \tag{8.4b}$$

$$\frac{1}{2} \rho (C_D + \mu_s C_L) \frac{\pi}{4} d^2 V_c^2 = \mu_s W_s \tag{8.4c}$$

According to Tørum (1992b) for a berm breakwater, there may also be a drag force component associated with the slope normal velocity. For the case of a horizontal bed with a non-horizontal velocity, eq (8.4) is extended to

$$\frac{1}{2}\rho\left(C_D+\mu_s C_L\right)\frac{\pi}{4}d^2V_C^2 \pm \frac{1}{2}\rho\,\mu_s C_{DN}\frac{\pi}{4}d^2V_{CN}^2 = \mu_s W_s \qquad (8.5)$$

where C_{DN} and V_{CN} refer to the normal drag coefficient and critical velocity respectively. The term on the right-hand side is positive for flow out of the bed and negative for flow into the bed.

According to Tørum (1992b), the proposed model only gives little consistency with respect to the slope normal forces.

For the case of outflow, one could expect that an expression of the type

$$\frac{1}{2}\rho C_{DT}\frac{\pi}{4}d^2\left(V_C + V_{CN}\right)^2 = \mu_s W_s \qquad (8.6)$$

ie a drag model based on the entire speed of the outflowing water would be relevant, however, the direction of the force is not known.

Actually, eq (8.6) conforms to the measurements by Thompson and Burcharth (1984) who examined the stability of rock and dolosse armour layers with different slope angles, α, and different angles, $(\gamma-\alpha)$, between the slope and the stationary outflow, cf Fig 8.2. It appeared that the failure conditions, related to the total speed of the outflowing water, were not related to $(\gamma-\alpha)$, thus supporting the validity of eq (8.6).

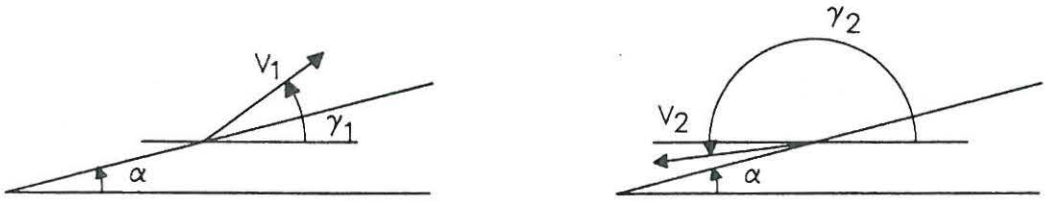

Fig 8.2 Definition of α and γ for uprush and downrush respectively.

Sandström (1974) measured the wave forces on individual spheres placed on a slope exposed to regular waves. The results were presented as force hodographs, cf Fig 8.3.

Similar tests with irregular waves on horizontal cylinders on a slope were carried out by Jensen and Juhl (1988), see also Juhl and Jensen (1990).

The preceeding considerations indicate that in general the best drag model for outflow conditions is related to the maximum total speed squared appearing within a wave cycle

$$F_D \sim V_{max}^2 \qquad (8.7)$$

and for inflow conditions the maximum projected total speed squared

$$F_D \sim \left(V^2\cos(\gamma-\alpha)\right)_{max} \qquad (8.8)$$

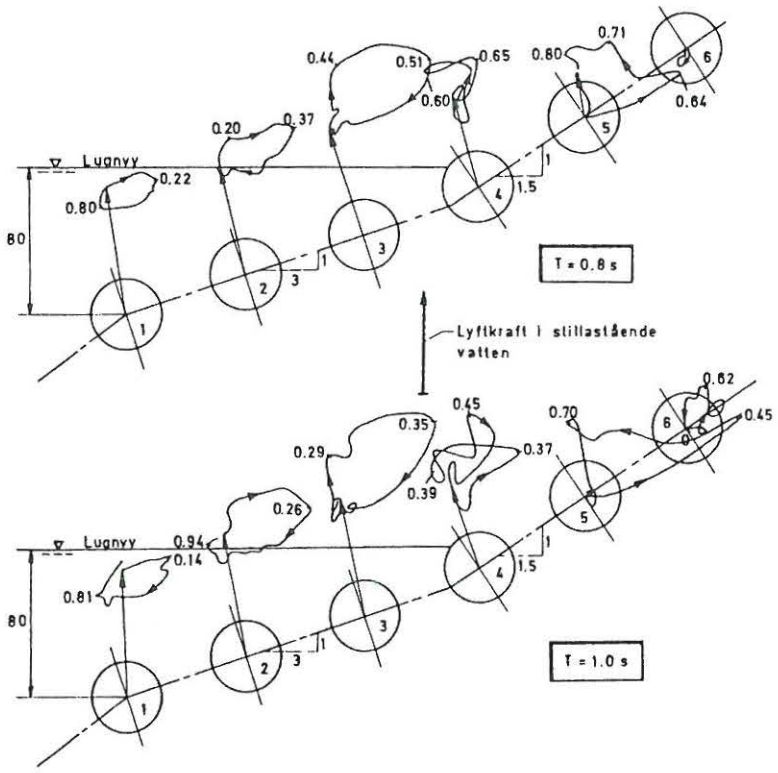

Fig 8.3 Force hodographs, from Sandström (1974).

For the present purpose, however, it is chosen to apply eq (8.8) for both the outflow and inflow cases in order to have consistency with the dynamic solutions based on a slope parallel force balance, cf Sections 8.3 and 8.4. Hence, the maximum uprush and downrush velocities within a wave cycle and at any position along the slope are defined by, cf Fig 8.2

$$V_{1,max}^2 = \left(V_1^2 \cos(\gamma_1 - \alpha) \right)_{max} \quad , \quad V_1^2 = u^2 + w^2 \tag{8.9}$$

$$V_{2,max}^2 = \left(V_2^2 \mid \cos(\gamma_2 - \alpha) \mid \right)_{max} \quad , \quad V_2^2 = u^2 + w^2 \tag{8.10}$$

In eq (8.4c), the left-hand side represents the agitating forces and the right-hand side represents the stabilising forces. This equation corresponds to the wellknown Shields criterion, Shields (1936), relating the agitating forces on the stones to the bed shear stress. The Shields parameter, Θ, is defined as the ratio between the agitating and stabilising forces:

$$\theta = \frac{\tau_b d^2}{\Delta \rho g d^3} = \frac{\tau_b}{\Delta \rho g d} \tag{8.11}$$

$$\Delta = \frac{\rho_a}{\rho} - 1 \tag{8.12}$$

From experiments a threshold value, the critical Shields parameter, Θ_c, has been found as a function of the Grain Reynolds number, Re^*, cf Fig 8.4. Re^* is defined as

$$Re^* = \frac{U_f d}{\nu} \tag{8.13}$$

where the friction velocity, U_f, is defined from

$$\tau_b = \rho U_f^2 \tag{8.14}$$

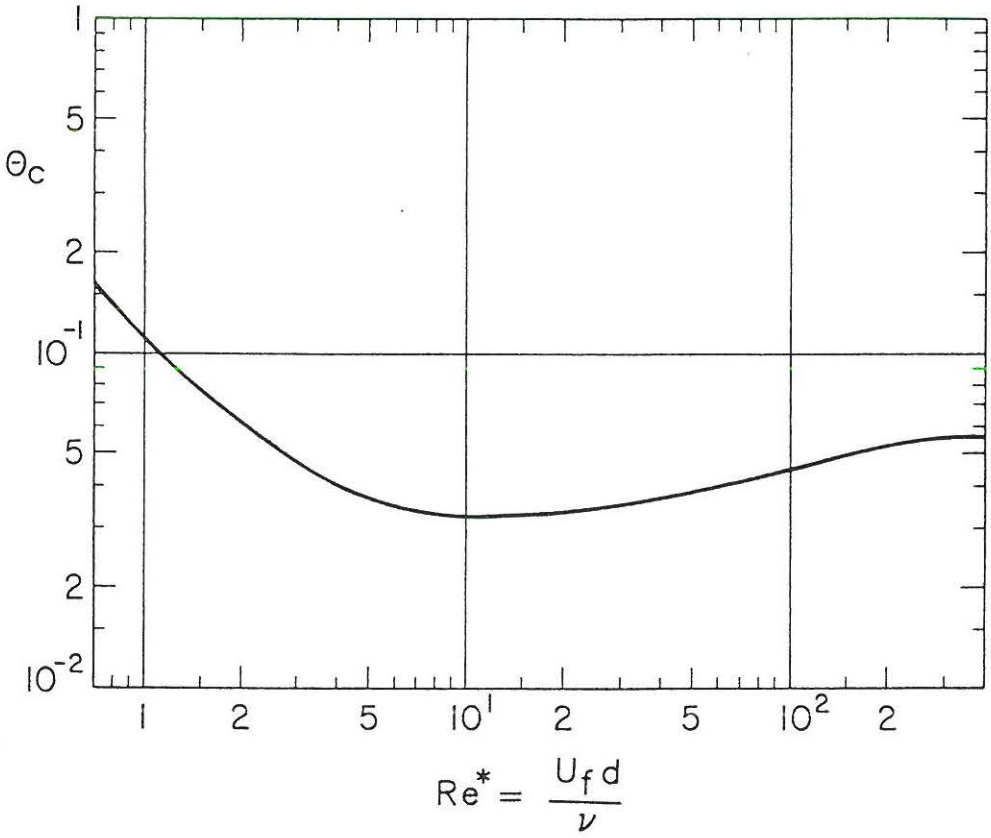

Fig 8.4 Critical Shields parameter vs Grain Reynolds number. From Madsen and Grant (1976)

Inserting the threshold value, eq (8.11) can be written in the form

$$\tau_{bc} d^2 = \theta_c \, \Delta \rho g d^3 \tag{8.15}$$

which actually conforms to eq (8.4c), as $\tau_{bc} \sim \rho V_c^2$ (8.16)

The static Shields criterion has traditionally been applied to sand and to channel revetments made of riprap. As shown by Madsen and Grant (1975) and Komar and Miller (1974), the critical Shields parameter also applies to the case of wave motion, if the maximum bed shear stress is calculated according to Jonsson (1976), cf Section 7.3.

As pointed out in Section 7.3, the maximum bed shear stress may include inertia forces as well as drag forces, although the coefficient, f_w, is defined on the squares of the velocity.

As to the value of Θ_c for the breakwater case, only the values valid for high Reynolds numbers are relevant. Further, it is necessary to distinguish between the values of Θ_c relevant for initiation of sediment transport and the values of Θ_c relevant for description of static stability. The former are related to an instantaneous condition implying that always some grains will be moving. The cumulative damage after eg 1000 waves is large. For the case of static stability, the value of Θ_c is associated with a certain value of the cumulative damage, lower than at initiation of sediment transport. These aspects are reflected in Table 8.1 showing characteristic values of Θ_c. The experiments by Burcharth and Thompson (1982) were carried out with rock and dolosse.

Table 8.1 Characteristic values of Θ_c

Description	Θ_c	Data source
Onset of rocking, oscillatory motion	0.017	B
Stability of rockfill, steady current	0.03	C
A few displacements, oscillatory motion	0.034	B
Stability of riprap channel revetments	0.04	SPM
Initiation of sediment transport, steady current	0.045	E
Initiation of sediment transport, oscillatory motion	0.047	S

Legend: *B: Burcharth and Thompson (1982), C: CIRIA/CUR (1991),*
E: Engelund (1975), S: Sleath (1978), SPM: Shore Protection Manual (1984).

It should be noted that Θ can be approximately related to the stability number, $H/\Delta D$, and the surf similarity parameter (Iribarren number), ξ_o, which are usually applied within the description of breakwaters. Eqs (8.11) and (7.9) lead to

$$\theta = \frac{\tau_b}{\Delta \rho g d} = \frac{\frac{1}{2} f_w V^2}{\Delta g d} \sim \frac{\frac{1}{2} f_w V^2}{\Delta g D_n} \tag{8.17}$$

Eq (6.16) valid for a relatively flat slope and eq (6.18) yield

$$\frac{1}{2} V^2 \sim g R_u \sim g \xi_o H \tag{8.18}$$

Eqs (8.17) and (8.18) together lead to

$$\theta \sim f_w \xi_o \frac{H}{\Delta D_n} \tag{8.19}$$

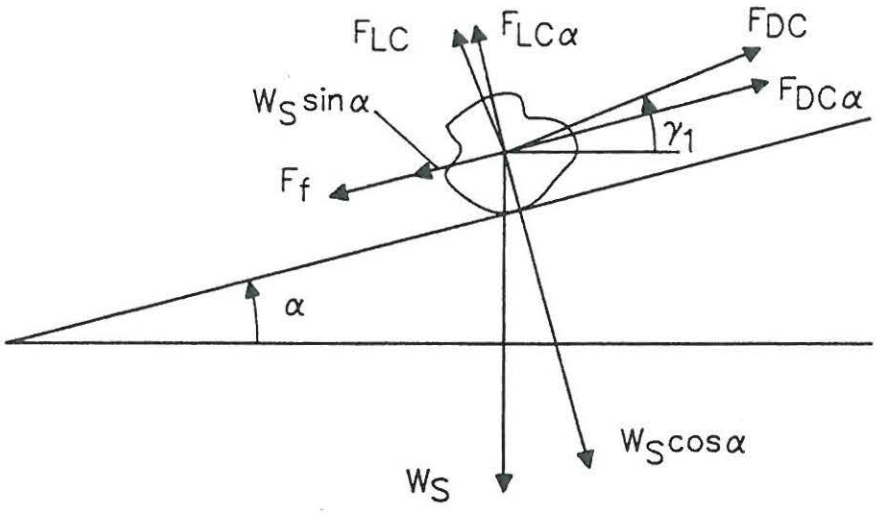

Fig 8.5 Forces acting on a single stone

Considering now an infinitesimal element of the sloping breakwater surface, the static force balance for a single stone under uprush conditions reads, cf Fig 8.5, where F_f denotes the friction force leading to the third term of eq (8.20a):

$$F_{DC\alpha} - W_s \sin\alpha - \mu_s (W_s \cos\alpha - F_{LC\alpha}) = 0 \tag{8.20a}$$

$$F_{DC\alpha} + \mu_s F_{LC\alpha} = W_s \sin\alpha + \mu_s W_s \cos\alpha \tag{8.20b}$$

$$\frac{1}{2} \rho \left(C_D + \mu_s C_L\right) \frac{\pi}{4} d^2 V_{c\alpha 1}^2 = W_s \left(\mu_s \cos\alpha + \sin\alpha\right) \tag{8.20c}$$

where $V^2_{c\alpha 1} \sim V^2 \cos(\gamma_1 - \alpha)$ is found according to eq (8.9). As can be seen from Fig 8.5, F_{DC} contributes to a slope normal drag force component $\sim V^2 \sin(\gamma_1 - \alpha)$ and F_{LC} contributes to a slope parallel force $\sim V^2 \sin(\gamma_1 - \alpha)$. For simplicity, these terms are omitted. Further, the direction of the buoyancy force is orthogonal to the streamlines. For simplicity, the buoyancy force is approximated as a vertical force, which together with the stone weight gives the submerged stone weight, W_s.

Eqs (8.4c) and (8.20c) yield:

$$\frac{\theta_{c\alpha 1}}{\theta_c} = \frac{\tau_{bc\alpha 1}}{\tau_{bc}} = \frac{V_{c\alpha 1}^2}{V_c^2} = \cos\alpha + \frac{1}{\mu_s} \sin\alpha \tag{8.21}$$

Similarly, for downrush conditions we get:

$$- F_{DC\alpha} - W_s \sin\alpha + \mu_s \left(W_s \cos\alpha - F_{LC\alpha}\right) = 0 \tag{8.22a}$$

$$- \left(F_{DC\alpha} + \mu_s F_{LC\alpha}\right) = W_s \sin\alpha - \mu_s W_s \cos\alpha \tag{8.22b}$$

$$\frac{1}{2}\rho \left(C_D + \mu_s C_L\right) \frac{\pi}{4} d^2 V_{c\alpha 2}^2 = W_s \left(\mu_s \cos\alpha - \sin\alpha\right) \tag{8.22c}$$

where $V^2_{c\alpha 2} \sim V^2 |\cos(\gamma_2 - \alpha)|$ is found according to eq (8.10).

Eqs (8.4c) and (8.22c) yield:

$$\frac{\theta_{c\alpha 2}}{\theta_c} = \frac{\tau_{bc\alpha 2}}{\tau_{bc}} = \frac{V_{c\alpha 2}^2}{V_c^2} = \cos\alpha - \frac{1}{\mu_s} \sin\alpha \tag{8.23}$$

Eqs (8.21) and (8.23), which are both applied in the proceeding sections concerning the dynamic solutions, imply that the threshold conditions depend on the actual slope angle.

A static solution related to the downrush can be found from eq (8.23) by demanding $\Theta_2 = \Theta_{c\alpha 2}$, ie

$$\frac{\theta_2}{\theta_c} = \cos\alpha_s - \frac{1}{\mu_s} \sin\alpha_s \tag{8.24}$$

which leads to the following iterative expression in the static slope angle, α_s

$$\tan\alpha_s = \mu_s \left(1 - \frac{\theta_2/\theta_c}{\cos\alpha_s}\right) \tag{8.25}$$

A special case is found on top of the upper slope:

$$\tan\alpha_s = \mu_s \quad \text{for} \quad \theta_2 = 0 \tag{8.26}$$

As representative wave height and period, it is chosen to apply as reference values

$$H_{ref} = H_{m0} \simeq H_s \tag{8.27}$$

$$T_{ref} = T_{02} \simeq T_m \tag{8.28}$$

It should be noticed that the present solution is an equilibrium solution which formally corresponds to exposure of a large number of waves.

8.3 Dynamic Solution-1

In the static case, the shear stresses in the water column are transferred to the surfaces of the grains fixed in the bed. In the dynamic case, as shown by Engelund (1975) for stationary current, part of the shear stresses in the water column are transferred as intergranular contact stresses, when moving stones encounter fixed stones.

The fraction of displaced particles in a single layer is defined as

$$p = \frac{N_{disp}}{N} \tag{8.29}$$

where N_{disp} is the number of displaced particles and N is the total number of surface particles within the area, A. For a distinct plane layer of rock, N is found as the solid part of the surface area divided by the projected area of a single stone, and hence N/A depends on the porosity, n

$$\frac{N}{A} \sim \frac{1}{d^2}(1-n) \tag{8.30}$$

For a distorted surface like on a developed berm breakwater profile, the dependence on the porosity is not so obvious, and hence it is omitted for simplicity

$$\frac{N}{A} \sim \frac{1}{d^2} \tag{8.31}$$

Eqs (8.29) and (8.31) together yield

$$p = \frac{N_{disp}\, d^2}{A} \tag{8.32}$$

or

$$\frac{N_{disp}}{A} = \frac{p}{d^2} \tag{8.33}$$

The force, F, arising from the moving water equals a static part acting on the fixed grains and a dynamic part acting on the displaced particles.

$$F - \mu_s (W_s - F_{LC}) - pN\mu_d W_s = 0 \tag{8.34}$$

$$F - F_{DC} - pN\mu_d W_s = 0 \tag{8.35}$$

μ_s and μ_d are the static and dynamic friction coefficients respectively.

Dividing by the reference area, A, we get by use of eq (8.31)

$$\tau - \tau_c - p\mu_d \frac{1}{d^2} W_s = 0 \tag{8.36}$$

Dividing by $\Delta\rho gd$, this leads to

$$\theta - \theta_c - \frac{\pi}{6} p\mu_d = 0 \tag{8.37}$$

For coarse sand in stationary current, Engelund (1975) applied Θ_c=0.045 and found μ_d=0.65, cf the full drawn curve in Fig 8.6. There is a good agreement with the experiments by Luque, which were all carried out with flat bed. In the experiments, Θ is ranging from approximately Θ_c to $2\Theta_c$, which is an interval relevant to berm breakwaters when the appropriate value of Θ_c is applied, cf Table 8.1 and Section 9.3. The value of μ_d for rock relevant to the present study is found by calibration, cf Sections 9.4 and 9.5.

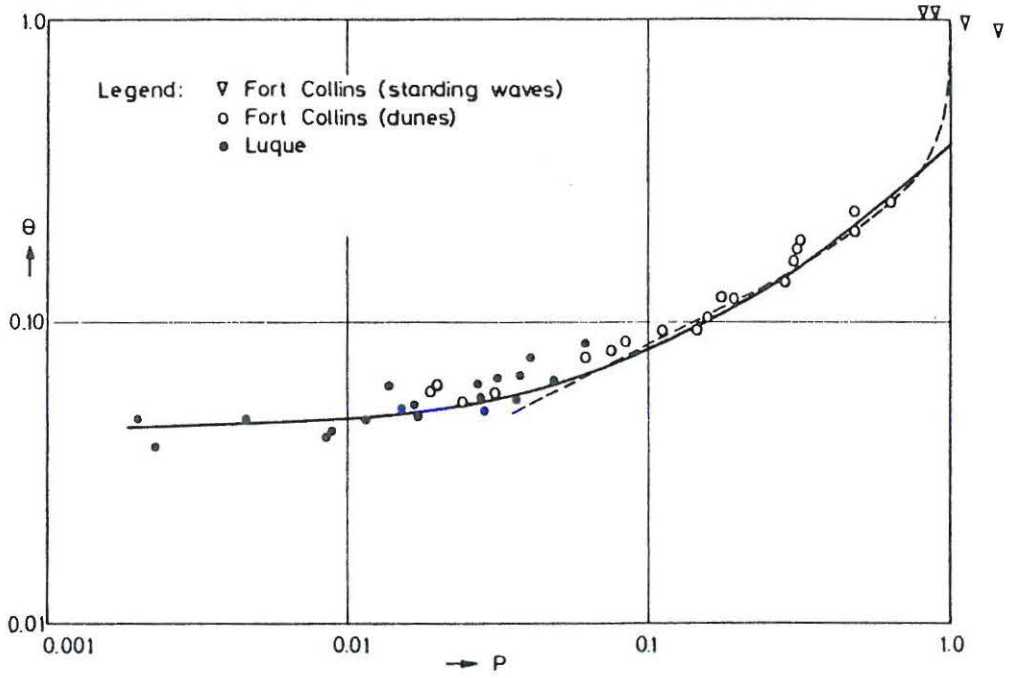

Fig 8.6 p vs Θ. From Engelund (1975)

Like with the static case, the dynamic case can be adapted to a sloping breakwater surface. The uprush case reads

$$F - W_s \sin\alpha - \mu_s\left(W_s \cos\alpha - F_{LC}\right) - p_1 N\left(\mu_d W_s \cos\alpha + W_s \sin\alpha\right) = 0 \tag{8.38a}$$

$$F - F_{DC\alpha} - p_1 N W_s \left(\mu_d \cos\alpha + \sin\alpha\right) = 0 \tag{8.38b}$$

$$\theta_1 - \theta_{c\alpha 1} - \frac{\pi}{6} p_1 \left(\mu_d \cos\alpha + \sin\alpha\right) = 0 \tag{8.38c}$$

which can also be written as

$$p_1 = \frac{\frac{6}{\pi}(\theta_1 - \theta_{c\alpha 1})}{\mu_d \cos\alpha + \sin\alpha} \tag{8.39}$$

Inserting eq (8.21) yields

$$p_1 = \frac{6}{\pi\mu_d} \frac{\theta_1 - \theta_c \left(\cos\alpha + \frac{1}{\mu_s}\sin\alpha\right)}{\cos\alpha + \frac{1}{\mu_d}\sin\alpha} \tag{8.40}$$

For downrush we get

$$-F - W_s\sin\alpha + \mu_s(W_s\cos\alpha - F_{LC\alpha}) + p_2 N(\mu_d W_s\cos\alpha - W_s\sin\alpha) = 0 \tag{8.41a}$$

$$-(F - F_{DC\alpha}) + p_2 N W_s(\mu_d\cos\alpha - \sin\alpha) = 0 \tag{8.41b}$$

$$\theta_2 - \theta_{c\alpha 2} - \frac{\pi}{6} p_2(\mu_d\cos\alpha - \sin\alpha) = 0 \tag{8.41c}$$

which can also be written as

$$p_2 = \frac{\frac{6}{\pi}(\theta_2 - \theta_{c\alpha 2})}{\mu_d\cos\alpha - \sin\alpha} \tag{8.42}$$

Inserting eq (8.23) yields

$$p_2 = \frac{6}{\pi\mu_d} \frac{\theta_2 - \theta_c \left(\cos\alpha - \frac{1}{\mu_s}\sin\alpha\right)}{\cos\alpha - \frac{1}{\mu_d}\sin\alpha} \tag{8.43}$$

For transport of sand in a stationary current, formulae for the bed load, q can be constituted from the above expressions for p (stirring expression) in combination with a semi-empirical expression for the migration velocity of the grains (transporting expression). For the berm breakwater case, two alternative approaches are followed. In the first, only the lateral variation of the stirring term is included in the berm breakwater model, whereas the lateral variation in the transporting term is assumed negligible for this specific case. Secondly, in Section 8.4, also the lateral variation in the transporting term is included. The results of both methods are compared in Chapter 9.

The continuity equation for the stones reads

$$\frac{\partial z}{\partial t} + \frac{1}{1-n} \frac{\partial}{\partial x} \left(\bar{q}_1 - \bar{q}_2 \right) = 0 \tag{8.44}$$

where q_1 and q_2 are the upwards and downwards transports respectively and the over bar denotes time averaged over the entire wave period, T, cf Fig 8.7. The x-axis is defined such that it is pointing from offshore towards the structure.

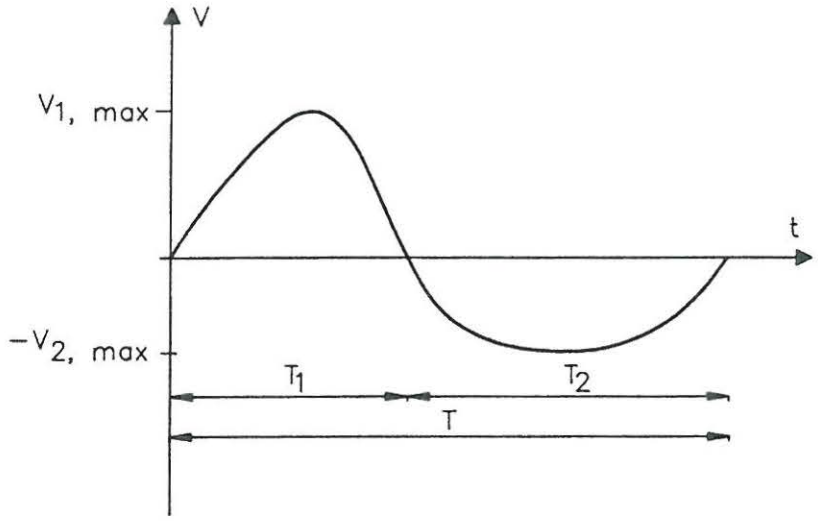

Fig 8.7 Velocity variation

For the equilibrium profile we have

$$\frac{\partial z}{\partial t} = 0 \quad \text{for all x} \tag{8.45}$$

and hence

$$\frac{\partial}{\partial x} \left(\bar{q}_1 - \bar{q}_2 \right) = 0 \quad \text{for all x} \tag{8.46}$$

or as in the equilibrium state $\bar{q}_1$ and $\bar{q}_2$ only depend on x

$$\bar{q}_1 - \bar{q}_2 = \text{constant} \quad \text{for all x} \tag{8.47}$$

As no net transport takes place we have

$$\bar{q}_1(x) = \bar{q}_2(x) \quad \text{for all x} \tag{8.48}$$

By use of eq (8.33), the instantaneous transport rates can be found as

$$q_1(x) = \frac{\pi}{6} d^3 \frac{N_{disp.1}}{A} V_{G1} = \frac{\pi}{6} dp_1(x) V_{G1} \tag{8.49}$$

$$q_2(x) = \frac{\pi}{6} d^3 \frac{N_{disp.2}}{A} V_{G2} = \frac{\pi}{6} dp_2(x) V_{G2} \tag{8.50}$$

$p_1(x)$ and $p_2(x)$ are related to the local maximum velocities $V_{1,max}$ and $V_{2,max}$. In the theory by Engelund (1975), q divided by $\sqrt{\Delta g d^3}$ is denoted the non-dimensional bed load transport, ϕ_b.

The average transport rates over the entire wave period, T, can be expressed as

$$\bar{q}_1(x) = q_1(x) \frac{\delta_1}{T} \tag{8.51}$$

$$\bar{q}_2(x) = q_2(x) \frac{\delta_2}{T} \tag{8.52}$$

where δ_1 and δ_2 denote the durations of the upwards and downwards transport events respectively.

Eqs (8.48) to (8.52) imply

$$\frac{\pi}{6} dp_1(x) V_{G1} \frac{\delta_1}{T} = \frac{\pi}{6} dp_2(x) V_{G2} \frac{\delta_2}{T} \tag{8.53}$$

The quantities V_{G1}, V_{G2}, δ_1, and δ_2 are unknown. The simplest assumption one can do is that the process is mainly governed by the number of displaced stones in each direction, and hence omitting V_{G1}, V_{G2}, δ_1, and δ_2, we get

$$\frac{\pi}{6} dp_1(x) = \frac{\pi}{6} dp_2(x) \tag{8.54}$$

or

$$p_1(x) = p_2(x) \tag{8.55}$$

Eq (8.55) can also be derived without omitting V_{G1}, V_{G2}, δ_1, and δ_2. It is assumed that, once the stones are moving, the ratio between the upwards and downwards stone velocities equals

$$\frac{V_{G1}}{V_{G2}} = \frac{V_{1,max}}{V_{2,max}} \tag{8.56}$$

The ratio between the durations of the transports are assumed to be equal to the ratio between the first and second half periods of the wave, ie the durations are governed by the wave kinematics

$$\frac{\delta_1}{\delta_2} = \frac{T_1}{T_2} \tag{8.57}$$

Demanding continuity of the water, we get

$$V_{1,max} T_1 = V_{2,max} T_2 \tag{8.58}$$

Now, eqs (8.53) and (8.56) to (8.58) lead to eq (8.55).

Combining the above eq (8.55) with eqs (8.40) and (8.43), we get as Θ_1 and Θ_2 are now the maximum values during the first and second half periods respectively

$$\frac{\theta_1 - \theta_c \left(\cos\alpha_d + \frac{1}{\mu_s} \sin\alpha_d \right)}{\cos\alpha_d + \frac{1}{\mu_d} \sin\alpha_d} = \frac{\theta_2 - \theta_c \left(\cos\alpha_d - \frac{1}{\mu_s} \sin\alpha_d \right)}{\cos\alpha_d - \frac{1}{\mu_d} \sin\alpha_d} \tag{8.59}$$

or

$$\frac{1 + \frac{1}{\mu_d} \tan\alpha_d}{1 - \frac{1}{\mu_d} \tan\alpha_d} = \frac{\theta_1 - \theta_c \left(\cos\alpha_d + \frac{1}{\mu_s} \sin\alpha_d \right)}{\theta_2 - \theta_c \left(\cos\alpha_d - \frac{1}{\mu_s} \sin\alpha_d \right)} \tag{8.60}$$

or

$$\tan\alpha_d = \mu_d \frac{\theta_1 - \theta_2}{\theta_1 + \theta_2 + 2\theta_c \left(\frac{\mu_d}{\mu_s} - 1 \right) \cos\alpha_d} \tag{8.61}$$

which is an iterative expression in the dynamic slope angle, α_d.

As an example, it is seen from eq (8.61) that in case of a first order wave on a horizontal bottom, we have $\Theta_1 = \Theta_2$, and hence $\tan\alpha_d = 0$.

Demanding $p_2 \geq 0$, eq (8.43) yields

$$\frac{\theta_2}{\theta_c} \geq \cos\alpha - \frac{1}{\mu_s} \sin\alpha \tag{8.62}$$

which can be written as

$$\tan\alpha \geq \mu_s \left(1 - \frac{\frac{\theta_2}{\theta_c}}{\cos\alpha} \right) = \tan\alpha_s \tag{8.63}$$

cf eq (8.25).

This implies that allowing a certain transport of stones on the middle slope yields a steeper slope than the static equilibrium slope. In Chapter 9 is shown that when increasing the severity of the wave attack, the static solution decreases below the dynamic solution given by $\tan\alpha_d$.

Inserting

$$\frac{\theta_2}{\theta_c} = \cos\alpha - \frac{1}{\mu_s}\sin\alpha \tag{8.64}$$

corresponding to $p_2=0$, cf eq (8.62) into eq (8.61) yields

$$\tan\alpha_d = \mu_d \tag{8.65}$$

independent of Θ_1.

An implication of eqs (8.62) to (8.65) is that for waves higher than at transition from static to dynamic equilibrium of the middle slope, on the upper slope, when $p_2=0$, the dynamic solution goes into the static solution at $\tan\alpha_d=\mu_d$.

At the top of the slope, we have $\tan\alpha_s=\mu_s$, cf eq (8.26). At this point, the upwards transport, p_1, forming the natural crest can be found from eq (8.40)

$$p_1 = \frac{6}{\pi}\,\frac{\theta_1\sqrt{1+\mu_s^2} - 2\theta_c}{\mu_s + \mu_d} \tag{8.66}$$

which is increasing with Θ_1.

The criterion for crest formation is

$$p_1 \geq 0 \tag{8.67}$$

which together with eq (8.66) yields

$$\frac{\theta_1}{\theta_c} \geq \frac{2}{\sqrt{1+\mu_s^2}} \tag{8.68}$$

Finally, when $\Theta_1 \gg \Theta_c$ and $\Theta_2 \gg \Theta_c$, we get for the middle slope

$$\tan\alpha_d = \mu_d\,\frac{\theta_1-\theta_2}{\theta_1+\theta_2} = \mu_d\,\frac{\frac{\theta_1}{\theta_2}-1}{\frac{\theta_1}{\theta_2}+1} = \mu_d\,\frac{\left(\frac{V_{1,max}}{V_{2,max}}\right)^2-1}{\left(\frac{V_{1,max}}{V_{2,max}}\right)^2+1} \tag{8.69}$$

ie a limit profile is reached. This is in contradiction to the static solution which yields $\tan\alpha_s<0$, cf eq (8.25), ie no stability.

Van der Meer (1988) carried out physical model tests with different stone shapes, rounded gravel, angular rock and flat/long stones. It was found that the stone shape has no or only minor influence on the equilibrium profile. As the dynamic solution is very much governed by μ_d, μ_d is thus likely to be independent or only weakly dependent on the stone shape. This is in contradiction to the strong dependency of μ_s on the stone shape, as irregular rock shows larger interlocking forces than round rock.

On a berm breakwater, the transport rates are small, dominantly taking place under the higher individual waves, implying that a representative regular wave height must compare to the higher individual waves. At present, it is not known which is the best measure of a representative wave height, and hence it is chosen to apply the same values as for the static solution, cf eqs (8.27) and (8.28). Also this solution is an equilibrium solution, which formally corresponds to exposure to a large number of waves.

8.4 Dynamic Solution-2

In Section 8.3, the stone velocities V_{G1} and V_{G2} and the durations δ_1 and δ_2 cancel out. As all of these quantities are unknown, it is possible to establish a variety of expression for the dynamic equilibrium slope. In the present section, it is assumed that the upwards and downwards durations of the stone transports are equal, ie $\delta_1=\delta_2$, and hence an alternative series of equations is made. The deduction is similar to that of Section 8.3, if nothing else is stated.

Eq (8.53) becomes

$$\frac{\pi}{6}\, dp_1(x) V_{G1}(x) = \frac{\pi}{6}\, dp_2(x) V_{G2}(x) \tag{8.70}$$

Assuming

$$\frac{V_{G1}}{V_{G2}} = \frac{V_{1,max}}{V_{2,max}} = \frac{\sqrt{\theta_1}}{\sqrt{\theta_2}} \tag{8.71}$$

we get

$$\frac{\pi}{6}\, dp_1(x) \sqrt{\theta_1(x)} = \frac{\pi}{6}\, dp_2(x) \sqrt{\theta_2(x)} \tag{8.72}$$

or

$$p_1(x) \sqrt{\theta_1(x)} = p_2(x) \sqrt{\theta_2(x)} \tag{8.73}$$

Inserting eqs (8.40) and (8.43) into eq (8.73), we get

$$\frac{\theta_1 - \theta_c\left(\cos\alpha_d + \frac{1}{\mu_s}\sin\alpha_d\right)}{\cos\alpha_d + \frac{1}{\mu_d}\sin\alpha_d}\sqrt{\theta_1} = \frac{\theta_2 - \theta_c\left(\cos\alpha_d - \frac{1}{\mu_s}\sin\alpha_d\right)}{\cos\alpha_d - \frac{1}{\mu_d}\sin\alpha_d}\sqrt{\theta_2} \qquad (8.74)$$

or

$$\frac{1 + \frac{1}{\mu_d}\tan\alpha_d}{1 - \frac{1}{\mu_d}\tan\alpha_d} = \frac{\theta_1^{3/2} - \theta_c\sqrt{\theta_1}\left(\cos\alpha_d + \frac{1}{\mu_s}\sin\alpha_d\right)}{\theta_2^{3/2} - \theta_c\sqrt{\theta_2}\left(\cos\alpha_d - \frac{1}{\mu_s}\sin\alpha_d\right)} \qquad (8.75)$$

or

$$\tan\alpha_d = \mu_d \frac{\theta_1^{3/2} - \theta_c\sqrt{\theta_1}\left(\cos\alpha_d + \frac{1}{\mu_s}\sin\alpha_d\right) - \theta_2^{3/2} + \theta_c\sqrt{\theta_2}\left(\cos\alpha_d - \frac{1}{\mu_s}\sin\alpha_d\right)}{\theta_1^{3/2} - \theta_c\sqrt{\theta_1}\left(\cos\alpha_d + \frac{1}{\mu_s}\sin\alpha_d\right) + \theta_2^{3/2} - \theta_c\sqrt{\theta_2}\left(\cos\alpha_d - \frac{1}{\mu_s}\sin\alpha_d\right)} \qquad (8.76)$$

Substituting $\sin\alpha_d$ by $\tan\alpha_d \cdot \cos\alpha_d$ and neglecting second order terms in $\tan\alpha_d$, we arrive at the following iterative expression in the dynamic slope angle, α_d

$$\tan\alpha_d = \mu_d \frac{\theta_1^{3/2} - \theta_2^{3/2} - \theta_c\left(\sqrt{\theta_1} - \sqrt{\theta_2}\right)\cos\alpha_d}{\theta_1^{3/2} + \theta_2^{3/2} + \theta_c\left(\sqrt{\theta_1} + \sqrt{\theta_2}\right)\left(\frac{\mu_d}{\mu_s} - 1\right)\cos\alpha_d} \qquad (8.77)$$

Like with the dynamic solution-1 discussed in Section 8.3, the alternative solution-2 can be examined for the condition close to the static equilibrium. Demanding $p_2 \geq 0$, we find that this is equivalent to having a steeper slope than the static equilibrium slope, cf eqs (8.43) and (8.63).

Inserting eq (8.64) into eq (8.77), we get

$$\tan\alpha_d = \mu_d \qquad (8.78)$$

independent of Θ_1.

This result is applicable to the upper slope where the dynamic solution goes into the static solution.

Also the number of stones forming the crest and the associated criterion for crest formation is like in Section 8.3, cf eqs (8.66) and (8.68).

Finally, when $\Theta_1 \gg \Theta_c$ and $\Theta_2 \gg \Theta_c$, we get the following limit solution for the middle slope:

$$\tan\alpha_d = \mu_d \frac{\theta_1^{3/2} - \theta_2^{3/2}}{\theta_1^{3/2} + \theta_2^{3/2}} = \mu_d \frac{\left(\frac{\theta_1}{\theta_2}\right)^{3/2} - 1}{\left(\frac{\theta_1}{\theta_2}\right)^{3/2} + 1} = \mu_d \frac{\left(\frac{V_{1,max}}{V_{2,max}}\right)^3 - 1}{\left(\frac{V_{1,max}}{V_{2,max}}\right)^3 + 1} \tag{8.79}$$

8.5 Matching Initial and Equilibrium Profiles

8.5.1 Berm breakwaters and steep slopes

In Sections 8.2 to 8.4, expressions are given for the equilibrium slope. In order to model the equlibrium profile, a boundary condition is needed, ie a relation between a point on the developed profile and a point on the initial profile, cf Fig 8.1. As both the area above SWL as well as the transition to the steep lower slope are presumably very sensitive to even small model inaccuracies, it is chosen to establish the boundary condition on the middle slope. In the following is shown that the point on the developing profile, x_{02}, where $\partial q_2/\partial x = 0$ is actually equal to the point where $\partial z/\partial t = 0$ during the reshaping process.

If we apply eqs (8.40) and (8.43) for the initial profile, we get

$$p_1 = \frac{6}{\pi\mu_d} \frac{\theta_1 - \theta_c\left(\cos\alpha_i + \frac{1}{\mu_s}\sin\alpha_i\right)}{\cos\alpha_i + \frac{1}{\mu_d}\sin\alpha_i} \tag{8.80}$$

$$p_2 = \frac{6}{\pi\mu_d} \frac{\theta_2 - \theta_c\left(\cos\alpha_i - \frac{1}{\mu_s}\sin\alpha_i\right)}{\cos\alpha_i - \frac{1}{\mu_d}\sin\alpha_i} \tag{8.81}$$

If we demand that initially in the reshaping process $p_1 \ll p_2$, the above equations (8.80) and (8.81) lead to

$$\tan\alpha_i \gg \mu_d \frac{\theta_1 - \theta_2}{\theta_1 + \theta_2 + 2\theta_c\left(\frac{\mu_d}{\mu_s} - 1\right)\cos\alpha_i} \tag{8.82}$$

which, by use of eq (8.61) can be written as

$$\tan\alpha_i \gg \tan\alpha_d \tag{8.83}$$

where α_d is the equilibrium slope angle, ie for steep initial slopes the downwards transport is dominant.

Now the equation of continuity reads, cf eq (8.44)

$$\frac{\partial z}{\partial t} - \frac{1}{1-n}\frac{\partial \bar{q}_2}{\partial x} = 0 \qquad (8.84)$$

and hence, as q_2 varies with x, only locally $\partial z/\partial t$ becomes zero, ie in the point x_{02}, where $\partial \bar{q}_2/\partial x$ is zero. As q_2 is a monotonous function of Θ_2, which is a monotonous function of $V_{2,max}$, we get that $\partial z/\partial t$ equals zero in the point of maximum downrush velocity or rather in the point with a maximum in $V_{2,max}$ according to eq (8.10). From Fig 8.8, the sign of $\partial z/\partial t$ can be evaluated:

- $x < x_{02}$: $\partial \bar{q}_2/\partial x > 0 \Rightarrow \partial z/\partial t > 0$
- $x > x_{02}$: $\partial \bar{q}_2/\partial x < 0 \Rightarrow \partial z/\partial t < 0$

This result is utilised in the description of the developed profile above x_{02}:

$$z = z_{02} + \int_{x_{02}}^{x} \tan\alpha_d \, dx \qquad (8.85)$$

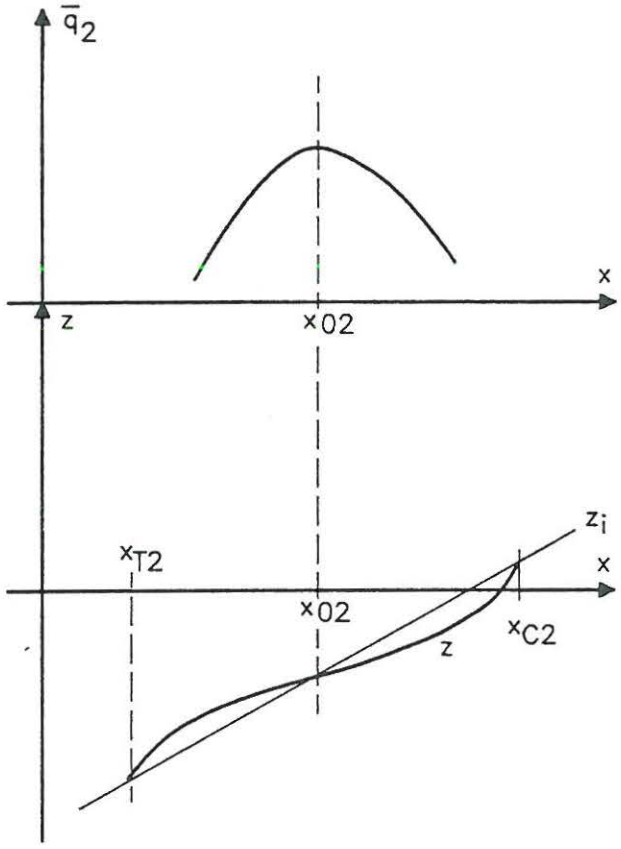

Fig 8.8 Stone transport and profile development at x_{02}

For the part of the developed profile below x_{02}, the profile is described by eq (8.85) intersected by the steep lower slope given by the natural angle of repose, ϕ, where $dz/dx=\tan\phi=\mu_s$. The intersection point with the initial slope, x_{T2}, is found from the continuity equation for the stone material, stating that the eroded area above x_{02} must be placed below x_{02}

$$\int_{x_{T2}}^{x_{02}} (z-z_i)dx = -\int_{x_{02}}^{x_{c2}} (z-z_i)dx \tag{8.86}$$

where z_i denotes the initial profile.

This model for the reshaping process actually conforms to the physics of berm breakwaters: The erosion, governed by the wave attack, takes place on the upper slope and part of the middle slope, whereas part of the middle slope and the lower slope are formed as deposition areas, only to a minor extent governed by the waves.

The procedure described above also applies to the case of a static solution to the equilibrium slope, ie in eq (8.85) $\tan\alpha_d$ is replaced by $\tan\alpha_s$.

8.5.2 Flat slopes

If we demand that $p_2 \ll p_1$, eqs (8.40), (8.43) and (8.61) lead to

$$\tan\alpha_i \ll \tan\alpha_d \tag{8.87}$$

where α_d is the equilibrium slope angle, ie for a flat slope initially the upwards transport is dominant.

The equation of continuity reads, cf eq (8.44):

$$\frac{\partial z}{\partial t} + \frac{1}{1-n}\frac{\partial \bar{q}_1}{\partial x} = 0 \tag{8.88}$$

The point with $\partial z/\partial t$ equal to zero is now found in the point x_{01} with $\partial \bar{q}_1/\partial x$ equal to zero, ie the point with maximum uprush velocity. From Fig 8.9, the sign of $\partial z/\partial t$ can be evaluated:

- $x < x_{01}$: $\partial \bar{q}_1/\partial x > 0 \Rightarrow \partial z/\partial t < 0$
- $x > x_{01}$: $\partial \bar{q}_1/\partial x < 0 \Rightarrow \partial z/\partial t > 0$

Like with berm breakwaters and steep slopes, the equilibrium profile can be drawn

$$z = z_{01} + \int_{x_{01}}^{x} \tan\alpha_d \, dx \tag{8.89}$$

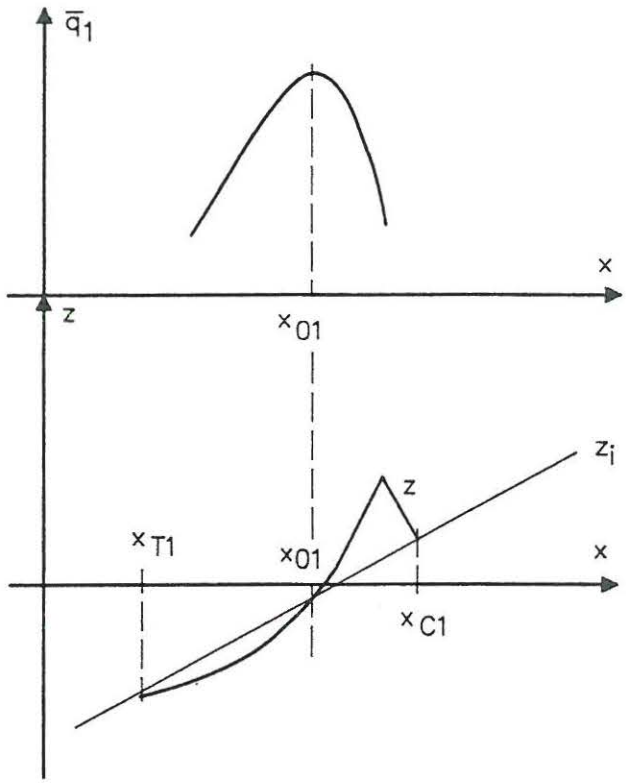

Fig 8.9 Stone transport and profile development at x_{01}

Also for this case, the continuity equation for the stone material must be fulfilled

$$\int_{x_{01}}^{x_{c1}} (z-z_i)dx = -\int_{x_{T1}}^{x_{01}} (z-z_i)dx \qquad (8.90)$$

8.5.3 Application of the theory

The theory developed in the present chapter is general in the sense that the equilibrium slope and the boundary condition depend on a hydrodynamic solution, which conforms to the developed equilibrium profile. This can be obtained by carrying out an iteration, ie consecutive simulations of hydrodynamics and equilibrium profile, until stationary conditions are reached.

For practical purposes, however, only one hydrodynamic simulation is made with a slope of 1:4, characteristic for the middle slope of a berm breakwater, governing the flow. It is assumed that the equilibrium slope and the boundary condition dominantly depend on the local water depth, h, and hence eqs (8.85) and (8.89) are solved iteratively with $\tan\alpha_d$ given as a function of h.

For all water depths, the maximum velocities calculated according to eqs (8.9) and (8.10) are found in the computation point immediately above the slope. A smoothing of the u and w composants over totally five points, all located one vertical increment above the slope, is carried out. The central point is weighted with a coefficient of 3/9, each of the two neighbouring points with 2/9, and finally 1/9 is applied to the two outermost points.

9 STRUCTURAL RESPONSE TO WAVE IMPACT

Chapter 7 describes the modelling of the flow on and in a straigth porous slope utilising the description of the porous flow resistance given in Chapters 4 and 5. In Chapter 8, the stone dynamics is described on an armour averaged level resulting in two types of solutions to the equilibrium profile for a berm breakwater: a static solution and dynamic solutions. Combining the flow description and the stone dynamics descriptions results in the equilibrium berm breakwater profile, which is compared to physical model test data on a macroscopic level.

Initially, it is shown that the intersection point between the initial and the reshaped profile keeps the same during the entire reshaping process, actually conforming to observations.

In Section 9.3, the friction factor, f_0, is found by calibration giving the best agreement with known criteria for initiation of stone movement applied to the static solution. This leads to a fairly good agreement between measured and simulated berm recessions according to the static solution.

In Sections 9.4 and 9.5 is shown that when increasing the severity of the wave attack, there is a change from the static to the dynamic solution on the middle slope. A calibration of the dynamic friction coefficient for each of the two dynamic solutions leads to a fairly good agreement between measured and modelled berm recessions.

Finally, in Section 9.6, the calibrated model is compared to data on physical model tests with initially straight porous slopes giving a fairly good agreement.

9.1 Overview of Computations

In Section 7.5, computations were made with an initial slope of 1:4 and with different hydraulic parameters. In the present section, the slope parallel velocities from these computations are used for calculation of the equilibrium slope. As the flow on and in a berm breakwater is dominantly governed by the middle slope, which is in the order of 1:4, it is chosen to apply initial slopes of 1:4 for the hydrodynamic simulations without any recalculation of the hydrodynamics, ie the equilibrium slope is calibrated on basis of hydrodynamic computations with 1:4 slopes. Table 9.1, identical to Table 7.1, shows the computations made with an initial slope of 1:4.

In order to examine the conditions during the reshaping process, an additional sensitivity analysis concerning the initial slope is carried out, cf Table 9.2 below. The purpose is to examine the behaviour of the points of maximum uprush and maximum downrush velocity, as these are relevant to the entire reshaping process from the initial profile to the reshaped profile, cf Section 8.5.3. Like with the slope of 1:4, also in this case eq (7.44) is applied for Δx with Δz fixed at 0.02 m. The time increment is found from eq (7.43) with c_s=20 m/s and σ_x=1.

Table 9.1 Computations made with an initial slope of 1:4

Run No	Slope	n	β'	C_m	C_m^*	f_0	H_{input}	H_{ref}	T_{ref}
cot4xj	1:4	0.41	3.0	8.58	3.1	0.6	0.160	0.149	2.00
cot4xc	1:4	0.41	2.0	8.58	3.1	0.9	0.160	0.149	2.00
cot4xa	1:4	0.41	3.0	8.58	3.1	0.9	0.160	0.149	2.00
cot4xh	1:4	0.41	2.0	8.58	3.1	0.9	0.200	0.186	2.00
cot4xd	1:4	0.41	3.0	8.58	3.1	0.9	0.200	0.186	2.00
cot4xi	1:4	0.41	2.0	8.58	3.1	0.9	0.256	0.238	2.21
cot4xf	1:4	0.41	3.0	8.58	3.1	0.9	0.256	0.238	2.21
cot4xg	1:4	0.41	2.0	8.58	3.1	0.9	0.280	0.260	2.21
cot4xe	1:4	0.41	3.0	8.58	3.1	0.9	0.280	0.260	2.21
cot4xk	1:4	0.41	3.0	8.58	3.1	1.2	0.160	0.149	2.00
cot4xl	1:4	0.39	3.0	8.82	$\simeq$3.1	0.9	0.200	0.186	2.00
cot4xm	1:4	0.43	3.0	8.34	$\simeq$3.1	0.9	0.200	0.186	2.00
cot4xn	1:4	0.41	3.0	7.40	2.6	0.9	0.200	0.186	2.00
cot4xo	1:4	0.41	3.0	9.76	3.6	0.9	0.200	0.186	2.00

Table 9.2 Computations made with different initial slopes

Run No	Slope	n	β'	C_m	f_0	H_{input}	H_{ref}	T_{ref}
cot5xa	1:5	0.41	3.0	8.58	0.9	0.200	0.186	2.00
cot4xd	1:4	0.41	3.0	8.58	0.9	0.200	0.186	2.00
cot3xa	1:3	0.41	3.0	8.58	0.9	0.200	0.186	2.00

For all tests in Tables 9.1 and 9.2, the following parameters have been kept constant:

h_s = 0.80 m
D_n = 0.034 m $\Rightarrow$ d = $(6/\pi)^{1/3}D_n$ = 0.042 m
Δ = 1.68
α' = 1000
ν = $1.14 \cdot 10^{-6}$ m^2/s

The equivalent spherical diameter, d, has been applied for calculation of the porous flow resistance as well as the Shields parameter.

Table 9.3 Computations made with parameters corresponding to test by Van der Meer (1988)

Run No	Slope	n	β'	C_m	f_0	H_{input}	H_{ref}	T_{ref}
cot4xv	1:4	0.41	3.0	8.58	0.9	0.194	0.180	1.75
cot4xw	1:4	0.41	3.0	8.58	0.9	0.204	0.190	2.50

For both tests, the following parameters have been kept constant:

h_s = 0.80 m
D_n = 0.026 m $\Rightarrow$ d = $(6/\pi)^{1/3} D_n$ = 0.032 m
Δ = 1.615
α' = 1000
ν = $1.14 \cdot 10^{-6}$ m²/s

In the computer model, the wave height at the toe of the straight slope equals approximately 93 percent of the value at the model boundary, and hence for all runs the reference wave height is chosen as 93 percent of the input wave height at the boundary.

As pointed out in Section 8.5, the depths of maximum uprush and downrush velocity are of interest to the integration of the equilibrium slope when establishing the equilibrium profile. Table 9.4 shows the simulated values of h_{01} and h_{02} for all computer runs. The depths h_{01} and h_{02} are likely to depend on the water depth, h_s, in front of the structure and on the wave height, H_{ref}, and the wave period, T_{ref}. It appears from Table 9.4 that for h_{02}, the dependence on H_{ref} and T_{ref} and other parameters as well is weak, ie within the tested range there is no significant variation in h_{02}. The behaviour of h_{01} and h_{02} as function of a broader range of h_s, H_{ref} and T_{ref} could be a subject for further research.

As the structure is rough and as the ratio between H_{ref} and h_s is lower than the limit of 0.45 given by Sawaragi et al (1983), cf Section 6.2, it is to be expected that all runs in Table 9.4 correspond to non-resonant conditions.

Table 9.4 h_{01} and h_{02} for all computer simulations

Run No	h_{01} (m)	h_{02} (m)
cot4xj	0.00/0.02	0.10/0.12
cot4xc	0.00/0.02	0.10
cot4xa	0.00	0.10/0.12
cot4xh	-0.02/0.00	0.08/0.10
cot4xd	-0.04/-0.02	0.10/0.12
cot4xi	-0.04	0.10/0.12
cot4xf	-0.04	0.12
cot4xg	-0.04/-0.02	0.10
cot4xe	-0.04	0.12
cot4xk	-0.02/0.00	0.10/0.12
cot4xl	-0.02	0.08/0.10
cot4xm	-0.02/0.00	0.08/0.10
cot4xn	-0.04/-0.02	0.10
cot4xo	-0.02	0.12/0.14
cot5xa	-0.02/0.00	0.10/0.12
cot3xa	-0.02/0.00	0.10/0.12
cot4xv	0.00	0.10/0.12
cot4xw	-0.06/-0.04	0.10/0.12

9.2 Overview of Physical Model Tests

Comparison has been made to physical model tests carried out at DHI. The purpose was twofold: to carry out a parameter study concerning rear side stability of berm breakwaters, cf Andersen et al (1992), and to establish a reference set of data concerning the reshaping of the sea side of berm breakwaters. The model tests were done by students from the Danish Engineering Academy, DIA, as a part of their B.Sc. dissertations. A complete description of data can be seen in the reports from DIA (1991-92) by F.J. Andersen and Poulsen, by Johannsen and Sørensen, and by Jensen and Stenberg.

A wave flume with a length of 65 m and a width of 1.8 m was used for model testing in four water depths of 0.67 m, 0.77 m, 0.87 m and 0.97 m. The profile tested is shown in Fig 9.1. Crushed stones were used both for the core, $D_{50}=0.011$ m (50% exceedance), and for the berm and armour layer, $D_{n50}=0.034$ m. D_{n50} is the nominal diameter given as $(M_{50}/\rho_a)^{1/3}$, where M_{50} is the mass of the stones (50% exceedance) and ρ_a is the density of the stones. The grading of the berm and armour material equalled $D_{n85}/D_{n15}=1.35$, the relative density equalled $\Delta=1.68$, the porosity equalled $n=0.41$ and the static friction coefficient equalled $\mu_s=0.9$. The armour layer thickness on the crest and rear side was twice the value of D_{n50}. The model study covered variations in the following parameters:

- w_c, width of the crest, 0.175 m and 0.30 m (for three tests applied in the present comparison 0.50 m and for a single test 0.70 m)
- R_c, freeboard of the crest, 0.20 m, 0.30 m and 0.40 m
- b_h, width of the berm, 0.45 m, 0.65 m, 0.85 m and 1.05 m
- b_v, freeboard of the berm, 0.10 m and 0.20 m.

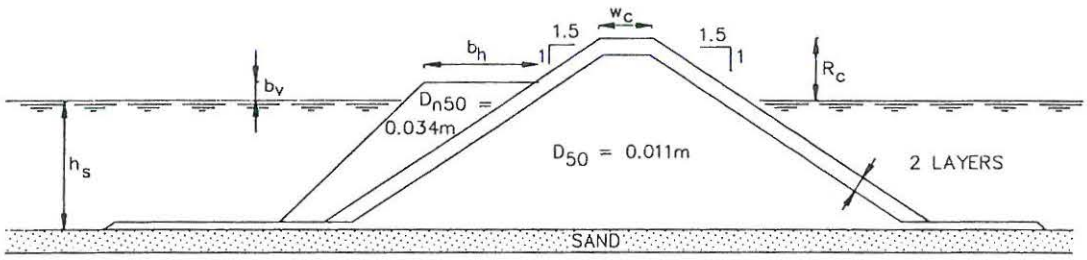

Fig 9.1 Test profile

Tests were carried out in test series with successively increasing wave height, H_{mo}, and wave period, T_{02}, from test run to test run, with a fixed fictitious wave steepness $s_{02}=2\pi H_{mo}/gT_{02}^2$ equal to approximately 0.030 and 0.044 respectively. Each test series consisted of approximately 1,000 irregular waves. The incident wave characteristics in front of the berm breakwater, H_{mo} and T_{02}, and the reflection coefficient were calculated using a multi-gauge technique.

After each test run the berm profile was measured, and the recession, r, of the berm was calculated, cf Fig 9.2.

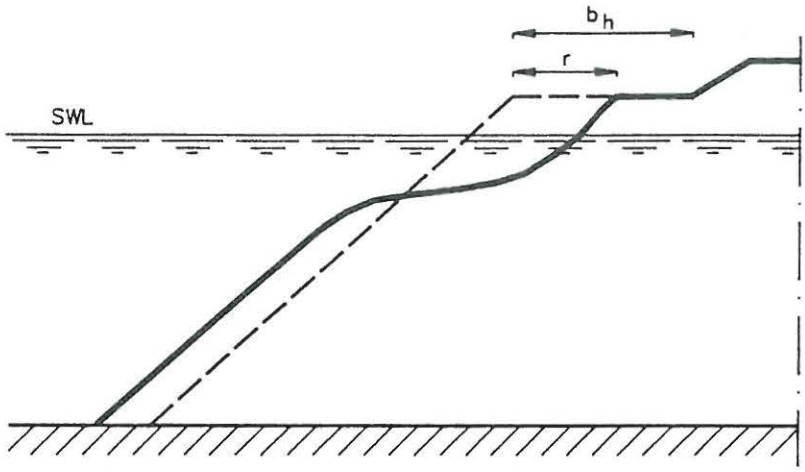

Fig 9.2 Definition of berm recession, r

Tables 9.6 to 9.9 show the observed berm recession for tests with wave height and period corresponding to the values used in the computer model within a range of 5 percent, for the first run, however, within a range of 8 per cent. In the computer model, the wave height at the toe of the straight slope equals approximately 93 percent of the value at the model boundary, and hence for all runs the reference wave height is chosen as 93 percent of the input wave height at the boundary. Table 9.5 shows the reference values for the computations.

Table 9.5 Reference values for selected computer runs and corresponding physical model tests

H_{input}	H_{ref}	H-range	T_{ref}	T-range	$s_{0,ref}$	$\xi_{o,ref}$	H^*	T^*	H^*T^*
0.160	0.149	0.137-0.161	2.00	1.84-2.16	0.0239	1.62	2.61	34.0	88.7
0.200	0.186	0.177-0.195	2.00	1.90-2.10	0.0298	1.45	3.26	34.0	111
0.256	0.238	0.226-0.250	2.21	2.10-2.32	0.0312	1.42	4.17	37.5	156
0.280	0.260	0.247-0.273	2.21	2.10-2.32	0.0341	1.35	4.55	37.5	171

$s_{0,ref}$ and $\xi_{0,ref}$ are calculated according to eqs (6.3) and (6.4). H^* and T^* are defined as, cf also eqs (6.32) and (6.33).

$$H^* = \frac{H_{mo}}{\Delta D_{n50}} \tag{9.1}$$

$$T^* = \sqrt{\frac{g}{D_{n50}}}\, T_{02} \tag{9.2}$$

where H_{ref} is applied for H_{m0} and T_{ref} for T_{02}.

Table 9.6 Measured berm recession, H_{ref}=0.149 m, T_{ref}=2.00 s

Start Prof.	Test	h_s	b_v	H_{m0}	T_{02}	r
22111	13	0.77	0.10	0.146	1.89	0.40
22112	25	0.77	0.10	0.148	1.88	0.23
22113	25	0.77	0.10	0.148	1.88	0.30
22115	31	0.77	0.10	0.137	2.09	0.21
22115	32	0.77	0.10	0.137	2.09	0.21
22114	31	0.77	0.10	0.137	2.09	0.23
22114	32	0.77	0.10	0.137	2.09	0.24
23113	61	0.77	0.10	0.149	1.87	0.21
23213	70	0.77	0.20	0.155	1.85	0.26
23211	70	0.77	0.20	0.155	1.85	0.23
12211	235	0.77	0.20	0.158	1.90	0.28
12213	235	0.77	0.20	0.158	1.90	0.23
12111	245	0.77	0.10	0.156	1.90	0.39
12113	245	0.77	0.10	0.156	1.90	0.36
31113	415	0.77	0.10	0.157	1.89	0.19

b_v = 0.10: $\overline{r}$ = 0.27 m
b_v = 0.20: $\overline{r}$ = 0.25 m
all data: $\overline{r}$ = 0.26 m

Table 9.7 Measured berm recession, H_{ref}=0.186 m, T_{ref}=2.00 s

Start Prof.	Test	h_s	b_v	H_{m0}	T_{02}	r
22113	28	0.77	0.10	0.184	2.06	0.65
22115	34	0.77	0.10	0.184	2.10	0.44
22114	34	0.77	0.10	0.184	2.10	0.34
23113	63	0.77	0.10	0.178	2.00	0.53
23213	72	0.77	0.20	0.184	2.03	0.44
23213	73	0.77	0.20	0.195	2.06	0.52
23211	72	0.77	0.20	0.184	2.03	0.40
23215	90	0.77	0.20	0.195	2.06	0.30
23214	90	0.77	0.20	0.195	2.06	0.45
22213	116	0.77	0.20	0.179	1.95	0.29
22213	117	0.77	0.20	0.180	2.00	0.32
22211	116	0.77	0.20	0.179	1.95	0.36
22211	117	0.77	0.20	0.180	2.00	0.42
13115	214	0.77	0.10	0.177	2.00	0.35
13114	214	0.77	0.10	0.177	2.00	0.39
22213	231	0.77	0.20	0.184	2.00	0.29
22213	232	0.77	0.20	0.194	2.06	0.41
12211	236	0.77	0.20	0.178	2.00	0.36
12213	236	0.77	0.20	0.178	2.00	0.33
12213	237	0.77	0.20	0.186	2.06	0.35
12113	247	0.77	0.10	0.185	2.05	0.59
31113	417	0.77	0.10	0.182	1.96	0.33
31114	423	0.77	0.10	0.181	1.96	0.22
41113	457	0.77	0.10	0.177	1.96	0.35

b_v = 0.10: $\overline{r}$ = 0.42 m
b_v = 0.20: $\overline{r}$ = 0.37 m
all data: $\overline{r}$ = 0.39 m

Table 9.8 Measured berm recession, H_{ref}=0.238 m, T_{ref}=2.21 s

Start Prof.	Test	h_s	b_v	H_{m0}	T_{02}	r
22115	38	0.77	0.10	0.233	2.18	0.89
22115	39	0.77	0.10	0.238	2.21	1.00
22115	40	0.77	0.10	0.249	2.20	1.08
23215	93	0.77	0.20	0.231	2.22	0.67
23215	94	0.77	0.20	0.239	2.18	0.87
22215	120	0.77	0.20	0.233	2.13	0.50
22215	121	0.77	0.20	0.241	2.19	0.74
22215	123	0.77	0.20	0.248	2.19	0.89
22214	120	0.77	0.20	0.233	2.13	0.64
22214	121	0.77	0.20	0.241	2.19	0.87
13115	218	0.77	0.10	0.233	2.24	0.86
12115	257	0.77	0.10	0.228	2.20	0.87
12115	258	0.77	0.10	0.235	2.22	0.91
12115	260	0.77	0.10	0.250	2.24	0.99
12114	257	0.77	0.10	0.228	2.20	0.85
12215	279	0.77	0.20	0.230	2.20	0.63
12215	280	0.77	0.20	0.240	2.21	0.71
12215	281	0.77	0.20	0.241	2.21	0.78
12215	282	0.77	0.20	0.241	2.22	0.78
12214	279	0.77	0.20	0.230	2.20	0.66

b_v = 0.10: $\overline{r}$ = 0.93 m
b_v = 0.20: $\overline{r}$ = 0.73 m
all data: $\overline{r}$ = 0.81 m

Table 9.9 Measured berm recession, H_{ref}=0.260 m, T_{ref}=2.21 s

Start Prof.	Test	h_s	b_v	H_{m0}	T_{02}	r
22115	40	0.77	0.10	0.249	2.20	1.08
23215	95	0.77	0.20	0.251	2.18	0.91
23215	96	0.77	0.20	0.256	2.21	0.95
23215	97	0.77	0.20	0.266	2.21	1.01
22215	123	0.77	0.20	0.248	2.19	0.89
12115	260	0.77	0.10	0.250	2.24	0.99

b_v = 0.10: $\overline{r}$ = 1.04 m
b_v = 0.20: $\overline{r}$ = 0.94 m
all data: $\overline{r}$ = 0.97 m

Fig 9.3 shows the development of start profile 23215, of which data appear in Tables 9.7 to 9.9. The dotted line shows the as-built initial profile from which the recession, r, of the berm is counted, cf Tables 9.6 to 9.9.

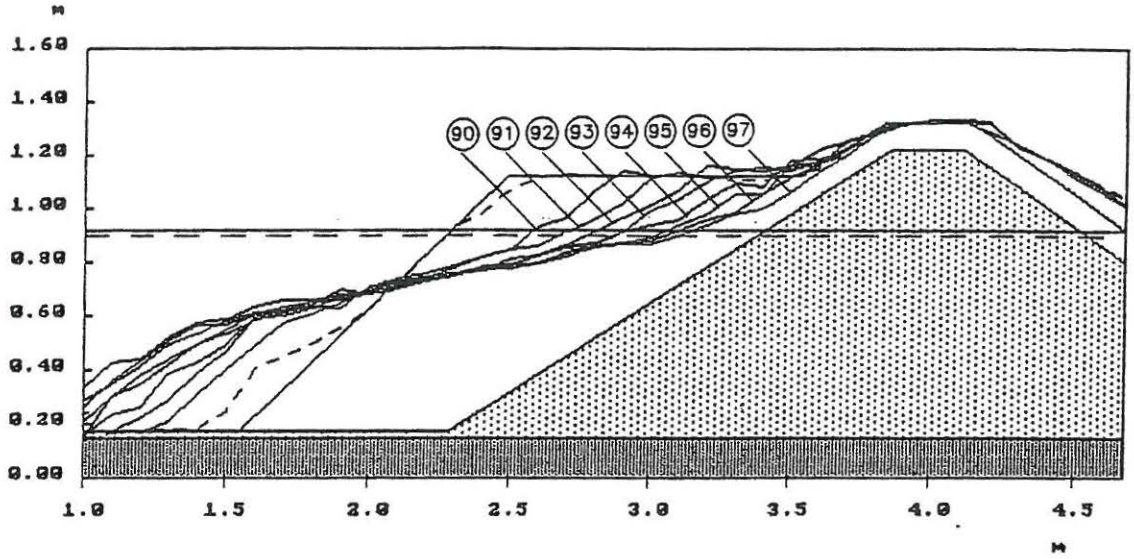

Fig 9.3 Example of physical model test at DHI, start profile 23215.
The dotted line shows the as-built initial profile, from which the berm recession is counted. The test numbers are shown in the circles.

From an experiment with an initially reshaped and painted berm breakwater profile exposed to stepwise intensified wave attack, cf Table 9.10, two conditions are particularly interesting: slight downwards movement of stones and slight movement of stones in both directions. The latter condition is interpreted as the initiation of dynamic behaviour of the middle slope, whereas the first condition corresponds to the static solution applied to the entire profile. It should be noted that this static solution corresponds to a relatively large cumulated damage to the upper layer of stones as compared to static stability of conventional breakwaters.

Table 9.10 Berm breakwater data for photo sequence

Test No	H_{m0} (m)	T_{02} (s)	H^*	T^*	H^*T^*
1	0.049	1.17	0.86	19.9	17.1
2	0.101	1.57	1.77	26.7	47.3
3	0.154	1.89	2.70	32.1	86.7
4	0.184	2.05	3.22	34.8	112
5	0.216	2.15	3.78	36.5	138
6	0.229	2.20	4.01	37.4	150
7	0.241	2.23	4.22	37.9	160
8	0.247	2.25	4.32	38.2	165

During test No 2, incipient stone movement was observed on the upper slope. In test No 3, there was a slight downwards movement of stones, and in test No 4, stone movement in both directions was observed. The initial reshaping was done with a 'design wave' corresponding to test No 7 with the number of waves, N_w, equal to 3000.

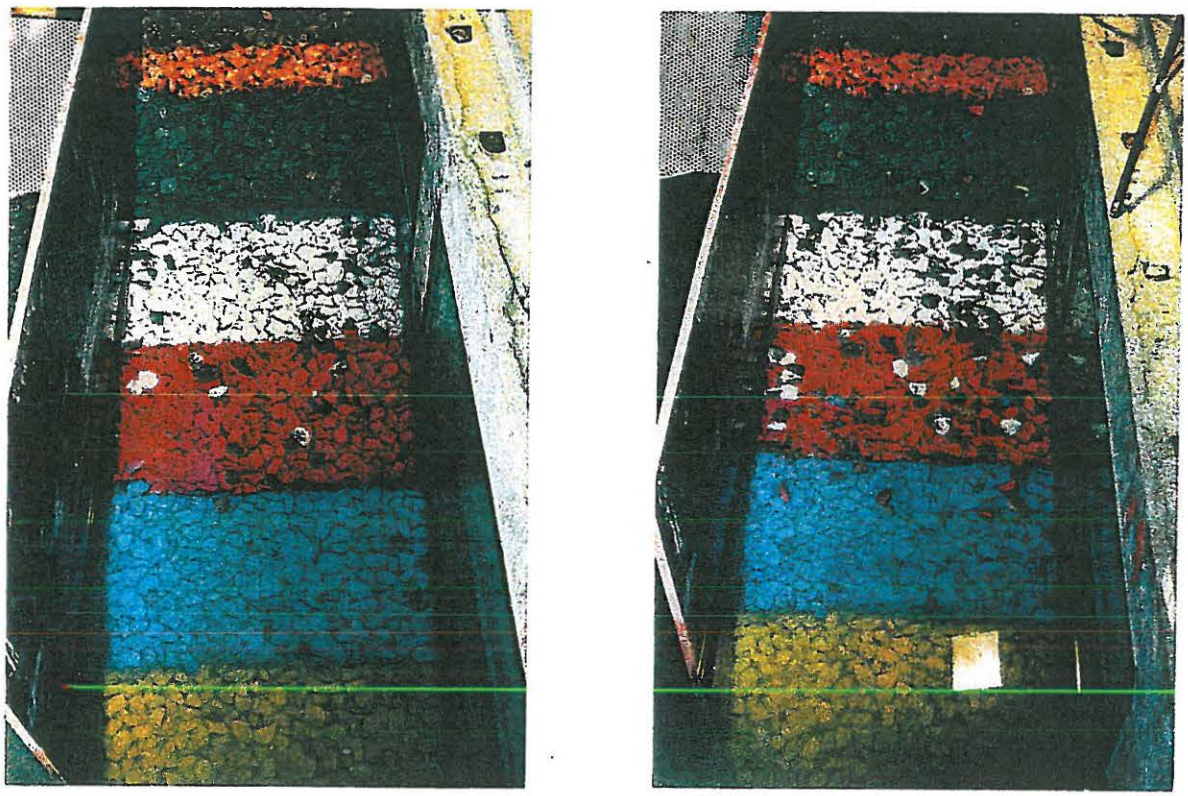

Test No 3, $H^* = 2.70$ Test No 4, $H^* = 3.22$

Fig 9.4 Berm breakwater profile after wave attack, $N_w=1000$

Lissev (1993) carried out physical model tests with berm breakwaters. One of his conclusions was that berm breakwaters become dynamically stable for values of H^* above 2.5 to 2.7. It should be noted that Lissev defines the dynamic stability, appearing at $H^*=2.72$, as 'more significant 'damage'' than at $H^*=2.26$. It is likely that this condition is identical to the above test No 3, and hence it should rather be denoted static stability with slight downwards movements of stones.

It is noticeable that in Van der Meer and Veldman (1992) the criterion for initiation of breakwater parallel transport under oblique wave attack is given as $H^*T_p^*=105$ based on physical model tests by Burcharth and Frigaard (1987) and (1988) and by the authors. T_p^* corresponds to T^*, but is based on the peak period. Assuming the following approximate relationship between the two types of wave period

$$T_{02} \simeq 0.71 \cdot T_p \qquad (9.3)$$

the H^*T^* becomes approximately 74.6, which is in fact close to the value of 86.7 associated with the above test No 3.

As a consequence of the above observations, it is chosen to apply computer simulations with $H^* \sim 2.6$ as a reference for the case of static stability with slight downwards movements of stones and $H^* \sim 3.25$ as a reference for the onset of dynamic stability.

9.3 Equilibrium Profile, Static Solution

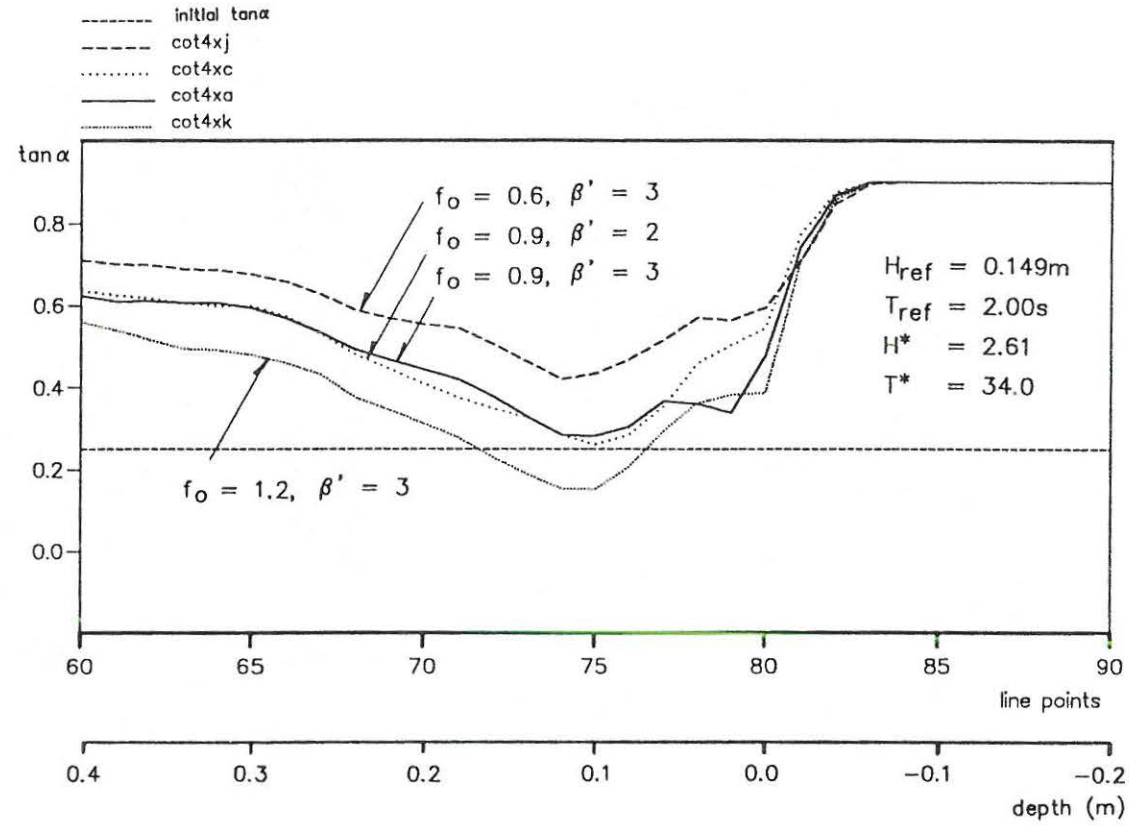

Fig 9.5 Static solution for cot4xj, cot4xc, cot4xa and cot4xk with Θ_c = 0.036.

As discussed in the preceeding section, it is chosen to apply computer simulations with $H^* \sim 2.6$ for statically stable profiles, ie with only slight downwards movements of stones. As seen in Fig 9.5, static equilibrium, cf eq (8.25), is obtained for a slope of 1:4 with runs cot4xc and cot4xa, ie the friction factor, f_0, equals 0.9. For the critical Shields parameter, a value of 0.036 is applied, cf Table 8.1. Hence, the model is calibrated in such a way that the too flat velocity profile immediately above the structure is counteracted, cf Section 7.6 and a realistic value of Θ_c is applied. As found from the physical model tests, the static friction coefficient, μ_s, equals 0.9.

Fig 9.8 illustrates the relation between Θ_c and the level of cumulated damage. If we allow a very high cumulated damage by choosing Θ_c=0.045, cf Table 8.1, computer runs cot4xh and cot4xd can be interpreted as statically stable with slopes of 1:4. The value of Θ_c=0.036 is, however, considered to be the most correct value for the present purpose, and hence it is applied in all computer simulations apart from those shown in Fig 9.8.

Comparing the runs with β'=2 and β'=3, it is seen from Figs 9.6 and 9.7 that only minor differences in the static solution occur.

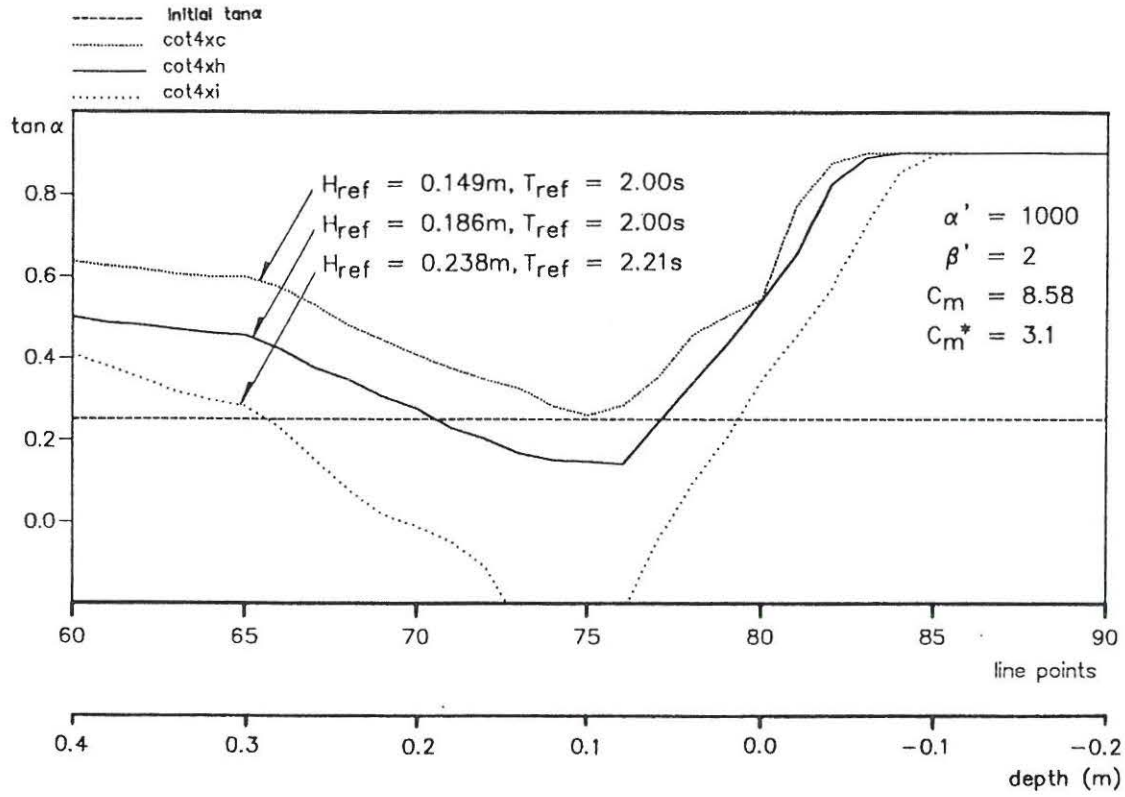

Fig 9.6 Static solution for cot4xc, cot4xh, and cot4xi with $\Theta_c = 0.036$

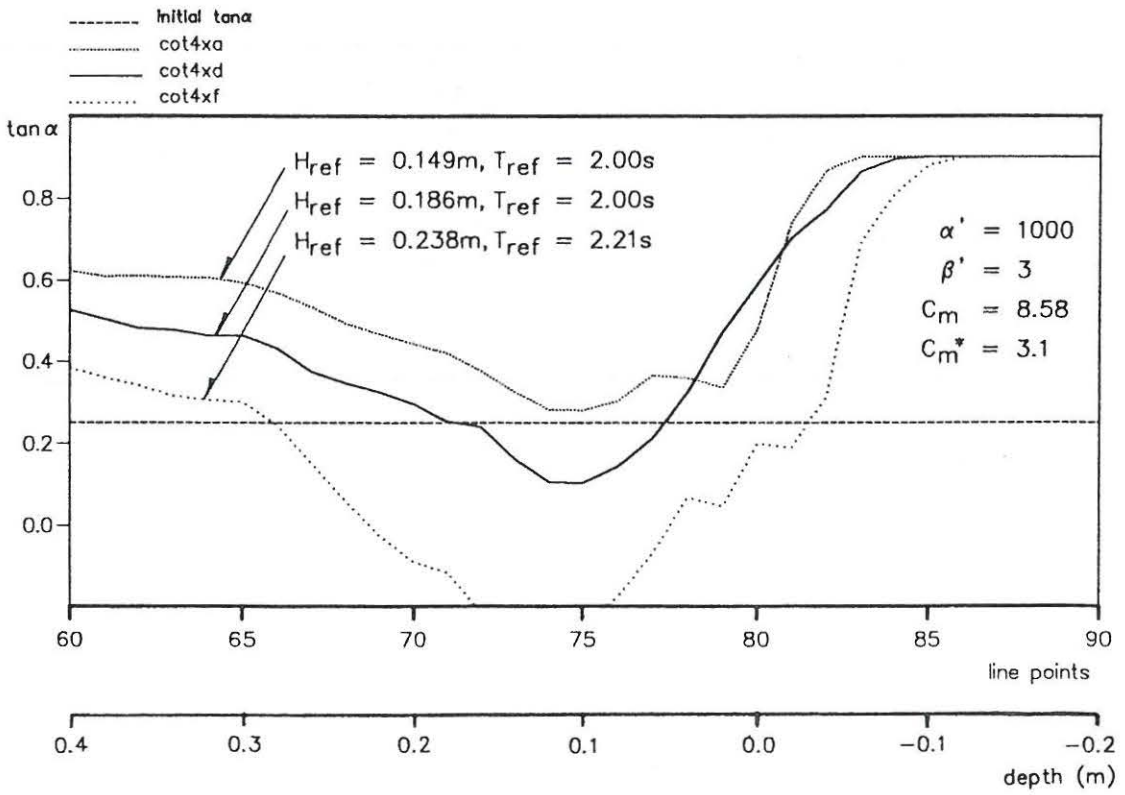

Fig 9.7 Static solution for cot4xa, cot4xd, and cot4xf with $\Theta_c = 0.036$

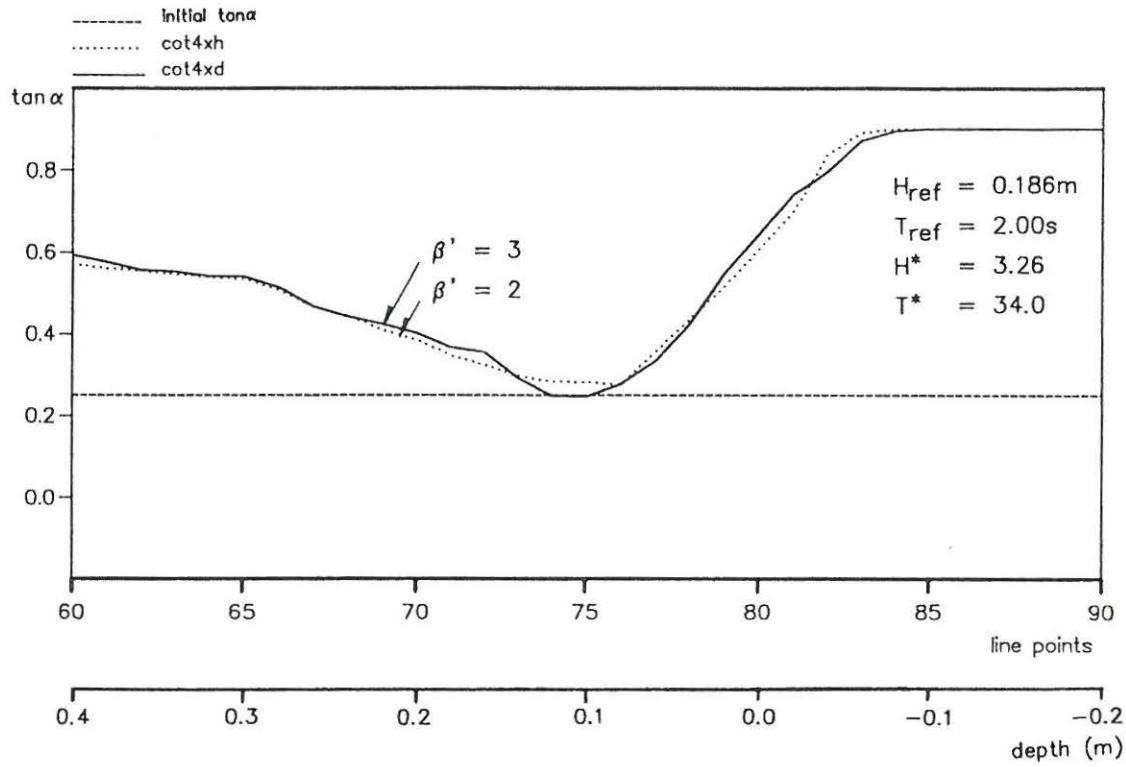

Fig 9.8 Static solution for cot4xh and cot4xd with $\Theta_c = 0.045$

In order to establish the equilibrium profile, an integration of the equilibrium slope is carried out as decribed in Section 8.5. This implies that the developed profile intersects the initial profile in the depth, h_{02} of maximum downrush velocity. It appears from Table 9.4 that h_{02} is invariant to the initial slope, cf run cot4xd and runs cot3xa and cot5xa. This is an important result to the reshaping process: despite the change from an initially steep profile exposed to low values of H_{ref} and T_{ref}, in the case of a berm breakwater, to a relatively flat developed profile exposed to high values of H_{ref} and T_{ref}, the intersection point between the initial and the developed profile keeps the same. This result conforms to observations, cf Fig 9.3. Hence, the development in the equilibrium profile with H_{ref} and T_{ref} is caused by the development in the equilibrium slope. As shown previously with $n=0.41$, $\beta'=2$ or $\beta'=3$ and $C_m=8.58$, the depth of maximum downrush velocity for the present example equals 0.10 m to 0.12 m apart from run cot4xh, cf Table 9.4. Table 9.11 and Fig 9.9 show the sensitivity of the berm recession to the choise of h_{02}.

Table 9.11 Sensitivity of static solution to h_{02}.

Run No	h_{02} (m)	r (m), $b_v \geq 0.03$ m
cot4xc	0.10	0.17
cot4xc	0.12	0.22
cot4xa	0.10	0.19
cot4xa	0.12	0.24
cot4xh	0.10	0.31
xot4xh	0.12	0.43
cot4xd	0.10	0.35
cot4xd	0.12	0.52

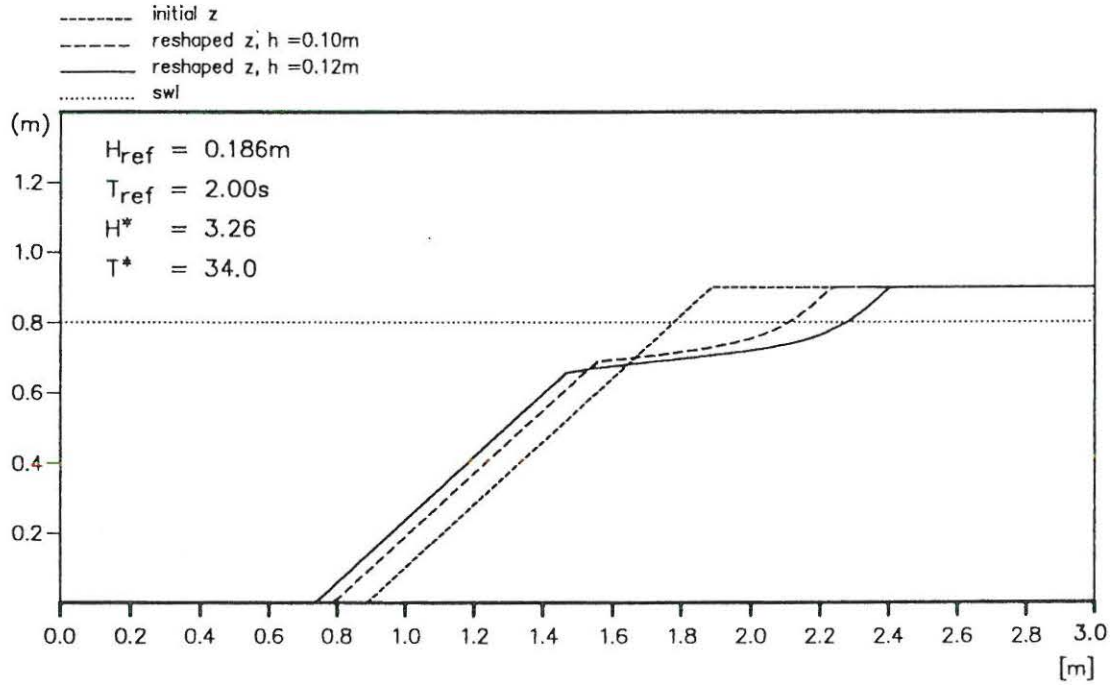

Fig 9.9 Sentitivity of predicted static equilibrium profile to h_{02}, Run No cot4xd, b_v=0.10 m

The physical model tests, however, indicate that the depth of intersection is somewhat lower, ie in the order of 0.20 m, cf Fig 9.3. Sawaragi et al (1983) found $h_{02}/h_s \sim 0.20$, which for the present example would imply h_{02}=0.16 m. Hence, it is chosen to apply the value of 0.12 m still bearing relation to the predictive model. The results are shown in Tables 9.12 and 9.13 and Fig 9.10.

The predicted damage is independent of b_v for $b_v \geq 0.03$ m (in the tested range) as both the initial face of the berm breakwater and the upper part of the equilibrium profile have slopes equal to the static friction coefficient, μ_s. This is in good agreement with the observations, cf Tables 9.6 to 9.9.

Table 9.12 Simulated berm recession based on static solution

Run No	r_{sim} (m), $b_v \geq 0.03$ m	$\overline{r}_{meas}$ (m)
cot4xc	0.22	0.26
cot4xa	0.24	0.26
cot4xh	0.43	0.39
cot4xd	0.52	0.39

Table 9.13 Simulated berm recession based on static solution

Run No	r_{sim} (m), $b_v \geq 0.03$ m	$\overline{r}_{meas}$ (m)
cot4xd	0.52	0.39
cot4xl	0.62	0.39
cot4xm	0.57	0.39
cot4xn	0.39	0.39
cot4xo	0.47	0.39

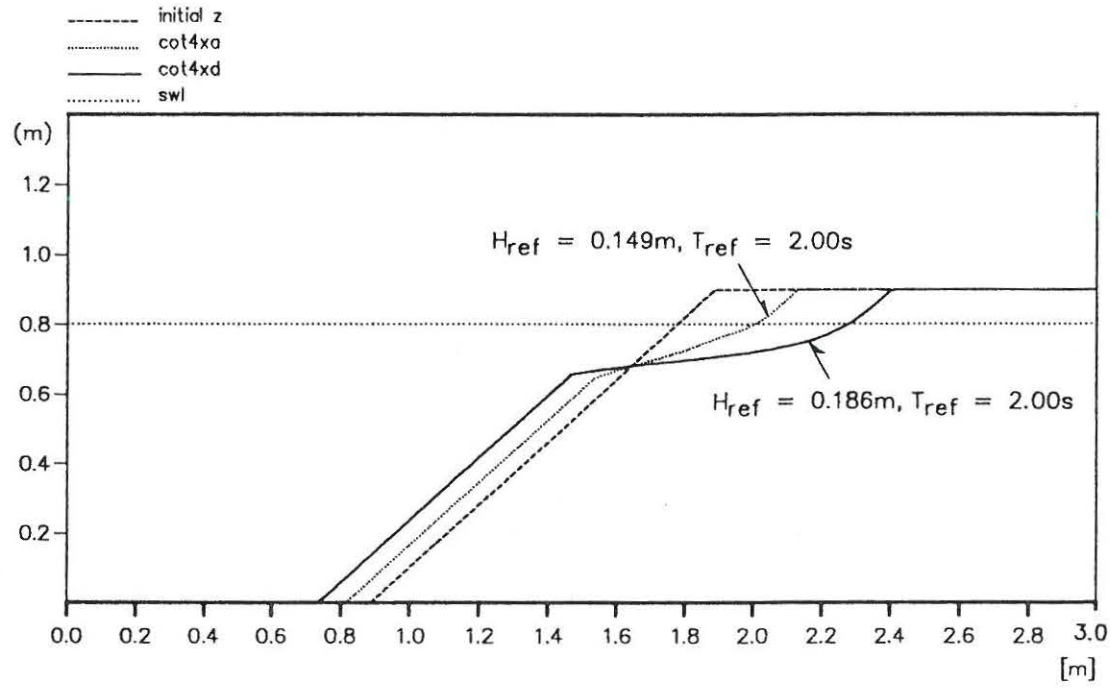

Fig 9.10 Static equilibrium profile for cot4xa and cot4xd

9.4 Equilibrium Profile, Dynamic Solution-1

As discussed in Section 9.2 for wave attack with $H/\Delta D_n$ in the order of 3.25 and above, it is relevant to apply a dynamic solution to the equilibrium slope. In this section, the expression given by eq (8.61) is examined. The quantities found by calibration in Section 9.3 are kept unchanged:

f_o = 0.9
Θ_c = 0.036
h_{02} = 0.12 m

As found from the physical model tests, the static friction coefficient, μ_s, equals 0.9.

From calibration, it is found that a value of 0.44 for the dynamic friction coefficient, μ_d, gives a fairly good overall agreement between the calculated and measured berm recessions.

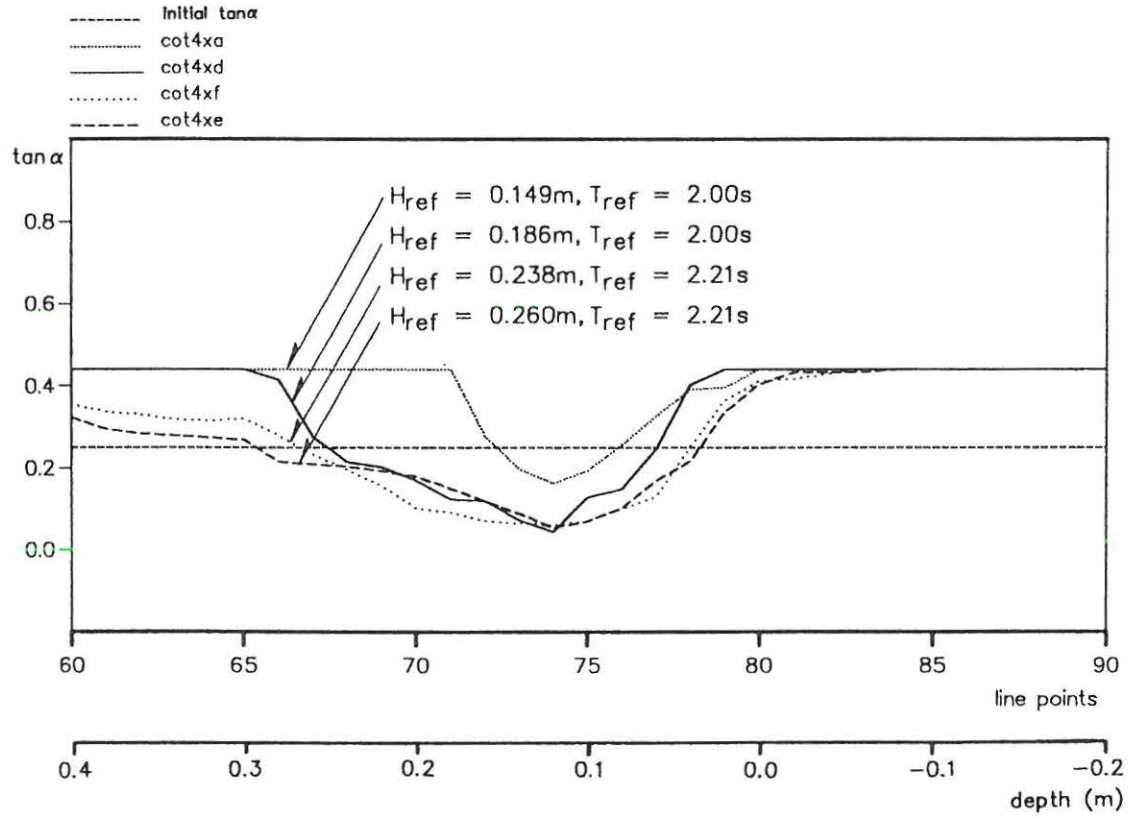

Fig 9.11 Dynamic solution-1 for cot4xa, cot4xd, cot4xf and cot4xe

Table 9.14 Simulated berm recession based on dynamic solution-1

Run No	r_{sim} (m), $b_v \geq 0.03$ m	$\overline{r}_{meas}$ (m)
cot4xh	0.34	0.39
cot4xd	0.45	0.39
cot4xi	0.89	0.81
cot4xf	0.88	0.81
cot4xg	0.90	0.97
cot4xe	0.91	0.97

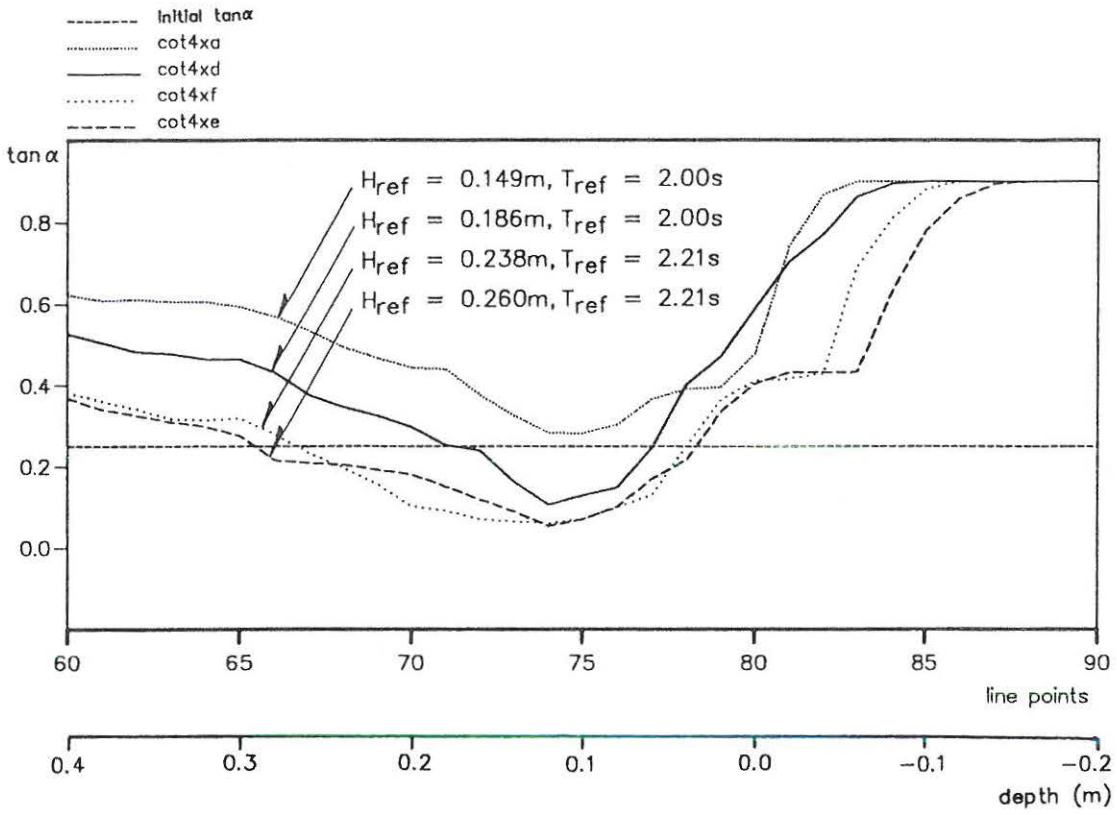

Fig 9.12 Dynamic solution-1 combined with static solution for cot4xa, cot4xd, cot4xf and cot4xe

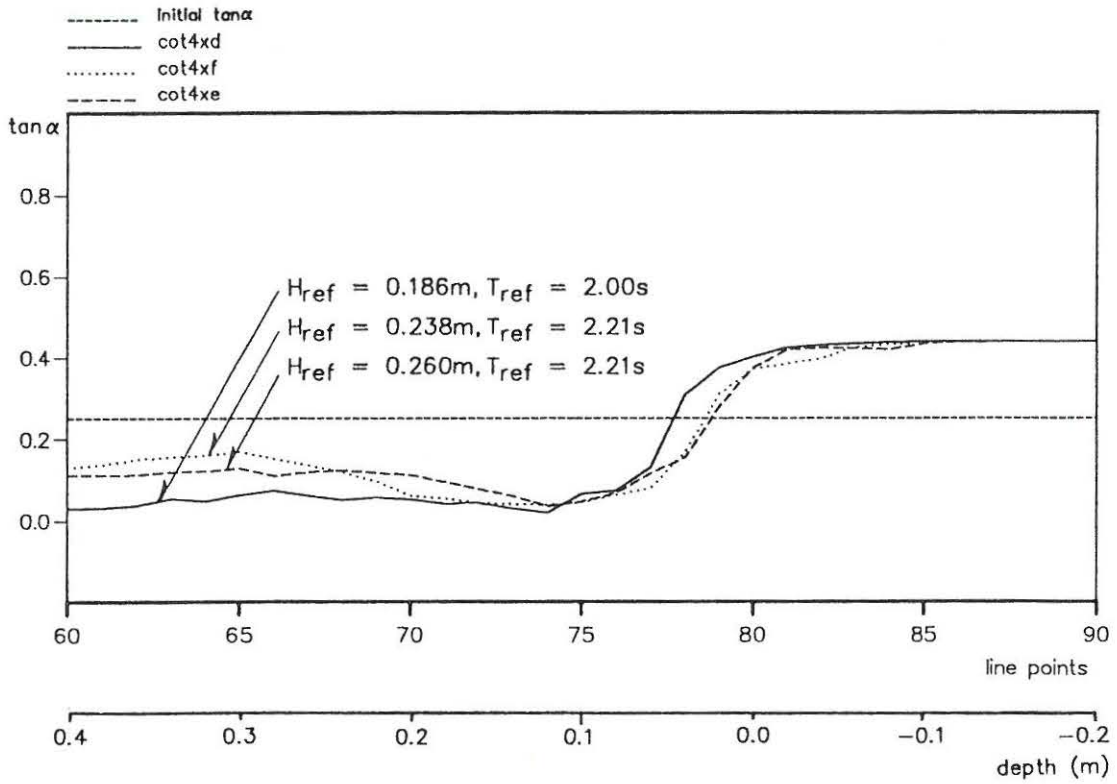

Fig 9.13 Dynamic limit solution-1 for cot4xd, cot4xf and cot4xe

Table 9.15 Simulated berm recession based on dynamic solution-1

Run No	r_{sim} (m), $b_v \geq 0.03$ m	$\overline{r}_{meas}$ (m)
cot4xd	0.45	0.39
cot4xl	0.44	0.39
cot4xm	0.40	0.39
cot4xn	0.35	0.39
cot4xo	0.42	0.39

Comparing Figs 9.7 and 9.12 showing the static solution and the dynamic solution-1 combined with the static solution is seen that:

- for relatively low values of H_{ref} and T_{ref}, ie for run cot4xa, the static solution yields larger slopes than the combined solution for practically all water depths
- for run cotxd, there is a transition between the two types of solutions, ie the slopes are practically identical
- for relatively high values of H_{ref} and T_{ref}, ie runs cot4xf and cot4xe, the combined solution implies larger slopes than the static solution, and the static solution itself leads to unstable profiles, as the slope becomes negative for some water depths

Comparing Figs 9.11 and 9.13, it appears that for both runs, cot4xf and cot4xe, the dynamic solutions valid for the middle slope are approaching the dynamic limit solutions. In Chapter 8, it is predicted that such limit solutions will be reached when increasing the wave height and wave period. It further appears from the above figures that the limit solutions for runs cot4xf and cot4xe are approximately identical. Comparing the simulated and the measured berm recessions, however, indicates that the development in r from run cot4xf to cot4xe is too low, cf Table 9.14. Table 9.15 shows the influence of varying the porosity and the virtual mass coefficient respectively.

In Fig 9.14, the simulated profile development is shown for the case of $\beta'=3$. For the mildest wave climate, ie for run cot4xa, the static solution is applied, and for the more severe wave climates, the dynamic solution-1 combined with the static solution is applied.

9.5 Equilibrium Profile, Dynamic Solution-2

Like the preceeding section, this section is relevant for wave attack with $H/\Delta D_n$ in the order of 3.25 and above. The expression for the dynamic solution-2 given by eq (8.77) is examined. The same quantities as applied in Sections 9.3 and 9.4 are applied:

$$f_o = 0.9$$
$$\Theta_c = 0.036$$
$$h_{02} = 0.12 \text{ m}$$

The static friction coefficient, μ_s, equals 0.9. The dynamic friction coefficient, μ_d, is found by calibration leading to a value of 0.37 resulting in the best overall agreement between the calculated and measured berm recessions. For dynamic solution-2, the value of μ_d is slightly lower than for dynamic solution-1, but still in the same order of magnitude, ie $\mu_d \sim 0.4$.

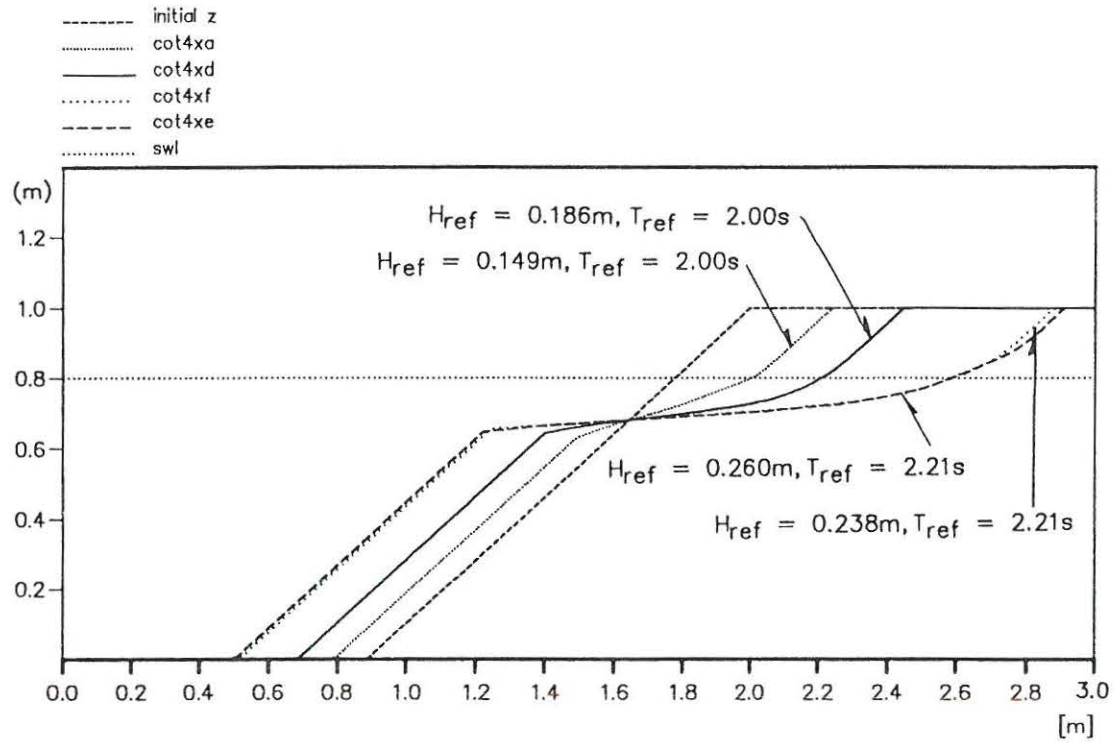

Fig 9.14 Simulated profile development for cot4xa, cot4xd, cot4xf and cot4xe

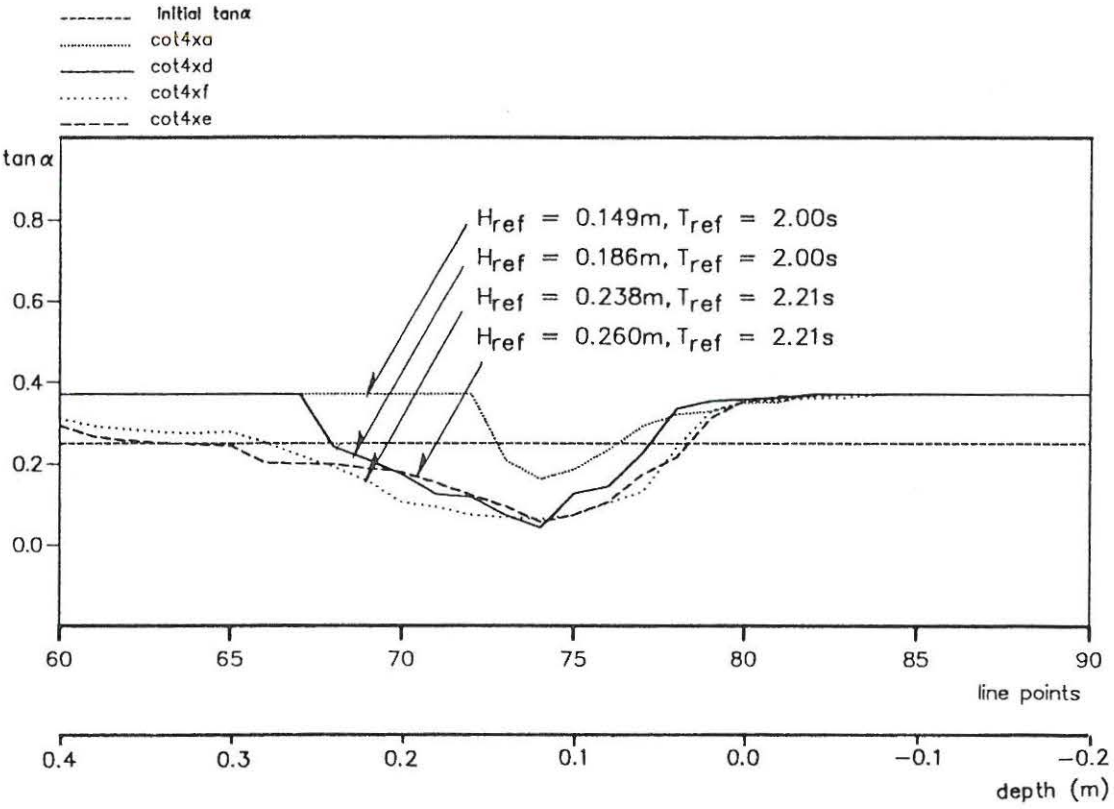

Fig 9.15 Dynamic solution-2 for cot4xa, cot4xd, cot4xf and cot4xe

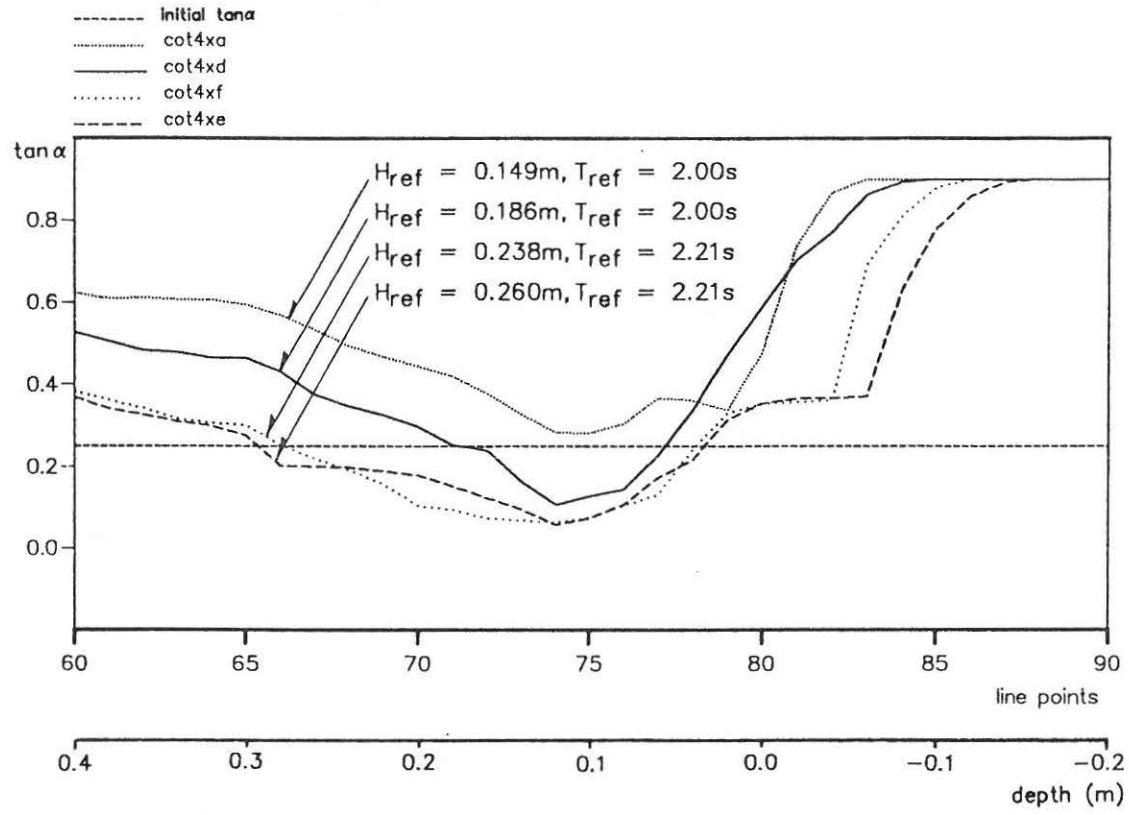

Fig 9.16 Dynamic solution-2 combined with static solution for cot4xa, cot4xd, cot4xf and cot4xe

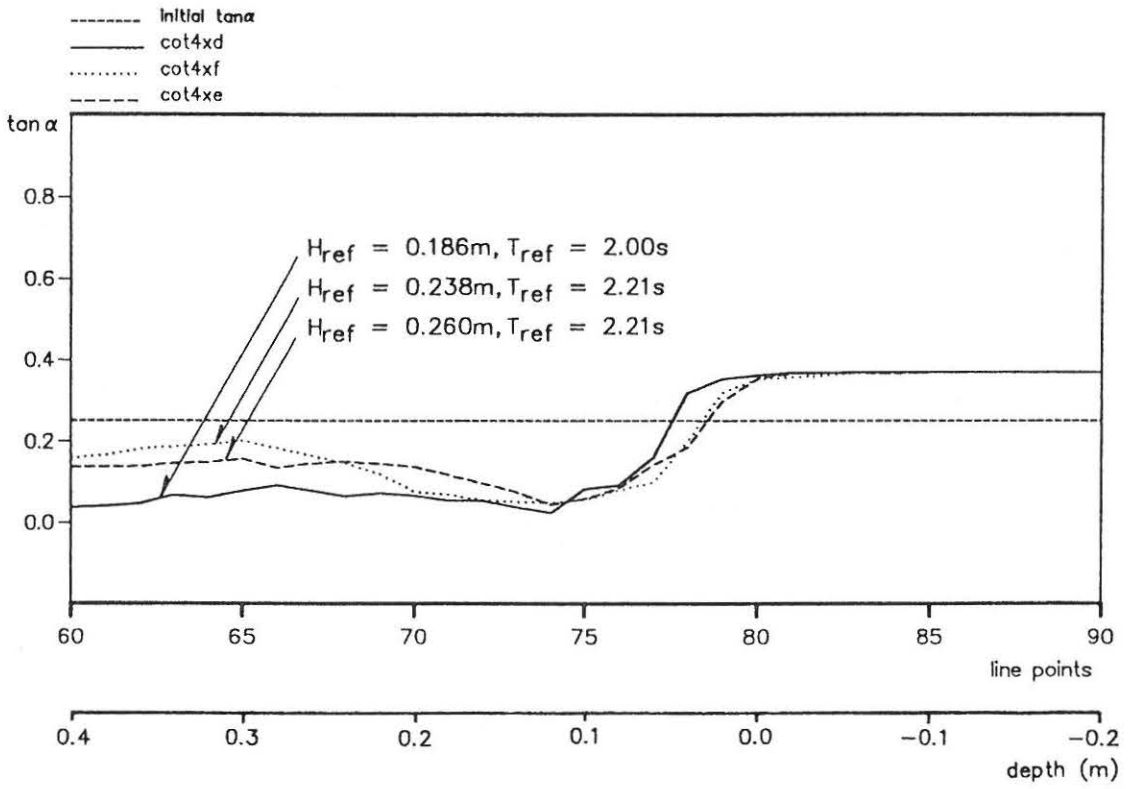

Fig 9.17 Dynamic limit solution-2 for cot4xd, cot4xf and cot4xe

Table 9.16 Simulated berm recession based on dynamic solution-2

Run No	r_{sim} (m), $b_v \geq 0.03$ m	$\overline{r}_{meas}$ (m)
cot4xh	0.36	0.39
cot4xd	0.47	0.39
cot4xi	0.88	0.81
cot4xf	0.89	0.81
cot4xg	0.90	0.97
cot4xe	0.91	0.97

Table 9.17 Simulated berm recession based on dynamic solution-2

Run No	r_{sim} (m), $b_v \geq 0.03$ m	$\overline{r}_{meas}$ (m)
cot4xd	0.47	0.39
cot4xl	0.46	0.39
cot4xm	0.43	0.39
cot4xn	0.38	0.39
cot4xo	0.45	0.39

Comparing Figs 9.7 and 9.16 is seen that at run cot4xd there is a transition from the static solution to the dynamic solution-2 combined with the static solution equivalent to the transition with the dynamic solution-1, cf the preceeding section.

Comparing Figs 9.15 and 9.17, the same observations as with the dynamic solution-1 can be made: with runs cot4xf and cot4xe, the limit profile is almost reached, and the two limit profiles are approximately identical. Again, a comparison between the simulated and the measured berm recessions indicate that the development in r is too low from run cot4xf to cot4xe, cf Table 9.16. Table 9.17 shows the influence of varying the porosity and the virtual mass coefficient respectively.

The simulated profile development is shown in Fig 9.18 with $\beta'=3$ applied for all simulations. For the mildest wave climate, the static solution is applied and for the three more severe conditions, the dynamic solution-2 combined with the static solution is applied.

9.6 Comparison to Straight Slopes

Van der Meer (1988) carried out physical model tests with straight porous slopes and berm breakwater profiles. The present equilibrium profile model is compared to two selected tests, with data as shown in Table 9.18. For both tests, D_{n50} equals 0.026 m and Δ equals 1.615.

Table 9.18 Selected tests by Van der Meer (1988)

Initial slope	H_s (m)	T_m (s)	H^*	T^*	H^*T^*
1:3	0.19	2.50	4.52	48.6	220
1:5	0.18	1.75	4.29	34.0	146

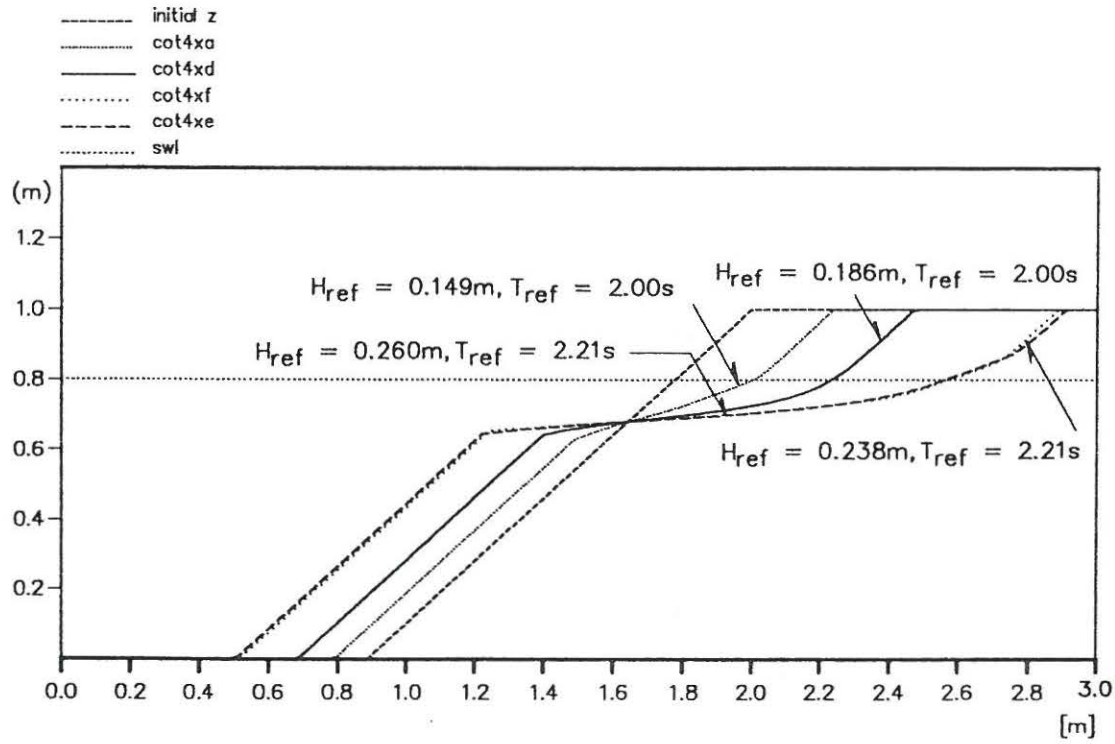

Fig 9.18 Simulated profile development for cot4xa, cot4xd, cot4xf and cot4xe

The input data for the corresponding computer runs are shown in Table 9.3. The values of n, β' and C_m are assumed. Like with the previous computer runs, the wave heights are adjusted with a factor of 0.93. The simulations are carried out with the same parameters as with the berm breakwaters described in Sections 9.3 to 9.5. For both cases, the wave climates, expressed through H^* and T^*, yield combined dynamic and static solutions to the equilibrium profiles, which are in both cases found by dynamic solution-1 combined with the static solution as well as dynamic solution-2 combined with the static solution.

For the initially steep slope, the reshaped profiles shown in Figs 9.20 and 9.21 compare well to the measured profile shown in Fig 9.19. The intersection point between the initial and the reshaped profile is the same as with the berm breakwater simulations, ie h_{02}=0.12 m.

For the computation with an initial slope of 1:5, the sensitivity of the equilibrium profile to the location of the point of maximum uprush velocity, x_{01} has been considered. From the computations, it was found that h_{01} is approximately equal to zero, cf Table 9.4. Also with h_{01}, there is no or only insignificant variation with the initial slope, cf Table 9.4, and hence the intersection point keeps the same during the entire reshaping process. Comparing to the physical model test, it is found that the best overall agreement is obtained for h_{01} equal to 0.02 m, ie h_{01}/h_s equal to 0.025, as there is a slight tendency to outwards movement of the profile in SWL as known from observations. Also the velocity measurements by Sawaragi et al (1983) indicate that the point x_{01} is close to SWL, cf Section 6.2.

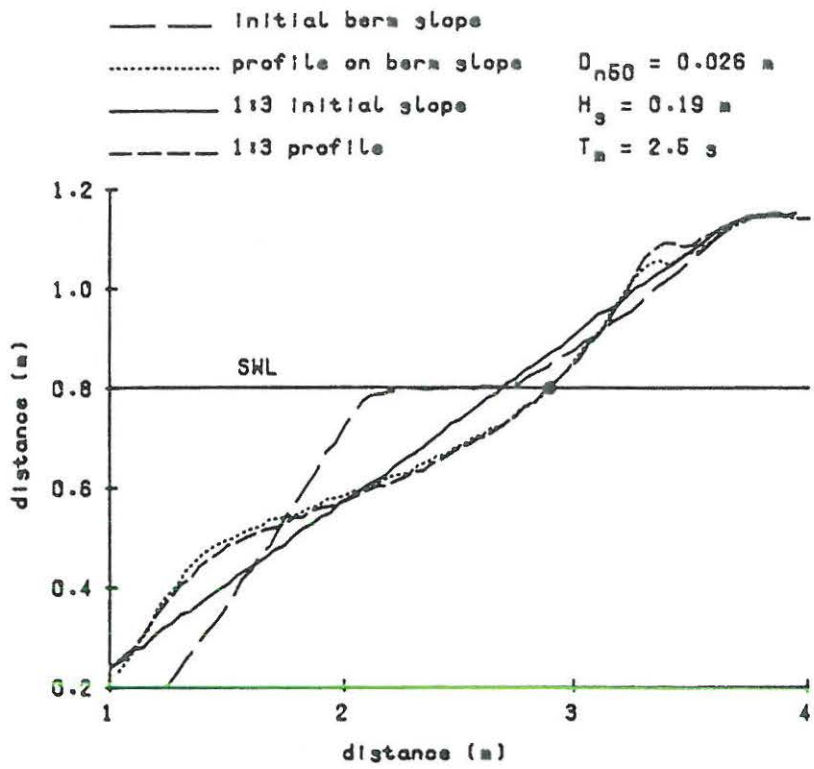

Fig 9.19 Physical model tests with initially steep slope, from Van der Meer (1988)

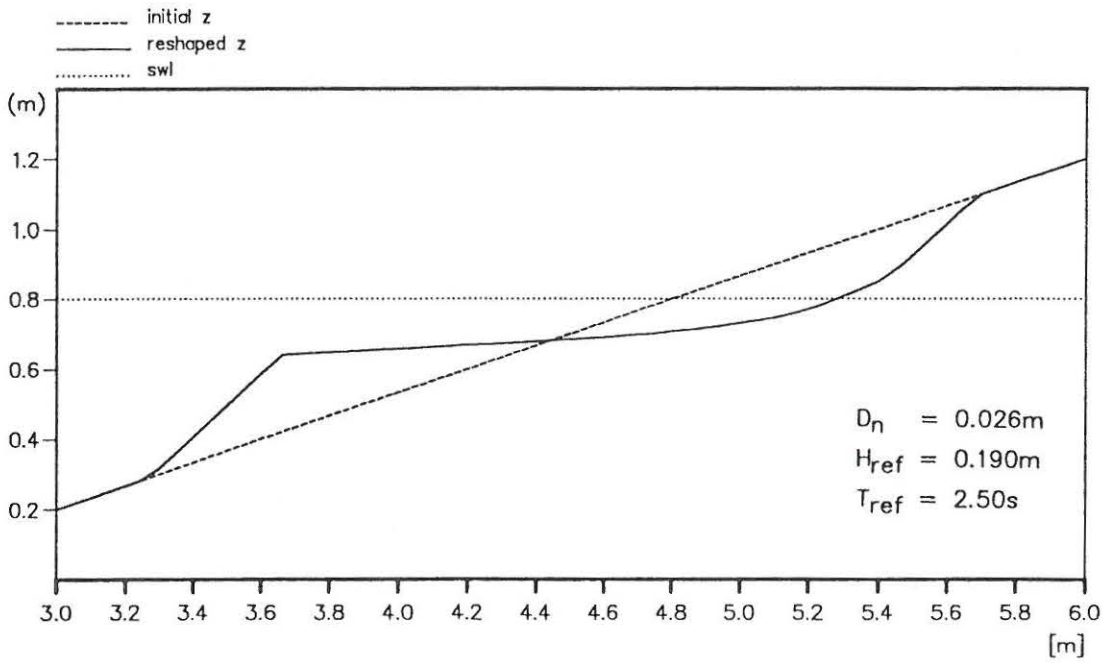

Fig 9.20 Predicted profile for initially steep slope, dynamic solution-1 combined with static solution

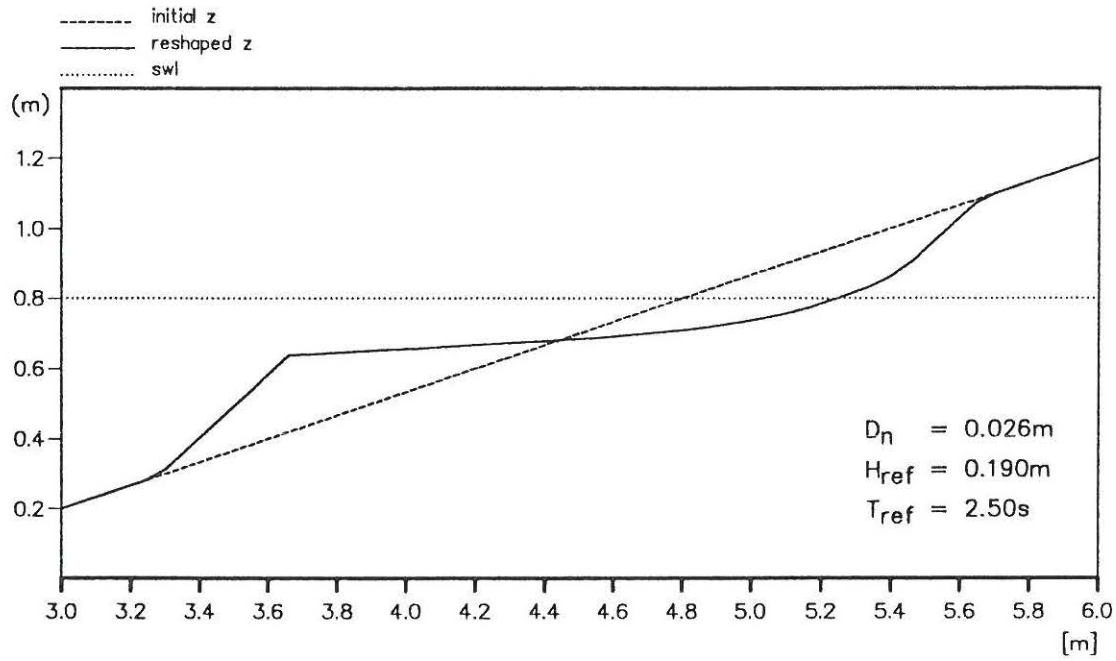

Fig 9.21 Predicted profile for initially steep slope, dynamic solution-2 combined with static solution

Fig 9.22 shows the measured development of initially flat rock slopes and gravel beaches. As can be seen, there is a step in the profile with an outer flat slope in the order of 0.1 and a steeper slope, cf Van der Meer (1988). The step is most pronounced for high values of H^* and T^*. It is likely that the flat part of the step is associated with plunging breakers impinging on the bed. If this is the case, we have in this place reached the limit of the capabilities of the present hydrodynamic model, as no wave breaking is included. Figs 9.23 and 9.24, modelled with D_n equal to 0.026 m, show that the steeper part of the step, actually being in static equilibrium, and the rest of the profile above is modelled correctly. On the figures is also indicated the impact of an artificially imposed lower limit of the reshaped profile, in the present example equal to a water depth of 0.20 m.

As the above simulations with straight slopes are carried out with the same calibrated hydrodynamic model and the same calibrated reshaping model as the berm breakwater profiles, further evidence of the theory is thus made. In order to simulate berm breakwater profiles, it is not necessary to solve the problems associated with the step appearing on initially flat slopes, however, it is a subject for further research.

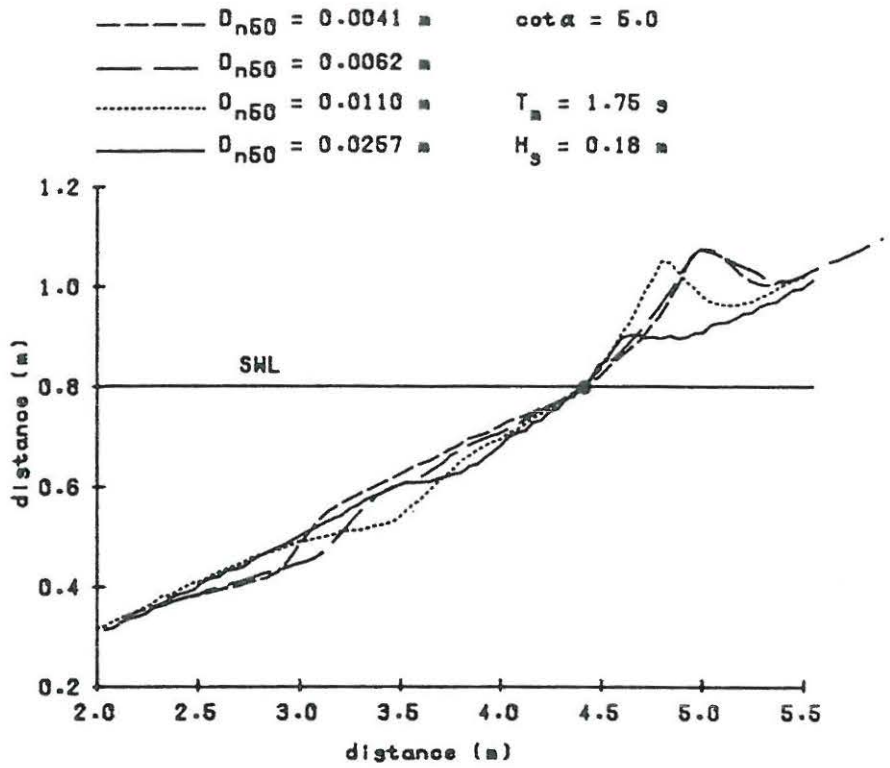

Fig 9.22 Physical model tests with initially flat slope, from Van der Meer (1988)

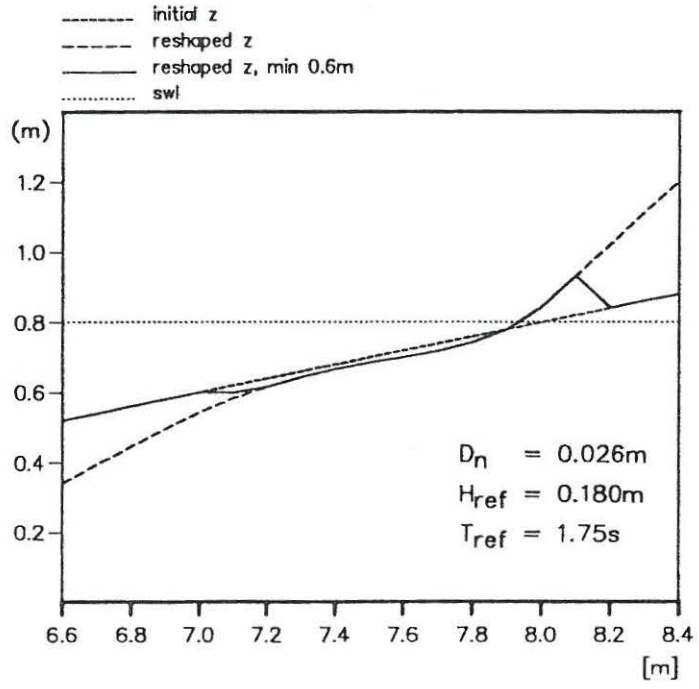

Fig 9.23 Predicted profile for initially flat slope, dynamic solution-1 combined with static solution

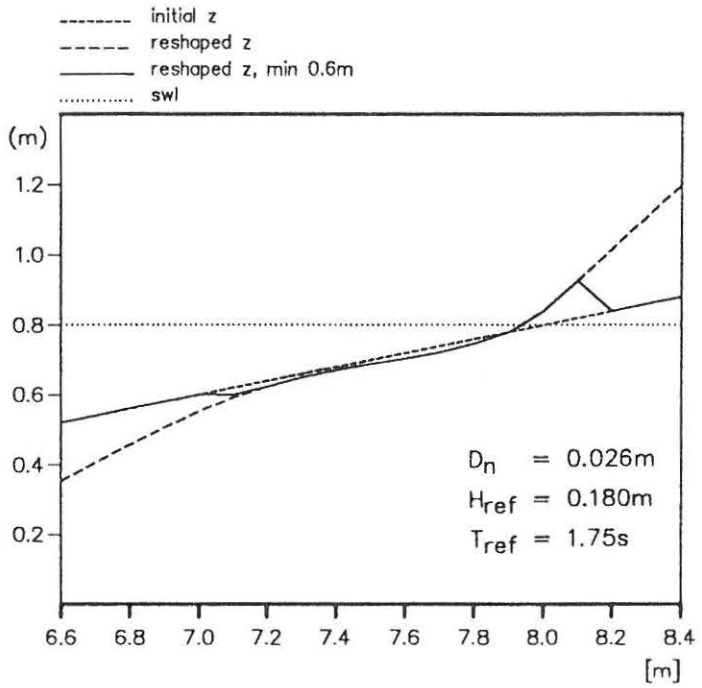

Fig 9.24 Predicted profile for initially flat slope, dynamic solution-2 combined with static solution

10 CONCLUSIONS

From the literature study, it is found that the hydraulic radius formulation of the stationary porous flow resistance as function of the porosity and grain diameter, given by Ergun (1952) is applicable in the Forchheimer flow regime as well as in the turbulent flow regime. This is justified by considering Navier-Stokes' equations and from a dimensional analysis. From the literature porous flow resistance coefficients are found: Section 4.4 deals with the Darcy and Forchheimer flow regimes and Section 4.5 with the fully turbulent flow regime. It appears that almost all experiments with unidirectional flow, known to the author, have been carried out with the direction of the flow normal to the longitudinal axis of the stones. For the scarse tests with parallel flow, there may be a tendency towards lower flow resistance coefficients. As a suggestion for further research, experiments comprising both directions applied to the same material should be carried out.

For non-stationary flow, the linear and quadratic flow resistance terms can be described by the hydraulic radius theory. The inertia term of the extended Forchheimer expression is described by a cylinder/sphere analogy. In principle, the quadratic flow resistance can also be described by the drag term of the cylinder/sphere analogy, but as the detailed velocity distribution as a function of the porosity is unknown for separated flow, the drag analogy has no practical importance. The inertia term of the cylinder/sphere analogy consists of a part related to the volume of water and to a part related to the volume of solids, the latter being quantified by a virtual mass coefficient. The virtual mass coefficient with the discharge velocity as reference velocity is described by a potential theory based on the method of images usually applied to groups of cylinders, and for the present purpose extended to a porous medium. Comparing to the oscillatory water tunnel tests the following can be concluded:

- a plot of the ratio between measured oscillatory and stationary quadratic flow resistance coefficients vs the Keulegan-Carpenter number shows that for low values of the Keulegan-Carpenter number, there is a slight increase in the flow resistance

- from comparison to measurements with the cylinders, it is found that the predicted variation with the porosity of the virtual mass coefficient based on the discharge velocity is correct. A coefficient is fitted to the measurements, one for cylinders and one for spheres and rock respectively

- the measurements with the cylinders show that the alternative description based on the pore velocity yields a virtual mass coefficient which can be regarded as constant over a wide range of porosities.

In order to further examine the variation of the flow resistance coefficients with the Keulegan-Carpenter number, the porosity, gradation, stone shape, stone orientation and surface roughness, it is suggested that more experiments with non-stationary flow should be carried out.

Considering the macroscopic flow on and in a straight porous slope, it is found that DHI's numerical model, SYSTEM 3xz, is applicable. Some limitations, however, are the description of the velocity profile above the surface of the slope and the lack of wave breaking in the model. It is found that the stepped surface of the structure, due to the discretisation, yields velocities immediately above the structure that are too low. This discrepancy is counteracted by application of an artificially high value of the friction factor in the hydrodynamic model as well as in the proceeding reshaping model. The friction factor

is fitted giving the best concordance with known criteria for initiation of armour stone movements and observations. In this way, the value of the bed shear stress becomes correct. As a suggestion for further development of SYSTEM 3xz, the problem with the velocity profile should be overcome. It is anticipated, however, that the friction factor for the complex flow case in consideration will have to be fitted to some extent, unless very precise models, including wave breaking, will be available.

The lack of wave breaking in the model may be important to the ratio between the uprush and downrush velocities which is essential to the berm breakwater equilibrium model developed. The problem with the wave breaking may possibly hinder a correct description of the variation of the equilibrium profile with the water depth, as the impact of lowering the water depth, which is equivalent to increasing the Ursell parameter, is an increase in the ratio between the uprush and downrush velocities, considering a plane and impervious bottom. In the case of wave breaking on a slope, this ratio is likely to be altered by the wave breaking. In the authors opinion, high priority should be given to inclusion of wave breaking in the two-dimensional hydrodynamic models in general, as the significance to the berm breakwater profile is uncertain.

A parameter important to the present model is the depth of maximum downrush velocity, which is interpreted as the intersection point between the developed and the initially steep profile. It appears from the computer simulations that a representative value is a water depth of 0.12 m. This value seems too low as compared to physical model tests yielding a value around 0.20 m and compared to velocity measurements indicating a value around 0.16 m. The entire model, however, shows a fairly good agreement between the simulated and measured berm recessions. Similarly, the point of maximum uprush velocity is interpreted as the intersection point between the developed profile and the initially flat profile. The computer model, the physical model tests with flat slopes and the velocity measurements all imply a point around SWL. The behaviour of these maximum velocity points as function of a broader range of the water depth in front of the structure, the wave height and the wave period could be a subject for further research. As an important result to the reshaping process, the maximum velocity points appear to be independent of the initial slope and the wave height and wave period actually conforming to observations.

Two different types of models decribing the equilibrium berm breakwater profile have been developed: a static model based on a Shields' approach and dynamic models based on the theory for transfer of shear stress due to occasional encounters of moving and fixed stones. Despite the uncertainties associated with the selection of a proper set of model coefficients, which are always present in models of complex phenomena, several conclusions can be drawn, actually conforming to observations:

- the models imply an S-shaped profile with a steep lower slope (angle of repose), a middle slope and an upper slope

- there is clearly a shift from static to dynamic equilibrium when the wave climate is intensified, typically the transition happens at a value of $H/\Delta D_n$ at approximately 3.25

- comparing to physical model tests, it appears that the berm recession, is described fairly good for values of $H/\Delta D_n$ ranging between 2.6 and 4.6, which is the tested range

- application of the model to initially straight slopes gives good results in case of an initially steep slope, whereas the lack of wave breaking in the hydrodynamic model becomes pronounced in the case of an initially flat slope.

Further, the following conclusions can be drawn based on the model alone, but with no support in observations:

- concerning the dynamic models, two different solutions based on slightly different assumptions are applied yielding only minor differences in the results

- the impact of varying the porous flow resistance parameters within realistic ranges is visible, but still within the range of uncertainty concerning the measured berm recessions.

The impact of the reshaped model on the hydrodynamics is included in the model by assuming the equilibrium slope to be a function of the local water depth. It can be discussed whether the model should be extended to include consecutive recalculations of the hydrodynamics and the reshaped profile until stationary conditions are obtained. In the authors opinion the aforementioned limitations in the hydrodynamic model should be overcome before such a model should be made, as the discrepancies due to the uncertainties in the present hydrodynamic model available are likely to be in the same order of magnitude as the improvements which can be obtained by recalculations.

The present model gives a comprehension of the physics of berm breakwaters. In order to develop the model to a design method, the problems with the hydrodynamic model should be solved and secondly an extensive verification/calibration of the entire model complex should be carried out.

11 REFERENCES

Ahmed, N. and Sunada, D.K. (1969): *Non-linear flow in porous media*. Journal of the Hydraulics Div., ASCE, Vol 95, No HY6, pp 1847-1857.

Ahrens, J.P. and McCartney, B.L. (1976): *Wave period effect on the stability of riprap*. Civil Engineering in the Oceans, pp 1019-1034.

Andersen, O.H., Juhl, J., and Sloth, P. (1992): *Rear side stability of berm breakwaters*. 23rd International Conference on Coastal Engineering, pp 1020-1029.

Andersen, O.H., Van Gent, M.R.A., Van der Meer, J.W., Burcharth, H.F., and den Adel, H. (1993): *Non-steady oscillatory flow in coarse granular materials*. MAST G6-S, Project I.

Austin, D.I. and Schlueter, R.S. (1982): *A numerical model of wave/breakwater interactions*. 18th International Conference on Coastal Engineering, pp 2079-2096.

Battjes, J.A. (1974): *Computation of set-up, longshore currents, run-up and overtopping due to wind-generated waves*. Delft University of Technology.

Bruun, P. (Ed.) (1985): *Design and construction of mounds for breakwaters and coastal protection*. Elsevier.

Burcharth, H.F. and Andersen, O.H. (1993): *On the one-dimensional unsteady porous flow equation*. MAST G6-S, Project I, Aalborg University, Department of Civil Engineering and Danish Hydraulic Institute.

Burcharth, H.F. and Christensen, C. (1991): *On stationary and non-stationary porous flow in coarse granular materials*. MAST G6-S, Project I, Aalborg University, Department of Civil Engineering, Report.

Burcharth, H.F. and Frigaard, P. (1987): *Reshaping breakwaters. On the stability of roundheads and trunk erosion in oblique waves*. Berm Breakwaters: Unconventional Rubble-Mound Breakwaters, ASCE, pp 55-72.

Burcharth, H.F. and Frigaard, P. (1988): *On three-dimensional stability of reshaping breakwaters*. 21st International Conference on Coastal Engineering, pp 2284-2298.

Burcharth, H.F. and Thompson, A.C. (1982): *Stability of armour units in oscillatory flow*. Presented at Coastal Structures '83.

Carman, P.C. (1937): *Fluid flow through granular beds*. Transactions, Institution of Chemical Engineers, Vol 15, pp 150-166.

CIRIA/CUR (1991): *Manual on the use of rock in coastal and shoreline engineering*. CIRIA Special Publication 83/CUR report 154.

Dalrymple, R.A., Losada, M.A., and Martin, P.A. (1991): *Reflection and transmission from porous structures under oblique wave attack*. Journal of Fluid Mechanics, Vol 224, pp 625-644.

Danish Engineering Academy (1991-92): *B.Sc. Dissertations by Andersen, F.J. and Poulsen, C., by Johannsen, J. and Sørensen, B.H, and by Jensen, J.G. and Steenberg, C.M.* In Danish.

Danish Hydraulic Institute (1992): *Numerical geohydrodynamic methods*. Final Report.

Delft Geotechnics (1993): *MBREAK, Computer model for the water motion on and inside a rubble mound breakwater*. MAST G6-S, Project I.

Delft Hydraulics (1990): *BREAKWAT, Design tool for rubble mound breakwaters*. Manual.

Dybbs, A. and Edwards, R.V. (1984): *A new look at porous media fluid mechanics - Darcy to turbulent*. In Bear, J. and Corapcioglu, M.Y. (Eds.), Fundamentals of Transport Phenomena in Porous Media, Martinus Nijhoff Publishers, pp 199-256.

Dudgeon, C.R. (1966): *An experimental study of the flow of water through coarse granular media*. La Houille Blanche, No 7, pp 785-801.

Engelund, F.A. (1953): *On the laminar and turbulent flows of ground water through homogeneous sand*. Danish Academy of Technical Sciences.

Engelund, F. (1975): *Steady transport of moderately graded sediment (Part 2)*. Prog. Rep. 35, Inst. Hydrodyn. and Hydraulic Engrg., Tech. Univ. Denmark, pp 31-36.

Ergun, S. (1952): *Fluid flow through packed columns*. Chemical Engineering Progress, Vol 48, No 2, pp 89-94.

Fand, R.M., Kim, B.Y.K., Lam. A.C.C. and Phan, R.T. (1987): *Resistance to the flow of fluids through simple and complex porous media whose matrices are composed of randomly packed spheres*. Journal of Fluids Engineering, ASME, Vol 109, pp 268-274.

Fischer, M., Juhl, J., and Rasmussen, E.B. (1992): *Numerical modelling of waves and currents with regard to coastal structures*. 23rd International Conference on Coastal Engineering, pp 170-183.

Hall, K.R. and Foster, D.N. (1990): *Internal and external pressure measurements in reshaped breakwaters*. Coastal Engineering, Vol 14, pp 215-232.

Hall, K.R. and Kao, J.S. (1991): *The influence of armour stone gradation on dynamically stable breakwaters*. Coastal Engineering, Vol 15, pp 333-346.

Hannoura, A.A. and McCorquodale, J.A. (1978a): *Virtual mass of coarse granular media*. Journal of the Waterway, Port, Coastal and Ocean Div., ASCE, Vol 104, No WW2, pp 191-200.

Hannoura, A.A. and McCorquodale, J.A. (1978b): *Air-water flow in coarse granular media*. Journal of the Hydraulics Div., ASCE, Vol 104, No HY7, pp 1001-1010.

Hannoura, A.A. and McCorquodale, J.A. (1985a): *Rubble mounds: Hydraulic conductivity equation*. Journal of Waterway, Port, Coastal and Ocean Engineering, ASCE, Vol 111, No 5, pp 783-799.

Hannoura, A.A. and McCorquodale, J.A. (1985b): *Rubble Mounds: Numerical modelling of wave motion.* Journal of Waterway, Port, Coastal and Ocean Engineering, ASCE, Vol 111, No 5, pp 800-816.

Hannoura, A.A. and Barends, F.B.J. (1981): *Non-Darcy flow; a state of the art.* Euromech. 143, Flow and Transport through Porous Media, pp 37-51.

Hibberd, S., and Peregrine, D.H. (1979): *Surf and run-up on a beach: A uniform bore.* Journal of Fluid Mechanics, Vol 95, Part 2, pp 323-345.

Hirt, C.W. and Nichols, B.D. (1981): *Volume of fluid method for the dynamics of free boundaries.* Journal of Computational Physics 39, pp 201-225.

Hölscher, P., De Groot, M.B. and Van der Meer, J.W. (1988): *Simulation of internal water movement in breakwaters.* Modelling Soil-Water-Structure Interactions, Kolkman et al (eds), pp 427-433.

Irmay, S. (1958): *On the theoretical derivation of Darcy and Forchheimer formulas.* Transactions, American Geophysical Union, Vol 39, No 4, pp 702-707.

Jensen, O.J. (1984): *A monograph on rubble mound breakwaters.* Danish Hydraulic Institute, Hørsholm.

Jensen, O.J. and Juhl, J. (1988): *Results of model tests on 2D breakwater structure.* Breakwaters '88, pp 13-25.

Jensen, O.J. and Klinting, P. (1983): *Evaluation of scale effects in hydraulic models by analysis of laminar and turbulent flows.* Coastal Engineering, Vol 7, No 4, pp 319-329.

Jensen, O.J. and Sørensen, T. (1987): *Hydraulic performance of berm breakwaters.* Berm Breakwaters: Unconventional Rubble-Mound Breakwaters, ASCE, pp 73-91.

Jonsson, I.G. (1976): *Discussion of 'Friction factor under oscillatory waves' by J.W. Kamphuis.* Journal of the Waterways, Harbors and Coastal Engineering Division, ASCE, Vol 102, No WW1, pp 108-109.

Jonsson, I.G. and Carlsen, N.A. (1976): *Experimental and theoretical investigations in an oscillatory turbulent boundary layer.* Journal of Hydraulic Research, IAHR, Vol 14, No 1 pp 45-60.

Juhl, J. and Jensen, O.J. (1990): *Wave forces on breakwater armour units.* 22nd International Conference on Coastal Engineering, pp 1538-1551.

Juhl, J. and Jensen, O.J (1993): *Practical experience with berm breakwaters.* MAST G6-S, Project I, Danish Hydraulic Institute.

Kobayashi, N. and Otta, A.K. (1987): *Hydraulic stability analysis of armor units.* Journal of Waterway, Port, Coastal and Ocean Engineering, ASCE, pp 171-186.

Kobayashi, N., Roy, I. and Otta, A.K. (1986): *Numerical simulation of wave run-up and armor stability.* Offshore Technology Conference, pp 51-60.

Kobayashi, N. and Wurjanto, A. (1990a): *Numerical model for waves on rough permeable slopes*. Journal of Coastal Research, pp 149-166.

Kobayashi, N. and Wurjanto, A. (1990b): *Irregular waves on rough permeable slopes*. Journal of Coastal Research, pp 167-184.

Komar, P.D. and Miller, M.C. (1974): *Sediment threshold under oscillatory waves*. 14th International Conference on Coastal Engineering, pp 756-775.

Le Méhauté, B. (1957): *Perméabilité des digues en enrochements aux ondes de gravité périodiques (the perviousness of rock fill breakwaters to periodic gravity waves)*. La Houille Blanche, No 6, pp 903-919.

Lissev, N. (1993): *Influence of the core configuration on the stability of berm breakwaters*. Department of Structural Engineering, University of Trondheim, The Norwegian Institute of Technology, Report No R-6-93.

Madsen, O.S. (1974): *Wave transmission through porous structures*. Journal of the Waterways, Harbours and Coastal Engineering Div, ASCE, Vol 100, No WW3, pp 169-188.

Madsen, O.S. and Grant, W.D. (1975): *The threshold of sediment movement under oscillatory waves: A discussion*. Journal of Sedimentary Petrology, Vol 45, No 1, pp 360-361.

Madsen, O.S. and Grant, W.D. (1976): *Sediment transport in the coastal environment*. Massachusetts Institute of Technology, Department of Civil Engineering, Report No 209.

Madsen, O.S. and White, S.M. (1975): *Reflection and transmission characteristics of porous rubble mound breakwaters*. Massachusetts Institute of Technology, Department of Civil Engineering, Report No 207.

Madsen, P.A. (1983): *Wave reflection from a vertical permeable wave absorber*. Coastal Engineering, Vol 7, No 4, pp 381-396.

Massel, S.R. and Mei, C.C. (1977): *Transmission of random wind waves through perforated or porous breakwaters*. Coastal Engineering, Vol 1, No 1, pp 63-78.

McCorquodale, J.A. (1970): *Finite element analysis of non-Darcy flow*. Ph.D. Thesis presented to the University of Windsor, Canada.

McCorquodale, J.A., Hannoura, A.A. and Nasser, M.S. (1978): *Hydraulic conductivity of rockfill*. Journal of Hydraulic Research, IAHR, Vol 16, No 2, pp 123-137.

Mei, C.C. (1983): *The applied dynamics of ocean surface waves*. Wiley, New York.

Milne-Thomsen, L.M. (1968): *Theoretical hydrodynamics*. Macmillan, London.

Munk, W. and Wimbush, M. (1969): *A rule of thumb for wave breaking over sloping beaches*. Oceanology, Vol 9, pp 56-59.

Nasser, M.S. and McCorquodale, J.A. (1975): *Wave motion in rockfill.* Journal of the Waterways, Harbors and Coastal Engineering Division, ASCE, Vol 101, No WW2, pp 145-159.

Norton, P.A. and Holmes, P. (1992): *Armour displacements on reshaping breakwaters.* 23rd International Conference on Coastal Engineering, pp 1448-1460.

Oumeraci, H. (1991): *Wave-induced pore pressure in rubble round breakwaters.* MAST G6-S, Project I, Report, Franzius Institute.

Rance, P.J. and Warren, N.F. (1968): *The threshold of movement of coarse material in oscillatory flow.* 11th International Conference on Coastal Engineering, pp 487-491.

Ribberink, J.S. (1989): *The large oscillating water tunnel.* Delft Hydraulics, Report H840.

Sandström, Å. (1974): *Vågkrafter på block i vågbrytarsländer (wave forces on blocks of rubble mound breakwaters).* Bulletin No 83, Hydraulics Laboratory, Royal Inst. of Technology, Stockholm, Sweden.

Sarpkaya, T. and Isaacson, M. (1981): *Mechanics of wave forces on offshore structures.* Van Nostrand Reinhold Company, New York, N.Y.

Sawaragi, T., Ryu, C. and Iwata, K. (1983): *Considerations of the destruction mechanism of rubble mound breakwaters due to the resonance phenomenon.* 8th International Harbour Congress, Session 3, pp 3.197-3.208.

Scheidegger, A.E. (1974): *The physics of flow through porous media.* University of Toronto Press, Toronto.

Shih, R.W.K. (1990): *Permeability characteristics of rubble material - New formulae.* 22nd International Conference on Coastal Engineering, pp 1499-1512.

Shore Protection Manual (1984). US Army Corps of Engineers, Coastal Eng. Res. Center, US Govt. Printing Office, Washington, DC.

Sleath, J.F.A. (1978): *Measurements of bed load in oscillatory flow.* Journal of the Waterway, Port, Coastal and Ocean Division, ASCE, Vol 104, No WW4, pp 291-307.

Smith, G. (1991): *Comparison of stationary and oscillatory flow through porous media.* M.Sc. thesis, Queen's University, Canada.

Sollitt, C.K. and Cross, R.H. (1972a): *Wave reflection and transmission at permeable breakwaters.* Massachusetts Institute of Technology, Department of Civil Engineering, Report No 147.

Sollitt, C.K. and Cross, R.H. (1972b): *Wave transmission through permeable breakwaters.* 13th International Conference on Coastal Engineering, pp 1827-1846.

Solvik, Ø. and Svee R. (1976): *Flow condition criteria and some throughflow problems in rockfill.* Commission Internationale des Grands Barrages, Douzième Congrès des Grands Barrages, Q.45, R.37, pp 637-646.

Sun, Z.C., Williams, A.F. and Allsop, N.W.H. (1992): *Numerical determination of wave induced flow in rubble mound breakwaters.* 23rd International Conference on Coastal Engineering, pp 1599-1612.

Svendsen, I.A. and Jonsson, I.G. (1980): *Hydrodynamics of coastal regions.* Den Private Ingeniørfond, Techn. Univ. Denmark.

Thompson, A.C. (1988): *Numerical model of breakwater wave flows.* 21st International Conference on Coastal Engineering, pp 2013-2027.

Thompson, A.C. and Burcharth, H.F. (1984): *Stability of armour units in flow through a layer.* 19th International Conference on Coastal Engineering, pp 2608-2619.

Tørum, A. (1992a): *Flow through porous media.* MAST G6-S, Project I, Norwegian Hydrotechnical Laboratory, Note.

Tørum, A. (1992b): *Wave Induced Water Particle Velocities and Forces on an Armour Unit on a Berm Breakwater.* MAST G6-S, Project III-B, SINTEF NHL, Report.

Tørum, A. and Van Gent, M.R.A. (1992): *Water particle velocities on a berm breakwater.* 23rd International Conference on Coastal Engineering, pp 1651-1665.

Underwood, E.E. (1970): *Quantitative stereology.* Addison-Wesley Publishing Company, Massachusetts.

Van der Meer, J.W. (1988): *Rock slopes and gravel beaches under wave attack.* Ph.D. thesis presented to Delft University of Technology, Delft Hydraulics, Publ No 396.

Van der Meer, J.W. and Breteler, M.K. (1990): *Measurement and computation of wave induced velocities on a smooth slope.* 22nd International Conference on Coastal Engineering, pp 191-204.

Van der Meer, J.W., Petit, H.A.H., Van den Bosch, P., Klopman, G., and Broekens, R.D. (1992): *Numerical simulation of wave motion on and in coastal structures.* 23rd International Conference on Coastal Engineering, pp 1772-1784.

Van der Meer, J.W. and Veldman, J.J. (1992): *Singular points at berm breakwaters: Scale effects, rear, round head and longshore transport.* Coastal Engineering, Vol 17, pp 153-171.

Van Gent, M.R.A. (1992a): *Formulae to describe porous flow.* Communications on Hydraulic and Geotechnical Engineering, Delft University of Technology.

Van Gent, M.R.A. (1992b): *Manual of ODIFLOCS.* MAST G6-S, Project I.

Van Gent, M.R.A. (1993): *Stationary and oscillatory flow through coarse porous media.* Communications on Hydraulic and Geotechnical Engineering, Delft University of Technology.

Wang, H. and Gu, Z. (1988): *Gravity waves over porous bottom.* 2nd International Symposium on Wave Research and Coastal Engineering, Hannover, Germany, pp 1-21.

Ward, J.C. (1964): *Turbulent flow in porous media*. Journal of the Hydraulics Div., ASCE, Vol 90, No HY5, pp 1-12.

Wibbeler, H. and Oumeraci, H. (1992): *Finite element simulation of wave-induced internal flow in rubble mound structures*. 23rd International Conference on Coastal Engineering, pp 1706-1719.

Williams, A.F. (1992): *Permeability of rubble mound material*. Mast G6-S, Project I, Hydraulics Research, Draft Report.

Yamamoto, T. (1976): *Hydrodynamic forces on multiple circular cylinders*. Journal of the Hydraulics Div., ASCE, Vol 102, No HY9, pp 1193-1210.

ISBN 87-90034-06-6